FUNDAMENTAL STUDY OF NEAR-LIMIT SMOULDERING FIRE DYNAMICS

SHAORUN LIN

PhD

The Hong Kong Polytechnic University

2021

The Hong Kong Polytechnic University

Department of Building Environment and Energy Engineering

Fundamental Study of Near-Limit Smouldering Fire Dynamics

Shaorun Lin

A thesis submitted in partial fulfilment of the requirements for the degree of

Doctor of Philosophy.

June 2021

CERTIFICATE OF ORIGINALITY

I hereby declare that this thesis is my own work and that, to the best of my knowledge and belief, it reproduces no material previously published or written, nor material that has been accepted for the award of any other degree or diploma, except where due acknowledgement has been made in the text.

______________________(Signed)

Shaorun Lin (Name of Student)

DEDICATION

To my beloved parents

whom bring support and inspiration to my study and life.

ABSTRACT

Fundamental Study of Near-Limit Smouldering Fire Dynamics

by

Shaorun Lin

Doctor of Philosophy in Department of Building Environment and Energy Engineering
The Hong Kong Polytechnic University, June 2021
Supervised by Dr Xinyan Huang and Dr Michael J. Gollner

Smouldering fire is slow, low-temperature and flameless, and is one of the largest and longest-lasting combustion phenomena on Earth, different from flaming fire regarding chemistry, transport processes and time scales. Smouldering fire is a heterogeneous process sustained when oxygen directly attacks the hot fuel surface. Smouldering fire is the dominant burning behaviours of porous and charring fuels, such as wood, char, peat, and polyurethane (PU). For example, smouldering wildfire is a significant disturbance to peatlands worldwide, and it contributes significantly to global carbon emissions and provides positive feedback to climate change. Despite its critical hazard to humans and the environment, our understanding of it remains limited.

Compared to the flaming fire, smouldering fire can be initiated by a much weaker ignition source and provide a shortcut to flaming through smouldering-to-flaming transition. Traditionally, smouldering spreads in a creeping fashion, typically on the order of 1 cm/h, which is at least two orders of magnitude smaller than the spread rate of flaming fires. On the other hand, smouldering fire can be sustained in an extremely low oxygen concentration (~11%). However, very few works have been conducted to systematically study the near-limit smouldering fire dynamics before the research undertaken in this report.

This thesis is divided into eleven chapters: except for the chapter of introduction (Chapter 1) and concluding remarks (Chapter 11), each chapter takes the form of an independent paper, which has been published or submitted to a journal or conferences.

Part A includes three chapters (2-4), with the focus on the ignition limits of smouldering combustion. **Chapter 2** investigates the ignition limits of moist peat soil with moisture up to 100 wt.% under external radiation, and the critical ignition heat flux, ignition temperature, heat release rate and

CO/CO_2 ratio are compared thoroughly. **Chapter 3** explores the effect of the diameter of irradiation spot on the ignition limit of smouldering combustion experimentally and numerically, which reveals that the lateral conductive cooling effect within the fuel becomes more dominant for a smaller spotting area. **Chapter 4** describes the limits of transition from flaming to smouldering, where a unique wood combustion mode showing a near-limit blue flame was identified as an intermediate combustion mode between the buoyancy-controlled yellow flame and the smouldering combustion.

PART B includes three chapters (5-7), focusing on the quenching limit and quenching distance of smouldering combustion. **Chapter 5** explores the quenching limit and the applicability of quenching diameter in smouldering through laboratory-scale experiments, where the measured quenching diameter of smouldering was about 10 cm. **Chapter 6** develops a 2-D numerical model based on open-source code Gpyro and a previously developed 5-step kinetics of peat to verify the quenching diameter of smouldering combustion and further explore the effects of lateral overall heat transfer coefficient, oxygen concentration and ambient temperature on the quenching limits. **Chapter 7** explores the applications of quenching distance of smouldering combustion through constructing firebreak for extinguishing peat fire.

PART C includes three chapters (8-10), with the focus on the environmental impacts on the smouldering limits. **Chapter 8** quantifies the smouldering propagation rate on consolidated biomass and the blow-off limit under concurrent and opposed external airflows up to 50 m/s, where the effects of fuel diameter and density are thoroughly discussed. **Chapter 9** assesses the underlying mechanism of rain in suppressing the smouldering peat fire in the shallow soil layer up to 15 cm deep through laboratory experiments, where the extinction limit of suppressing smouldering peat fire is found. **Chapter 10** quantifies the minimum environmental temperature that allows the moist peat to smoulder, and then apply a typical vertical soil temperature profile to estimate the future depth of burn and carbon emissions in boreal peatland fires under the impact of global warming.

ACKNOWLEDGEMENTS

First and foremost, I would like to take this opportunity to express my appreciation to Dr Xinyan Huang who has brought me into the combustion and fire research in the first place. It is my great honour and fortune to be your first Ph.D. student at the Hong Kong Polytechnic University. Your education, guidance, encouragement, and assistance have enabled me to overcome all the difficulties in the process of my study and life. I deeply appreciate all your contributions of time, vigour, patience, ideas, and instructions that make my academic experience productive and fruitful.

I would like to thank my co-supervisor Dr Michael J. Gollner (University of California, Berkeley) who continuously looks after me from the other side of ocean. I would like to learn more from you and collaborate with you in my future academic career.

For this thesis, I would like to thank all my co-authors, Peiyi Sun (Chapter 2 and 3, assistance in experiments), Yanhui Liu (Chapter 3,7 and 10, assistance in experiments), Siyan Wang (Chapter 3, assistance in experiments and formal analysis), Y. K. Cheung (Chapter 9, assistance in experiments), T. H. Chow (Chapter 8, assistance in experiments), Yang Xiao (Chapter 9, assistance in experiments), Dr Han Yuan (Chapter 3 and 6, assistance in simulations), as well as Dr Jian Gao and Dr Jie. Ji (Chapter 4, assistance in data analysis).

I also wish to thank many research collaborators for their valuable pieces of advice, Prof. Carlos Fernandez-Pello (University of California, Berkeley), Prof. Asif Usmani, Atif Ali Khan (Hong Kong Polytechnic University), Prof Cangsu Xu (Zhejiang University), Dr Supan Wang (Nanjing Technology University), and Prof Guillermo Rein (Imperial College, London).

I also would like to express my deep gratitude to all the current and previous members of PolyU Fire Lab: Peiyi Sun (Sally), Anwar Orabi, Atif Ali Khan, Caiyi Xiong, Yanhui Liu, Supan Wang, Han Yuan, Lingchu Su (Sue), Xiqiang Wu, Xiaoning Zhang, Yuying Chen, Tianhang Zhang, Zilong Wang, Tejeswar Yarlagadda, Domada Veera Venkata Ramakanth, Jin Qiu, Cheng Chen, Siyan Wang, Jingze Zhu, Yau Kuen Cheung (Daniel), Yang Xiao, Haoran Fan, Younggi Park, Zhirong Liang, Tsz Him Chow (Alvis), and Haiwei Li (Flora), who make my life fabulous and glamorous. I had a memorable time working with you, and it is my honour to be in the same academic family with all of you.

I wish to thank Prof Albert Simeoni (Worcester Polytechnic Institute) and Dr Long Shi (Royal Melbourne Institute of Technology) for serving as my external examiners.

I own my special thanks to my old friends, Jiahao Liang, Chenxi Jia, Zhixin Shen, Lunqian Lin, Donghong Lin, and Yuzhi Chen. Despite the great distance between us, I still appreciate your time and encouragement.

I want to acknowledge the financial supports from the National Natural Science Foundation of China, the Hong Kong Polytechnic University, and Society of Fire Protection Engineers (SFPE) Education & Scientific Foundation, and the travel support from the Association for Fire Ecology (AFE), Combustion Institute (CI), and International Association of Wildland Fire (IAWF).

I sincerely appreciate that my parents, sisters, and brothers have created the best environment for me in my life. With their understanding and support, I can persevere on the way to study. I have also been deeply grateful for the company and encouragement from Meidan Zhang. Your understanding and encouragement enabled me to triumph over the difficulties and challenges and made me stronger!

Shaorun Lin

Hong Kong

June 2021

TABLE OF CONTENTS

PART A

Ignition Limits of Smouldering: Criteria, Dimension Effect and Transition

PART B

Quenching Limit of Smouldering: Theory, Numerical Verification and Application

PART C

Environmental Impacts on Smouldering Limits: Wind, Weather and Climate

NOMENCLATURE

Symbol

a	strain rate (s^{-1})
A	pre-exponential factor (1/s)/area (m^2)
c	solid specific heat capacity (J/kg-K)
C	gas specific heat capacity (J/kg-K)
C	fitting coefficient (-) / constant (-)
d	depth (m)
D	mass diffusivity (m^2/s)/diameter (m)
D^*	quenching diameter (m)
Da	Damkohler number (-)
DOB	depth of burn (m)
DTG	derivative of thermogravimetric
E	activation energy (kJ/mol)/Energy (MJ)
$\bar{h}$	specific enthalpy (J/kg)
h_c	convective coefficient (W/m^2-k)
h_m	mass-transfer coefficient (kg/m^2-s)
H	height (m)
ΔH	heat of combustion (MJ/kg)
I	thermal inertia (J/m^2-K-$s^{1/2}$)
I	rainfall intensity (mm/h)
k	thermal conductivity (W/m-K)
K	permeability (m^2)
L	length (m)
m	mass (kg)
$\dot{m}''$	mass flux (kg/m^2)
M	molar mass (kg/mol)
MC	Moisture content (%)
n	reaction order (-)

Greeks

α	thermal diffusivity (m^2/s)
α	warming rate (°C/decade)
γ	radiative conductivity coefficient (m)
δ	thickness (m)
ε	emissivity (-)
κ	permeability (m^2)
ρ	density (kg/m^3)
ν	viscosity (Pa · s)/stoichiometry (-)
ψ	porosity (-)
$\dot{\omega}'''$	volumetric reaction rate (kg/m^3-s)
τ	tortuosity (-)

Subscripts

0	initial
a	airflow/ambient
∞	ambient
α	α-char
β	β-char
a	ash
ch	chemical
con	concurrent
$cond$	conduction
$conv$	convection
d	destruction
dr	drying
eff	effective
ex	extinction

P	pressure (Pa)	f	formation/flaming
$\dot{q}''$	heat flux (kW/m^2)	g	gas
R	thermal resistance (m^2-K/W)	i	condensed species number
$\dot{R}$	regression rate (m/s)	j	gaseous species number
Re	Reynolds number (-)	k	reaction number
S	surface area (m^2)	o/ox	oxidation
S_{sm}	smouldering propagation rate (cm/h)	O_2	oxygen
t	time (s)	p	pyrolysis/peat/preheating
T	temperature (°C or K)	s	solid
TG	thermogravimetric	sm	smouldering
u_a	internal airflow velocity (m/s)	T	thermal
U	overall heat transfer coefficient (W/m^2-k)	w	water/wall
U_a	external airflow velocity (m/s)		
X	volume fraction (-)		
Y	mass fraction (-)/year (-)		
Δx	distance (m)		
Δz	cell size (m)		

PUBLICATION

Journal paper

Publication arising from this thesis are summarized as below:

1) S. Lin, P. Sun and X. Huang (2019) *Can Peat Soil Support a Flaming Wildfire?* **International Journal of Wildland Fire** 28: 601-603. doi: 10.1071/WF19018.
2) S. Wang, S. Lin (co-first author), Y. Liu, X. Huang and M. Gollner (2021) *Smouldering Ignition using a Concentrated Solar Irradiation Spot*, **Fire Safety Journal** (under review).
3) S. Lin, X. Huang, J. Gao and J. Ji (2021) *Extinction of Wood Fire: A Near-Limit Blue Flame above Hot Smouldering Surface.* **Fire Technology**. doi: 10.1007/s10694-021-01146-6
4) S. Lin, X. Huang (2021) *Quenching of Smouldering: Effect of Wall Cooling on Extinction*, **Proceedings of the Combustion Institute** 38(3): 5015-5022. doi: 10.1016/j.proci.2020.05.017.
5) S. Lin, H. Yuan and X. Huang (2021) *A Computational Study on the Quenching and Near-Limit Propagation of Smouldering Combustion,* **Combustion and Flame** (under review).
6) S. Lin, Y. Liu and X. Huang (2021) *How to Build a Firebreak to Stop Smouldering Peat Fire: Insight from a Laboratory-Scale Study.* **International Journal of Wildland Fire** 30(6): 454-461. doi: 10.1071/WF20155.
7) S. Lin, T. H. Chow, and X. Huang (2021) *Smouldering Propagation and Blow-off on Consolidated Fuel under External Airflow.* **Combustion and Flame** (Accepted).
8) S. Lin, Y. K. Cheung, Y. Xiao and X. Huang (2020) *Can Rain Suppress Smouldering Peat Fire?* **Science of the Total Environment** 727: 138468. doi: 10.1016/j.scitotenv.2020.138468.
9) S. Lin and X. Huang (2020) *An Experimental Method to Investigate the Water-Based Suppression of Smouldering Peat Fire*. **MethodsX** 7: 100934. doi: 10.1016/j.mex.2020.100934.
10) S. Lin, Y. Liu and X. Huang (2021) *Climate-induced boreal peatland fire and carbon loss in the 21st century.* **Science of the Total Environment** 796: 148924. doi: 10.1016/j.scitotenv.2021.148924

The following journal publications are not part of this thesis, but they are co-authored during the course of this PhD.

1) Y. Chen, Z. Liang, S. Lin, X. Huang (2021) *Limits of Sustaining a Flame above Smouldering Biomass*. **Combustion and Flame** (under review).

2) S. Wang, P. Ding, S. Lin, J. Gong, X. Huang (2021) *Smouldering and flaming of disc wood particles under external radiation: Auto-ignition and size effect.* **Frontiers in Mechanical Engineering** 7: 686638. doi: 10.3389/fmech.2021.686638.
3) A. Khan, S. Lin, X. Huang and A. Usmani (2021) *Facade Fire Hazards of Bench-Scale Aluminium Composite Panel with Flame-Retardant Core*. **Fire Technology**. doi: 10.1007/s10694-020-01089-4.
4) S. Wang, P. Ding, S. Lin, X. Huang and A. Usmani (2021) *Deformation of Wood Slice in Fire: Interactions between Heterogeneous Chemistry and Thermomechanical Stress*. **Proceedings of the Combustion Institute** 38(3): 5081-5090. doi: 10.1016/j.proci.2020.08.060.
5) Y. Liu, P. Sun, S. Lin, H. Niu and X. Huang (2020) *Self-Heating Ignition of Open-Circuit Cylindrical Li-ion Battery Pile: Towards Fire-Safe Storage and Transport*. **Journal of Energy Storage** 32: 101842. doi: 10.1016/j.est.2020.101842.
6) Q. Xie, Z. Zhang, S. Lin, Y. Qu, X. Huang (2020) S*mouldering Fire of High-Density Cotton Bale under Concurrent Wind*. **Fire Technology** 56(5): 2241-2256. doi: 10.1007/s10694-020-00975-1.
7) P. Sun, S. Lin and X. Huang (2020) *Ignition of Thin Fuel by Thermoplastic Drips: An Experimental Study for the Dripping Ignition Theory*. **Fire Safety Journal** 115: 103006. doi: 10.1016/j.firesaf.2020.103006.
8) S. Lin, X. Huang, J. Urban, S. McAllister and C. Fernandez-Pello (2019) *Piloted Ignition of Cylindrical Wildland Fuels under Irradiation.* **Frontiers in Mechanical Engineering** 5:54. doi: 10.3389/fmech.2019.00054.

Conference papers

1) S. Lin, X. Huang. Firebreak for Smouldering Wildfires: from Combustion Theory to Firefighting Application, **12th Asia-Oceania Symposium on Fire Science and Technology**, 7-9 Dec 2021, Queensland, Australia. [Oral]
2) S. Wang, S. Lin, X. Huang. Fire hazards of concentrated sunlight: smouldering ignition of thin fuels, **12th Asia-Oceania Symposium on Fire Science and Technology**, 7-9 Dec 2021, Queensland, Australia. [Oral]
3) S. Lin, Y. Liu, X. Huang. *Estimation of carbon loss from arctic peatland fire in 21st century,* **16th International Wildland Fire Safety Summit and 6th Human Dimensions of Wildland Fire Virtual Conference**, 24-27 May 2021. [Oral]

4) S. Wang, S. Lin, X. Huang. *Capability of concentrated sunlight on the smouldering ignition of wildland fuels*, **16th International Wildland Fire Safety Summit and 6th Human Dimensions of Wildland Fire Virtual Conference**, 24-27 May 2021. [Oral]
5) Y. Liu, P. Sun, S. Lin, H. Niu, X. Huang, *Can self-ignition theory explain the mysterious fire in Li-ion battery pile*, **38th International Symposium on Combustion**, 24-29 Jan 2021, Adelaide, Australia. [Poster]
6) S. Lin, X. Huang, *Extinction of Wood Fuels: A Near-limit Blue Flame Sustained above the Hot Smoldering Surface*, **38th International Symposium on Combustion**, 24-29 Jan 2021, Adelaide, Australia. [Poster]
7) S. Wang, S. Lin, X. Huang, *Smouldering Ignition of Thin Paper by Concentrated Sunlight*, **38th International Symposium on Combustion**, 24-29 Jan 2021, Adelaide, Australia. [Poster]
8) S. Lin, Y.K. Cheung, Y. Xiao, X. Huang (2020) *Critical rainfall to extinguish peat fires*, **16th International Peatland Congress (IPC) 2020**, Tallinn, Estonia. [Oral]
9) X. Huang, S. Lin, G. Rein (2020) *Laboratory experimental framework to study peat fire*, **16th International Peatland Congress (IPC) 2020**, Tallinn, Estonia. [Oral]
10) P. Sun, S. Lin, X. Huang, *Experimental study on the dripping ignition of thin fuel*, **13th International Symposium on Fire Safety Science**, 27 April – 1 May 2020, Waterloo, Canada. [Poster]
11) S. Wang, S. Lin, X. Huang, A. Usmani, *Deformation of smouldering wood particle under external radiation*, **13th International Symposium on Fire Safety Science**, 27 April – 1 May 2020, Waterloo, Canada. [Poster]
12) S. Lin, X. Huang, *Near-Limit Timber Fire Behaviour under External Radiation*, **13th International Symposium on Fire Safety Science**, 27 April – 1 May 2020, Waterloo, Canada. [Poster]
13) S. Lin, X. Huang, *What is the Rainfall Limit to Extinguish the Smouldering Peat Fire?* **13th International Symposium on Fire Safety Science**, 27 April – 1 May 2020, Waterloo, Canada. [Poster]
14) S. Lin, X. Huang, *Suppression of peat fire by rain: the effect of rainfall with different intensities on the carbon emission flux from peat fire*, **3rd International Smoke Symposium**, 20-24 April 2020, CA, USA. [Oral]

15) S. Lin, P. Sun, X. Huang, *Can peat soil support a flaming wildfire?* **3rd International Smoke Symposium**, 20-24 April 2020, CA, USA. [Oral]
16) P. Sun, S. Lin, X. Huang, *Fire Hazard and Ignition Mechanism of Thermoplastic Drips*, **1st Asia-Pacific Combustion Institute Summer School**, 10-16 Nov 2019, Viña del Mar, Chile. [Poster]
17) S. Lin and X. Huang, *Near-limit burning of timber material under irradiation-assisted smouldering*, **11st International Conference on Structure in Fire (SIF 2020)**, 24-26 Jun 2019, Australia. [Oral]
18) S. Lin and X. Huang, *Quenching of smouldering: effect of wall cooling and oxygen supply*, **1st Asia-Pacific Combustion Institute Combustion Summer School**, 10-15 Nov 2019, Chile [Poster]
19) S. Lin, J. Gao and X. Huang, *Near-limit flame and extinction limit of timber materials*, **Chinese National Combustion Meeting,** 24-28 Oct 2019, Tianjin, China [Oral]
20) S. Lin, J. Gao and X. Huang, *The Near Extinction Flame Behaviour of Charring Materials*, **12th Asia-Pacific Conference on Combustion**, 1st-5th, Jul, 2019, Fukuoka, Japan. [Oral]
21) P. Sun, S. Lin and X. Huang, *Experimental Study of Dripping Flames Ignition*, **12th Asia-Pacific Conference on Combustion**, 1st-5th, Jul, 2019, Fukuoka, Japan. [Oral]
22) P. Sun, S. Lin and X. Huang, *How dripping flames ignite a thin fuel*, **27th International Colloquium on the Dynamics on Explosions and Reactive systems**, 28th, Jul -2nd Aug, 2019, Beijing, China. [Oral]
23) S. Lin, P. Sun and X. Huang, *Critical Conditions for Flaming Peat Fire in Wildland*, **6th Fire Behaviour and Fuels Conference**, April 29-May 3, 2019, Sydney, Australia. [Oral]
24) S. Lin, H. Li, Y. Xiao and X. Huang, *Effect of Fire on the Drying Process of Soil*, **6th Fire Behaviour and Fuels Conference**, April 29-May 3, 2019, Sydney, Australia. [Poster]
25) S. Lin, P. Sun, X. Huang. *Three-Stage Combustion of Peat under External Radiation*, **8th East Asia Mechanical Engineering Workshop**, The Hong Kong Polytechnic University, 1-3 Dec 2018, Hong Kong, China. [Oral]

CHAPTER 1: Introduction

1.1 Background and motivation

Smouldering is slow, low-temperature and flameless burning of porous fuel and one of the most persistent types of combustion phenomena [1–3]. As a heterogeneous process, smouldering is sustained by the heat evolved when oxygen molecules directly attack the hot surface of condensed-phase reactive porous media [1–4]. In general, smouldering could be initiated by a weaker heat source or even self-heating [5–7], providing a shortcut to flaming combustion through the smouldering-to-flaming transition that follows a sudden increase in spread rate, heat release and hazard [8–11]. Smouldering combustion is the primary cause and driving phenomenon of residential fires (e.g., upholstered furniture and mattresses fires) [12,13], industrial fires (e.g., fires in silos and storage units) [14], and natural fires (e.g., subsurface fire in peatlands or abandoned coal mines) [15–18] (Fig. 1.1), posing severe threats to humans and environment. On the other hand, some beneficial applications of smouldering combustion have also been developed over the past few decades for energy production [19] and waste removal technology [20,21]. Thus, a better understanding of smouldering combustion is vital to mitigate the smouldering fire hazard and optimize the applications of smouldering system.

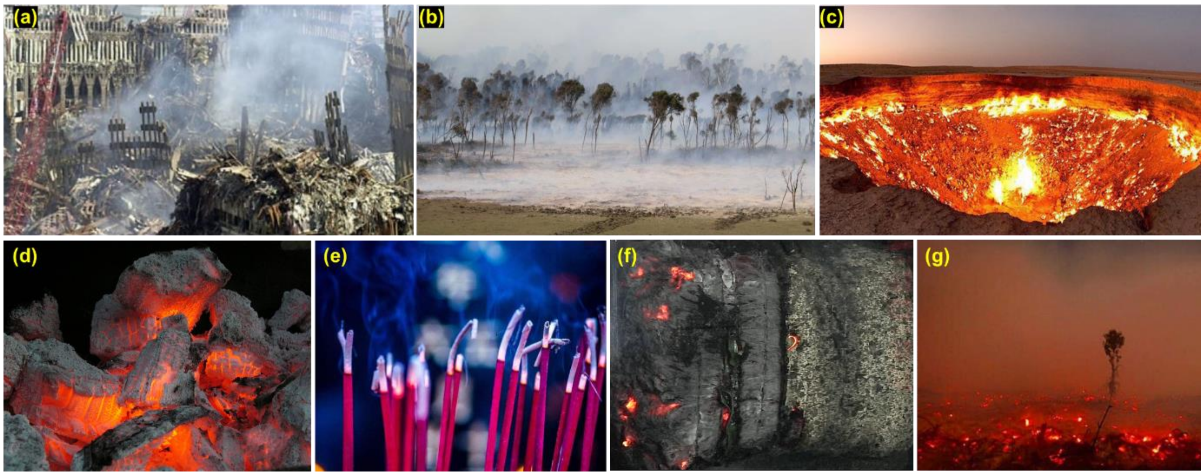

Fig. 1.1. Typical example of smouldering combustion in different fuels, (a) debris of WTC, (b) peat fire, (c) underground coal fire, (d) charcoal, (e) incenses, (f) cotton bale, and (g) wildland firebrands.

Heat loss and oxygen supply are two controlling mechanisms for smouldering combustion, and they play central roles in the ignition, propagation, and extinction [1,22]. Traditionally, smouldering spreads in a creeping fashion, typically on the order of 1 cm/h, which is at least two orders of magnitude smaller than the spread rate of flaming fires [23]. On the other hand, smouldering fire can be sustained in an extremely low oxygen concentration (~11%). However, very few works have been conducted to systematically study the near-limit smouldering fire dynamics, thus bringing a huge research gap.

The ignition of combustible materials is fundamental to fire safety analyses, defining initiation and leading to the eventual growth of sometimes devastating fire events. For different fuels, propensities for flaming and smouldering fires are different [5]. For example, grass, leaves, and twigs are prone to flaming fire, while ember, duff, and peat may be more likely to smoulder. Nevertheless, theoretically all charring fuels can support both forms of fires which can also transition to each other under specific conditions, but relevant studies on their propensities and ignition limits are quite limited.

Moreover, Many ignition events leading to both structure and wildland fires occur remotely by a point heating source [24], such as the deposition of lofted firebrands [25–27], hot metal particles [27,28], dripping molten materials [29], laser irradiation [30,31], lightning strikes [32], and concentrated irradiation [33–36]. A less-studied source of ignition is a concentrated sunlight spot, which can be reflected by a curved mirror or focused by a dew droplet, curved glass window and decorations, transparent fish bowls, or cylindrical bottles filled with water [37–39]. From 2010 to 2015, 125 fires in the United Kingdom were reported to be triggered by a concentrated sunlight spot [40], posing threats to both human lives and property. However, to the best of the authors' knowledge, this remote ignition phenomenon has not received a detailed and quantitative study, presenting a key knowledge gap.

On the other hand, even a flame could be piloted above the charring materials, it is sometimes found not to be able to sustain after ignition [41]. Nevertheless, extinction of the flame is not the end of a fire, as it may be followed by the smouldering [42]. However, such a transition limit of flaming-to-smouldering is also unclear, requiring further investigations.

After ignition, smouldering combustion may propagate until extinction. Heat loss or cooling is one of the critical mechanisms that control smouldering combustion [1,2,23], and therefore has substantial implications toward understanding its propagation limits and quenching behaviours [43,44]. For flaming combustion, the quenching distance (or thickness/diameter) is defined as a critical length, below which flame can no longer propagate through because of the flame-wall interaction that decreases the flame temperature below the threshold of chain reactions [45–48]. For a laminar premixed flame, quenching occurs on the scale of millimetre that is comparable to the flame thickness [49,50]. It is of practical significance in the design of flame arrestor as well as other fire protection systems [50,51].

Analogous to the quenching behaviour of premixed flame, heat loss or cooling is also an essential factor during smouldering propagation, which may weaken the chemical reactions [52] and hence lead to the occurrence of quenching [43,53]. However, to the best of authors' knowledge, no study has systematically addressed the quenching dynamics of smouldering and quantified the corresponding quenching distance, thus, there is a big knowledge gap.

Also, the numerical studies on quenching and quenching distance of premixed flame have been conducted for decades, establishing many insightful understandings [46,47,54]. However, to the best of the authors' knowledge, no computational study has been conducted yet to study the quenching behaviours of smouldering combustion. Therefore, a comprehensive computational model is required to better understand the underlying mechanisms behind this phenomenon.

The ignition and propagation of smoldering combustion depends on both environment (e.g., wind [13,23,55–57], oxygen [58–60], pressure [61,62], and gravity [63]) and fuel factors (e.g., type/array [64], moisture [53,56], density [65], orientation [66], and size [43,67]). Smouldering combustion is controlled by the competition between the oxygen supply and the heat transfer to and from the reaction zone [1,68,69]. Therefore, the airflow or wind is crucial to smouldering propagation, because it could increase both the oxygen supply and the heat loss [13,43,70]. By applying an external airflow (or environmental wind), smouldering propagation may become faster because of the increased oxygen supply (O_2-limit regime) [23,58,71]. Afterwards, the excessive airflow may also help trigger gas-phase homogenous oxidation under some specific conditions and result in smouldering-to-flaming (StF) transition [11]. Further increasing the airflow velocity, the cooling effect becomes dominant, so eventually smouldering extinction or blow-off will occur, just like the blow-off of flame [72]. In the literature, the blow-off of flame on solid fuels has been extensively studied over the last 50 years [4,23]. Comparatively, the research on the blow-off of smouldering is limited; and generally, it is more difficult to blow off persistent smouldering fire. Like the flame, most smouldering extinction processes result from a local energy imbalance, where the cooling rate is larger than the heat-release rate from exothermic oxidations [4,72,73]. So far, no study has addressed the smouldering propagation at large wind speeds over 10 m/s and the blow-off limits of persistent smouldering fire; thus, there is a big knowledge gap.

Except for the wind, the weather and climate are also strongly affecting the ignition and propagation of smouldering combustion, especially the smouldering wildfires in peatlands. Limited trials in the literature have demonstrated the ineffectiveness of all man-made suppression methods in controlling or extinguishing any massive peat fire [74–76], and most the real peat fires were suppressed until there was an heavy rain. Although the suppression effect of rain on smouldering wildfire is still mostly unknown, it is hypothesized that the rain droplets can penetrate the burning peat layer, and if the rainwater can overcome the combustion heat, eventually peat fire can be quenched. Nevertheless, if the peat fire was not entirely extinguished by rain, re-ignition could happen after an extended time, especially when the drought season arrives [76,77]. Thus, it is necessary to thoroughly explore the effectiveness of rain in suppressing peat fire and identify the critical rainfall intensity and depth. On the other hand, although it has been argued that the frequency and severity of wildfires in the boreal region have been increasing as a result of global warming [78], there is still not enough quantitative data on the ignition and propagation limits of smouldering combustion in peatlands [79–81]. Several Earth-system models have been applied to predict the carbon loss from the arctic and boreal regions under global warming [82], but the impact of peatland fires is rarely included. Therefore, it is urgent to understand the fire severity in the arctic and boreal peatlands and the associated fire carbon emissions under different global warming scenarios.

1.2 Literature review

A comprehensive literature review on the ignition, propagation, and extinction of smouldering combustion is conducted to provide the research background and a clear picture of what have been done and what needs to be done in the research domain of this study.

1.2.1 Ignition limits of smouldering combustion

For ignition, several researchers have quantified the ignition limits of different fuels. For many fuels, smouldering could be easier to initiate than flaming [2]. For a low-density (20 kg/m^3) polyurethane (PU) foam, the minimum radiant heat flux for smouldering ignition is 7 kW/m^2, while for flaming ignition, it is 13 kW/m^2 with a pilot igniter and 30 kW/m^2 without an igniter [2,83]. However, smouldering ignition could be more difficult for trees and twigs. For a redwood (~350 kg/m^3), if the heat flux is larger than 40 kW/m^2, the required heating time and surface temperature for piloted flaming ignition are lower than for smouldering ignition (or glowing) [84]. Whether it is easier to pilot a flame and support flame spread over a common peat soil (~200 kg/m^3 dry density) is still unclear. Moreover, peat, as a typical wildland fuel, can hold a wide range of moisture contents (MCs), from 10~50% under drought conditions to well above 300% under flooded conditions [85,86]. MC is also expected to alter the propensity of wildland fuels for flaming or smouldering [27,87].

Many past works have investigated the flaming ignition of wildland fuels like foliage and pine needles with MCs of 3~300% under wildfire intensity up to 10^3 kW/m^2 or above 10^5 W/m [88,89]. Several studies found for many wildland fuels, the piloted flaming ignition time under external heating increased almost linearly with the fuel MC, and there was a maximum MC above which flaming ignition could not occur [27,90,91]. Besides MC, whether the wildland fuel is fresh, aged, or dead has a significant impact on the flammability [89]. Many ignition theories have been proposed based on the critical ignition temperature, ignition energy, and critical mass flux [92]. These theoretical work reasonably well for common dry polymer materials but become less reliable for complex wildland fuels [93–95], thus, requiring a better ignition criterion.

Over the past 50 years, limited studies have investigated flaming ignition by a laser spot or concentrated irradiation. Kashiwagi [30,31] showed that the minimum radiant heat fluxes for flaming autoignition are 90 kW/m^2 for red oak and 160 kW/m^2 for PMMA, performed with a 2-3 cm diameter laser spot. By increasing the diameter of the heating spot to about 3.5 cm, the minimum radiant fluxes decreased to 80-90 kW/m^2, still much higher than the 25-50 kW/m^2 reported for auto-ignition of 10-cm width square wood samples more evenly heated in a cone calorimeter [96]. Later, the laser ignition of thin PMMA sheets with different orientations has also been investigated experimentally and numerically [97,98]. Grishin et al. [33] generated a light beam by a tungsten lamp to ignite a porous forest fuel layer with a bulk density of 6-24 kg/m^3 and revealed that the required irradiant heat flux for flaming ignition decreases as the heating diameter increases from 8 mm to 27 mm. Warren [34] concentrated sunlight using a spherical water-filled glass bowl with a diameter of 200 mm and demonstrated the possibility of smouldering ignition of print paper by concentrated irradiation. Recently, Sandia National Laboratories [35,36] used hundreds of reflection mirrors in a concentrated solar tower plant to generate an irradiation greater than 2,000 kW/m^2 (about 0.5-m diameter spot) that could ignite some common fuels within a few seconds.

On the other hand, a flame is sometimes found not to be able to sustain above the material after ignition, i.e., the self-extinction may occur [99–101]. However, very few studies have investigated the extinction mechanisms and quantified its combustion limits. Nevertheless, extinction of the flame is not the end of a fire, as it may be followed by the smouldering [42]. Therefore, such a extinction limit of flaming combustion is also a transition limit of flaming-to-smoldering transition. Previously, Babrauskas [102] used a flame to ignite a timber material for several minutes and found the self-extinction occurred once the igniting flame was removed. Emberley *et al.* [41,103] further studied the self-extinction of flaming timber and CLT under external radiation and found the critical heat flux of 43.6 ± 4.7 kW/m^2 and the minimum mass flux of 3.93 ± 0.45 g/m^2·s were required to sustain the flame. Vermesi *et al.* [104] found that for engineered wood, the critical mass flux for flameout varied in a wide range (1.4-17 g/m^2·s). Moreover, under specific conditions, smouldering may also transition back to the flaming, i.e., the smouldering-to-flaming (StF) transition [2,27]. Therefore, in a real fire, the ignition (and re-ignition) and extinction of the flame, as well as smouldering combustion, could repeatedly occur several times until the eventual burnout [103].

1.2.2 Propagation and extinction limits of smouldering combustion

In the literature, the extinction limit of flame on solid fuels has been extensively studied over the last 50 years [4,23]. For example, Loh and Fernandez-Pello [105] showed that the concurrent rate flame spread over the thin paper first increased with the airflow velocity (< 1 m/s) but became almost constant until blow-off at about 3 m/s. A similar trend and blow-off wind speed were also observed for the concurrent flame spread on thin electrical wires [106]. In general, the blow-off of opposed flame spread is easier, usually at an airflow velocity lower than 1 m/s [107,108]. Comparatively, there are quite limited studies on the propagation limits of smouldering combustion. Palmer [71] found that the blow-off limit of opposed smouldering propagation over fibreboard was about 7 m/s, but the concurrent smouldering propagation could still be sustained at 10 m/s [23,71]. Like the flame, most smouldering extinction processes result from a local energy imbalance, where the cooling rate is larger than the heat-release rate from exothermic oxidations [4,72,73]. Thus, decreasing oxygen concentration and pressure promotes the blow-off of smouldering under a smaller airflow [60,61].

With respect to the fire triangle, three methods can be applied to extinguish a fire, namely starving (by removing the fuel), smothering (by removing the oxygen), and cooling (or quenching by removing the heat) [51]. Because of the persistence of smouldering combustion, a short-term man-made water spray is not able to stop the fire spread [76]. For example, compared to flaming fire, smouldering wildland fire require at least 50% more water to extinguish the same amount of burning fuel [3]. Some chemical foaming agents can easily penetrate into burning fuels and shield the burning samples from the oxygen supply [109], but the required quantity to suppress any real fire is enormous. In fact, limited trials in the literature have demonstrated the ineffectiveness of all man-made suppression methods in controlling or extinguishing any massive smouldering fire [74–76]. Therefore, more effective methods are required to extinguish these persistent fire phenomena.

1.2.3 Computational study of smouldering combustion

The computational study on smouldering was initiated by Ohlemiller [1], who established the governing equations to simulate this persistent combustion phenomenon. Afterwards, a number of numerical simulations were performed to investigate the smouldering combustion of different porous media, including peat [15,65,77,86,110–116], cellulose [1,117], coal [118,119], polyurethane foam [120] and char [121] with chemical schemes of different complexities using the 1-D model. Based on these works, Yang et al. [115] developed a 2-D axis-symmetric model for the natural downward spread of peat fire and reported the importance of lateral heat loss. However, previous studies mainly focused on the ignition and propagation of smouldering, whereas the quenching behaviour of smouldering combustion has not received sufficient attention.

1.3 Aims and Objectives

The aim of this PhD study is to develop a thorough understanding of near-limit smouldering fire dynamics. It is accomplished by addressing the following objectives:

1. Investigate the propensities and ignition limits of smouldering and flaming combustion with different moisture contents under different irradiation levels. The ignition delay time, mass flux, CO/CO_2 ratio and minimum heat flux are quantified for both flaming and smouldering combustion.
2. Investigate the ignition limit of smouldering combustion by intense point irradiation, i.e., a sunlight spot concentrated by a spherical glass ball. The ignition delay time, critical heat flux, and ignition energy of smouldering by the irradiation spot are quantified. Afterwards, a simplified heat transfer model iss proposed to (1) explain the varying minimum irradiation and energy required for smouldering ignition and (2) quantify the potential ignition risk initiated by the concentrated sunlight in both structure and wildland fires. Finally, a 2-D computational model is developed to verify the experimental observation.
3. Investigate the transition limits of flaming-to-smouldering transition of charring materials. The

transition limits and the near extinction fire behaviours will be quantify using both laboratory experiments and phenomenological analysis.

4. Explore whether the classical concept of flame quenching and quenching diameter can be extended to smouldering. Different conditions of wall cooling and oxygen supply are applied to the reactor to determine the quenching limit of smouldering. The quenching diameter is compared with the thickness of the smouldering front, and the minimum values of the smouldering temperature and propagation rate before quenching are quantified.
5. Develop a comprehensive 2-D model for smouldering based on open-source code Gpyro and a previously developed 5-step smouldering kinetics (including 1-step drying). Numerical simulations are performed to investigate the smouldering quenching behaviours and near-extinction spread dynamics without forced airflow. Moreover, the influences of ambient temperature and oxygen concentration on the quenching dynamics of smouldering are explored.
6. Explore the application of quenching and quenching limits of smouldering combustion for smouldering peat fires through laboratory-scale experiments. The research outcomes provide a scientific foundation for underground wildfire fighting and the design criteria for the protective measures of large-scale peat fire experiments in the field.
7. Investigate both concurrent and opposed smouldering propagations over cylindrical consolidated biomasses (incenses) with different fuel diameters (1.5-5 mm) and densities (720-1,100 kg/m^3). The external airflow velocity up to 50 m/s in a small wind tunnel was applied to explore the blow-off limits. The theoretical analysis was proposed to explain the influence of environmental and fuel properties on smouldering propagation and critical conditions of blow-off.
8. Explore the extinction limit of smouldering wildfires under natural rainfall. The required rainfall duration, rainfall depth, as well as the mass loss per unit area of peat sample and carbon emissions of peat fire under different rainfall intensities are analysed in detail. The minimum rainfall intensity (I_{min}) and rainfall depth (d_{min}) to extinguish the peat fire is also quantified.
9. Interpret the ignition limits of organic peat soils as a function of the minimum environmental temperature vs soil gravimetric moisture content. Afterwards, based on the field measurement of the vertical soil temperature profile in the boreal peatland [122], this fire threshold will be used to estimate the depth of burn (DOB) in boreal peatlands. We then further project the carbon emissions

from the boreal peatland fires under different global warming scenarios in the 21st century.

1.4 General methodology

General methodology of this PhD study is briefly summarized here, and more detailed information could be found in each corresponding chapter.

The scale of the experiments can be divided into three categories: micro scale, small scale and large scale [123]. The micro-scale experiments refer to the testing of sample with milligram in mass and is independent of bulk behaviour and transport phenomena. Typical examples of micro-scale experiments are thermogravimetric analysis (TGA) and Fourier transform infrared spectroscopy (FTIR). For TGA, it could help propose the heterogeneous reaction scheme and acquire the corresponding kinetic parameters through optimization algorithm. Small-scale experiments commonly refer to the simplified experiments conducted in the laboratories, with several grams or kilograms in mass. Small-scale experiments are mainly used to study the dynamics of smouldering combustion by controlling a single variable. Large-scale experiments refer to the field experiments in the potential fire scenes. By collecting the information and analysing the data, large-scale experiments can improve the fire prevention strategies and emergency measures in the future.

Generally, the representativeness and authenticity of the experimental results will be improved as the scale of the experiment increases. However, the complexity of the system will gradually increase as the experimental scale increases, making it more difficult to summarize the laws of physics throughout quantitative analysis. Moreover, larger experiments will also face greater environmental impacts and safety issues. Small-scale experiments simplify the complex fire scenarios and ecosystems, which help explore the underlying mechanisms of smouldering combustion by controlling a single variable. Therefore, it is widely used in the study of ignition [5,124–126], fire spread [56,65,77], emissions [127], and extinction [18,43,76,128], which provides the necessary theoretical and scientific basis for the analysis of large-scale experiments. Meanwhile, the cost of small-scale experiments is relatively low, making it conducive to conduct a large number of repeating tests to improve the reliability of the experimental results, and provide necessary reference for the design and analysis of high-cost large-scale field experiments.

1.4.1 Method for the test of smouldering ignition limit

In 1980s, Frandsen first use small-scale experiments (9 cm×9 cm×4 cm) to test the flammability limits of organic peat soils with different organic and moisture contents (Fig. 1.2a) [125]. A 3-cm hot coil heater as point heating source was attached to fuel surface for 3 min. As it is impossible to judge the success of smouldering ignition, therefore, the heated sample was kept for several hours to observe if stable smouldering was successfully initiated. Afterward, Frandsen upscaled the smouldering reactor (10 cm×10 cm×5 cm) and used linear heating source to test the flammability limits of organic soils. As shown in Fig. 1.2(b), a long coil heater was buried below the fuel surface to heat the organic fuels for 3 min. Such method has been widely used for investigating horizontal smouldering propagation [56].

Radiative heating is a kind of surficial heating source, as shown in Fig. 1.2(c). Such method can simulate the radiation heating from nearby flame or smoke. By adjusting the radiation heat flux, the critical heat flux for smouldering ignition can be achieved. Self-heating ignition is a special ignition phenomenon without external heating source. The most commonly-used methods to explore the self-ignition phenomena are hot plate experiments and oven-basket experiments (Fig. 1.2d) [7].

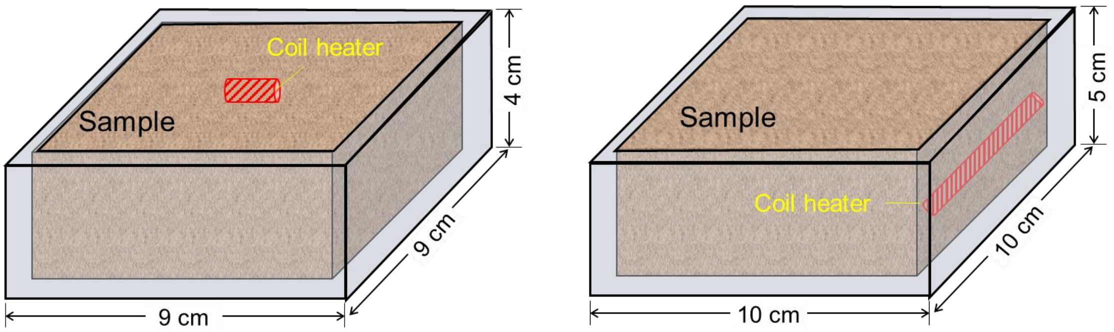
(a) Point heating source

(b) Linear heating source

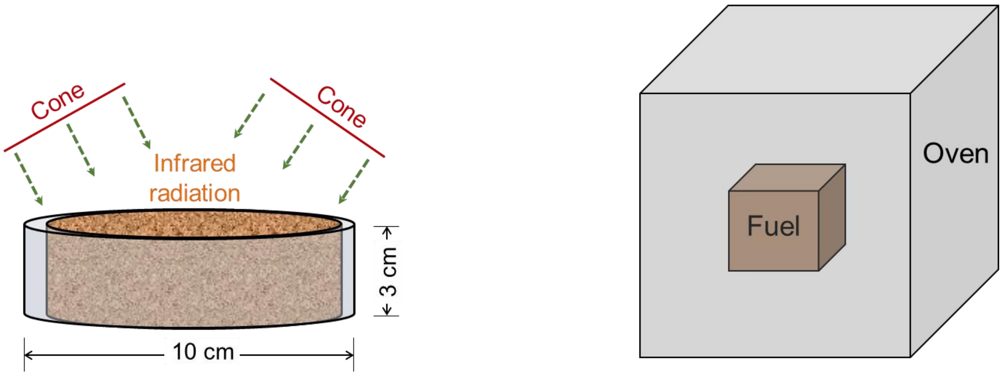
(c) Surficial heating source

(d) Self-heating ignition

Fig. 1.2. Schematic diagrams of small-scale experiments to investigate the ignition limits of smouldering fire.

1.4.2 Method for the test of smouldering propagation and extinction limit

Smouldering propagation is a three-dimensional process, and it can be divided into horizontal and vertical propagation. In the small-scale experiments, to better observe the characteristics of smouldering propagation, they are usually investigated in different reactors.

For the horizontal smouldering propagation, the internal dimension of smouldering reactor is 20 cm×20 cm×10 cm, as shown in Fig. 1.3(a). In general, the reactor is made of ceramic insulation board, and is covered by several layers of aluminium foil to limit the radiative heat loss. To monitor the smouldering temperature and propagation rate, a thermocouple array should be inserted into the sample. To reduce the effect of boundary, the thermocouple array should be arranged in the central plane and away from the reactor wall. In general, the distance between the adjacent thermocouples should be greater than 2 cm to alleviate the cooling effect on the smouldering front. After the experiment, the smouldering propagation rate can be calculated by the time interval between the peak temperatures of two continuous thermocouple readings.

For the vertical smouldering propagation, the cross-section area of the smouldering reactor should not be less than 10 cm×10 cm, and its height should be larger than 20 cm, as shown in Fig. 1.3(b). as the height of the reactor increases, the dimension of the cross section should be increased as well to ensure sufficient oxygen supply. Generally, the height-to-width ratio should not be greater than 3:1. Analogous to the experiment of horizontal smouldering propagation, the thermocouple array should be arranged in the central plane, and the distance between the adjacent thermocouples should be larger than 2 cm.

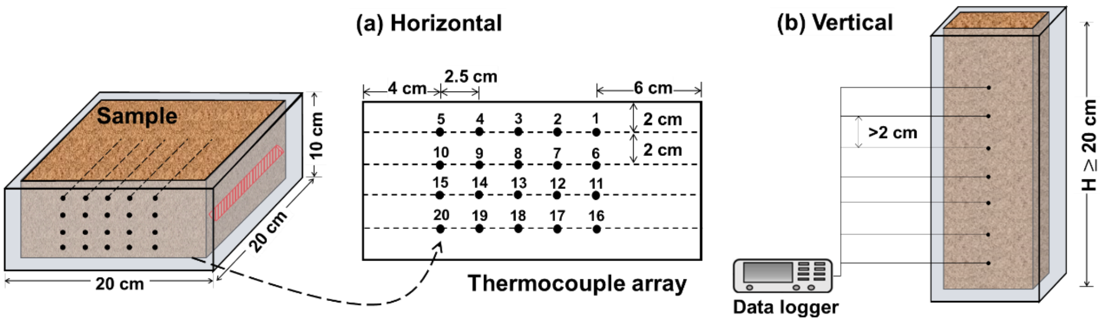

Fig. 1.3. Schematic diagrams of small-scale experiments to investigate the propagation limits of smouldering fire.

With respect to the fire triangle, three methods can be applied to extinguish a fire, namely starving (by removing the fuel), smothering (by removing the oxygen), and cooling (or quenching by removing the heat) [51]. Cooling can be achieved by gas or liquid cooling agents, and the cooling efficiency depends on the specific heat capacity and the heat of evaporation of the cooling agents. If the liquid cooling agent is applied, it is necessary to ensure that the reactor has a good drainage function. Therefore, the steel mesh is recommended here. Generally, it is more convenient to use stainless steel mesh to manufacture the cylindrical reactor. Note that the diameter of the reactor should be larger than 10 cm, so as to avoid excessive boundary heat loss caused by the larger specific surface area, which may make the experiment deviate from the actual situation. To study the extinction limits of smouldering peat fire at different depths, the height of the reactor should be larger than 15 cm.

For ignition, an 8-cm long coil igniter ($Cr_{20}Ni_{80}$) is placed 5 cm below the top free sample surface to start the smouldering peat fire. The ignition power is fixed to 60 W for 60 min to initiate a robust peat fire [29]. The temperature profiles of peat at 0 cm (surface) and 5 cm, 10 cm and 15 cm below the top surface are carefully monitored using armoured K-type thermocouples with 1-mm probe diameter. After ignition, the basket of peat sample is placed into a larger cylindrical mesh basket with a diameter of 200 mm and a height of 150 mm. To simulate the natural state and mimic a real boundary condition, the space between two baskets was filled with unheated peat soils. Afterward, the entire setup was left to burn and self-stabilize for another 30 min before the start of rain suppression.

The simulated rain-suppression experiments are conducted in a wet chamber with an area of 6 m × 10 m and a height of 3.5 m. The artificial rain is produced by a water sprinkler system that includes a sprinkler nozzle, a pressure gauge, and a valve, as illustrated in Fig. 1.4. The vertical distance between the nozzle and the sample surface was fixed to 2.5 m. The median water droplet diameter depends on the water pressure, sprinkler orifice diameter, and the surface tension of the air-water interface (0.073 N/m). The value of the median water droplet diameter was calculated to be about 1.5 mm, which is within the range of typical raindrop sizes [42]. Therefore, the simulated raindrop size in this experiment is close to the natural rain. With the sprinkler spray, the intensity of simulated rainfall changed with the location. Thus, the distribution of rainfall intensity (Fig. 1.4b) was measured by multiple cylindrical containers (with a diameter of 10 cm and a height of 15 cm) at the interval of 20 cm. Given a fixed rainfall duration ($\Delta t = 10$ min), the local rainfall intensity can be calculated by measuring rainfall depth (d) as $I = d/\Delta t$. Then, the desired rainfall intensity can be achieved by placing the burning sample at a specific location.

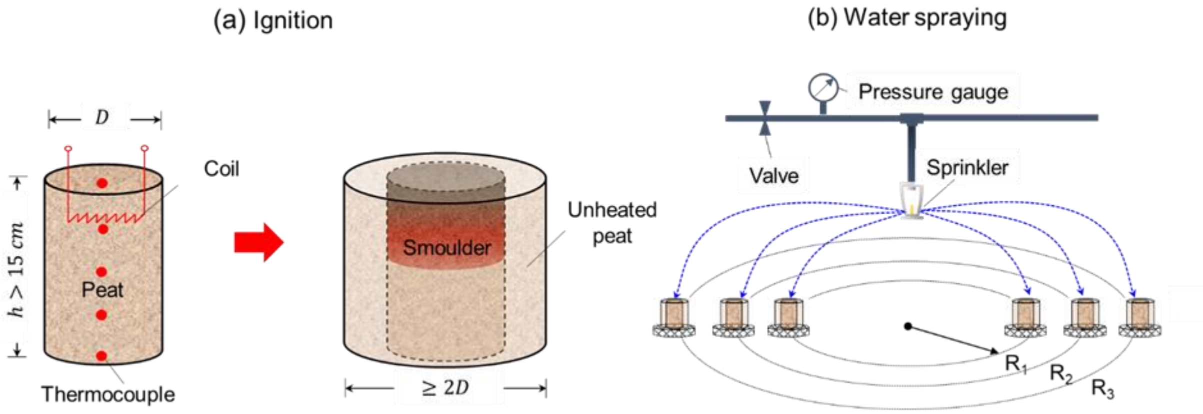

Fig. 1.4. Schematic diagrams of small-scale experiments to investigate the extinction limits of smouldering fire.

1.5 Organization of the thesis

In this thesis, smouldering combustion of peat (**Chapter 2, 5, 7,9** and **10**), wood (**Chapter 4**), tissue (**Chapter 3**), consolidated biomass (**Chapter 8**) has been experimentally studied to understand the near-limit smouldering fire dynamics including ignition limits, extinction limits and fire propagation limits. In addition, computational simulations are performed to understand the underlying mechanisms of smouldering ignition limits by irradiation spot (**Chapter 3**) and quenching limits of smouldering fire (**Chapter 6**).

This thesis is divided into eleven chapters: except for the chapter of introduction and concluding remarks, each chapter takes the form of an independent paper, which has been published or submitted to a journal or conferences.

PART A includes three chapters (2-4), with the focus on the ignition limits of smouldering combustion. **Chapter 2** investigates the ignition limits of moist peat soil with moisture up to 100 wt.% under external radiation, and the critical ignition heat flux, ignition temperature, heat release rate and CO/CO_2 ratio are compared thoroughly. **Chapter 3** explores the effect of the diameter of irradiation spot on the ignition limit of smouldering combustion, which reveals that the lateral conductive cooling effect within the fuel becomes more dominant for a smaller spotting area. **Chapter 4** describes the limits of transition from flaming to smouldering, where a unique near-limit blue flame is observed and discussed.

PART A is composed of three standalone journal articles and one conference paper:

Chapter 2: S. Lin, P. Sun and X. Huang (2019) *Can Peat Soil Support a Flaming Wildfire?* **International Journal of Wildland Fire** 28: 601-603. doi: 10.1071/WF19018.

Chapter 3: S. Wang, S. Lin (co-first author), Y. Liu, X. Huang and M. Gollner (2021) *Smouldering Ignition using a Concentrated Solar Irradiation Spot*, **Fire Safety Journal** (under review).

S. Lin, S. Wang, P. Sun, H. Yuan and X. Huang (2021) *Experimental and Computational Study of Smouldering Ignition by Concentrated Sunlight,* **2021 China National Symposium on Combustion** (submitted).

Chapter 4: S. Lin, X. Huang, J. Gao and J. Ji (2021) *Extinction of Wood Fire: A Near-Limit Blue Flame above Hot Smouldering Surface.* **Fire Technology**. doi: 10.1007/s10694-021-01146-6.

PART B includes three chapters (5-7), with the focus on the quenching limits and quenching diameter of smouldering combustion. **Chapter 5** explores the quenching limits and applicability of quenching diameter in smouldering through laboratory-scale experiments, where the measured quenching diameter of smouldering was about 10 cm. **Chapter 6** develops a 2-D numerical model based on open-source code Gpyro and a previously developed 5-step kinetics of peat to verify the quenching diameter of smouldering combustion and further explore the effects of lateral overall heat transfer coefficient, oxygen concentration and ambient temperature on the extinction limits. **Chapter 7** explores the applications of quenching distance of smouldering combustion through constructing firebreak for extinguishing peat fire.

PART B is composed of three standalone journal articles:

Chapter 5: S. Lin, X. Huang (2021) *Quenching of Smouldering: Effect of Wall Cooling on Extinction*, **Proceedings of the Combustion Institute** 38(3): 5015-5022. doi: 10.1016/j.proci.2020.05.017.

Chapter 6: S. Lin, H. Yuan and X. Huang (2021) *A Computational Study on the Quenching and Near-Limit Propagation of Smouldering Combustion,* **Combustion and Flame** (under review).

Chapter 7: S. Lin, Y. Liu and X. Huang (2021) *How to Build a Firebreak to Stop Smouldering Peat Fire: Insight from a Laboratory-Scale Study.* **International Journal of Wildland Fire** 30(6): 454-461. doi: 10.1071/WF20155.

PART C includes three chapters (8-10), with the focus of the environmental impacts on the smouldering limits. **Chapter 8** quantifies the smouldering propagation rate on consolidated biomass and the blow-off limit under concurrent and opposed external airflows up to 50 m/s, where the effects of fuel diameter and density are thoroughly discussed. **Chapter 9** assesses the underlying mechanism of rain in suppressing the smouldering peat fire in the shallow soil layer up to 15 cm deep through laboratory experiments, where the minimum rainfall intensity and depth to suppress smouldering peat fire is found. **Chapter 10** quantifies the minimum environmental temperature that allows the moist peat to smoulder, and then apply a typical vertical soil temperature profile to estimate the future depth of burn and carbon emissions in boreal peatland fires under the impact of global warming.

PART C is composed of four standalone journal articles:

Chapter 8: S. Lin, T. H. Chow, and X. Huang (2021) *Smouldering Propagation and Blow-off on Consolidated Fuel under External Airflow.* **Combustion and Flame** (Accepted).

Chapter 9: S. Lin, Y. K. Cheung, Y. Xiao and X. Huang (2020) *Can Rain Suppress Smouldering Peat Fire?* **Science of the Total Environment** 727: 138468. doi: 10.1016/j.scitotenv.2020.138468.

S. Lin and X. Huang (2020) *An Experimental Method to Investigate the Water-Based Suppression of Smouldering Peat Fire*. **MethodsX** 7: 100934. doi: 10.1016/j.mex.2020.100934.

Chapter 10: S. Lin, Y. Liu and X. Huang (2021) *Climate-induced boreal peatland fire and carbon loss in the 21st century.* **Science of the Total Environment** 796: 148924. doi: 10.1016/j.scitotenv.2021.148924.

A final section (Chapter 11) summarizes the conclusions and points out the potential areas of future research.

References

[1] Ohlemiller TJJ. Modeling of smoldering combustion propagation. Prog Energy Combust Sci 1985;11:277–310.
[2] Rein G. Smoldering Combustion. SFPE Handb Fire Prot Eng 2014;2014:581–603.
[3] Rein G. Smouldering Fires and Natural Fuels. In: Claire M. Belcher, editor. Fire Phenom. Earth Syst., New York: John Wiley & Sons, Ltd.; 2013, p. 15–34.
[4] Torero JL, Gerhard JI, Martins MF, Zanoni MAB, Rashwan TL, Brown JK. Processes defining smouldering combustion: Integrated review and synthesis. Prog Energy Combust Sci 2020;81.
[5] Lin S, Sun P, Huang X. Can peat soil support a flaming wildfire? Int J Wildl Fire 2019;28:601–13.
[6] Restuccia F, Huang X, Rein G. Self-ignition of natural fuels: Can wildfires of carbon-rich soil start by self-heating? Fire Saf J 2017;91:828–34.
[7] Yuan H, Restuccia F, Richter F, Rein G. A computational model to simulate self-heating ignition across scales, configurations, and coal origins. Fuel 2019;236:1100–9.

[8] Bar-Ilan A, Putzeys OM, Rein G, Fernandez-Pello AC, Urban DL. Transition from forward smoldering to flaming in small polyurethane foam samples. Proc Combust Inst 2005;30:2295–302.

[9] Putzeys O, Bar-Ilan A, Rein G, Fernandez-Pello AC, Urban DL. The role of secondary char oxidation in the transition from smoldering to flaming. Proc Combust Inst 2007;31 II:2669–76.

[10] Chao CYH, Wang JH. Transition from smoldering to flaming combustion of horizontally oriented flexible polyurethane foam with natural convection. Combust Flame 2001;127:2252–64.

[11] Santoso MA, Christensen EG, Yang J, Rein G. Review of the Transition From Smouldering to Flaming Combustion in Wildfires. Front Mech Eng 2019;5.

[12] Quintiere J. Principles of Fire Behaviour. New York: Alar Elken; 1997.

[13] Xie Q, Zhang Z, Lin S, Huang X, Qu Y. Smoldering Fire of High-Density Cotton Bale Under Concurrent Wind. Fire Technol 2020.

[14] Villacorta E, Haraldseid I, Mikalsen RF, Hagen BC, Erland S, Kleppe G, et al. Onset of smoldering fires in storage silos: Susceptibility to design, scenario, and material parameters. Fuel 2021;284.

[15] Huang X, Rein G. Smouldering combustion of peat in wildfires: Inverse modelling of the drying and the thermal and oxidative decomposition kinetics. Combust Flame 2014;161:1633–44.

[16] Turetsky MR, Benscoter B, Page S, Rein G, Van Der Werf GR, Watts A. Global vulnerability of peatlands to fire and carbon loss. Nat Geosci 2015;8:11–4.

[17] Zhao X, Xiao H, Wang Q, Ping P, Sun J. Study on spontaneous combustion risk of cotton using a micro-calorimeter technique. Ind Crops Prod 2013;50:383–90.

[18] Lin S, Cheung YK, Xiao Y, Huang X. Can rain suppress smoldering peat fire ? Sci Total Environ 2020;727:138468.

[19] Hernandez-Soriano MC, Kerré B, Kopittke PM, Horemans B, Smolders E. Biochar affects carbon composition and stability in soil: A combined spectroscopy-microscopy study. Sci Rep 2016;6:1–13.

[20] Yermán L, Wall H, Torero JL. Experimental investigation on the destruction rates of organic waste with high moisture content by means of self-sustained smoldering combustion. Proc Combust Inst 2017;36:4419–26.

[21] Solinger R, Grant GP, Scholes GC, Murray C, Gerhard JI. STARx Hottpad for smoldering treatment of waste oil sludge: Proof of concept and sensitivity to key design parameters. Waste Manag Res 2020;38:554–66.

[22] Rein G. Smoldering combustion. SFPE Handb. Fire Prot. Eng., Springer; 2016, p. 581–603.

[23] Huang X, Gao J. A review of near-limit opposed fire spread. Fire Saf J 2020:103141.

[24] Caton SE, Hakes RSP, Gorham DJ, Zhou A, Gollner MJ. Review of Pathways for Building Fire Spread in the Wildland Urban Interface Part I: Exposure Conditions. Fire Technol 2017;53:429–73.

[25] Fernandez-Pello AC. Wildland fire spot ignition by sparks and firebrands. Fire Saf J 2017;91:2–10.

[26] Manzello SL, Suzuki S, Gollner MJ, Fernandez-Pello AC. Role of firebrand combustion in large outdoor fire spread. Prog Energy Combust Sci 2020;76:100801.

[27] Wang S, Huang X, Chen H, Liu N. Interaction between flaming and smouldering in hot-particle ignition of forest fuels and effects of moisture and wind. Int J Wildl Fire 2017;26:71–81.

[28] Urban JL, Zak CD, Fernandez-Pello C. Cellulose spot fire ignition by hot metal particles. Proc Combust Inst 2015;35:2707–14.

[29] Sun P, Lin S, Huang X. Ignition of thin fuel by thermoplastic drips: An experimental study for the dripping ignition theory. Fire Saf J 2020;115:103006.

[30] Kashiwagi T. Experimental observation of radiative ignition mechanisms. Combust Flame 1979;34:231–44.

[31] Kashiwagi T. Effects of sample orientation on radiative ignition. Combust Flame 1982.

[32] Zhang H, Qiao Y, Chen H, Liu N, Zhang L, Xie X. Experimental study on flaming ignition of pine needles by simulated lightning discharge. Fire Saf J 2020:103029.

[33] Grishin AM, Golovanov AN, Medvedev V V. On the ignition of a layer of combustible forest materials by light radiation. Combust Explos Shock Waves 1999;35:618–21.

[34] Warren DW. Optical Modeling of Fire Hazards Arising from Sunlight Focused by Water. Fire Technol 2014;50:1327–34.

[35] Engerer JD, Brown AL, Christian JM. Ignition and damage thresholds of materials at extreme incident radiative heat flux. 2018 Jt Thermophys Heat Transf Conf 2018:1–27.

[36] Brown AL, Engerer JD, Ricks AJ, Christian J, Yellowhair J. Datasets for material ignition from high radiant flux. Fire Saf J 2020:103131.

[37] Goldstone BM. Hazards from the concentration of solar radiation by textured window glass. London: HMSO; 1982.

[38] Dyke KS Van. THE FISH BOWL AS A FIRE HAZARD. Science (80-) 1937;86:122–3.

[39] Wildfire in Guilin caused by a plastic bottle. Guilinlife 2019.

[40] Brigade step up sunlight warning after another refraction blaze. London Fire Brig 2015.

[41] Emberley R, Inghelbrecht A, Yu Z, Torero JL. Self-extinction of timber. Proc Combust Inst 2017;36:3055–62.

[42] Smucker BD, Mulky TC, Cowan DA, Niemeyer KE, Blunck DL. Effects of fuel content and density on the smoldering characteristics of cellulose and hemicellulose. Proc Combust Inst 2019;37:4107–16.

[43] Lin S, Huang X. Quenching of smoldering: Effect of wall cooling on extinction. Proc Combust Inst 2021;38:5015–22.

[44] Rashwan TL, Torero JL, Gerhard JI. Heat losses in applied smouldering systems: Sensitivity analysis via analytical modelling. Int J Heat Mass Transf 2021;172:121150.

[45] Turns S. An Introduction to Combustion: Concepts and Applications. McGraw-Hill Education; 2011.

[46] Ganter S, Heinrich A, Meier T, Kuenne G, Jainski C, C. Rißmann M, et al. Numerical analysis of laminar methane–air side-wall-quenching. Combust Flame 2017;186:299–310.

[47] Demesoukas S, Caillol C, Higelin P, Boiarciuc A, Floch A. Near wall combustion modeling in spark ignition engines. Part A: Flame-wall interaction. Energy Convers Manag 2015;106:1426–38.

[48] Kim KT, Lee DH, Kwon S. Effects of thermal and chemical surface-flame interaction on flame quenching. Combust Flame 2006;146:19–28.

[49] R.Turns S. An Introduction to Combustion: Concepts and Application. 3rd ed. India: McGraw-Hill Education (India) Private Limited; 2012.

[50] Williams FA. Combustion Theory. 2nd ed. CRC Press; 1985.

[51] Quintiere JG. Fundamental of Fire Phenomena. New York: John Wiley; 2006.

[52] Rashwan TL, Torero JL, Gerhard JI. Heat losses in a smouldering system: The key role of non-uniform air flux. Combust Flame 2021;227:309–21.

[53] Lin S, Liu Y, Huang X. How to Build a Firebreak to Stop Smouldering Peat Fire : Insights from a Laboratory-Scale Study. Int J Wildl Fire 2021.

[54] Han J, Yamashita H, Hayashi N. Numerical study on the spark ignition characteristics of a methane-air mixture using detailed chemical kinetics. Effect of equivalence ratio, electrode gap distance, and electrode radius on MIE, quenching distance, and ignition delay. Combust Flame 2010;157:1414–21.

[55] Fernandez-Pello a. C, Ray SR, Glassman I. Downward Flame Spread In an Opposed Forced Flow. Combust Sci Technol 1978;19:19–30.

[56] Huang X, Restuccia F, Gramola M, Rein G. Experimental study of the formation and collapse of an overhang in the lateral spread of smouldering peat fires. Combust Flame 2016;168:393–402.

[57] Gollner MJ, Miller CH, Tang W, Singh A V. The effect of flow and geometry on concurrent flame spread. Fire Saf J 2017;91:68–78.

[58] Kumar A, Shih HY, T'ien JS. A comparison of extinction limits and spreading rates in opposed and concurrent spreading flames over thin solids. Combust Flame 2003;132:667–77.

[59] Konno Y, Hashimoto N, Fujita O. Downward flame spreading over electric wire under various oxygen concentrations. Proc Combust Inst 2019;37:3817–24.

[60] Kadowaki O, Suzuki M, Kuwana K, Nakamura Y, Kushida G. Limit conditions of smoldering spread in counterflow configuration: Extinction and smoldering-to-flaming transition. Proc Combust Inst 2020;000:1–9.

[61] Yamazaki T, Matsuoka T, Nakamura Y. Near-extinction behavior of smoldering combustion under highly vacuumed environment. Proc Combust Inst 2019;37:4083–90.

[62] Sato J, Sato K, Hirano T. Fire spread mechanisms along steel cylinders in high pressure oxygen. Combust Flame 1983;51:279–87.

[63] Huang X, Link S, Rodriguez A, Thomsen M, Olson S, Ferkul P, et al. Transition from opposed flame spread to fuel regression and blow off: Effect of flow, atmosphere, and microgravity. Proc Combust Inst 2019;37:4117–26.

[64] Gollner MJ, Williams FA, Rangwala AS. Upward flame spread over corrugated cardboard. Combust Flame 2011;158:1404–12.

[65] Huang X, Rein G. Downward Spread of Smoldering Peat Fire: the Role of Moisture, Density and Oxygen Supply. Int J Wildl Fire 2017;26:907–18.

[66] Zhou Y, Gong J, Jiang L, Chen C. Orientation effect on upward flame propagation over rigid polyurethane foam. Int J Therm Sci 2018;132:86–95.

[67] Jiang L, He JJ, Sun JH. Sample width and thickness effects on upward flame spread over PMMA surface. J Hazard Mater 2018;342:114–20.

[68] Torero JL, Fernandez-Pello AC, KitanO M. Opposed forced flow smoldering of polyurethane foam. Combust Sci Technol 1993;91:95–117.

[69] Kuwana K, Suzuki K, Tada Y, Kushida G. Effective Lewis number of smoldering spread over a thin solid in a narrow channel. Proc Combust Inst 2017;36:3203–10.

[70] Valdivieso JP, Rivera J de D. Effect of Wind on Smoldering Combustion Limits of Moist Pine Needle Beds. Fire Technol 2014;50:1589–605.

[71] Palmer KN. Smouldering combustion in dusts and fibrous materials. Combust Flame

1957;1:129–54.

[72] Dosanjh SS, Pagni PJ, Fernandez-Pello AC. Forced cocurrent smoldering combustion. Combust Flame 1987;68:131–42.

[73] Leach S V, Ellzey JL, Ezekoye OA. Convection , Pyrolysis , and Damko Extinction of Reverse Smoldering Combustion. Twenty-Seventh Symp Combust 1998:2873–80.

[74] Dianti A, Ratnasari NG, Palamba P, Nugroho Y. Effect of Rewetting on Smouldering Combustion of a Tropical Peat. E3S Web Conf 2018;67:02042.

[75] Mikalsen RF, Hagen BC, Steen-Hansen A, Krause U, Frette V. Extinguishing Smoldering Fires in Wood Pellets with Water Cooling: An Experimental Study. Fire Technol 2018;55:257–84.

[76] Ramadhan ML, Palamba P, Imran FA, Kosasih EA, Nugroho YS. Experimental study of the effect of water spray on the spread of smoldering in Indonesian peat fires. Fire Saf J 2017;91:671–9.

[77] Huang X, Rein G. Upward-and-downward spread of smoldering peat fire. Proc Combust Inst 2019;37:4025–33.

[78] Gibson CM, Chasmer LE, Thompson DK, Quinton WL, Flannigan MD, Olefeldt D. Wildfire as a major driver of recent permafrost thaw in boreal peatlands. Nat Commun 2018;9:3041.

[79] Girardin MP, Mudelsee M. Past and Future Changes in Canadian Boreal Wildfire. Ecol Appl 2008;18:391–406.

[80] Hanes CC, Wang X, Jain P, Parisien MA, Little JM, Flannigan MD. Fire-regime changes in canada over the last half century. Can J For Res 2019;49:256–69.

[81] Flannigan M, Stocks B, Turetsky M, Wotton M. Impacts of climate change on fire activity and fire management in the circumboreal forest. Glob Chang Biol 2009;15:549–60.

[82] Schuur EAG, McGuire AD, Schädel C, Grosse G, Harden JW, Hayes DJ, et al. Climate change and the permafrost carbon feedback. Nature 2015;520:171–9.

[83] Hadden R, Alkatib A, Rein G, Torero JL. Radiant Ignition of Polyurethane Foam: The Effect of Sample Size. Fire Technol 2014;50:673–91.

[84] Boonmee N, Quintiere JG. Glowing and flaming autoignition of wood. Proc Combust Inst 2002;29:289–96.

[85] Watts AC. Organic soil combustion in cypress swamps: Moisture effects and landscape implications for carbon release. For Ecol Manage 2013;294:178–87.

[86] Huang X, Rein G. Computational study of critical moisture and depth of burn in peat fires. Int J Wildl Fire 2015;24:798–808.

[87] Valdivieso JP, Rivera JDD. Effect of Wind on Smoldering Combustion Limits of Moist Pine Needle Beds. Fire Technol 2013;50:1589–605.

[88] Finney MA, Cohen JD, McAllister SS, Jolly WM. On the need for a theory of fire spread. Int J Wildl Fire 2013;22:25–36.

[89] Jervis FX, Rein G. Experimental study on the burning behaviour of Pinus halepensis needles using small-scale fire calorimetry of live, aged and dead samples. Fire Mater 2016;40:385–195.

[90] McAllister S, Grenfell I, Hadlow A, Jolly WM, Finney M, Cohen J. Piloted ignition of live forest fuels. Fire Saf J 2012;51:133–42.

[91] Dimitrakopoulos AP, Papaioannou KK. Flammability Assessment of Mediterranean Forest Fuels. Fire Technol 2001;37:143–52.

[92] Drysdale D. An Introduction to Fire Dynamics. 3rd ed. Chichester, UK: John Wiley & Sons, Ltd; 2011.

[93] Lyon RE, Quintiere JG. Criteria for piloted ignition of combustible solids. Combust Flame 2007;151:551–9.

[94] McAllister S. Critical mass flux for flaming ignition of wet wood. Fire Saf J 2013;61:200–6.

[95] Wongchai P, Tachajapong W. Effects of Moisture Content in Para Rubber Leaf Litter on Critical Mass Flux and Piloted Ignition Time. Energy Procedia 2015;79:448–52.

[96] Lizhong Y, Yupeng Z, Yafei W, Jiakun D, Zhihua D, Xiaodong Z. Autoignition of solid combustibles subjected to a uniform incident heat flux: The effect of distance from the radiation source. Combust Flame 2011;158:1015–7.

[97] Nakamura Y, Kashiwagi T. Effects of sample orientation on nonpiloted ignition of thin poly(methyl methacrylate) sheet by a laser: 1. Theoretical prediction. Combust Flame 2005;141:149–69.

[98] Gotoda H, Manzello SL, Saso Y, Kashiwagi T. Effects of sample orientation on nonpiloted ignition of thin poly(methyl methacrylate) sheets by a laser. 2. Experimental results. Combust Flame 2006;145:820–35.

[99] Bartlett AI, Hadden RM, Hidalgo JP, Santamaria S, Wiesner F, Bisby LA, et al. Auto-extinction of engineered timber: Application to compartment fires with exposed timber surfaces. Fire Saf J 2017;91:407–13.

[100] Richter F, Jervis FX, Huang X, Rein G. Burning rate of wood pyrolysis, smouldering, and flaming: Effect of oxygen. Combust Flame 2021.

[101] Bilbao R, Mastral JF, Aldea ME, Ceamanos J, Betrán M, Lana JA. Experimental and theoretical study of the ignition and smoldering of wood including convective effects. Combust Flame 2001;126:1363–72.

[102] Babrauskas V. Journal of Fire Protection Ignition of Wood : A Review of the State of the Art. J Fire Prot Eng 2002;12:163–89.

[103] Emberley R, Do T, Yim J, Torero JL. Critical heat flux and mass loss rate for extinction of flaming combustion of timber. Fire Saf J 2017;91:252–8.

[104] Vermesi I, Richter F, Chaos M, Rein G. Ignition and Burning of Fibreboard Exposed to Transient Irradiation. Fire Technol 2020.

[105] Loh HT, Fernandez-Pello AC. Flow Assisted Flame Spread Over Thermally Thin Fuels. West States Sect Combust Inst 1984:65–74.

[106] Lu Y, Huang X, Hu L, Fernandez-Pello C. Concurrent Flame Spread and Blow-Off Over Horizontal Thin Electrical Wires. Fire Technol 2019;55:193–209.

[107] Fernandez-Pello AC, Ray SR, Glassman I. Flame spread in an opposed forced flow: the effect of ambient oxygen concentration. Symp Combust 1981;18:579–89.

[108] Carmignani L, Celniker G, Bhattacharjee S. The Effect of Boundary Layer on Blow-Off Extinction in Opposed-Flow Flame Spread over Thin Cellulose: Experiments and a Simplified Analysis. Fire Technol 2017;53:967–82.

[109] Ratnasari NG, Dianti A, Palamba P, Ramadhan ML, Prayogo G, Pamitran AS, et al. Laboratory Scale Experimental Study of Foam Suppression on Smouldering Combustion of a Tropical Peat. J Phys Conf Ser 2018;1107.

[110] Huang X, Rein G, Chen H. Computational smoldering combustion: Predicting the roles of moisture and inert contents in peat wildfires. Proc Combust Inst 2015;35:2673–81.

[111] Huang X, Rein G. Thermochemical conversion of biomass in smouldering combustion across scales: The roles of heterogeneous kinetics, oxygen and transport phenomena. Bioresour

Technol 2016;207:409–21.

[112] Huang X, Rein G. Interactions of Earth's atmospheric oxygen and fuel moisture in smouldering wildfires. Sci Total Environ 2016;572:1440–6.

[113] Yuan H, Restuccia F, Rein G. Spontaneous ignition of soils : a multi-step reaction scheme to simulate self-heating ignition of smouldering peat fires. Int J Wildl Fire 2021.

[114] Yang J, Chen H, Liu N. Modeling of Two-Dimensional Natural Downward Smoldering of Peat. Energy and Fuels 2016;30:8765–75.

[115] Yang J, Liu N, Chen H, Gao W, Tu R. Effects of atmospheric oxygen on horizontal peat smoldering fires: Experimental and numerical study. Proc Combust Inst 2018;000:1–9.

[116] Yang J, Chen H. Natural Downward Smouldering of Peat : Effects of Inorganic Content and Piled Bed. Fire Technol 2018.

[117] Di Blasi C. Mechanisms of Two-Dimensional Smoldering Propagation through Packed Fuel Beds. Combust Sci Technol 1995;106:103–24.

[118] Han Y, Richter F, Rein G. A multi-step reaction scheme to simulate self-heating ignition of coal: Effects of oxygen adsorption and smouldering combustion. Proc Combust Inst 2020;38:4717–25.

[119] Yuan H, Restuccia F, Rein G. Computational study on self-heating ignition and smouldering spread of coal layers in flat and wedge hot plate configurations. Combust Flame 2020;214:346–57.

[120] Rein G, Carlos Fernandez-Pello a., Urban DL. Computational model of forward and opposed smoldering combustion in microgravity. Proc Combust Inst 2007;31:2677–84.

[121] He F, Zobel N, Zha W, Behrendt F. Effects of physical properties on one-dimensional downward smoldering of char: Numerical analysis. Biomass and Bioenergy 2009;33:1019–29.

[122] Léger E, Dafflon B, Robert Y, Ulrich C, Peterson JE, Biraud SC, et al. A distributed temperature profiling method for assessing spatial variability in ground temperatures in a discontinuous permafrost region of Alaska. Cryosphere 2019;13:2853–67.

[123] Christensen E, Hu Y, Restuccia F, Santoso MA, Huang X, Rein G. Experimental methods and scales in smouldering wildfires. In: Pereira P, editor. Fire Eff. om Soil Prop., CSIRO; 2019, p. 267–80.

[124] Frandsen WH. Ignition probability of organic soils. Can J For Res 2011;27:1471–7.

[125] Frandsen WH. The influence of moisture and mineral soil on the combustion limits of smouldering forest duff. Can J For Res 1987;16:1540–4.

[126] Frandsen WH. Ignition probability of organic soils. Can J For Res 1997;27:1471–7.

[127] Hu Y, Fernandez-Anez N, Smith TEL, Rein G. Review of emissions from smouldering peat fires and their contribution to regional haze episodes. Int J Wildl Fire 2018;27(5):293.

[128] Lin S, Huang X. An experimental method to investigate the water-based suppression of smoldering peat fire. MethodsX 2020;7.

[129] Pruppacher HR, Klett JD. Microphysics of Clouds and Precipitation. Boston: D. Reidel Publishing Company; 1978.

PART A: Ignition Limits of Smouldering: Criteria, Dimension Effect and Transition

The ignition of combustible materials is fundamental to the fire safety analysis, defining the initiation and development of devastating fire events. Therefore, it is essential to explore and quantify the ignition limits of combustible materials to deepen our understanding of smouldering fire dynamics. In the literature, the limits of flaming ignition are profoundly studied, while the limits of smouldering ignition are rarely included. Moreover, many ignition events occur remotely by a point heating source, such as laser and concentrated sunlight. The ignition limit by the point heating source may differ from the smouldering ignition limit we obtain under the cone calorimeter but has not received a detailed and quantitative study, presenting a key knowledge gap. On the other hand, even though the charring fuel is directly flaming ignited, after the extinction of flame, it may follow a smouldering fire. However, such a transition limit from flaming to smouldering is still not fully understood.

This part includes three chapters (2-4), with the focus on the ignition limits of smouldering combustion. Chapter 2 investigates the ignition limits of moist peat soil with moisture up to 100 wt.% under external radiation, and the critical ignition heat flux, ignition temperature, heat release rate and CO/CO_2 ratio are compared thoroughly. Chapter 3 explores the effect of the diameter of irradiation spot on the ignition limit of smouldering combustion, which reveals that the lateral conductive cooling effect within the fuel becomes more dominant for a smaller spotting area. Chapter 4 describes the limits of transition from flaming to smouldering, where a unique near-limit blue flame is found to co-exist with the internal smouldering combustion.

CHAPTER 2: Ignition Limits of Flaming and Smouldering Fire under Irradiation

Summary

Smouldering wildfire in peatlands is one of the largest and longest-lasting fire phenomena on Earth, but whether peat can support a flaming fire like other surface fuels is still unclear. Our experiments demonstrate the successful piloted flaming ignition of peat soil with moisture up to 100 wt.% under external radiation, indicating that flame may rapidly spread on peatland before transitioning to the conventional smouldering peat fire. Compared to smouldering ignition, flaming ignition of peat is more difficult, requiring a higher minimum heat flux and triple ignition energy. The propensity for flaming increases with a drier peat and a larger external heating. We also found that the flaming ignition temperature increases from 290°C to 690°C, as the peat moisture increases to 100 wt.%. The flame of peat soil is much weaker than that of pine needles and wood, and it eventually transitions to smouldering. The heat of flaming is estimated to be 13 $MJ \cdot kg^{-1}$, close to the heat of smouldering. The measured CO/CO_2 ratio of flaming peat fires is less than 0.02, much smaller than 0.2 of smouldering peat fires. This research helps understand the development of peat fire and the interaction between flaming and smouldering wildland fires.

This chapter is based on "S. Lin, P. Sun and X. Huang (2019) *Can Peat Soil Support a Flaming Wildfire?* **International Journal of Wildland Fire** 28: 601-603. doi: 10.1071/WF19018. "

2.1 Introduction

Wildfire has become a severe global problem which poses severe threats to the safety of human lives and properties as well as the economy and environment [1]. Catastrophic wildfires in recent years reveal a dramatic increase in size, frequency and duration because of climatological and human factors [2–4], particularly in United States, Australia, Indonesia and many European countries [5,6]. In particular, smouldering wildfires in peatlands are the largest and longest fire phenomena on Earth [7]. Although peatlands only cover 3% of the Earth land surface, they store around 25% of the planet's terrestrial organic carbon, i.e., approximately the same amount of carbon in the atmosphere [8,9]. These peat fires result in the widespread destruction of ecosystems and regional haze event, e.g. recent mega-fires in Southeast Asia, North America and North Europe [7,10,11]. More importantly, peat fires contribute greatly to the global climate change, as annually they release the ancient carbon that is approximately equivalent to 15% of human-made emissions [9,11,12].

Peat soil is an accumulation of incompletely decomposed vegetation residues, and it is carbon-rich and formed in anaerobic conditions [11]. Peat is also a porous and charring natural fuel that is prone to smouldering combustion like plastic foams and coals [7]. Once ignited, smouldering peat fires can burn for weeks, months and even years despite extensive rains, weather changes, or firefighting attempts. Most research in the literature have focused on the smouldering characteristics of a peat fire, such as the chemical kinetics [13], smouldering ignition [14–17], fire spread [18–21], extinction [22,23], and emission gases [15,24]. Because most natural fuels can support both smouldering and flaming fires, such as pine needle beds [25], twigs, bark [26] and firebrands [27], it is logical to expect that peat soil can also support a flaming fire. Pyrolysis that occurs under external heating is the common prerequisite for both flaming and smouldering fires, as illustrated in Fig. 2.1. When the char oxidation dominates the oxygen consumption (Path I), smouldering fire occurs, while flaming fire is sustained by the oxidation of pyrolysis gases (Path II).

Fundamentally, the flaming fire spread is a continuous ignition process that is heated and piloted by the flame [28]. If a flame can be piloted on the peat soil, it means that the flame can spread on the peatland surface in a speed much faster than the conventional smouldering spread, resulting in a fast expansion of peat fire. As illustrated in Fig. 2.2, in real wildfire scenarios, the flame of burning grasses or trees can act as the heating and pilot sources, causing the piloted flaming ignition of peat soils. In turn, the pyrolysis gases generated from the peat, can also support the flaming wildfire via Path (II) in

Fig. 2.1. For different wildland fuels, propensities for flaming and smouldering fires are different. For example, grass, leaves, and twigs are prone to flaming fire, while ember, duff, and peat may be more likely to smoulder. Nevertheless, theoretically all charring fuels can support both forms of fires which can also transition to each other under specific conditions, but relevant studies are quite limited. Traditionally, smouldering spreads in a creeping fashion, typically around 1 cm/h, which is at least two orders of magnitude slower than the spread rate of flaming fires [7]. However, if flame can spread over the surface of peat soil, the size of peat fire can expand much faster than the expected creeping smouldering spread inside the peat layer. So far, no research has studied the critical conditions of flaming ignition of peat and the propensity for a flaming fire spreading on peatlands, so there is a big knowledge gap.

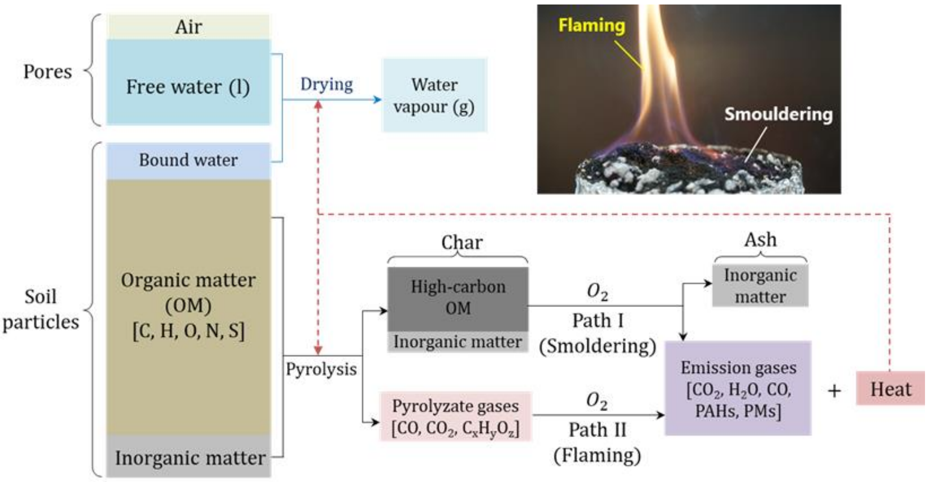

Fig. 2.1. Possible reaction paths for flaming and smouldering combustion of peat soils in wildfires.

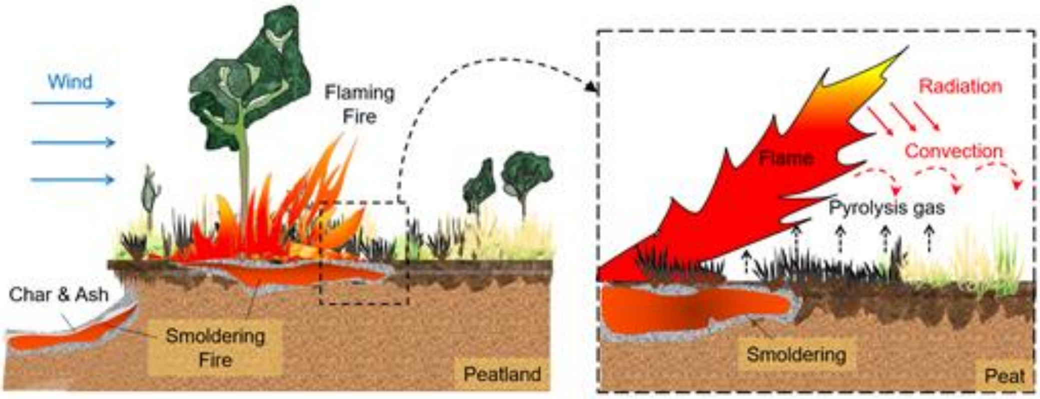

Fig. 2.2. Schematics of flaming and smouldering fires in peatland and the possible piloted flaming ignition of peat soils.

For many fuels, smouldering could be easier to initiate than flaming [29]. For a low-density (20 kg/m^3) polyurethane (PU) foam, the minimum radiant heat flux for smouldering ignition is 7 kW/m^2, while for flaming ignition, it is 13 kW/m^2 with a pilot igniter and 30 kW/m^2 without an igniter [29,30]. However, smouldering ignition could be more difficult for trees and twigs. For a redwood (~350 kg/m^3), if the heat flux is larger than 40 kW/m^2, the required heating time and surface temperature for piloted flaming ignition are lower than for smouldering ignition (or glowing) [31]. Whether it is easier to pilot a flame and support flame spread over a common peat soil (~200 kg/m^3 dry density) is still unclear. Moreover, peat, as a typical wildland fuel, can hold a wide range of moisture contents (MCs), from 10~50% under drought conditions to well above 300% under flooded conditions [22,32]. MC is also expected to alter the propensity of wildland fuels for flaming or smouldering [25,33].

Many past works have investigated the flaming ignition of wildland fuels like foliage and pine needles with MCs of 3~300% under wildfire intensity up to 10^3 kW/m^2 or above 10^5 W/m [34,35]. Several studies found for many wildland fuels, the piloted flaming ignition time under external heating increased almost linearly with the fuel MC, and there was a maximum MC above which flaming ignition could not occur [25,36,37]. Besides MC, whether the wildland fuel is fresh, aged, or dead has a significant impact on the flammability [35]. Many ignition theories have been proposed based on the critical ignition temperature, ignition energy, and critical mass flux [38]. These theoretical work reasonably well for common dry polymer materials but become less reliable for complex wildland fuels [39–41], thus, requiring a better ignition criterion.

In this work, the flaming ignition with a pilot source and smouldering ignition of peat is investigated under varying MCs (10 ~ 100%) and exposed to radiant heat fluxes (5 ~ 90 kW/m^2). The ignition delay time, mass flux, CO/CO$_2$ ratio and minimum heat flux are quantified for both flaming and smouldering ignition of peat.

2.2 Experiment

2.2.1 Apparatus and peat sample

All ignition experiments were conducted using the cone calorimeter (FTT iCone Plus) [42]. The cone-shape heater can provide a constant heat flux to the sample area of 10 cm ×10 cm. The schematic diagram of the experimental apparatus is illustrated in Fig. 2.3 (a), and it mainly consists of a cone-shape heater, a cylindrical sample container, a precision scale (± 1 mg), and a spark igniter.

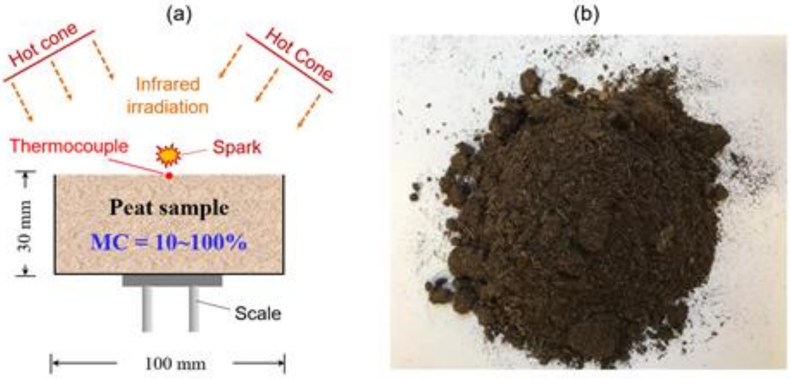

Fig. 2.3. (a) Schematic diagram of the cone calorimeter and sample, and (b) photo of moss peat sample.

The carbon-rich peat soil tested in the experiment is the moss peat from the Netherlands (Fig. 2.3b), and it has an organic matter content of about 96%. The element analysis for the peat organic matter shows 44.2/6.1/49.1/0.5/0.1% mass fraction for C/H/O/N/S, respectively. The peat was first oven-dried at 90°C for 48 h [10], and the oven-dried bulk density of peat was measured as 145 kg/m^3 (MC → 0%). In general, the drying process weakens the hydrophilicity of peat, but it does not affect the high-temperature pyrolysis and smouldering processes [43]. The peat bed has an open-pore structure and a porosity of about 0.90, considering a solid density of 1500 kg/m^3 [44]. When the oven-dried peat was in contact with air, it quickly absorbed ambient moisture and reached a new equilibrium with about 10% MC, defined as the air-dried peat [18]. In order to obtain other MCs, the oven-dried peat was mixed with water by following the same process in Huang *et al.* (2016). For example, 2 kg of 100% MC peat can be produced by mixing 1 kg of dry peat with 1 kg of water. Afterwards, samples were shaken to enhance the mixing process and left into the sealed boxes for homogenization for at least 48 h. The other two targeted MCs for peat were 50% (drought) and 100% (wet).

The cylindrical container (with a diameter of 100 mm and a height of 30 mm) was made of metal mesh, so aluminium foil was placed between the peat and container to prevent oxygen leakage from the side and bottom. During the water absorbing process, the volume of peat sample tended to expand naturally [10]. To avoid this issue, after filling in, moist samples were compressed manually to ensure the dry bulk density of peat was fixed to 145 kg/m^3, regardless of the MC. The bulk densities of peat samples with different MCs are listed in Table 2.1. During the test, the ambient temperature was 22 ± 2 °C, and the humidity of 50 ± 10%, and the ambient pressure was 1 atm.

2.2.2 Ignition methods

For the piloted ignition, the cone temperature was varied for producing various radiant heat flux ($\dot{q}''_r$) from 5 kW/m^2 to 90 kW/m^2. As illustrated in Fig. 2.3 (a), the spark was inserted and placed at 5 mm above the top surface of the peat sample prior to heating. In real wildland fires, flaming embers or surface fires can act as the piloted source for the peat soils, as shown in Fig. 2.2. In experiment, the radiant heating started once the shield of cone heater was removed. The surface temperature of peat was carefully monitored using two K-type thermocouple (0.5 mm bead diameter) that was in contact with the peat top surface. The moment of flaming ignition ($t_{ig,f}$) and the following burning process were captured by a video camera. Once the flaming ignition occurred, the spark was removed while the heating was continued until the sample mass no longer changed (or burnout). A failed flaming ignition was considered if the flame did not occur after heating for 10 min. Then, the radiant heat flux was adjusted to find the minimum heat flux for flaming ($\dot{q}''_{min,f}$). Throughout the experiment, flaming autoignition, i.e., the smouldering peat fire self-transitioning to flaming fire without a spark, was not observed.

For the smouldering ignition, the piloting spark was removed under the same radiant heat flux. The peat sample was placed under the cone heater for a prescribed heating duration, and then, moved to the nearby fume hood. Unlike the flaming ignition, it was not possible to determine the success of smouldering ignition instantaneously and visually. Thus, the sample was left for another half an hour to observe if a stable smouldering was successfully initiated, e.g. strong smoke released from the sample, visual hot spots or burnout. If successful, the heating time was reduced until the minimum time for smouldering ignition ($t_{ig,sm}$) was found. Typically, the release of smoke was also observed during the heating for a smouldering ignition, but the amount of smoke was not enough to pilot a flame. Like the flaming ignition, the radiant heat flux was adjusted to find the minimum heat flux for the smouldering ignition ($\dot{q}''_{min,sm}$). For both ignition forms, 3~5 repeating experiments were conducted to obtain the average ignition time.

2.3 Results and discussions

2.3.1 Peat's propensity for flaming and smouldering

Figure 1.4 shows an example of the piloted flaming ignition process of peat soil under a high radiant heat flux of 70 kW/m^2 with different MCs. The average ignition time of several repeating tests for smouldering ignition and piloted flaming ignition are indicated in Fig. 2.4 as well. During the heating process, smoke was always observed before any form of ignition, and this visible smoke should be a mixture of water vapor and pyrolysis gases. Continuing the heating, smouldering ignition was first achieved, and then, a flame could be piloted, if the heating flux was larger than the minimum value for flaming ignition (Table 2.1). Therefore, we can conclude that peat soils can support a flaming wildfire under external radiation, even when the fuel MC as high as 100%, thus, it is similar to other wildland fuels like leaves, twigs, and bark. In other words, the flame can spread over peat soils because the spread of flame is a process of continuous piloted ignition. Note that as the peat MC is increased, the intensity of flame becomes weaker (see Fig. 2.4), discussed more in Section 1.3.4.

Table 2.1. Average values and standard deviations of bulk density, minimum ignition heat flux, ignition temperature, and ignition energy of peat soils of different MCs, where the dry bulk density of peat is fixed to 145 kg/m^3.

Fire	Parameters	MC = 10% (air-dried)	MC = 50% (drought)	MC = 100% (wet)
Smouldering	ρ [kg/m^3]	160	218	290
	$T_{ig,\,sm}$ (°C)	270 ± 5	275 ± 10	280 ± 5
	$\dot{q}''_{min,sm}$ [kW/m^2]	6.5 ± 0.5	6.5 ± 0.5	6.5 ± 0.5
	$\dot{q}''_{min,sm,cal}{}^{\#}$ [kW/m^2]	6.3 ± 0.2	6.6 ± 0.5	6.8 ± 0.3
	$E_{ig,sm}$ [MJ/m^2]	0.10 ± 0.02	0.39 ± 0.03	0.65 ± 0.08
Flaming	$T_{ig,\,f}$(°C)	285 ± 5	590 ± 10	690 ± 10
	$\dot{q}''_{min,f}$ [kW/m^2]	7.5 ± 0.5	43 ± 2	53 ± 2
	$\dot{q}''_{min,f,cal}{}^{\#}$ [kW/m^2]	7.1 ± 0.5	35 ± 1	52 ± 1
	$E_{ig,f}$ [MJ/m^2]	0.30 ± 0.05	1.1 ± 0.12	2.0 ± 0.21
	$\dot{m}''_{min,f}$ [g·/(m^2·s^1)]	4.3 ± 0.1	7.9 ± 0.3	10.4 ± 0.4

*Oven-dried peat cannot be tested as it quickly absorbs the ambient water to reach a new equilibrium.

$^{\#}$Calculated using the measured T_{ig} and the thermal equilibrium in Eq. (2.1).

By plotting the ignition time of flaming ($t_{ig,f}$) and smouldering ($t_{ig,sm}$) versus radiant heat flux in Fig. 2.5, the propensity of air-dried and wet peat for flaming and smouldering ignition can be quantified. Like all other ignition phenomena, the required heat time decreased with increasing radiant heat flux [40]. More importantly, as the heating duration and heat flux decrease, there are three ignition regions,

(I) piloted flaming ignition,

(II) smouldering ignition, and

(III) no ignition.

Clearly, the longer heating duration and larger heat flux are required to initiate the flaming combustion of peat soil. Therefore, the propensity of peat soil for smouldering is greater than that of flaming. This behaviour is the same as the low-density PU foam [29,30], while unlike the high-density redwood, probably because peat has a relatively small bulk density (160 kg/m^3 for air-dried peat) and a similar open-pore structure like PU foam.

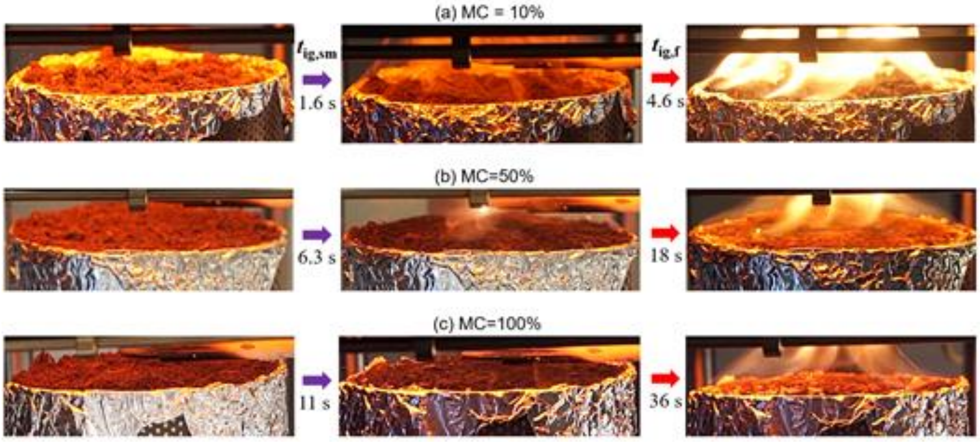

Fig. 2.4. Pilot flaming ignition process of peat under the radiant heat flux of 70 kW/m^2, (a) MC = 10%, (b) MC = 50%, and (c) MC = 100%, where the average ignition time for smouldering and flaming are provided.

For the air-dried peat (MC = 10%) in Fig. 2.5(a), under the same radiant heat flux, only a slightly longer heating duration is required for flaming than for smouldering. For example, under $\dot{q}_r'' = 30$ kW/m^2, a heating time of 5.5 ± 0.5 s is required for smouldering ignition, and 12.5 ± 0.6 s is required for piloted flaming ignition. Nevertheless, both ignition forms are relatively easy to achieve (i.e., very small Region II), and the minimum heating flux for flaming ignition is $\dot{q}''_{min,f}$ = 7.5 ± 0.5 kW/m^2, and for smouldering ignition, it is only slightly smaller as $\dot{q}''_{min,sm}$ = 6.5 ± 0.5 kW/m^2.

For the wet peat (MC =100%) in Fig. 2.5(c), the minimum heat flux for smouldering ignition ($\dot{q}''_{min,sm}$) approaches to 6.5 kW/m^2 that is the same as the air-dried peat in Fig. 2.5(a), because the wet peat will be eventually dried by the long-term heating. On the other hand, the minimum heat flux for flaming ignition ($\dot{q}''_{min,sm}$) increases significantly to 55 kW/m^2. For Region II with the heat flux between 6.5 and 53 kW/m^2, only smouldering ignition can take place, and even if the spark is kept during the continuous heating, flaming will not occur, and the peat is burnt out by smouldering. Therefore, as the peat MC is increased, the propensity for flaming is decreased significantly. Moisture has three effects on the peat: (1) changing the thermal properties of the material (density, thermal conductivity, and specific heat increases, as shown in Table 2.1), (2) enhancing the heat transfer via molecular diffusion, and (3) acting as a strong heat sink during evaporation [36]. Therefore, for the wet peat, a higher heating intensity is needed to trigger the flaming ignition, and the propensity for flaming is significantly decreased.

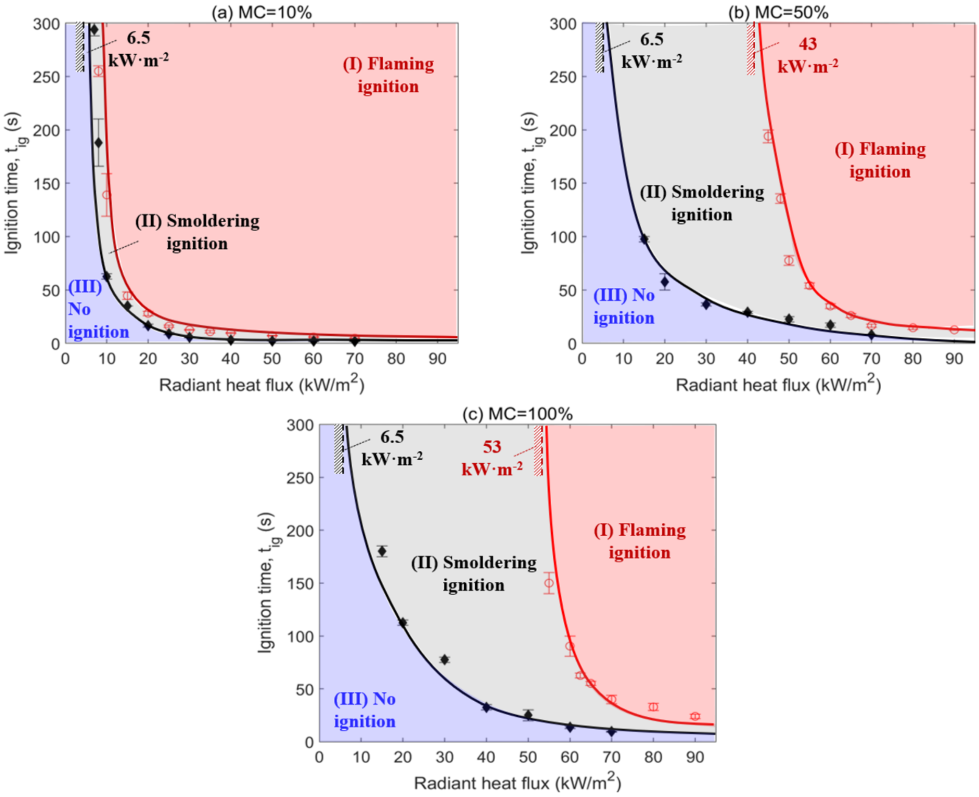

Fig. 2.5. The ignition delay time for piloted flaming ignition and smouldering ignition for (a) air-dried peat sample (MC = 10%), (b) drought peat sample (MC=50%), and (c) wet peat sample (MC = 100%), where three ignition regions (I-III) are identified. The symbols show the experimental data (with standard deviations), and lines are manual fitting curves.

2.3.2 Flaming ignition limit of peat

For the piloted flaming ignition, Fig. 2.6(a) further compares the ignition delay time and the minimum heat fluxes ($\dot{q}''_{min,f}$) for different peat MCs. The measured ignition temperatures are listed in Table 2.1 and shown in Fig.1.6(b). As the peat MC is increased from 10% (air-dried) to 50% (drought) and 100% (wet), the required minimum heat flux increases from 7.5 kW/m^2 to 43 kW/m^2 and 53 kW/m^2, respectively; and the ignition temperature increases from 285 °C to 590 °C and 690 °C, respectively. As expected, the measured flaming ignition temperature for dry peat (285 °C) is close to the peat pyrolysis point, and it is higher than the 270 °C found for smouldering, similar to many other fuels with a low density and a high porosity [29]. However, a significant increase of ignition temperature due to moisture is unexpected.

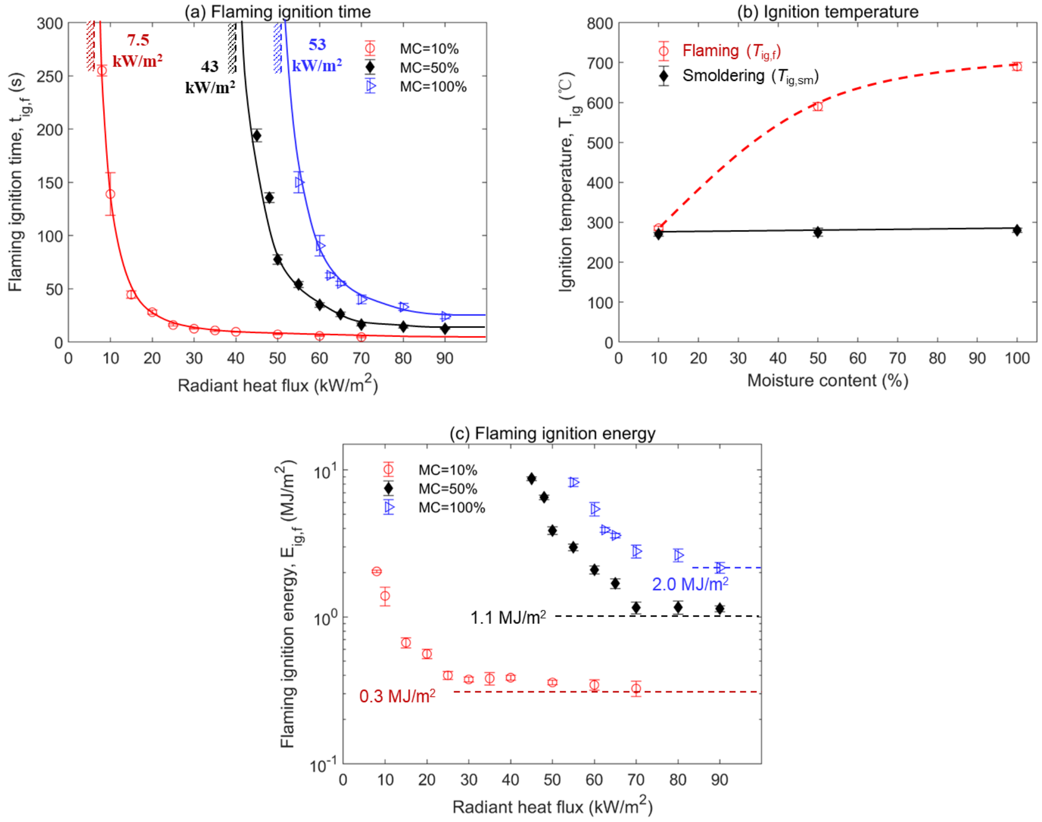

Fig. 2.6. Piloted flaming ignition of peat soil sample under different radiant heat flux and MCs, (a) the flaming ignition time, (b) the surface ignition temperature for flaming and smouldering, and (c) the flaming ignition energy by using Eq. (2.3), where the horizontal lines indicate the minimum ignition energy. The symbols show the experimental data (with standard deviations), and the lines are the manual fitting curves.

In order to verify the measurement of ignition temperature and minimum heat flux, a simple calculation based on thermal equilibrium is proposed. Based on the definition [45], the minimum heat flux should balance the environmental heat loss right below the ignition temperature (T_{ig}) as

$$\dot{q}''_{min} = \dot{q}''_{loss} = \varepsilon\sigma\left(T_{ig}^4 - T_a^4\right) + h\left(T_{ig} - T_a\right) \tag{2.1}$$

where $\varepsilon = 0.9$ is the emissivity of peat; $\sigma = 5.67 \times 10^{-8}$ J/(m^2·s^1·K^4) is the Stefan–Boltzmann constant; T_a is the ambient temperature. The free-convection heat transfer coefficient (h) for a horizontal hot plate can be estimated by an empirical equation [46] as

$$h = 1.52\left(T_{ig} - T_a\right)^{1/3} \tag{2.2}$$

Then, the minimum heat flux can be calculated ($\dot{q}''_{min,f,cal}$) based on the measured flaming ignition temperatures ($T_{ig,f}$), as listed in Table 2.1, which shows a good agreement with the measured minimum heat flux. Thus, we confirm the reliability of the measured ignition temperature and minimum heat flux.

In the literature, although the piloted ignition temperature has been found to change with environment (e.g. heat flux and air flow) and fuel conditions (e.g. MC and density) [31,39–41,47–50], the variation is relatively small (<50°C), and most of the fuels have a low MC (<30%). Therefore, it is reasonable to assume that the piloted flaming ignition temperature for a given fuel is nearly a constant and slightly above the fuel pyrolysis point [45]. Comparatively, the change of ignition temperature found in this work is as large as 300°C (see Fig. 2.6b), and such change should be attributed to the much higher MC and peat's strong tendency to smouldering (explained more in Section 3.3). Therefore, the assumption of near-constant flaming ignition temperature completely fails for the wet wildland fuels like peat, that can hold a wide range of MCs, even reach above 300%.

At the same time, the ignition energy provided by the cone heater can be simply calculated as

$$E''_{ig} = \dot{q}''_r t_{ig} \tag{2.3a}$$

The ignition energy for piloting a flame on peat is plotted in Fig. 2.6(c). When the radiant heat flux is much larger than the heat loss ($\dot{q}''_r \gg \dot{q}''_{loss}$), the minimum ignition energy per unit area (E''_{min}) can be estimated as

$$E''_{min} = \dot{q}''_{r,max} t_{ig} \tag{2.3b}$$

The minimum flaming ignition energy ($E''_{min,f}$) for different peat MCs is shown as the trendline in Fig. 2.6(c) and listed in Table 2.1. In particular, the minimum energy increases almost 7 times from 0.3 MJ/m^2 to 2.0 MJ/m^2, as the peat MC is increased from 10% to 100%, because additional energy is required to heat and evaporate the soil water [40]. Moreover, it is found that regardless of the peat MC, the minimum ignition energy for flaming is about 3 times of that for smouldering, as shown in Table 2.1. As demonstrated in our previous work and numerical model [16,22], the peat moisture content, inorganic content, and density are most important parameters for peat ignition.

2.3.3 Critical mass flux for flaming ignition

For the piloted flaming ignition, the critical mass flux (or mass loss rate per unit area, $\dot{m}''_{ig,f}$) is considered as one of the most fundamental criteria [48]. It is because the value of mass flux is more related to the profile of fuel concentration and the flammability region above the fuel surface.

Nevertheless, the importance of critical mass flux also indicates its sensitivity to the location of the piloted source [38]. In contrast, the mass flux may not be appropriate to characterize the moment of smouldering ignition, because smouldering is dominated by heterogenous oxidations in the solid phase, rather than the mixing process and flammability limit in the gas phase.

The mass flux was computed as the time differentiation of the original sample mass measurements. Figure 1.7(a-c) shows some examples of the measured mass flux time evolution during the entire ignition and burning process of peat, where the symbol indicates the moment of piloted flaming ignition and the critical mass flux. The scrutiny reveals very different locations of the ignition moment in the mass flux curve of different MCs. It is particularly clear in Fig. 2.7(c) that the flaming ignition occurs in the ascending period for the air-dried peat (MC = 10%), near the peak mass flux for the drought peat (MC = 50%), and in the descending period for the wet peat (MC = 100%). For any wet fuel, the measured overall mass flux includes both the water vapor due to drying ($\dot{m}''_w$) and the pyrolysis gas due to the peat degradation ($\dot{m}''_{py}$) as

$$\dot{m}'' = \dot{m}''_w + \dot{m}''_{py} \tag{2.4}$$

Because of the low evaporation point, the mass flux of water vapor most likely contributes to the initial stage as well as the peak in the total mass flux.

When the heat flux is relatively small, for example in Fig. 2.7(a-b), the water both near the surface and in-depth will first evaporate. When the top surface just reaches the pyrolysis point, there is still a large flux of water vapor from the sample in-depth which alters the flammability limit at the location of the pilot spark. Thus, despite a large overall mass flux ($\dot{m}''$), no flaming ignition occurs because of a small mass flux of the pyrolysis gas ($\dot{m}''_{py}$). As the heating continues, both $\dot{m}''_w$ and $\dot{m}''_{py}$ start to decrease, because the reaction front moves in-depth, and the char layer forms on the sample surface to block the radiant heating. At the same time, the continuous heating initiates a robust smouldering fire that dominates the following burning process. However, gas products from smouldering emissions, i.e., mostly H_2O, CO_2, and CO [15,24], are not large and flammable enough to pilot a flame. Therefore, throughout the heating process, the mixture of air, the water vapor, and pyrolysis gases near the spark never exceeds the lower flammability limit unless $\dot{q}''_{min,f}$ is reached. This is the fundamental reason why the minimum heat flux for flaming ignition (Fig. 2.6(a)) as well as the area of Region II (Fig. 2.5) increases with the fuel MC. More detailed numerical simulations with both gas-phase and solid-phase processes are needed to quantify the time evolution of $\dot{m}''_w$ and $\dot{m}''_{py}$ and the minimum heat flux.

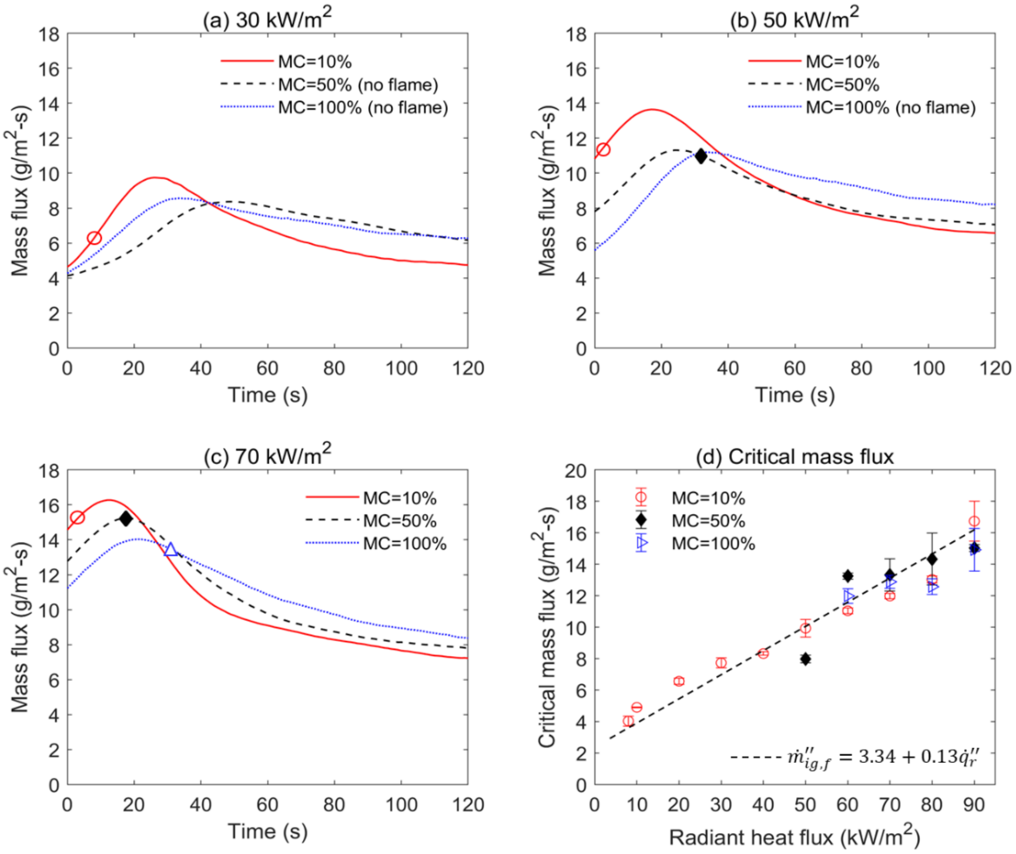

Fig. 2.7. Time evolution of mass flux under the radiant heat flux of (a) 30 kW/m^2, (b) 50 kW/m^2, and (c) 70 kW/m^2, where the symbol indicates the moment of the piloted flaming ignition of peat, and (d) critical mass flux for piloted flaming ignition ($\dot{m}''_{ig,f}$) under all radiant heat fluxes and peat MCs, where the symbols show the experimental data (with standard deviations), and the dashed line is the result of OLS regression.

Figure 1.7(d) summarizes the average critical mass flux of repeating tests under various MC and radiant heat flux, where the symbols show the experimental data and the error bars show the standard deviations. Interestingly, the critical mass flux is found to increase almost linearly with the radiant heat flux up to 90 kW/m^2. In particular, the $\dot{m}''_{ig,f} = 4.9$ g·m^{-2}·s^{-1} at 10 kW/m^2 while it increases more than 3 times to 16.8 g·m^{-2}·s^{-1} at 90 kW/m^2. Then, an empirical correlation based on OLS regression can be fitted for all data points of different MCs as

$$\dot{m}''_{ig,f} = 3.4 + 0.13\dot{q}''_r \tag{2.5}$$

where $\dot{m}''_{ig,f}$ has a unit of g·m^{-2}·s^{-1}, and $\dot{q}''_r$ has a unit of kW/m^2. The R^2 coefficient is found to be 0.97, indicating excellent linearity. Such an increase with the radiant heat flux has also been observed for PMMA (polymethyl methacrylate), the most widely used plastic material in fire research, up to $\dot{q}''_r$ = 24 kW/m^2 [48], and wet wood up to $\dot{q}''_r$ = 50 kW/m^2 [40]. So far, the reason for such a trend has not been well explained yet.

As the peat MC increases from 10% to 100% in Fig. 2.7(d), the minimum mass flux for flaming ignition ($\dot{m}''_{min,f}$) is also increased from 4.3 g·m^{-2}·s^{-1} to 10.4 g·m^{-2}·s^{-1}, as also listed in Table 2.1. More importantly, under the same radiant heat flux, the critical mass flux is found to be insensitive to the peat MC, which has not been observed before. All these abnormal phenomena suggested that care should be taken in using a fixed critical mass flux to describe the flaming ignition of wet wildland fuels [40,49].

2.3.4 Characteristics of peat flame

Once a flame is ignited and attached to the peat, stable burning is achieved. Based on the principle of oxygen calorimetry, the heat release rate per unit area ($\dot{Q}''$) or HRR can be calculated to quantify the intensity of peat flame, as shown in Eq. (2.6) [38]:

$$\dot{Q}'' = \left(0.21 - X_{O_2}\right) V_a \rho_{O_2} \Delta H_{ox} / A \tag{2.6}$$

where V_a is the volumetric flow rate of air (m^3/s), ρ_{O_2} is the density of oxygen (kg/m^3) at the normal temperature and pressure; X_{O_2} is the mole fraction of oxygen in the 'scrubbed' gases (removing water vapor and acid gases); $\Delta H_{ox} \approx 13.1$ MJ/kg is the heat of oxygen for hydrocarbon-based fuel [51]; and A is the cross-section area of the sample, respectively.

Figure 1.8 shows some examples of the flame heat release rate under different radiant heat fluxes and peat MCs. To better compare with the flame intensity of other wildland fuels, the HRR curves of dry wood [52,53], liquorice herb [54] and pine needle beds [55,56] are also plotted in Fig. 2.8(a-c). The comparison shows that once ignited, the flame intensity of peat is much lower than those of other wildland fuels. For example, in Fig. 2.8(b) under 30 kW/m^2, the peak HRR of dry peat is about 20% of dry pine needle, 24% of oak wood, and 45% of liquorice herb. Moreover, as compared in Fig. 2.8(d), as the MC is increased from 10% to 100%, the intensity of the flame is reduced by about 60%, consistent with visual observations in Fig. 2.4. Therefore, for wet fuel, more than half of the mass loss is attributed to water vapor. As a result, the flame temperature decreases as the mass flux of water vapor increases, so the flame becomes weak and easy to extinguish.

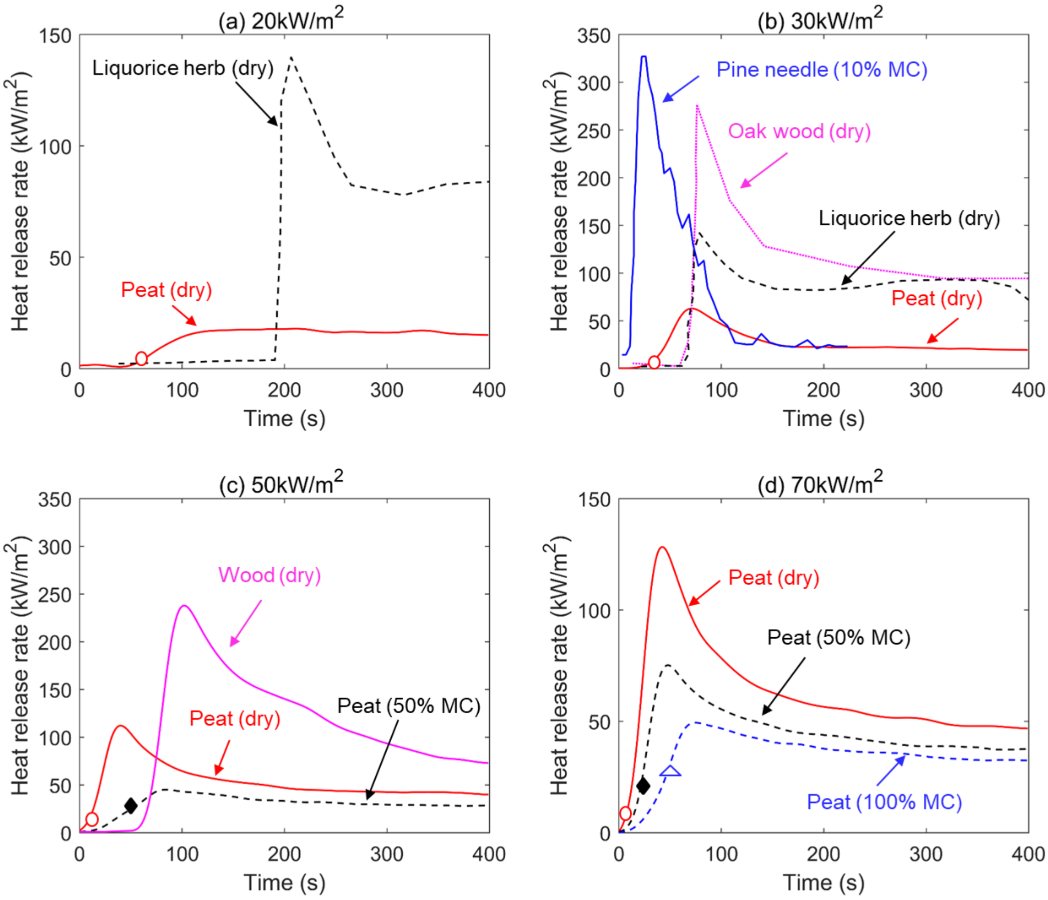

Fig. 2.8. Time evolution of the heat release rate under radiant heat flux of (a) 20 kW/m^2, (b) 30 kW/m^2, (d) 50 kW/m^2, (d) 70 kW/m^2, where data of dry wood [52,53], liquorice herb [54], and pine-needle bed [55,56] under the same heat flux are presented for comparison.

The effective heat of (flaming) combustion [38] can be estimated from the heat release rate and the mass flux as

$$\Delta H_f = \frac{Q''}{\dot{m}''} \tag{2.7}$$

Calculation shows that ΔH_f =18.4 ± 1.7 MJ/kg^1 for the pyrolysis gases of dry peat. Thermogravimetric analysis (TGA) shows that the pyrolysis of peat produces about 70% of pyrolysis gas and 30% black char (see Fig. A1.1). Thus, the heat of flaming combustion of dry peat is about 18.4 × 0.7 = 13 MJ/kg.

The heat of smouldering combustion (ΔH_{sm}) can be measured from the differential scanning calorimeter (DSC). For this peat, ΔH_{sm} is measured to be about 12 MJ/kg, which is close to 14.2 MJ/kg of similar peat previously measured by Frandsen [57], but higher than 10 MJ/kg for wood [38]. Therefore, we can conclude that for this organic-rich peat soil, the heat of flaming and the heat of smouldering are comparable. Also, the total heat of combustion for peat is approximately the combination of flaming and smouldering, i.e., 13 + 12 = 25 MJ/kg. This value is similar to methanol and ethanol [58], while slightly lower than typical coal (about 30 MJ/kg) [59], considering peat soil is often called as "young" coal.

Note that the HRR from the flame is not only controlled by the heat of flaming combustion, but also by factors influencing the mass loss such as the pyrolysis point, density and porosity of fuel [45]. In fact, the heat of flaming combustion of peat is only slightly lower than that of the pine needle and wood (both about 20 MJ/kg [45], but the HRR of peat is much lower, as compared in Fig. 2.8. For wood, its high density allows for more gaseous fuels released per unit area (i.e., larger fuel mass flux), while for pine needle beds, the flame can be sustained in the larger pores and heat each piece of pine needle, both of which make the flame heating more effective. Comparatively, for peat, (1) the flame cannot be sustained inside the pore; (2) the bulk density is small; and (3) heat of flaming is lower, so all these three factors make the flame weaker on peat soils.

2.3.5 Carbon emission from peat fires

Peatlands play an important role in the global carbon balance and recent environmental changes [9,11]. For example, the 1997 peatland fires in Indonesia may have released 13–40% of the mean annual global carbon emissions from fossil fuels [11]. More importantly, compared to regular flaming wildland fires, the amount of toxic carbon monoxide (CO) released from smouldering peat fires is much higher. Laboratory measurements have shown that if 1 kg of dry peat is burnt in smouldering, 0.17~0.25 kg of CO is released (i.e., a CO emission factor of 0.17~0.25 kg/kg), and the CO/CO_2 ratio is between 0.15 and 0.43 [24,60,61]. Comparatively, the emission factor of CO for flaming wildland fuel is less than 0.02 kg/kg [62], and the CO/CO2 ratio is less than 0.03 [63,64].

Figure 1.9 plots the typical time evolution of CO/CO_2 ratio for smouldering and flaming peat fire under different MCs and external radiation. The solid symbol indicates the moment of flame ignition, and the hollow symbol indicates the moment of flame extinction and smouldering peat fire. Based on the change in CO/CO_2 ratio, three stages of peat fire can be observed:

1. Before the flaming ignition or during drying and pyrolysis, the carbon emission through CO increases, and the CO/CO_2 ratio is high (0.1~0.35);

2. Once flaming ignited, the CO emission starts to decrease, and the CO/CO_2 ratio decreases to about 0.02 which is similar to other flaming wildland fires [63,64]. In general, the duration of flame

lasts longer under larger external radiation;

3. After flame extinction, there is a continuation of smouldering, and the CO/CO_2 ratio increases to about 0.2 until burnout, similar to past measurements in [24,60,61].

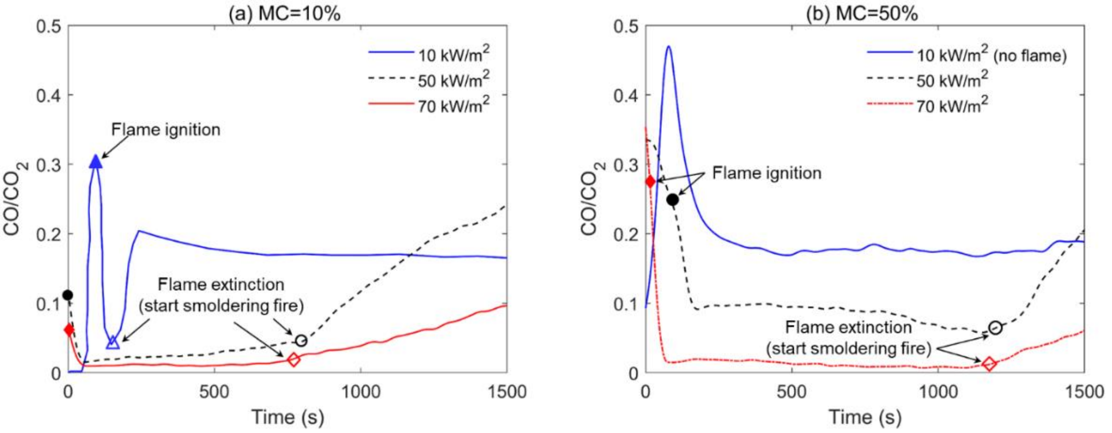

Fig. 2.9. Time evolution of CO/CO_2 ratio under different heat fluxes with the peat moisture content (MC) of (a) 10% and (b) 50%, where the solid symbol indicates the moment of flame ignition, and the hollow symbol indicates the moment of flame extinction and smouldering peat fire.

For peat MC of 50% (Fig. 2.9b), flaming ignition does not occur under the radiation of 10 kW/m^2. Instead, smouldering dominates the entire burning process, and the CO/CO_2 is always high (~0.2). Increasing the radiant heat flux to 50 kW/m^2, despite a successful flaming ignition, the flame is very weak and breaks into multiple small flamelets that do not cover the entire fuel surface. Thus, both flaming and smouldering peat fire coexist, leading to a medium level of CO/CO_2 ratio (~0.1).

2.4 Conclusions

In this experimental work, we found that peat soils can support a flaming wildfire, like leaves, twigs and bark, even when the peat moisture content (MC) is as high as 100%. Piloting a flame on peat is found to be more difficult than starting a smouldering peat fire, requiring a higher minimum heat flux and three times more ignition energy.

Moisture significantly lowers the flammability of peat soil. As the MC increases from 10% (air-dried) to 100% (wet), the minimum heat flux of flaming ignition increases from 7.5 kW/m^2 to 53 kW/m^2, the ignition temperature increases significantly from 285°C to 690°C; and the minimum flaming ignition energy increases from 0.3 MJ/m^2 to 2.0 MJ/m^2. The critical mass flux of flaming ignition is found to be insensitive to peat MC, but increases linearly with the heat flux, as $\dot{m}''_{ig,f} = 3.4 + 0.13\dot{q}''_r$.

These phenomena suggest that defining a constant ignition temperature or mass flux is inappropriate for wet wildland fuels.

The heat of flaming combustion for dry peat is estimated to be 13 MJ/kg, similar to its heat of smouldering combustion (12 MJ/kg). The heat release rate of peat flame is significantly lower than that of pine needles, wood, and other wildland fuels, suggesting that the peat flame is weak and easy to suppress. Also, the CO/CO_2 ratio of flaming peat fires is less than 0.02, much smaller than 0.2 of smouldering peat fires. In our future work, experiments will be conducted to quantify the ignition temperature, and rate of flame spread over peat soil under external radiation. Also, future numerical simulations are needed to understand the minimum heat flux, critical mass flux, and the interaction between flaming and smouldering peat fire.

Acknowledgements

This study received financial support from the National Natural Science Foundation of China (NSFC No. 51876183) and HK PolyU (1-BE04). The authors thank Dr. Wei Gao (USTC) for conducting thermal analysis for the peat sample. S. Lin would like to thank co-author Peiyi Sun for assistance in conducting experiments.

References

[1] Pel AJ, Bliemer MCJ, Hoogendoorn SP. A review on travel behaviour modelling in dynamic traffic simulation models for evacuations. Transportation (Amst) 2012;39:97–123.

[2] McClure CD, Jaffe DA. Investigation of high ozone events due to wildfire smoke in an urban area. Atmos Environ 2018;194:146–57.

[3] Toledo T, Marom I, Grimberg E, Bekhor S. Analysis of evacuation behaviour in a wildfire event. Int J Disaster Risk Reduct 2018;31:1366–73.

[4] Liu Y, Stanturf J, Goodrick S. Trends in global wildfire potential in a changing climate. For Ecol Manage 2010;259:685–97.

[5] Koksal K, McLennan J, Every D, Bearman C. Australian wildland-urban interface householders' wildfire safety preparations: 'Everyday life' project priorities and perceptions of wildfire risk. Int J Disaster Risk Reduct 2018:1–13.

[6] Gibson CM, Chasmer LE, Thompson DK, Quinton WL, Flannigan MD, Olefeldt D. Wildfire as a major driver of recent permafrost thaw in boreal peatlands. Nat Commun 2018;9:3041.

[7] Rein G. Smouldering Fires and Natural Fuels. In: Claire M. Belcher, editor. Fire Phenom. Earth Syst., New York: John Wiley & Sons, Ltd.; 2013, p. 15–34.

[8] Gorham E. The future of research in canadian peatlands: A brief survey with particular reference to global change. Wetlands 1994;14:206–15.

[9] Turetsky MR, Benscoter B, Page S, Rein G, Van Der Werf GR, Watts A. Global vulnerability of peatlands to fire and carbon loss. Nat Geosci 2015;8:11–4.

[10] Huang X, Rein G. Downward Spread of Smouldering Peat Fire: the Role of Moisture, Density

and Oxygen Supply. Int J Wildl Fire 2017;26:907–18.

[11] Page SE, Siegert F, Rieley JO, Boehm H V., Jayak A, Limink S, et al. The amount of carbon released from peat and forest fires in Indonesia during 1997. Nature 2002;420:61–6.

[12] Ballhorn U, Siegert F, Mason M, Limin S. Derivation of burn scar depths and estimation of carbon emissions with LIDAR in Indonesian peatlands. Proc Natl Acad Sci 2009;106:21213–8.

[13] Huang X, Rein G. Smouldering combustion of peat in wildfires: Inverse modelling of the drying and the thermal and oxidative decomposition kinetics. Combust Flame 2014;161:1633–44.

[14] Frandsen WH. The influence of moisture and mineral soil on the combustion limits of smouldering forest duff. Can J For Res 1987;16:1540–4.

[15] Hadden RM, Rein G, Belcher CM. Study of the competing chemical reactions in the initiation and spread of smouldering combustion in peat. Proc Combust Inst 2013;34:2547–53.

[16] Huang X, Rein G, Chen H. Computational smouldering combustion: Predicting the roles of moisture and inert contents in peat wildfires. Proc Combust Inst 2015;35:2673–81.

[17] Restuccia F, Huang X, Rein G. Self-ignition of natural fuels: Can wildfires of carbon-rich soil start by self-heating? Fire Saf J 2017;91:828–34.

[18] Huang X, Restuccia F, Gramola M, Rein G. Experimental study of the formation and collapse of an overhang in the lateral spread of smouldering peat fires. Combust Flame 2016;168:393–402.

[19] Prat-Guitart N, Belcher CM, Thompson DK, Burns P, Yearsley JM. Fine-scale distribution of moisture in the surface of a degraded blanket bog and its effects on the potential spread of smouldering fire. Ecohydrology 2017;10(8).

[20] Kreye JK, Varner JM, Dugaw CJ, Engber EA, Quinn-davidson LN. Patterns of Duff Ignition and Smouldering beneath Old Pinus palustris: Influence of Tree Proximity, Moisture Content, and Ignition Vectors. For Sci 2017;63:165–72.

[21] Huang X, Rein G. Upward-and-downward spread of smouldering peat fire. Proc Combust Inst 2019;37:4025–33.

[22] Huang X, Rein G. Computational study of critical moisture and depth of burn in peat fires. Int J Wildl Fire 2015;24:798–808.

[23] Ramadhan ML, Palamba P, Imran FA, Kosasih EA, Nugroho YS. Experimental study of the effect of water spray on the spread of smouldering in Indonesian peat fires. Fire Saf J 2017;91:671–9.

[24] Hu Y, Christensen E, Restuccia F, Rein G. Transient gas and particle emissions from smouldering combustion of peat. Proc Combust Inst 2019;37:4035–42.

[25] Wang S, Huang X, Chen H, Liu N. Interaction between flaming and smouldering in hot-particle ignition of forest fuels and effects of moisture and wind. Int J Wildl Fire 2017;26:71–81.

[26] Simeoni A. Wildland Fires. In: 5, editor. SFPE Handb. Fire Prot. Eng., New York: Springer; 2016, p. 3283–302.

[27] Fernandez-Pello AC. Wildland fire spot ignition by sparks and firebrands. Fire Saf J 2017;91:2–10.

[28] Williams FA. Mechanisms of fire spread. Symp Combust 1977;16:1281–94.

[29] Rein G. Smouldering Combustion. SFPE Handb Fire Prot Eng 2014;2014:581–603.

[30] Hadden R, Alkatib A, Rein G, Torero JL. Radiant Ignition of Polyurethane Foam: The Effect of Sample Size. Fire Technol 2014;50:673–91.

[31] Boonmee N, Quintiere JG. Glowing and flaming autoignition of wood. Proc Combust Inst

2002;29:289–96.

[32] Watts AC. Organic soil combustion in cypress swamps: Moisture effects and landscape implications for carbon release. For Ecol Manage 2013;294:178–87.

[33] Valdivieso JP, Rivera JDD. Effect of Wind on Smouldering Combustion Limits of Moist Pine Needle Beds. Fire Technol 2013;50:1589–605.

[34] Finney MA, Cohen JD, McAllister SS, Jolly WM. On the need for a theory of fire spread. Int J Wildl Fire 2013;22:25–36.

[35] Jervis FX, Rein G. Experimental study on the burning behaviour of Pinus halepensis needles using small-scale fire calorimetry of live, aged and dead samples. Fire Mater 2016;40:385–195.

[36] McAllister S, Grenfell I, Hadlow A, Jolly WM, Finney M, Cohen J. Piloted ignition of live forest fuels. Fire Saf J 2012;51:133–42.

[37] Dimitrakopoulos AP, Papaioannou KK. Flammability Assessment of Mediterranean Forest Fuels. Fire Technol 2001;37:143–52.

[38] Drysdale D. An Introduction to Fire Dynamics. 3rd ed. Chichester, UK: John Wiley & Sons, Ltd; 2011.

[39] Lyon RE, Quintiere JG. Criteria for piloted ignition of combustible solids. Combust Flame 2007;151:551–9.

[40] McAllister S. Critical mass flux for flaming ignition of wet wood. Fire Saf J 2013;61:200–6.

[41] Wongchai P, Tachajapong W. Effects of Moisture Content in Para Rubber Leaf Litter on Critical Mass Flux and Piloted Ignition Time. Energy Procedia 2015;79:448–52.

[42] Babrauskas V. The Cone Calorimeter. In: Hurley M, editor. SFPE Handb. Fire Prot. Eng. 5th Editio, London: Springer; 2016, p. 952–80.

[43] Perdana LR, Ratnasari NG, Ramadhan ML, Palamba P, Nasruddin, Nugroho YS. Hydrophilic and hydrophobic characteristics of dry peat. IOP Conf Ser Earth Environ Sci 2018;105.

[44] Jacobsen RT, Lemmon EW, Penoncello SG, Shan Z, N.T. Wright. Thermophysical Properties of Fluids and Materials. In: Bejan A, Kraus AD, editors. Heat Transf. Handb., Hoboken: John Wiley & Sons; 2003, p. 43–159.

[45] Quintiere JG. Fundamental of Fire Phenomena. New York: John Wiley; 2006.

[46] Holman JP. Heat Transfer. 10th ed. New York: McGraw-Hill; 2008.

[47] Zabetakis M. Flammability characteristics of combustible gases and vapors. U.S.: 1965.

[48] Rich D, Lautenberger C, Torero JL, Quintiere JG, Fernandez-Pello C. Mass flux of combustible solids at piloted ignition. Proc Combust Inst 2007;31:2653–60.

[49] Janssens M. Piloted Ignition of Wood: A Review. Fire Mater 1991;15:151–67.

[50] Babrauskas V. Journal of Fire Protection Ignition of Wood : A Review of. J Fire Prot Eng 2002;12:81–8.

[51] Huggett C. Estimation of rate of heat release by means of oxygen consumption measurements. Fire Mater 1980;4:61–5.

[52] Chung YJ, Spearpoint M. Combustion properties of native Korean wood species. Int J Eng Performance-Based Fire Codes 2008;9:118–25.

[53] Zachar M, Martinka J, Balog K. Impact of Oak wood ageing on the heat release rate and the yield of carbon monoxide during fire. Eur J Environ Saf Sci 2014;2:1–4.

[54] Pei B, Song GY, Lu C. The application of cone calorimeter on the study of burning performance of liquorices. Procedia Eng 2014;71:291–5.

[55] Jerry Alexander T, Martin B, Surya Theja Rao J, Ali A. Development of a transformable

electrically powered wheel chair into a medical emergency stretcher. Int J Pharm Technol 2016;8:12793–800.

[56] Thomas JC, Hadden RM, Simeoni A. Experimental investigation of the impact of oxygen flux on the burning dynamics of forest fuel beds. Fire Saf J 2017;91:855–63.

[57] Frandsen WH. Heat Evolved From Smouldering Peat. Int J Wildl Fire 1991;1:197–204.

[58] Thomas G. Overview of Storage Development DOE Hydrogen Program: Sandia National Laboratories Livermore, California. San Ramon, California: 2000.

[59] Tan Y, Croiset E, Douglas MA, Thambimuthu K V. Combustion characteristics of coal in a mixture of oxygen and recycled flue gas. Fuel 2006;85:507–12.

[60] Rein G, Cohen S, Simeoni A. Carbon emissions from smouldering peat in shallow and strong fronts. Proc Combust Inst 2009;32 II:2489–96.

[61] Hu Y, Fernandez-Anez N, Smith TEL, Rein G. Review of emissions from smouldering peat fires and their contribution to regional haze episodes. Int J Wildl Fire 2018;27(5):293.

[62] Grexa O, Lübke H. Flammability parameters of wood tested on a cone calorimeter. Polym Degrad Stab 2001;74:427–32.

[63] Fateh T, Richard F, Batiot B, Rogaume T, Luche J, Zaida J. Characterization of the burning behaviour and gaseous emissions of pine needles in a cone calorimeter - FTIR apparatus. Fire Saf J 2016;82:91–100.

[64] Schemel CF, Simeoni A, Biteau H, Rivera JD, Torero JL. A calorimetric study of wildland fuels. Exp Therm Fluid Sci 2008;32:1381–9.

CHAPTER 3: Effect of Heating Dimension on the Smouldering Ignition

Summary

Ignition of materials by a point source of heating plays an important role in initiating many structure and wildland fires, such as spotting by hot particles, lightning, and concentrated irradiation. Herein, we study the smouldering ignition of tissue paper by a concentrated sunlight spot with heat fluxes up to 780 kW/m^2, which is focused by a transparent glass sphere with a diameter of 150 mm and a focal length of 108 mm. The diameter of the sunlight spot on the targeted paper ranges from 1.5 mm to 20.0 mm by varying the position of the paper within the focal length, where a smaller spot has an increased intensity of sunlight irradiation. Given the size of the irradiation spot, the smouldering ignition time decreases as the concentrated irradiation increases, similar to the classical piloted flaming ignition theory. However, the measured minimum spot irradiation for smouldering ignition is not a constant but is much higher than the 11 kW/m^2 measured in a traditional cone-calorimeter test. As the diameter of the irradiation spot decreases from 20.0 mm to 1.5 mm, the minimum irradiation for smouldering ignition increases from 17.5 kW/m^2 to 205 kW/m^2, and the ignition energy increases from 0.084 MJ/m^2 to 2.0 MJ/m^2. A simplified heat transfer analysis reveals that lateral conductive cooling within the fuel becomes dominant for a smaller spot ignition area. Finally, a physical-based 2-D computational model is built to demonstrate and reproduce the experimental phenomena. This work ultimately quantifies the potential fire risk from concentrated sunlight spots and helps elucidate the underlying mechanisms leading to smouldering ignition.

This chapter is partially based on "S. Wang, S. Lin (co-first author), Y. Liu, X. Huang and M. Gollner (2021) *Smouldering Ignition Using a Concentrated Solar Irradiation Spot*, **Fire Safety Journal** (submitted)" and "S. Lin, S. Wang, P. Sun, H. Yuan and X. Huang (2021) *Experimental and Computational Study of Smouldering Ignition by Concentrated Sunlight,* **2021 China National Symposium on Combustion** (submitted)".

3.1 Introduction

The ignition of combustible materials is fundamental to fire safety analyses, defining initiation and leading to the eventual growth of sometimes devastating fire events. Many ignition events leading to both structure and wildland fires occur remotely by a point heating source [1], such as the deposition of lofted firebrands [2–4], hot metal particles [4,5], dripping molten materials [6], laser irradiation [7,8], lightning strikes [9], and concentrated irradiation [10–13]. Significant studies have recently focused on spotting ignition of various fuels by lofted firebrands, which can sometimes dominate the fire spread rate in both wildland and wildland-urban interface (WUI) fires [2,3]. A less-studied source of ignition is a concentrated sunlight spot, which can be reflected by a curved mirror or focused by a dew droplet, curved glass window and decorations, transparent fish bowls, or cylindrical bottles filled with water [14–16]. From 2010 to 2015, 125 fires in the United Kingdom were reported to be triggered by a concentrated sunlight spot [17], posing threats to both human lives and property. However, to the best of the authors' knowledge, this remote ignition phenomenon has not received a detailed and quantitative study, presenting a key knowledge gap.

Over the past 50 years, limited studies have investigated flaming ignition by a laser spot or concentrated irradiation. Kashiwagi [7,8] showed that the minimum radiant heat fluxes for flaming autoignition are 90 kW/m^2 for red oak and 160 kW/m^2 for PMMA, performed with a 2-3 cm diameter laser spot. By increasing the diameter of the heating spot to about 3.5 cm, the minimum radiant fluxes decreased to 80-90 kW/m^2, still much higher than the 25-50 kW/m^2 reported for auto-ignition of 10-cm width square wood samples more evenly heated in a cone calorimeter [18]. Later, the laser ignition of thin PMMA sheets with different orientations has also been investigated experimentally and numerically [19,20]. Grishin et al. [10] generated a light beam by a tungsten lamp to ignite a porous forest fuel layer with a bulk density of 6-24 kg/m^3 and revealed that the required irradiant heat flux for flaming ignition decreases as the heating diameter increases from 8 mm to 27 mm. Warren [11] concentrated sunlight using a spherical water-filled glass bowl with a diameter of 200 mm and demonstrated the possibility of smouldering ignition of print paper by concentrated irradiation. Recently, Sandia National Laboratories [12,13] used hundreds of reflection mirrors in a concentrated solar tower plant to generate an irradiation greater than 2,000 kW/m^2 (about 0.5-m diameter spot) that could ignite some common fuels within a few seconds.

Compared to spotting ignition by direct contact with a hot metal spark or firebrand (i.e., transfer of both a physical heat source and fuel) [2,4], ignition by a concentrated irradiation spot involves only energy transfer. Thus, such an ignition process is simpler, which may also provide valuable information applicable to other spotting ignition processes. Once an intense irradiation spot is applied, a recipient fuel may first be heated, dried, decompose, and then begin to smoulder. Auto-ignition directly to a flaming mode of combustion is also possible if the radiation is strong enough [8,21]. Smouldering combustion is slow, low-temperature and flameless burning of porous fuel, which is sustained as a heterogeneous oxidative process and different from flaming combustion [22]. Smouldering is a common fire phenomenon in both structures and wildland, such as the burning of upholstered furniture, mattresses, firebrands, duff, and peatlands [23,24]. Smouldering can be easily initiated by a weaker ignition source or even self-ignited, providing a shortcut to severe fire events through the smouldering-to-flaming transition [22–27]. Therefore, it is of vital significance to fully understand smouldering ignition, but so far, little research has studied the smouldering ignition by a point heating source, and the ignition criteria are still poorly understood.

This work investigates the smouldering ignition of multiple-layered tissue paper samples by intense point irradiation, i.e., a sunlight spot concentrated by a spherical glass ball. Within the focus length, the diameter of the heating spot was varied from 1.5 mm to 20 mm, and the intensity of irradiation was varied up to 780 kW/m^2. The ignition delay time, critical heat flux, and ignition energy of smouldering by the irradiation spot were quantified. Afterwards, a simplified heat transfer model was proposed to (1) explain the varying minimum irradiation and energy required for smouldering ignition and (2) quantify the potential ignition risk initiated by the concentrated sunlight in both structure and wildland fires. Finally, a 2-D computational model was developed to verify the experimental observation.

3.2 Experimental methods

3.2.1 Materials and apparatus

Thin tissue paper made of unbleached pulp was used in the experiment, as it was a typical thin fuel that could be found in residential buildings and similar in nature to cellulosic wildland fuels. Before the test, the tissue paper was first oven-dried at 75 °C for 48 h, and its dried bulk density was measured to be 98 ± 5 kg/m^3. Afterward, it was placed into an electronic dry cabinet to avoid re-absorption of moisture from the air. For the test, the tissue was first cut into a size of 60 mm × 60 mm, and six layers of tissue were packed into a sample with an overall thickness (δ) of about 2 mm (see Fig. 3.1a). For a single layer of tissue (about 0.1-mm thick), the concentrated irradiation spot would create a hole on the tissue directly without ignition, so multiple layers of tissue were used.

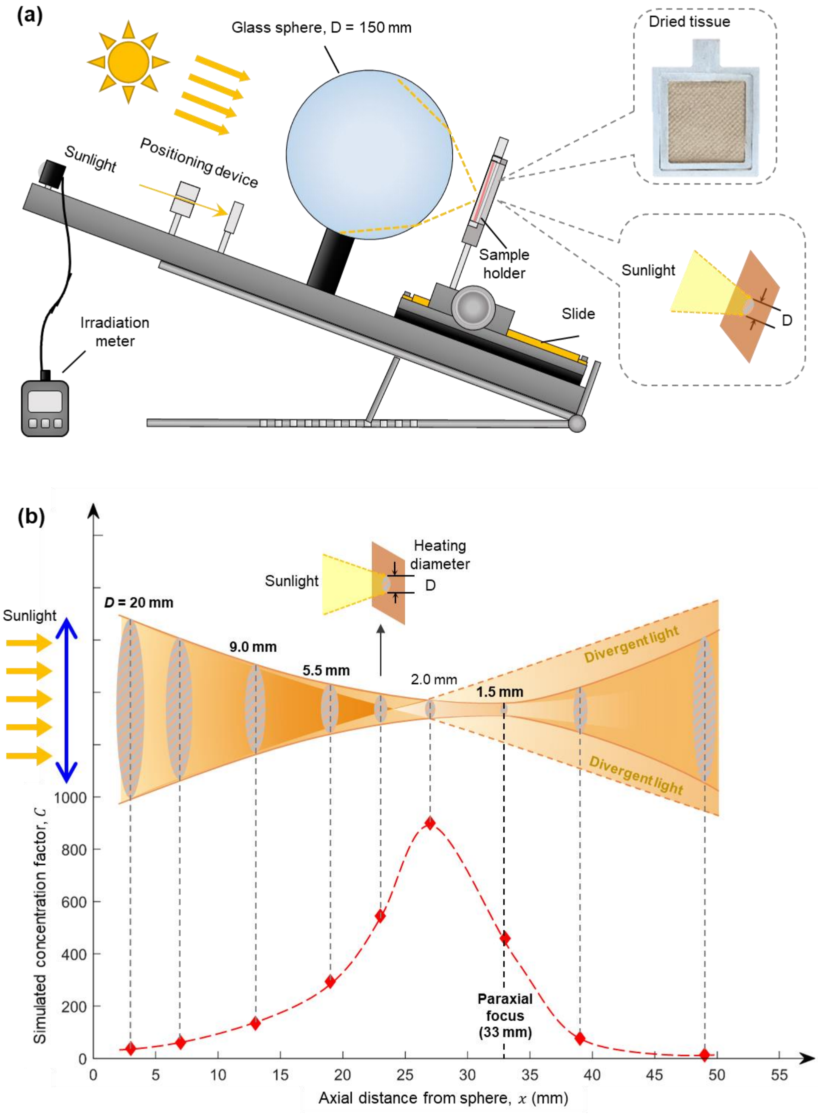

Fig. 3.1. (a) Schematic diagram of the designed experiment apparatus, and (b) simulated concentration factor at different axial distance from sphere.

In the experiment, natural sunlight was concentrated by a 150-mm K9 crown glass sphere with a refractive index (n_c) around 1.53. The spherical lens minimized the operation of the concentrator during the experiment, because its projection of sunlight beam was fixed and insensitive to the position of the sun. The focal length and back focal length of the crown glass sphere were theoretically calculated to be 108 mm and 33 mm [28], as illustrated in Fig. 3.1b.

A positioning device was fixed perpendicular to the surface of the base stand (Fig. 3.1a). To ensure that the device was parallel to the sunlight, the angle of the base stand was adjusted until the light beam passed through the hole in the middle of the front aluminium block and projected on the middle of the back aluminium block. A solar power meter was fixed at the front towards the sunlight direction to record real-time solar irradiation ($\dot{q}_s''$). The sample frame was a hollow box that provided a volume of $60 \times 60 \times 2$ mm^3 for the tissue sample and was inserted into the sample holder. The sample holder was installed on a slide that can adjust its distance between the tissue sample and the glass sphere with a precision of 0.5 mm.

3.2.2 Irradiation heat flux of concentrated light spot

Traditionally, the value of incident radiant heat flux can be measured by a radiometer. However, as the diameter of the light spot decreases, the heat flux of sunlight concentrated by the glass sphere could exceed 500 kW/m^2, which was much higher than the upper limit (usually 100-200 kW/m^2) of a conventional radiometer. Thus, to quantify the high irradiation of concentrated sunlight spot, an optical simulation performed in *TracePro* [29] was first used to correlate the size of the light spot and theoretical irradiation ($\dot{q}_c''$) concentrated by a 150-mm crown glass sphere.

In the optical simulation, the overall concentration factor (C) considered not only optical concentration, but also the actual energy dissipation, such as the light reflected, refracted, and absorbed by the glass sphere in the transmitting process [11]. Fig. 3.1b shows the simulated concentration factor (C) vs. light spot diameter (*D*) of a 150-mm glass sphere. Note that the peak concentration factor is about 900 at about $D = 2$ mm, which is not at the optical back focal length. Due to losses resulting from reflection, refraction, and spherical aberration, the concentration factor of the smallest light spot ($D = 1.5$ mm) is about 460 at the back focal length.

With the instant solar irradiation ($\dot{q}_s''$) and the concentration factor for different light spots determined, the actual concentrated solar radiant heat flux to the fuel sample can be calculated as

$$\dot{q}_c'' = C\dot{q}_s'' \tag{3.1}$$

For example, if the solar irradiation is 1 kW/m^2 [30], the resultant heat flux peaks at around 900 kW/m^2, which is close to the literature value [11]. In addition, the conventional radiometer was used to measure the concentrated solar irradiation of large spots up to 200 kW/m^2 and compare with the calculated values by Eq. (3.1) in Fig. A3.1. Good agreement was found between the radiometer and calculated values, confirming the accuracy of the irradiation heat flux based on the optical simulation.

Sunlight through the glass sphere will also form a caustic zone instead of a focal point due to the existence of spherical aberration, that is, the blurry appearance of the outer part of the view of a convex lens [15]. As the spots become intensively blurry beyond the focus length, their edge could be hard to identify. Therefore, to maintain better precision, only light spots within the back focal length with clearly defined boundary were adopted in the experiment [31]. In total, four different positions (x) of 3 mm, 13 mm, 19 mm, and 33 mm within the glass sphere's back focal length were tested, with respect to four heating diameters (D) of 20.0 mm, 9.0 mm, 5.5 mm, and 1.5 mm, as summarized in Table 3.1.

Table 3.1. Summary of diameters of the concentrated irradiation spots (D) and concentration factors (C) at different distances from the glass sphere.

Distance from sphere, x (mm)	**33.0**	**19.0**	**13.0**	**3.0**
Irradiation spot diameter, D (mm)	1.5	5.5	9.0	20
Concentration factor, C	460	294	134	38

3.2.3 Experimental procedures

Before the test, the diameter of the light spot was adjusted by controlling the distance between the glass sphere and sample. Afterward, the light spot was shielded by a piece of black cardboard, and the tissue sample was inserted into the sample holder. Once the solar irradiation heat flux ($\dot{q}_s''$) read by the solar power meter was relatively constant, the back cardboard was removed to allow the light spot to irradiate the fuel surface. Then, the sample was heated by the light spot for a prescribed duration (t).

For flaming ignition, the time of ignition can be determined by the appearance of a flame. However, it was not possible to instantaneously determine the success of smouldering ignition and the exact ignition time [26]. Thus, the tissue sample was first heated for a prescribed duration, and then it was left in the controlled environment without wind for another 5 min for further observation. Successful smouldering ignition was then identified if the smouldering spot was self-sustaining. A self-sustained smouldering is defined as the smouldering front successfully propagating outwards from the heating region within 5 min, eventually burning out the sample. If smouldering ignition was not observed, the heating duration was increased until smouldering ignition was successful. Then, more than 100 tests were conducted using the same heating diameter under a range of concentrated irradiations. Afterward, the diameter of the heating spot was varied by moving the sample within the focal length to investigate its effect on smouldering ignition.

In total, more than 600 tests were conducted outdoors on typical summer sunny days with a clear blue sky. Depending on the weather and solar zenith angle, the instant solar radiation ranged from 0.2 kW/m^2 (at nightfall) to 1.6 kWm^2 (at noon). During the test, the ambient temperature was 29 ± 2 °C, the relative humidity was 82 ± 10 %, the wind speed was 5.5 ± 0.9 m/s, and the ambient pressure was 101 kPa.

3.3 Experimental results

3.3.1 Smouldering spotting ignition phenomena

Fig. 3.2a shows an example of a successful smouldering ignition process by a concentrated irradiation spot with a diameter of 1.5 mm and a resultant irradiation heat flux of 560 kW/m^2. Once the irradiation spot was applied on the sample surface, some smoke was released, likely a combination of condensed water vapor and pyrolysis gases [26]. Continuing the heating, the surface layer within the light spot turned black (or charred) and cracked, allowing the light beam to heat the lower layers directly. After heating for about 8 s, the sample detached from the apparatus but remained in the controlled environment (without wind) for another 5 min. As a result, the black spot expanded outwards evenly, expanding at a stable rate, and eventually burned out the sample. Fig. 3.2b shows an example of a failed smouldering ignition process by the concentrated irradiation spot with a diameter of 1.5 mm and a resultant radiant heat flux of 300 kW/m^2. Initially, smoke and a charring tendency were also observed. However, after heating for 8 s, no smouldering propagation phenomenon was observed, indicating a failed ignition.

3.3.2 Irradiation duration for ignition and critical irradiation

The experimental outcomes under different diameters of concentrated irradiation spots (D) and the resultant irradiant heat fluxes ($\dot{q}_c''$) are summarized in Fig. 3.3, where the solid and hollow markers represent failed and successful ignition, respectively. Note that the instant solar radiation ($\dot{q}_s''$) changed from time to time, so there was a large scattering in the irradiation value. Given the diameter of the concentrated irradiation spot, the required heating duration for the smouldering ignition (t_{ig}) decreases as the external irradiation increases. This trend is similar to the piloted flaming ignition theory, where the flaming ignition time is mainly the required heating time for pyrolysis [26,32,33].

(a) Successful smoldering ignition (D = 1.5 mm, $\dot{q}''_c$= 560 kW/m^2)

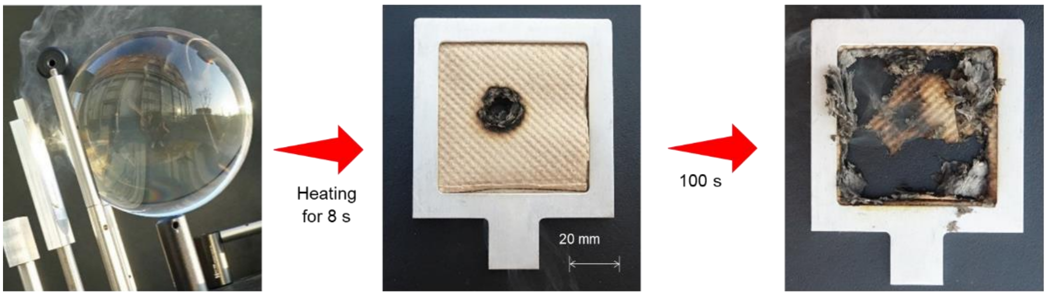

(b) Failed smoldering ignition (D = 1.5 mm, $\dot{q}''_c$= 300 kW/m^2)

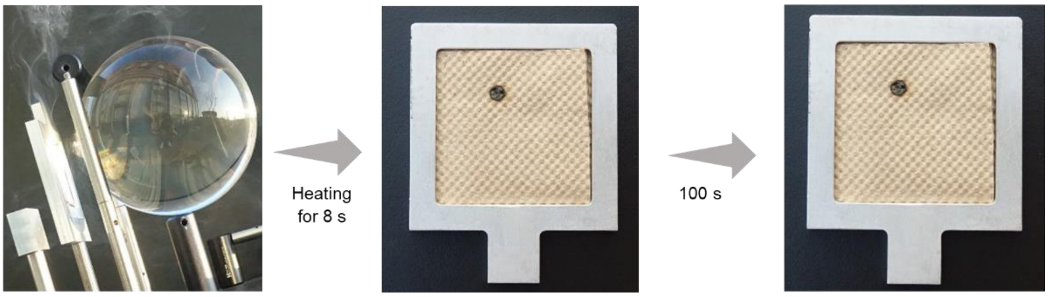

Fig. 3.2. Smouldering ignition of dried tissue samples by concentrated irradiation spot with a diameter of 1.5 mm for 8 s, (a) successful ignition under irradiation of 560 kW/m^2, and (b) failed ignition under irradiation of 300 kW/m^2.

In general, the required duration for smouldering ignition (t_{ig}) is the time to heat the fuel surface to a critical smouldering temperature (T_{sm}) which is the threshold temperature of char oxidation [26]. For a typical 1-D thermally-thin material (i.e., small Biot number $Bi < 0.1$), if heat transfer inside the fuel is neglected, the ignition time can be approximated as

$$t_{ig} \approx \frac{\rho c_p \delta (T_{sm} - T_0)}{\dot{q}''_c - \dot{q}''_{crt}} \tag{3.2}$$

where ρ, c_p, and δ are the density, specific heat, and thickness of fuel, respectively; T_0 is the initial fuel temperature; and $\dot{q}''_{crt}$ is the critical heat flux for smouldering ignition.

Fig. 3.4 further verifies the relationships between t^{-1} and $\dot{q}''_c$ with different diameters of the concentrated irradiation spots, where the linear correlations of the ignition boundaries (i.e., t_{ig}) were obtained from the logistic regression model [34]. Based on Eq. (3.2), the critical heat flux for smouldering ignition ($\dot{q}''_{crt}$) can be estimated by a linear extrapolation of ignition boundary towards the x-axis (i.e., $t_{ig} \to \infty$), as indicated in Fig. 3.4. Interestingly, as the diameter of concentrated irradiation spot decreases from 20 mm to 1.5 mm, the critical heat flux increases dramatically from 18 kW/m^2 to 205 kW/m^2 (see the summary in Table 3.2).

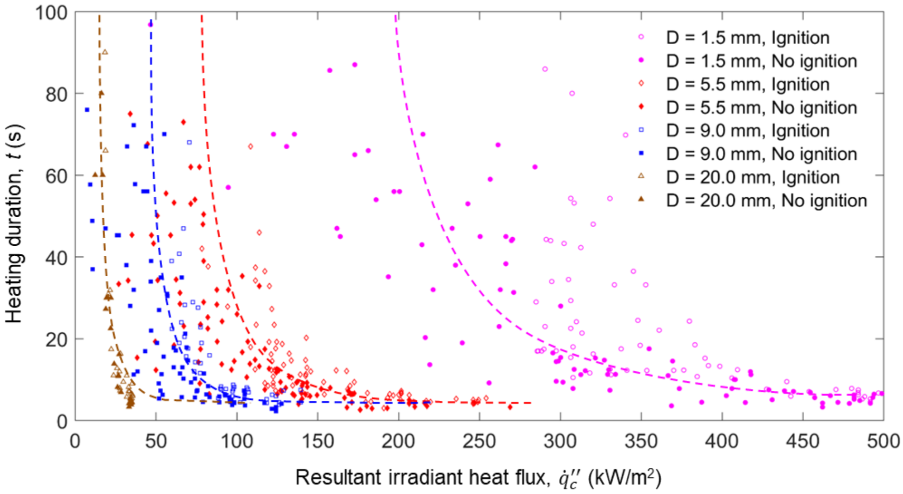

Fig. 3.3. The experimental outcomes under different diameters of irradiation spots (D) and the resultant irradiant heat fluxes ($\dot{q}''_c$), where the solid and hollow markers represent failed and successful ignition, respectively.

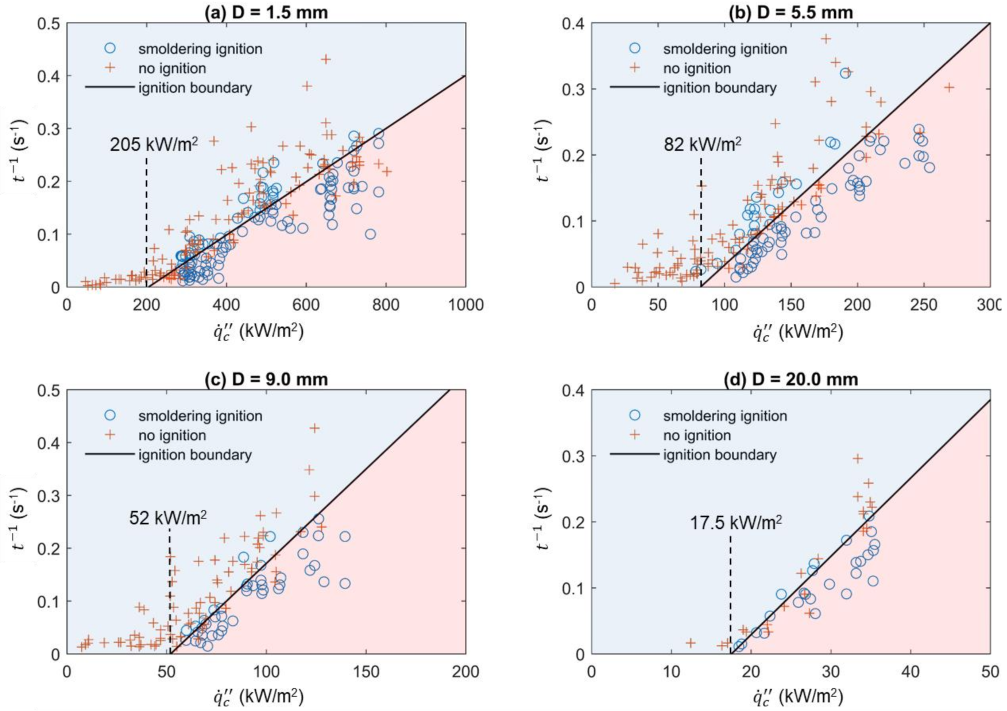

Fig. 3.4. The relationship between t^{-1} and $\dot{q}''_c$ under different spot diameters and the critical irradiation levels, where the fitting curves of ignition boundaries were obtained from the logistic regression model.

Fig. 3.5a further plots the critical irradiation heat fluxes for smouldering ignition vs. the spot diameters. The critical irradiation for the smouldering ignition of a tissue sample under the cone calorimeter is also shown, where the cone calorimeter has a 100-mm heating diameter which would fully cover the whole surface of 60 mm × 60 mm tissue sample (i.e., equivalent $D = 60$ mm). Clearly, as the diameter of the irradiation spot increases, the critical heat flux for smouldering ignition decreases, and eventually, it approaches a near-minimum value obtained from the cone calorimeter (about 11 kW/m^2).

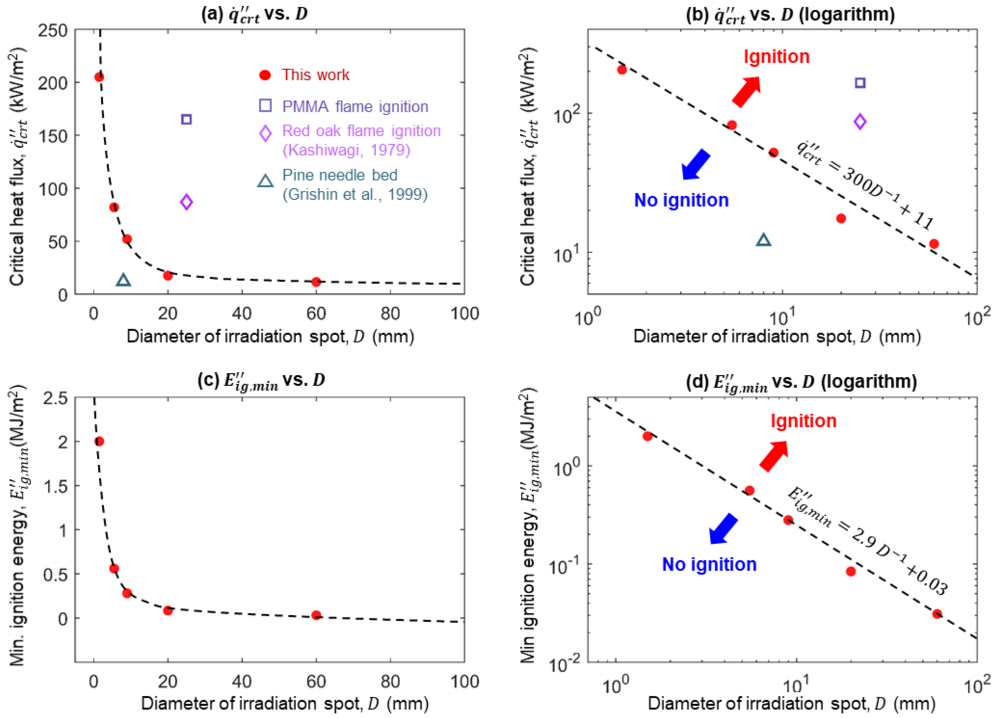

Fig. 3.5. The relationship between diameters of irradiation spots (D) and (a-b) critical ignition heat fluxes ($\dot{q}''_{crt}$); and (c-d) smouldering ignition energy ($E''_{ig,min}$), where the laser ignition data of PMMA and red oak sheet are from Kashiwagi [7], and data of the pine needle bed are from Grishin et al. [10].

As a reference, critical heat fluxes for flaming auto-ignition of the 12-mm thick PMMA sheet and the 17-mm thick red oak wood by a 25-mm laser spot [7] and a loose pine needle bed (~20 kg/m^3) by a light beam [10] are also plotted in Fig. 3.5a. In general, the thickness of the fuel sample should not affect the critical irradiation heat flux when radiant heating and environmental cooling reach a balance. As expected, under the same irradiation-spot size (25 mm), a much large irradiation heat flux is needed to achieve a flame auto-ignition [7]. For very porous pine needles, the smouldering ignition was first achieved and then transitioned to a flame [10]. More importantly, the absorption of irradiation by a porous fuel was a volumetric process, which is more effective than the surface absorption by a more compact tissue in this work, so its critical irradiation heat flux for smouldering ignition was smaller.

For the current experiments, an empirical correlation between the critical heat flux ($\dot{q}''_{crt}$) for smouldering ignition and the diameter of concentrated irradiation spot (D) can be formulated as

$$\dot{q}''_{crt} = 11 + \frac{300}{D} \tag{3.3}$$

where units of [kW/m^2] for $\dot{q}''_{crt}$ and [mm] for D are used. Excellent linearity is found using logarithmic coordinates in Fig. 3.5b, with an R^2 coefficient of 0.97, indicating a strong power-law correlation.

Table 3.2. Summary of critical heat flux ($\dot{q}''_{crt}$) and minimum ignition energy ($E''_{ig,min}$) for smouldering spotting ignition with different light spot diameters.

Irradiation spot diameter, ***D*** (mm)	1.5	5.5	9.0	20	60*
Critical irradiation for ignition, $\dot{q}''_{c,crt}$ (kW/m^2)	205	82	52	17.5	11.5
Minimum ignition energy, $E''_{ig,min}$ (MJ/m^2)	2.0	0.56	0.28	0.084	0.031

*The whole 60 mm × 60 mm sample was tested under the irradiation of the cone calorimeter.

3.3.3 Ignition energy

The smouldering ignition energy per unit area (E''_{ig}) for the thin tissue sample provided by the concentrated irradiation can be approximately calculated as

$$E''_{ig} = \dot{q}''_c t_{ig} \approx \rho c_p \delta (T_{sm} - T_0) \frac{\dot{q}''_c}{\dot{q}''_c - \dot{q}''_{crt}} \tag{3.4}$$

where the minimum heating duration for ignition (t_{ig}) could be obtained from Fig. 3.4. The smouldering ignition energy for different diameters of the irradiation spot is shown in Fig. 3.6. As the irradiation level ($\dot{q}''_c$) increases, the ignition time decreases, and the ignition energy gradually decreases, eventually approaching a minimum value [26], as shown in Fig. 3.6. Then, the minimum ignition energy per unit area of smouldering ($E''_{ig,min}$) can be defined. Eq. (3.4) suggests that $E''_{ig,min}$ should be a material constant of $\rho c_p \delta (T_{sm} - T_0)$ at $\dot{q}''_c \gg \dot{q}''_{crt}$, which disagrees with the different trendlines in Fig. 4.6.

Fig. 3.5c-d further compares the values of $E''_{ig,min}$ for different spot diameters (also see Table 3.2). As the diameter of the irradiation spot increases from 1.5 mm to 20 mm, the $E''_{ig,min}$ decreases from 2.0 MJ/m^2 to 0.084 MJ/m^2. An empirical correlation between minimum ignition energy flux ($E''_{ig,min}$) and spot diameter (D) can be found as

$$E''_{ig,min} = 0.03 + \frac{2.9}{D} \tag{3.5}$$

where units of [MJ/m^2] for $E''_{ig,min}$ and [mm] for D are used. An excellent degree of fit (R^2 coefficient of 0.99) can be seen using logarithmic coordinates in Fig. 3.5d. In other words, both the critical irradiation heat flux and the minimum ignition energy per unit area change with the diameter of irradiation spot, indicating that the conventional 1-D heat transfer analysis becomes invalid for an irradiation spot smaller than 20 mm, even if the fuel is relatively thin.

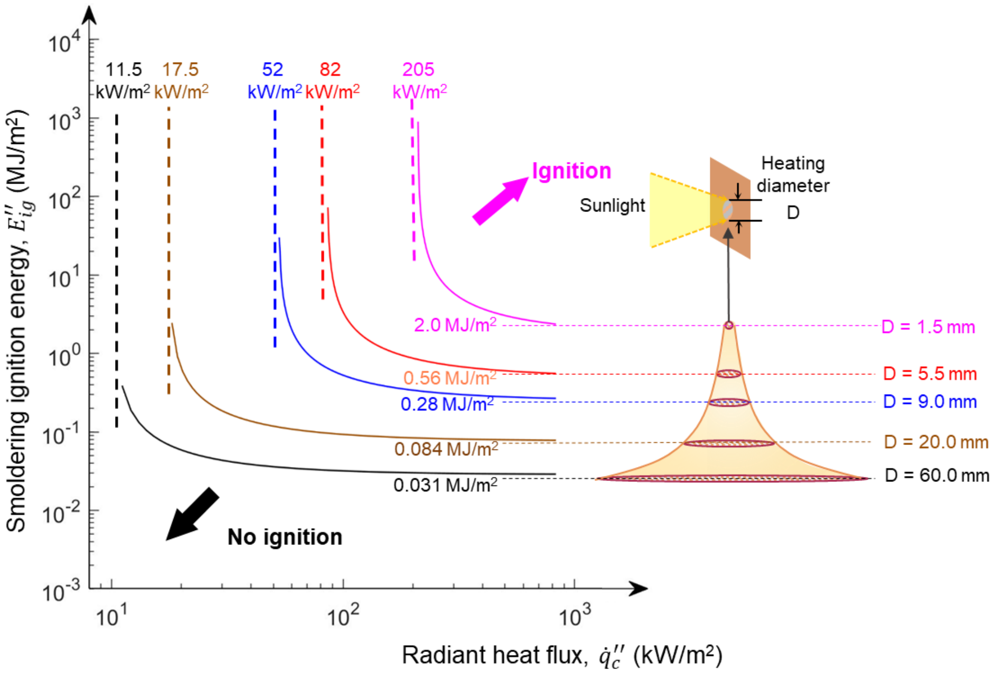

Fig. 3.6. The relationship between ignition energy (E''_{ig}) and the irradiation heat flux ($\dot{q}''_c$) with different spot diameters (D), where the minimum ignition energy ($E''_{ig,min}$) could be represented as the dashed trendline.

3.3.4 Theoretical analysis

To scientifically understand the effect of the small irradiation spot on the critical heat flux of smouldering ignition, a characteristic smouldering ignition temperature (T_{sm}) is needed. Such a temperature should be high enough to initiate a robust char oxidation, which ranges from 230 ℃ to

400 ℃, depending on the type and chemistry of fuel [26,33,35,36]. Then, a simplified 2-D heat transfer analysis based on thermal equilibrium (i.e., the thermally-thin assumption) is proposed for a sample heated by a small irradiation spot, as shown in Fig. 3.7. Because the diameter of the spot is very small, the conductive cooling outwards from the heating spot perimeter has to be considered.

Therefore, the critical irradiation heat flux for smouldering ignition ($\dot{q}''_{crt}$) should be determined via a balance between the incident radiation, environmental heat losses from the top and back sides ($\dot{q}''_{\infty}$) and the radial conductive heat loss to the virgin fuel ($\dot{q}''_{cond}$) [26,37] at the smouldering temperature (T_{sm}) as

$$\dot{q}''_{crt}\left(\frac{\pi D^2}{4}\right) = \dot{q}''_{\infty}\left(\frac{\pi D^2}{4}\right) \times 2 + \dot{q}''_{cond}(\pi D \delta) \tag{3.6}$$

which can be further expressed and simplified as

$$\dot{q}''_{crt} = 2\dot{q}''_{\infty} + \frac{4\delta \dot{q}''_{cond}}{D} \qquad \text{(small spot)} \tag{3.7}$$

where the diameter of the irradiation spot is comparable to the thickness of fuel (δ). Therefore, as the diameter of the irradiation spot increases, the critical heat flux for smouldering ignition decreases, agreeing with the trend in Fig. 3.5a. Based on the fitting correlation of $\dot{q}''_{crt} = 11 + 300/D$ in Eq. (3.3), the average conductive heat flux ($\dot{q}''_{cond}$) is found to be 37.5 kW/m^2 approximately, which is much larger than the environmental heat loss ($\dot{q}''_{\infty}$) of 5.5 kW/m^2. Thus, for a small irradiation spot, the internal conductive heat transfer in the solid phase is the dominant heat loss.

As the diameter of the irradiation spot (D) increases, the effect of conduction in Eq. (3.3) gradually approaches zero. Thus, for a larger irradiation spot, heat transfer can be approximated as a conventional 1-D process. The critical heat flux for smouldering ignition then approaches 11 kW/m^2, which approximately equals the environmental heat losses [26,33] from the top and back surfaces,

$$\dot{q}''_{crt} = 2\dot{q}''_{\infty} = 2[\varepsilon\sigma(T_{sm}^4 - T_{\infty}^4) + 2h(T_{sm} - T_{\infty})] \qquad \text{(large spot)} \tag{3.8}$$

where $\varepsilon = 0.9$ is the emissivity of the tissue paper, $\sigma = 5.67 \times 10^{-8}\ \mathrm{Jm^{-2}s^{-1}K^{-4}}$ is the Stefan-Boltzmann constant, T_{∞} is the ambient temperature, and $h = 1.52(T_{sm} - T_{\infty})^{1/3}$ is the free-convection heat transfer coefficient for a hot horizontal flat plate [38,39]. Therefore, the smouldering ignition temperature can be calculated as $T_{sm} \approx 251$ ℃, agreeing with thermal analysis data in the literature [26,33,36].

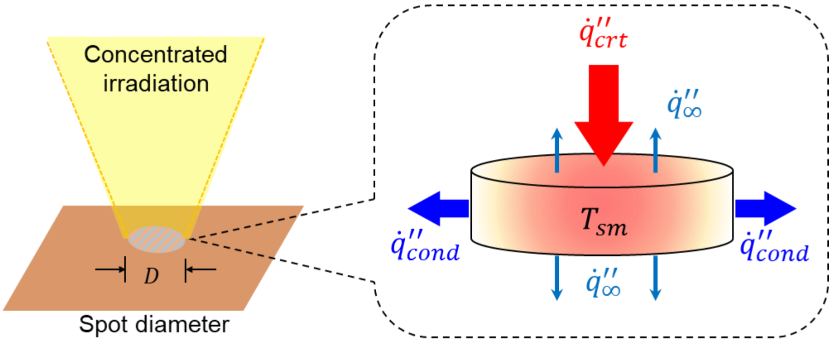

Fig. 3.7. Schematic diagram of smouldering ignition by concentration irradiation spot, where the critical heat flux for ignition should balance environmental heat loss ($\dot{q}''_{\infty}$) and internal conductive heat loss from the perimeter ($\dot{q}''_{cond}$).

As the irradiation level ($\dot{q}''_{c}$) increases above 1,000 kW/m^2, the ignition energy flux for smouldering eventually approaches a minimum value ($E''_{ig,min}$ in Fig. 3.6), which is not a constant but increases as the diameter of irradiation spot decreases (Fig. 3.5c-d). This primarily occurs because, for a small irradiation spot, the minimum ignition energy needs to not only to heat the fuel up to its ignition temperature (T_{sm}), but also to overcome the large radial conductive heat loss to the surrounding fuel. Thus, the energy balance for the minimum ignition energy can be expressed as

$$E_{ig,min} = \rho c_p\, \delta_T (T_{sm} - T_0)\left(\frac{\pi D^2}{4}\right) + \dot{q}''_{cond} t_{min}(\pi D \delta_T) \tag{3.9}$$

where δ_T is the thermal penetrated depth. Then, the required minimum ignition energy per unit area becomes

$$E''_{ig,min} = \rho c_p \delta (T_{sm} - T_0) + \frac{4\delta \dot{q}''_{cond} t_{min}}{D} \tag{3.10}$$

Therefore, as the diameter of the irradiation spot increases, the minimum ignition energy per unit area for smouldering ignition decreases, agreeing with the fitting correlation of $E''_{ig,min} = 0.03 + 2.9/D$ in Eq. (3.5). Based on this experimental fitting correlation and $\dot{q}''_{cond} \approx 37.5$ kW/m^2 estimated from Eq. (3.7), the thermal penetration depth could be estimated as $\delta_T = 0.8$ mm and the minimum heating time for smouldering ignition as $t_{min} = 0.024$ s, which is a theoretical limit.

The thermal penetration time (t_T) may also be estimated by heat conduction or thermal diffusion and the oxygen diffusion time (t_{O_2}), which can be estimated as

$$t_T = \frac{\delta^2}{\alpha_p} \approx \frac{\delta^2}{D_{O_2}} \approx 1 \text{ s} \tag{3.11}$$

where $\alpha_p \approx D_{O_2} \approx 5 \times 10^{-7}$ m^2/s [40] because of the comparable thermal and gas diffusion processes into the paper. The calculated t_T is much larger than the $t_{min} = 0.024$ s estimated from the experimental data. Thus, under an extremely large irradiation heat flux ($\dot{q}_c'' > 1{,}000$ kW/m^2), the limiting time scale may no longer be controlled by the thermal diffusion in the solid fuel, where the diffusion of oxygen is also not fast enough to maintain any smouldering. As observed in the preliminary experiment with a single-layer tissue (0.01 mm), when the irradiation is extremely high, the irradiation spot will break the tissue instantaneously, leaving a hole without any form of ignition. Within such a short period, the super-heated tissue and the formed char are likely to be evaporated within a few milliseconds, so that this process is controlled by gasification chemistry and the thermomechanical resilience of the material, rather than the heat transfer process.

3.4 Numerical modelling

To better explain the experimental results and understanding the role of the diameter of heating spot, a 2-D numerical model is developed using Gpyro [41–43], which is a generalized open-source code for reactive porous media such as peat [26,44–48], wood [49–52] and coal [53,54]. Gpyro is capable of calculating the transient composition of gaseous species (both reactant and products) at different locations [53,55]. By coupling the solver with separate transient conservation equations of gaseous and condensed phase mass, species and energy, the temperature and species distributions inside the reacting porous media can be well simulated [41,42,56].

The computational domain has the same sample length as that in the experiment. To save computational cost and time, the computational domain can be half of the real sample owing to the geometrical symmetry, as illustrated in Fig. 3.8.

3.4.1 2-D governing equations

The model solves the 2-D transient conservation equations for condensed and gaseous phases in the absence of gravity, and thermal equilibrium is assumed between gas and condensed-phase species. The governing conservation equations are provided here, including the conservation of mass (Eq. 3.12), species (Eq. 3.13) and energy (Eq. 3.14) in the condensed phase as well as the mass (Eq. 3.15), species (Eq. 3.16) and momentum (Darcy's law) (Eq. 3.17) in the gas phase. The subscripts i, j and k represent the number of condensed-phase species, gas-phase species, and reaction, d and f refer to the destruction and formation of species, and z and x refer to vertical and horizontal directions, respectively. The details of the mathematical formation of these equations can be found in [42].

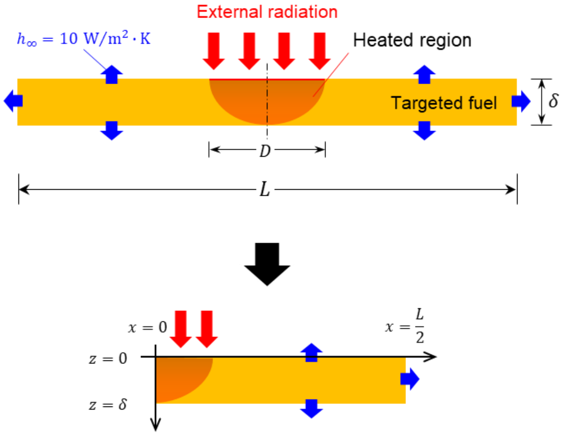

Fig. 3.8. Schematic diagram of the 2-D computational domain.

$$\frac{\partial \bar{\rho}}{\partial t} = -\dot{\omega}'''_{fg} \tag{3.12}$$

$$\frac{\partial (\bar{\rho} Y_i)}{\partial t} = \dot{\omega}'''_{fi} - \dot{\omega}'''_{di} \tag{3.13}$$

$$\frac{\partial (\bar{\rho} \bar{h})}{\partial t} = k \frac{\partial}{\partial x}\left(\frac{\partial T}{\partial x}\right) + k \frac{\partial}{\partial z}\left(\frac{\partial T}{\partial z}\right) + \dot{\omega}'''_{di}(-\Delta H_i) \tag{3.14}$$

$$\frac{\partial}{\partial t}\left(\rho_g \bar{\psi}\right) + \frac{\partial \dot{m}''_x}{\partial x} + \frac{\partial \dot{m}''_z}{\partial z} = \dot{\omega}'''_{fg} \tag{3.15}$$

$$\frac{\partial}{\partial t}\left(\rho_g \bar{\psi} Y_j\right) + \frac{\partial}{\partial x}\left(\dot{m}''_x Y_j\right) + \frac{\partial}{\partial z}\left(\dot{m}''_z Y_j\right)$$
$$= -\frac{\partial}{\partial x}\left(\bar{\psi} \rho_g D_{eff} \frac{\partial Y_j}{\partial x}\right) - \frac{\partial}{\partial z}\left(\bar{\psi} \rho_g D_{eff} \frac{\partial Y_j}{\partial z}\right) + \dot{\omega}'''_{fj} - \dot{\omega}'''_{dj} \tag{3.16}$$

$$\dot{m}''_z = -\frac{\kappa}{\nu}\frac{\partial p}{\partial z} \quad \dot{m}''_x = -\frac{\kappa}{\nu}\frac{\partial p}{\partial x} \quad \left(\rho_g = \frac{P\bar{M}}{RT}\right) \tag{3.17}$$

For the symmetrical plane $(x = 0)$, adiabatic and impermeable boundary conditions are applied, as shown in Eq. (3.18) and Eq. (3.19). At the top free surface $(z = 0)$, initially, irradiation $(\dot{q}''_e)$ with a heating diameter of D is applied for a prescribed duration (t_h) to simulate the concentrated sunlight, and both convective $(h_{c,z=0} = 10\ \mathrm{W/m^2 \cdot K})$ and radiative heat loss are considered (Eq. 3.20). The mass transfer of gas species on the top free surface is calculated through Eq. (3.21). Based on the heat-mass transfer analogy, the mass transfer coefficient can be approximated as $h_{m,z=0} = h_{c,z=0}/C_g = 9.09\ \mathrm{g/m^2 \cdot s}$, where C_g is the specific heat capacity of gas species and is assumed to be constant at $1{,}100\ \mathrm{J/kg \cdot K}$ in the simulation [55]. At the right and bottom boundary $(z = \delta$ and $x = L/2)$, similar to the top free surface, both convective $(h_{c,z=0} = 10\ \mathrm{W/m^2 \cdot K})$ and radiative heat loss are considered, and a same mass transfer of gas species is applied. The ambient pressure and temperature are assumed to be 1 atm and 300 K. The whole computational domain has the same initial gas composition as the ambient air ($Y_{O_2} = 0.232$ and $Y_{N_2} = 0.768$). The solution starts to converge at $\Delta z = \Delta x = 0.1$ mm and $\Delta t = 0.01$ s. Further reducing the cell size and time step by a factor of 2 gives no significantly different results, so the calculations are sufficiently resolved.

$$k\frac{\partial T}{\partial x}\bigg|_{x=0} = 0 \tag{3.18}$$

$$\bar{\psi}\rho_g D_{eff}\frac{\partial Y_j}{\partial x}\bigg|_{x=0} = 0 \tag{3.19}$$

$$-k\frac{\partial T}{\partial x}\bigg|_{z=0} = \dot{q}_e'' - h_{c,z=0}(T|_{z=0} - T_\infty) - \varepsilon\sigma(T^4|_{z=0} - T_\infty^4)\ (0 \le t \le t_h)$$

$$-k\frac{\partial T}{\partial x}\bigg|_{z=0} = -h_{c,z=0}(T|_{z=0} - T_\infty) - \varepsilon\sigma(T^4|_{z=0} - T_\infty^4)\ (t > t_h) \tag{3.20}$$

$$-\bar{\psi}\rho_g D_{eff}\frac{\partial Y_j}{\partial x}\bigg|_{z=0} = -h_{m,z=0}\left(Y_j\big|_{z=0} - Y_j^\infty\right) \tag{3.21}$$

3.4.2 Chemical kinetics

As tissue paper is mainly made of wood fibres, thus, the chemical kinetics of wood is applied here. In general, wood as natural biomass has three major components with different pyrolysis temperature, hemicellulose (~250 °C), cellulose (~300°C), and lignin (~350°C) [57–59], and their pyrolysis processes can be expressed by a 3-step pyrolysis kinetic scheme

$$\text{Hemicellulose} \rightarrow \text{Char} + \text{Pyrolyzates} \tag{3.22}$$

$$\text{Cellulose} \rightarrow \text{Char} + \text{Pyrolyzates} \tag{3.23}$$

$$\text{Lignin} \rightarrow \text{Char} + \text{Pyrolyzates} \tag{3.24}$$

For modelling any smouldering combustion, the char oxidation (Eq. 3.25) has to be included in the model.

$$\text{Char} + O_2 \rightarrow \text{Ash} + \text{gas} \tag{3.25}$$

The non-dimensional (*) reaction rate of reaction (k) and reaction (A) can be expressed by Arrhenius law as

$$\dot{\omega}_k^* = Z_k \exp\left(-\frac{E_k}{RT}\right) f(m_A^*) g(Y_{O_2}) \tag{3.26}$$

where Z_k is the pre-exponential factor, and E_k is the activation energy. The function for mass action of reactant A is

$$f(m_A^*) = (m_A^*)^{n_k} = \left(\frac{m_A}{m_{sA,0}}\right)^{n_k} \tag{3.27}$$

where $m_{sA,0}$ is the original source mass of the species A [58], and n_k is the reaction order. The oxidation model considers the oxidative pyrolysis as

$$g(Y_{O_2}) = \left(1 + Y_{O_2}\right)^{n_{k,O_2}} - 1 \tag{3. 28}$$

where n_{k,O_2} is the order of oxidation. The kinetic parameters for the smouldering of tissue paper are obtained by optimizing the TG data in both inert and oxidative atmospheres using the Kissinger-Genetic Algorithm (K-GA) method (see detailed description in [60,61]) and are listed in Table 3.3. The averaged properties in each cell are calculated using the appropriate mass fraction or volume fraction. The detailed species thermophysical properties and kinetic parameters can be found in [62] and Table 3.4.

Table 3.3. Chemical kinetic parameters and yields of 4-step reaction for tissue paper; reaction expression is $A_k + \nu_{O_2,k}O_2 \rightarrow \nu_{B,k}B_k + \nu_{g,k}\text{gas}$, and $\Delta H > 0$ is endothermic and $\Delta H < 0$ is exothermic.

Parameter	*Hemicellulose pyrolysis*	*Cellulose pyrolysis*	*Lignin pyrolysis*	*Char oxidation*
lgA_k (lg (s^{-1}))	8.2	11.4	21.4	12.9
E_k (kJ/mol)	106	154	229	184
n_k (-)	1.49	0.95	8.7	1.27
n_{k,O_2} (-)	0.18	7.5	8.2	1
$\nu_{B,k}$ (kg/kg)	0.24	0.27	0.40	0.06
ΔH_k (MJ/kg)	0.2	0.2	0.2	-20
$\nu_{O_2,k}$ (kg/kg)	0.5	0.5	0.5	1.5

Table 3.4. Physical parameters of condensed-phase species [62,63].

Species	Y_0 (-)	ρ (kg/m^3)	k (W/m-K)	c (J/kg-K)
Hemicellulose	0.209	150	0.05	1500
Cellulose	0.529	150	0.05	1500
Lignin	0.262	150	0.05	1500

Char	0	100	0.03	3000
Ash	0	15	0.01	3000

3.4.3 Numerical results

In the present study, two base cases are first presented to demonstrate the successful and failed ignition of smouldering combustion. To better display the transient characteristics, the 2-D profiles of temperature and heat release rate (HRR) are shown simultaneously here (Fig. 3.9), where the left and right sides of the symmetric plane represent the profiles of temperature and HRR, respectively. With a heating diameter of 20 mm, right after the heating for 50 s, a hot region with intense heat emitted emerges at the heated region. Afterwards, it gradually spread outwards without clear temperature decrease or deceleration of propagation rate. At $t = 500$ s, the smouldering propagates to the end of the sample and eventually burns out the sample. For comparison, a failed ignition case, where the heating diameter is decreased to 5 mm, is shown in Fig. 3.9b. it could be seen in this case, right after the heating for 200 s, the sample temperature also reaches about 300 ºC. However, after that, the temperature starts to decrease with no heat emitted. Eventually, the temperature decreases to ambient temperature at about 300 s. All these phenomena are consistent with our experimental observations.

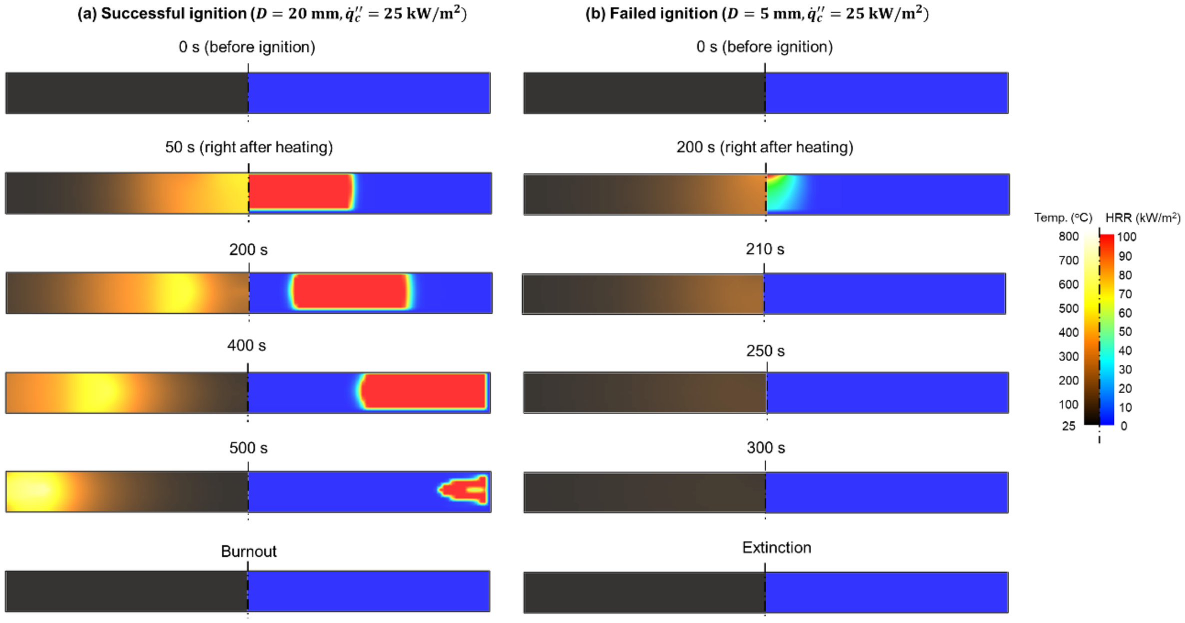
(a) Successful ignition ($D = 20$ mm, $\dot{q}_c'' = 25$ kW/m^2)

(b) Failed ignition ($D = 5$ mm, $\dot{q}_c'' = 25$ kW/m^2)

Fig. 3.9. Transient profiles of temperature and heat release rate of (a) successful ignition case with a heating diameter of 20 mm and (b) failed ignition case with a heating diameter of 5 mm under the irradiation of 25 kW/m^2.

Following the two base cases above, we further simulate the critical heat flux for successful ignition with different diameters of irradiation spots. Fig. 3.10 summarizes the predicted results (dashed line) and compares with the experimental measurements (markers). In general, simulations show a satisfactory agreement with experimental data, and our model is therefore further validated. The effect of the diameter of irradiation spot is also well predicted by the model; that is, the critical heat flux for ignition decreases with the diameter of irradiation spot increases. For example, as the diameter of irradiation spot increases from 1 mm to 20 mm, the critical heat flux for ignition decreases dramatically from 290 kW/m^2 to 13 kW/m^2. All these predictions agree with our experimental measurement.

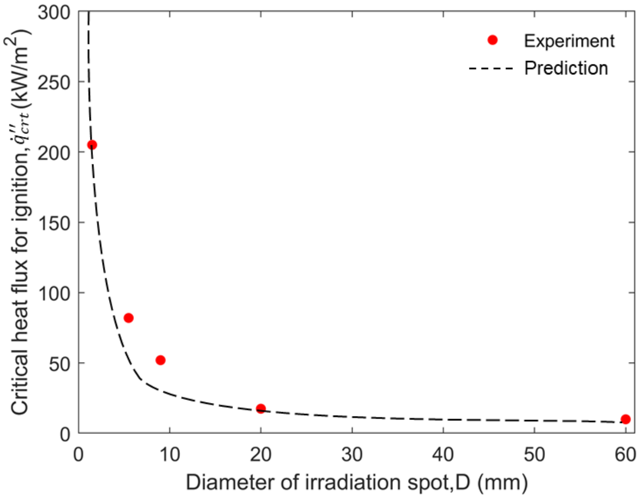

Fig. 3.10. Predicted critical heat flux for ignition with different diameters of irradiation spots, where the experimental results are plotted for comparison.

3.5 Conclusions

In this work, we investigated the smouldering ignition of multi-layered thin tissue paper by small irradiation spots. Irradiant spots were experimentally generated via concentrating sunlight by a transparent glass sphere with a diameter of 150 mm and a focal length of 108 mm. To quantify the concentrated radiant heat flux, optical simulations using *TracePro* were conducted to model the diameter of the irradiation spot and the resulting radiation distribution.

We found that as the solar irradiation increases or the diameter of the irradiation spot decreases, the resultant irradiance increases. Given a fixed-size irradiation spot, the smouldering ignition time decreases as the concentrated irradiation increases, following the classical piloted ignition theory.

However, the measured minimum spot irradiation for smouldering ignition is not constant but remains much higher than the 11 kW/m^2 measured from cone-calorimeter tests. As the diameter of irradiation spots decreases from 20.0 mm to 1.5 mm, the minimum irradiation necessary for smouldering ignition increases from 17.5 kW/m^2 to 205 kW/m^2, and the ignition energy increases from 0.084 MJ/m^2 to 2.0 MJ/m^2.

A simplified heat transfer analysis was proposed, which explains the critical smouldering ignition heat flux and the minimum ignition energy for tiny irradiation spots by including two-dimensional cooling effects. A 2-D model using open-source code Gpyro was established to reproduce the experimental phenomena and verify the results. Future numerical simulations are needed to further reveal the underlying physical and chemical process of smouldering spot ignition for other fuels.

Acknowledgements

This research is funded by the National Natural Science Foundation of China (NSFC) No. 51876183 and the Society of Fire Protection Engineers (SFPE) Educational & Scientific Foundation. S. Lin would like to thank S. Wang for helping conduct experiments and data analysis, Y. Liu and P. Sun for helping conduct experiments, and Dr H. Yuan for computational simulation.

References

[1] Caton SE, Hakes RSP, Gorham DJ, Zhou A, Gollner MJ. Review of Pathways for Building Fire Spread in the Wildland Urban Interface Part I: Exposure Conditions. Fire Technol 2017;53:429–73.

[2] Fernandez-Pello AC. Wildland fire spot ignition by sparks and firebrands. Fire Saf J 2017;91:2–10.

[3] Manzello SL, Suzuki S, Gollner MJ, Fernandez-Pello AC. Role of firebrand combustion in large outdoor fire spread. Prog Energy Combust Sci 2020;76:100801.

[4] Wang S, Huang X, Chen H, Liu N. Interaction between flaming and smouldering in hot-particle ignition of forest fuels and effects of moisture and wind. Int J Wildl Fire 2017;26:71–81.

[5] Urban JL, Zak CD, Fernandez-Pello C. Cellulose spot fire ignition by hot metal particles. Proc Combust Inst 2015;35:2707–14.

[6] Sun P, Lin S, Huang X. Ignition of thin fuel by thermoplastic drips: An experimental study for the dripping ignition theory. Fire Saf J 2020;115:103006.

[7] Kashiwagi T. Experimental observation of radiative ignition mechanisms. Combust Flame 1979;34:231–44.

[8] Kashiwagi T. Effects of sample orientation on radiative ignition. Combust Flame 1982.

[9] Zhang H, Qiao Y, Chen H, Liu N, Zhang L, Xie X. Experimental study on flaming ignition of pine needles by simulated lightning discharge. Fire Saf J 2020:103029.

[10] Grishin AM, Golovanov AN, Medvedev V V. On the ignition of a layer of combustible forest materials by light radiation. Combust Explos Shock Waves 1999;35:618–21.

[11] Warren DW. Optical Modeling of Fire Hazards Arising from Sunlight Focused by Water. Fire Technol 2014;50:1327–34.

[12] Engerer JD, Brown AL, Christian JM. Ignition and damage thresholds of materials at extreme incident radiative heat flux. 2018 Jt Thermophys Heat Transf Conf 2018:1–27.

[13] Brown AL, Engerer JD, Ricks AJ, Christian J, Yellowhair J. Datasets for material ignition from high radiant flux. Fire Saf J 2020:103131.

[14] Goldstone BM. Hazards from the concentration of solar radiation by textured window glass. London: HMSO; 1982.

[15] Dyke KS Van. THE FISH BOWL AS A FIRE HAZARD. Science (80-) 1937;86:122–3.

[16] Wildfire in Guilin caused by a plastic bottle. Guilinlife 2019.

[17] Brigade step up sunlight warning after another refraction blaze. London Fire Brig 2015.

[18] Lizhong Y, Yupeng Z, Yafei W, Jiakun D, Zhihua D, Xiaodong Z. Autoignition of solid combustibles subjected to a uniform incident heat flux: The effect of distance from the radiation source. Combust Flame 2011;158:1015–7.

[19] Nakamura Y, Kashiwagi T. Effects of sample orientation on nonpiloted ignition of thin poly(methyl methacrylate) sheet by a laser: 1. Theoretical prediction. Combust Flame 2005;141:149–69.

[20] Gotoda H, Manzello SL, Saso Y, Kashiwagi T. Effects of sample orientation on nonpiloted ignition of thin poly(methyl methacrylate) sheets by a laser. 2. Experimental results. Combust Flame 2006;145:820–35.

[21] Drysdale D. An Introduction to Fire Dynamics. 3rd ed. Chichester, UK: John Wiley & Sons, Ltd; 2011.

[22] Rein G. Smouldering Combustion. SFPE Handb Fire Prot Eng 2014;2014:581–603.

[23] Quintiere J. Principles of Fire Behaviour. New York: Alar Elken; 1997.

[24] Lin S, Huang X. Quenching of smouldering: Effect of wall cooling on extinction. Proc Combust Inst 2021;38:5015–22.

[25] Urban JL, Song J, Santamaria S, Fernandez-pello C. Ignition of a spot smoulder in a moist fuel bed by a fi rebrand. Fire Saf J 2019;108:102833.

[26] Lin S, Sun P, Huang X. Can peat soil support a flaming wildfire? Int J Wildl Fire 2019;28:601–13.

[27] Santoso MA, Christensen EG, Yang J, Rein G. Review of the Transition From Smouldering to Flaming Combustion in Wildfires. Front Mech Eng 2019;5.

[28] Springer Handbook of Lasers and Optics. 2007.

[29] TracePro. Software for design and analysis of illumination and optical systems. n.d.

[30] Kopp G, Lean JL. A new, lower value of total solar irradiance: Evidence and climate significance. Geophys Res Lett 2011.

[31] Avendaño-Alejo M, Castañeda L, Moreno I. Properties of caustics produced by a positive lens: meridional rays. J Opt Soc Am A 2010.

[32] Wang S, Ding P, Lin S, Huang X, Usmani A. Deformation of wood slice in fire: Interactions between heterogeneous chemistry and thermomechanical stress. Proc Combust Inst 2021;38:5081–90.

[33] Lin S, Huang X, Urban J, McAllister S, Fernandez-Pello C. Piloted ignition of cylindrical wildland fuels under irradiation. Front Mech Eng 2019;5:54.

[34] Hosmer DW, Lemeshow S, Sturdivant RX. Applied Logistic Regression: Third Edition. 2013.

[35] Lin S, Cheung YK, Xiao Y, Huang X. Can rain suppress smouldering peat fire ? Sci Total Environ 2020;727:138468.

[36] Boonmee N, Quintiere JG. Glowing ignition of wood: The onset of surface combustion. Proc Combust Inst 2005;30 II:2303–10.

[37] Quintiere JG. Fundamentals of Fire Phenomena. New York: John Wiley; 2006.

[38] Incropera FP. Principles of heat and mass transfer. John Wiley; 2007.

[39] Holman JP. Heat Transfer. 10th ed. New York: McGraw-Hill; 2008.

[40] Thomas James. Thermal Properties of Paper. SCIENCING 2017.

[41] Lautenberger C. Gpyro-A Generalized Pyrolysis Model for Combustible Solids: Users'Guide. Berkeley: 2016.

[42] Lautenberger C. Gpyro-A Generalized Pyrolysis Model for Combustible Solids:Technical Reference. Berkeley: 2014.

[43] Yuan H, Huang X, Zhao G, Rein G. Gpyro Workbook on Pyrolysis & Smouldering Problems. London: 2019.

[44] Huang X, Rein G, Chen H. Computational smouldering combustion: Predicting the roles of moisture and inert contents in peat wildfires. Proc Combust Inst 2015;35:2673–81.

[45] Huang X, Rein G. Computational study of critical moisture and depth of burn in peat fires. Int J Wildl Fire 2015;24:798–808.

[46] Huang X, Rein G. Upward-and-downward spread of smouldering peat fire. Proc Combust Inst 2019;37:4025–33.

[47] Huang X, Rein G. Interactions of Earth's atmospheric oxygen and fuel moisture in smouldering wildfires. Sci Total Environ 2016;572:1440–6.

[48] Huang X, Rein G. Downward Spread of Smouldering Peat Fire: the Role of Moisture, Density and Oxygen Supply. Int J Wildl Fire 2017;26:907–18.

[49] Richter F, Rein G. Heterogeneous kinetics of timber charring at the microscale. J Anal Appl Pyrolysis 2019;138:1–9.

[50] Richter F, Jervis FX, Huang X, Rein G. Burning rate of wood pyrolysis, smouldering, and flaming: Effect of oxygen. Combust Flame 2021.

[51] Richter F, Atreya A, Kotsovinos P, Rein G. The effect of chemical composition on the charring of wood across scales. Proc Combust Inst 2019;37:4053–61.

[52] Richter F, Rein G. A multiscale model of wood pyrolysis in fire to study the roles of chemistry and heat transfer at the mesoscale. Combust Flame 2020;216:316–25.

[53] Yuan H, Restuccia F, Richter F, Rein G. A computational model to simulate self-heating ignition across scales, configurations, and coal origins. Fuel 2019;236:1100–9.

[54] Yuan H, Restuccia F, Rein G. Computational study on self-heating ignition and smouldering spread of coal layers in flat and wedge hot plate configurations. Combust Flame 2020;214:346–57.

[55] Lautenberger C, Fernandez-Pello C. Generalized pyrolysis model for combustible solids. Fire Saf J 2009;44:819–39.

[56] Yuan H, Restuccia F, Rein G. Spontaneous ignition of soils : a multi-step reaction scheme to simulate self-heating ignition of smouldering peat fires. Int J Wildl Fire 2021.

[57] Di Blasi C. Modeling chemical and physical processes of wood and biomass pyrolysis. Prog Energy Combust Sci 2008;34:47–90.

[58] Huang X, Rein G. Thermochemical conversion of biomass in smouldering combustion across

scales: The roles of heterogeneous kinetics, oxygen and transport phenomena. Bioresour Technol 2016;207:409–21.

[59] Niu H, Liu N. Thermal decomposition of pine branch: Unified kinetic model on pyrolytic reactions in pyrolysis and combustion. Fuel 2015;160:339–45.

[60] Li K, Huang X, Fleischmann C, Rein G, Ji J. Pyrolysis of Medium-Density Fiberboard : Optimized Search for Kinetics Scheme and Parameters via a Genetic Algorithm Driven by Kissinger’s Method. Energy & Fuels 2014;28:6130−6139.

[61] Huang X, Rein G. Smouldering combustion of peat in wildfires: Inverse modelling of the drying and the thermal and oxidative decomposition kinetics. Combust Flame 2014;161:1633–44.

[62] Huang X, Li K, Zhang H. Modelling bench-scale fire on engineered wood : Effects of transient flame and physicochemical properties. Proc Combust Inst 2017;36:3167–75.

[63] Lautenberger C, Fernandez-Pello C. A model for the oxidative pyrolysis of wood. Combust Flame 2009;156:1503–13.

CHAPTER 4: Transition from Flaming to Smouldering and Limiting Conditions

Summary

Timber is one of the most cost-effective and environmentally friendly materials that has the potential to offer great benefits to a sustainable future, but its fire safety is still a significant concern. In this work, we investigate the burning behaviours of different types of woods and their self-extinction mechanism under external radiation. A unique near-limit flame is observed when the irradiation is above a critical value of about 40 kW/m^2. Such a near-limit flame is weak, blue, and discrete that tends to attach to the wood residue surface, different from the normal buoyancy-controlled sooty yellow flame. If the irradiation is low (<40 kW/m^2), the yellow flame extinguishes and transits directly to smouldering at the mass flux of about 4 g/m^2·s. However, above the critical irradiation level, the yellow flame transits to the blue flame that does not extinguish until the mass flux of around 1 g/m^2·s, extending the flame extinction limit of timber materials. The near-limit blue flame may appear only if the char surface temperature exceeds 700 °C. Two critical conditions are hypothesized for this unique blue flame, (I) in-depth pyrolysis (mainly lignin) sustained by the internal smouldering combustion, and (II) the hot surface maintained by large external radiation to extend the flammability limit. This unique blue flame may play an essential role in the transition between flaming and smouldering and help evaluate the fire risk of timber materials under real fire scenarios.

This chapter is based on "S. Lin, X. Huang, J. Gao and J. Ji (2021) *Extinction of Wood Fire: A Near-Limit Blue Flame above Hot Smouldering Surface.* **Fire Technology**. doi: 10.1007/s10694-021-01146-6.

4.1 Introduction

Timber is natural, renewable and sustainable, and has been reconsidered as a preferred construction material for high-rise buildings owing to its abundance in nature, high stiffness, and the high strength-to-weight ratio [1–3]. In recent years, many environmental-friendly high-rise timber buildings have sprung up rapidly all around the world, e.g., the 18-story timber building (85 m) in Brumunddal, Norway (Fig. 4.1a). Attributed to innovative timber materials like the cross-laminated timber (CLT) [4,5], Sumitomo made a plan to build a 70-story (350 m) timber skyscraper in Tokyo by 2041 [6]. However, the fire risk of timber is still the primary concern, and the application of high-rise timber building is highly controversial [1,3], because of its flammable nature and large fuel load in structures [7]. For example, a recent fire in Notre Dame Cathedral (Fig. 4.1b) burnt out its wooden frame that was made of oak about 800 years ago [8]. Thus, it is urgent to fully understand the fire dynamics and combustion limits of timber materials owing to the fast growing market of timber buildings [2,9].

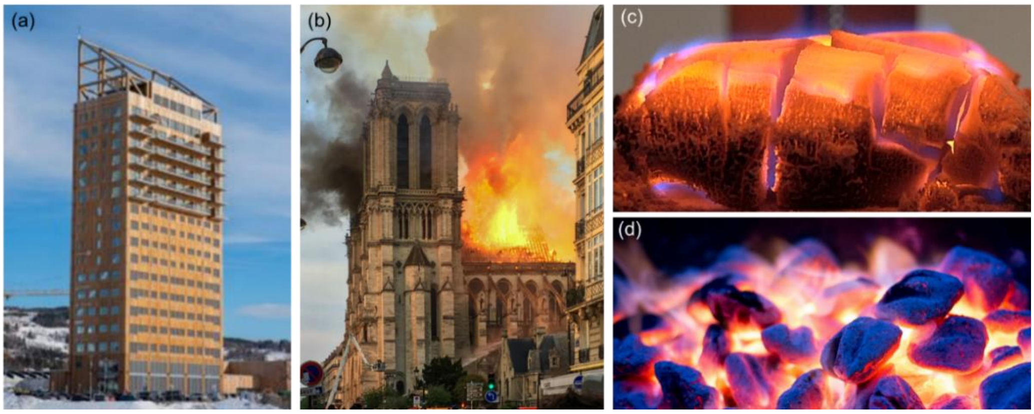

Fig. 4.1. (a) The 18-story apartment building Mjøstårnet in Norway (Photo courtesy the Council on Tall Buildings and Urban Habitat), (b) the Notre-Dame de Paris fire on 15 April 2019 (Photo courtesy Wiki Commons), and the blue flame above the (c) timber (cc by S. Lin), and (d) charcoal (cc by M. Simon).

In the literature, the ignition of various timbers or wooden materials has been studied extensively to understand the initiation and growth of timber fires [10–16]. Like most flammable materials, the combustion limits and fire behaviours of timber materials can be influenced by both environmental (*e.g.,* heating source, oxygen concentration, and wind velocity) and material (*e.g.,* density, composition, moisture, and age) factors [17–21]. Moreover, timber, as a typical charring material, can sustain both flaming and smouldering combustion [13]. Flaming is a homogeneous combustion process, while smouldering is the slow, low-temperature, and flameless burning of porous fuels and is the most persistent type of combustion phenomenon [22]. For high-density wood fuels, the difficulty of ignition in terms of the ignition delay time under the external irradiation is found to increase from the piloted flaming ignition to flaming autoignition, and to smouldering (or glowing/surface) ignition [23–25]. This is different from low-density and high-porosity materials (e.g., PU foam and peat soil), for which smouldering ignition is the easiest [22,25].

On the other hand, a flame is sometimes found not to be able to sustain above the timber material after ignition, i.e., the self-extinction may occur [10,26,27]. The self-extinction of timber flame is a crucial concept that supports the fire safety of high-rise timber building and its fast-growing market [9,26,28,29]. However, very few studies have investigated the extinction mechanisms of timber and quantified its combustion limits. Previously, Babrauskas [30] used a flame to ignite a timber material for several minutes and found the self-extinction occurred once the igniting flame was removed. Emberley *et al.* [9,15] further studied the self-extinction of flaming timber and CLT under external radiation and found the critical heat flux of 43.6 ± 4.7 kW/m^2 and the minimum mass flux of 3.93 ± 0.45 $g/m^2{\cdot}s$ were required to sustain the flame. Vermesi *et al.* [17] found that for engineered wood, the critical mass flux for flameout varied in a wide range (1.4-17 $g/m^2{\cdot}s$). Nevertheless, extinction of the flame is not the end of a fire, as it may be followed by the smouldering [31]. Moreover, under specific conditions, smouldering may also transition back to the flaming, i.e., the smouldering-to-flaming (StF) transition [22,32]. Therefore, in a real timber fire, the ignition (and re-ignition) and extinction of the flame, as well as smouldering combustion, could repeatedly occur several times until the eventual burnout, during which the timber material loses its stability or even collapses [15].

In our recent wood fire tests, a thin layer of weak blue flame (Fig. 4.1c) was observed floating above the wood surface near the flaming extinction limit. A similar blue flame is also widely observed in the burning charcoal (Fig. 4.1d). Such a near-limit blue flame may play an important role in defining the true extinction limit of timber flame and the transition between flaming and smouldering, while to the best of authors' knowledge, the combustion mechanism dominating this unique phenomenon has not been systematically studied yet, posing a knowledge gap. In this work, we will quantify the extinction limits of timber flame and its near extinction fire behaviours using both laboratory experiments and phenomenological analysis.

4.2 Experimental methods

Six different types (species) of natural woods, which have the same dimension of 10 cm × 10 cm × 3 cm and different densities, were tested (Fig. 4.2a). Before the experiments, all wood samples were first oven-dried at 70 °C for 48 h, and then, placed into an electronic dry cabinet to avoid the re-absorption of moisture from the air. Their dry bulk densities from low to high are listed in Table 4.1.

All experiments were conducted under the cone calorimeter (FTT iCone Plus), which mainly includes a conical heater, spark igniter, sample holder, and precision scale, as illustrated in Fig. 4.2(b). The conical heater could provide relatively constant and uniform irradiation ($\dot{q}_e''$) to the sample area of 10 cm ×10 cm, so that the whole top surface of the wood sample would have uniform irradiation [33]. Before the test, the temperature of the conical heater was calibrated with the irradiation level, which was measured by a radiometer. The test section, including the wood sample, sample holder, and cone heater, was partially open to ensure a sufficient air supply and smoke ventilation.

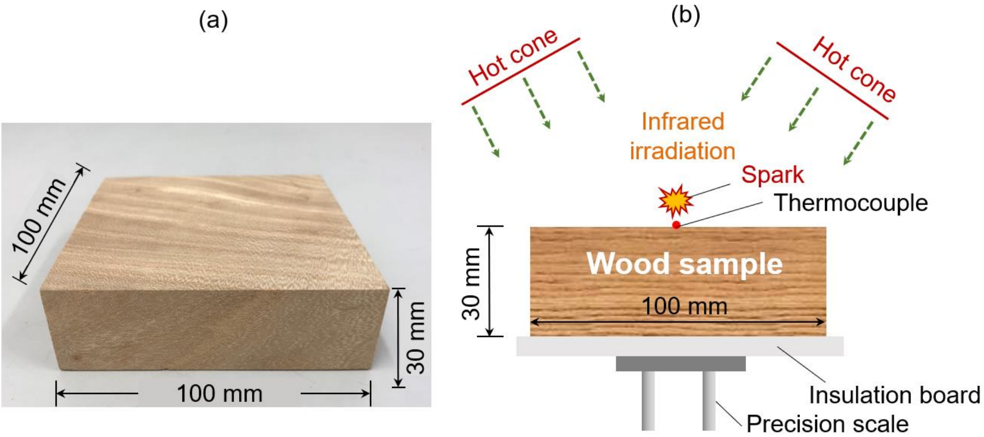

Fig. 4.2. (a) A photo of the wood sample, and (b) a schematic diagram of the experimental apparatus.

The piloting spark was placed at 5 mm above the top surface of the wood sample. Once the flame was piloted, the spark was removed, while heating was continued until the sample mass no longer changed or the wood sample completely turned into white ashes (i.e., burnout). The test process was recorded by a side-view camera, and the sample mass was monitored by the precision scale (± 0.1 mg). The surface temperature of wood was carefully monitored using a K-type thermocouple (0.5 mm junction bead diameter) that was contacted with the wood top surface. During the test, the ambient temperature was 22 ± 2 °C, the relative humidity was 50 ± 10%, and the ambient pressure was 1 atm.

For each test, at least two repeating experiments were conducted to ensure the experimental repeatability and quantify the experimental random uncertainty.

Table 4.1. The dry bulk density (ρ), ignition mass flux at 50 kW/m^2 ($\dot{m}''_{ig}$), critical heat flux ($\dot{q}''_{B,crt}$) for near-limit blue flame, and extinction mass flux for yellow flame ($\dot{m}''_{ex,Y}$) and blue flame ($\dot{m}''_{ex,B}$) for different wood types, where the standard error of repeating tests is within 5%.

Wood sample	ρ (kg/m^3)	$\dot{m}''_{ig}$ (g/m^2·s)	$\dot{q}''_{B,crt}$ (kW/m^2)	$\dot{m}''_{ex,Y}$ (g/m^2·s)	$\dot{m}''_{ex,B}$ (g/m^2·s)
A	406	7.4	52	3.9	0.91
B	560	8.4	37	4.0	1.08
C	570	9.6	37	3.9	0.89
D	588	10.5	37	4.2	0.93
E	781	12.5	32	4.0	0.96
F	816	12.8	32	3.9	0.92

4.3 Experimental results

4.3.1 Fire phenomena and critical heat flux

Figure 4.3 shows the examples of fire phenomena of Wood C under different external radiation ($\dot{q}''_e$) of 30 kW/m^2 and 60 kW/m^2, respectively. The critical mass fluxes and time moments of transitioning to different stages are also indicated in Fig. 4.3. Before the piloted flaming ignition, smoke was always observed, likely the pyrolysis gases [25,34]. Continuing the heating, a strong buoyancy-controlled yellow flame was piloted by the spark and maintained.

Under the lower irradiation of 30 kW/m^2, a two-stage burning process was observed (Fig. 4.3a). After the extinction of the initial strong yellow flame, a stable smouldering fire in the solid phase occurred and sustained until burnout. On the other hand, under the higher irradiation of 60 kW/m^2, a three-stage burning process was observed (Fig. 4.3b). Specifically, after the extensive burning of yellow flame, a near-limit blue flame appeared and lasted for more than 20 min before transitioning to smouldering. This flame is weak, blue, flat, discrete above parts of the wood residue surface, and only slightly affected by buoyancy effect, all of which are quite different from the regular yellow flame, as compared and summarized in Table 4.2. Fig. 4.4(a) compares the durations of strong yellow flame and near-limit blue flame of wood C as a function of external radiation, where the blue flame can last around 10 min longer than the yellow flame. The durations for both flame types decrease as the external irradiation increases, because the external irradiation accelerates the burning processes.

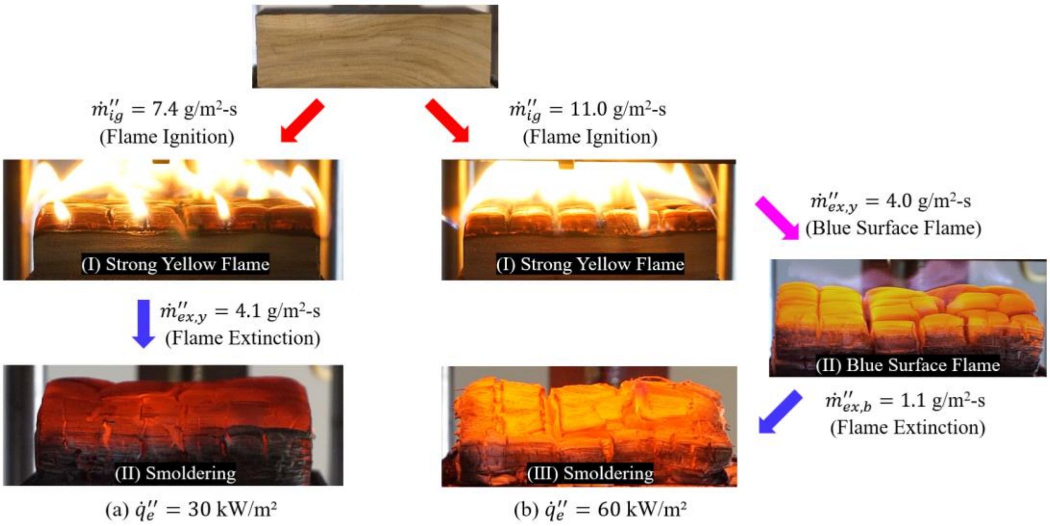

Fig. 4.3. Different burning phenomena of Wood C under the external radiation ($\dot{q}''_e$) of (a) 30 kW/m^2, and (b) 60 kW/m^2.

Moreover, the experiments have quantified the critical (minimum) irradiation level for the appearance of this near-limit blue flame ($\dot{q}''_b$) and the three-stage combustion processes. As showed in Table 4.1 and Fig. 4.4(b), the required critical heat flux is found to increase as wood density decreases, where the average value is about 40 ± 10 kW/m^2. Specifically, Wood F with the highest bulk density of 816 kg/m^3 can maintain the blue flame at the lowest critical irradiation of 32 kW/m^2, while the Wood A with the lowest density of 406 kg/m^3 requires the highest critical irradiation of 52 kW/m^2.

In the real fire scenarios, wood materials may receive high irradiation from nearby hot smokes or flames (e.g., > 80 kW/m^2 in post-flashover compartment fires and wildland fires) [9]. Therefore, one can expect that after the disappearance of intense yellow flame, this kind of blue flame can still be sustained on timber for an extended period, although it may be too weak to be clearly visible. Also, as the blue flame does not entirely cover the wood surface, oxygen molecules may diffuse into the charred wood, so that smouldering may co-exist with the flame. Thus, this unique blue flame may not only help evaluate the fire risk of timber materials under real fire scenarios, but also play an essential role in the transition between flaming and smouldering.

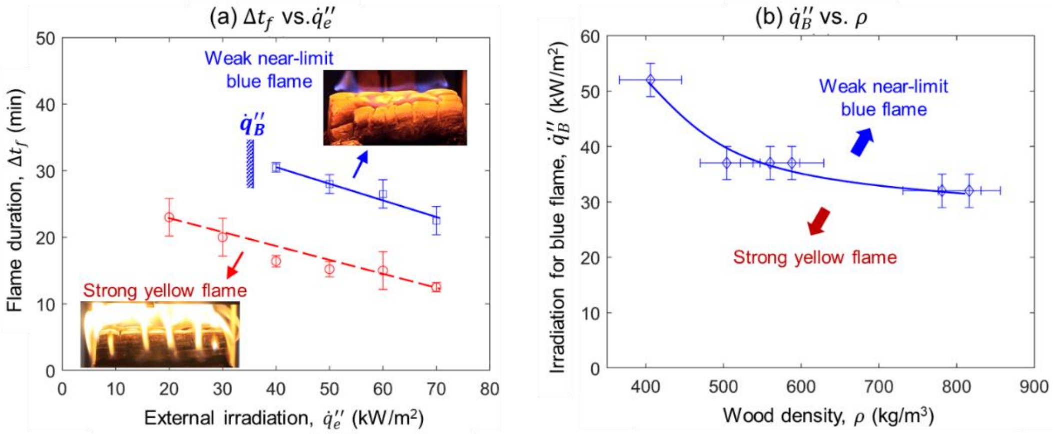

Fig. 4.4. (a) Durations of strong yellow flame and near-limit blue flame of wood C as a function of external irradiation, and (b) critical irradiation for blue flame vs. wood density.

Table 4.2. Phenomenological comparison between the near-limit blue flame and normal yellow flame.

Flame	**Colour**	**Intensity**	**Smoke**	**Continuity**	**Shape**	**Height**	**Buoyancy effect**	**Cover sample**
Near-limit flame	blue	weak	invisible	discrete	flat	< 5 cm	slight	partial
Normal flame	yellow	strong	visible	continuous	conic	> 5 cm	strong	complete

4.3.2 Critical mass flux

The mass flux ($\dot{m}''$) is the mass-loss rate (or burning rate) per unit area, which is considered as one of the most important parameters to quantify different forms of combustion [35]. During the flaming combustion, the increasing thickness of the char layer can reduce the amount of the heat the pyrolysis front receives like a thermal insulator, and extinction occurs when heating is too small to maintain the minimum mass flux ($\dot{m}''_{ex}$) [15,16]. Fig. 4.5 illustrates the evolution of mass flux of Wood C (570 kg/m^3) under external radiations of (a) 30 and (b) 60 kW/m^2, where CO/CO$_2$ ratio is also plotted for further comparison.

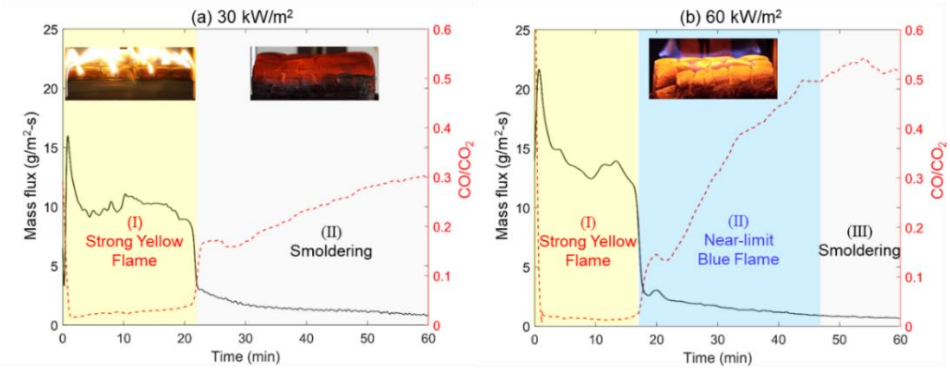

(c) Evolution of blue flame

Fig. 4.5. Evolution of mass flux and CO/CO$_2$ ratio of Wood C under the external radiation ($\dot{q}_e''$) of (a) 30 kW/m^2, and (b) 60 kW/m^2; (c) evolution of blue flame above the wood surface.

At the lower irradiation of 30 kW/m^2 (Fig. 4.5a), the mass flux curve is similar to the typical evolution in [12]. Once exposed to the irradiation, the mass flux increases dramatically to a peak value, and then, it decreases gradually due to the build-up of the char layer on the top surface. Continuing the heating, the pyrolysis front gradually reaches the bottom of the wood sample and approaches to the top of the insulation board, so that the in-depth heat conduction into the wood is reduced. As a result, the pyrolysis is accelerated and results in the second peak of the mass loss curve. Afterward, the whole sample surface is mostly charred, and the mass flux goes through a sharp drop. Eventually, the self-extinction of the yellow flame occurs when the mass flux decreases to about 4 g/m^2·s. This value is consistent with previous studies on the critical mass flux for flaming extinction [9,15,36,37].

On the other hand, under the higher irradiation of 60 kW/m^2, as shown in Fig. 4.5(b), extinction of the yellow flame also occurs when the mass flux decreases to about 4 g/m^2·s. Afterward, a blue flame closely attached to the sample surface occurs and maintains for more than 20 minutes at a lower mass flux (1~4 g/m^2·s), rather than directly transitioning to smouldering at 4 g/m^2·s. In this circumstance, the self-extinction of the flame should be the extinction of this blue flame, rather than the traditional buoyancy-controlled yellow flame. Therefore, the existence of this blue flame may extend the extinction limit of timber materials. As the mass flux decreases, the CO/CO$_2$ ratio continuously increases from 0.03 to 0.5. As one can see from Fig. 4.5c, as time goes by, the blue flame splits into discrete blue flamelets, reducing the area covered by flame so that more unburned CO may release to the ambient.

Eventually, the near-limit blue flame extinguishes and transitions to smouldering at the critical (minimum) mass flux around $\dot{m}''_{ex} \approx 1$ g/m^2·s, re-defining the flame extinction limit of timber materials. During the smouldering stage, the CO/CO$_2$ ratio remains almost constant at about 0.5.

Fig. 4.6 further summarizes the true critical mass flux for the flame extinction ($\dot{m}''_{ex}$) under real fire scenarios with different external radiations. The critical mass fluxes for the piloted flaming ignition (8-14 g/m^2·s) are also presented, which is above the extinction limit. When the external radiation is lower than 40 kW/m^2, the yellow flame extinguishes at about 4 g/m^2·s, agreeing with the literatures [9,15]. When the external radiation is above 40 kW/m^2, the persistent blue flame can be sustained until $\dot{m}''_{ex} \approx 1$ g/m^2·s. Moreover, this redefined flame-extinction limit was found to be insensitive to the wood type, as shown in Table 4.1. This blue flame significantly reduces the minimum mass flux to sustain flaming wood combustion and extends the flame extinction limit, therefore suggesting that the blue flame combustion mode as well as the extinction mass flux measured herein should be considered in evaluating the fire risk of timber materials in the future.

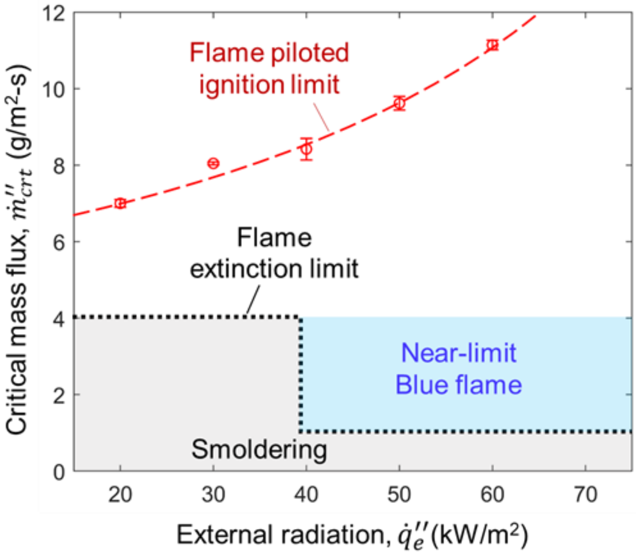

Fig. 4.6. The critical mass flux ($\dot{m}''$) as a function of the external radiation ($\dot{q}''_e$) for ignition, extinction, and different combustion phenomena of wood C.

4.3.3 Surface temperature

As the external radiation increases, the sample top-surface temperature (T_s) will increase as well. Fig. 4.7(a) shows the time evolution of the top surface temperature under 30 and 60 kW/m^2 of the same tests in Fig. 4.5(a-b). Essentially, the top surface temperature approaches to the quasi-steady state by balancing the heat loss and, as expected, increases with the external radiation. Fig. 4.7(b) further shows how the steady surface temperature varies with external radiation and affects the fire phenomena. It can be seen that the near-limit blue flame may survive only when the surface temperature is sufficiently high, that is, $T_s > T_B \approx 700$ °C at $\dot{q}_e'' > \dot{q}_B'' \approx$ 40 kW/m^2. If the external radiation is lowered during the blue-flame region ($\dot{m}''$= 1-4 g/m^2·s), the surface temperature decreases to be lower than 700 °C, and the blue flame eventually disappears. Once reapplying the irradiation, the blue flame will re-occur. Thus, a hot enough surface temperature (maintained by a high external irradiation) may be a necessary condition for the occurrence of this blue flame (see more discussion in Section 2.3.4).

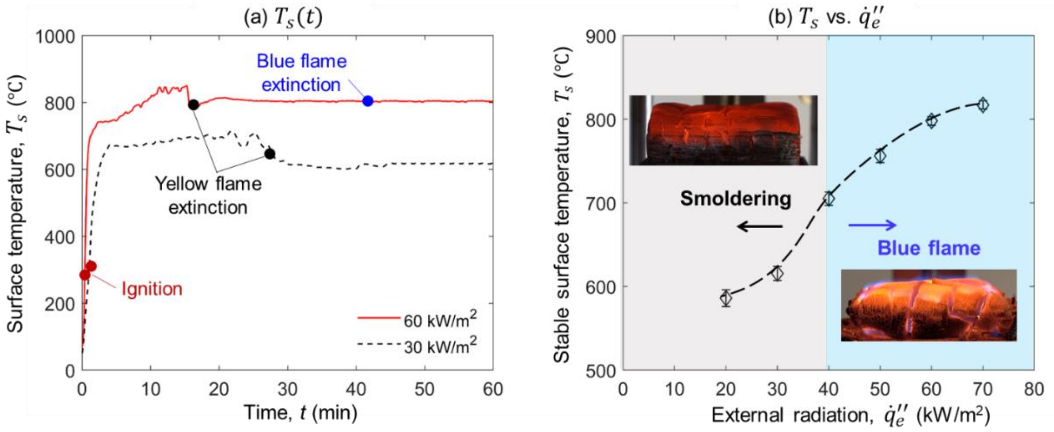

Fig. 4.7. (a) Time evolution of the top surface temperature under 30 and 60 kW/m^2, and (b) steady surface temperature (T_s) as a function of external radiation ($\dot{q}_e''$) of Wood C.

4.3.4 Phenomenological analysis

Considering the blue flame is never observed in PMMA regardless of the irradiation level, the decomposition chemistry and charring tendency of wood fuels are expected to play an important role in this near-limit flame behaviour. To maintain a wood flame, at least two kinds of reactions are needed, namely, the pyrolysis of solid fuel to release pyrolyzates and the subsequent oxidation reaction of the pyrolyzates in the gas phase:

$$\text{Wood} \xrightarrow[\text{Flame/radiation}]{\text{External heating}} \text{Char} + \text{Pyrolyzates} \qquad \text{(Wood pyrolysis)} \qquad (4.1a)$$

$$\text{Pyrolyzates} + O_2 \rightarrow CO_2 + H_2O(g) \qquad \text{(Strong yellow flame)} \qquad (4.2)$$

Pyrolysis is maintained by the heating from flame and external irradiation, and a robust sooty yellow flame will persist until the pyrolysis is weakened by the thick char layer which is a good thermal insulator [16] (Fig. 4.8a). In contrast, for non-charring fuels like PMMA, there will always be a yellow flame until burnout (see Fig. A4.2). Compared to the low-temperature solid-phase oxidation, gas-phase flame reactions are much faster. Thus, almost all ambient oxygen will be consumed within the flame sheet, whereas little oxygen can diffuse into the porous char to sustain robust smouldering combustion.

As the char layer builds up to weaken the effectiveness of the heating, less fuel is produced to support the flame. Under such a negative feedback, eventually, the yellow flame extinguishes at $\dot{m}''_{ex} \approx 4\ \mathrm{g/m^2 \cdot s}$, which may leave undecomposed wood in-depth and unburned char near the surface. Afterward, without the blockage of flame, oxygen may diffuse into the cracked and porous char layer to sustain smouldering combustion.

$$\mathrm{Char} + \mathrm{O_2} \rightarrow \mathrm{Ash} + \mathrm{C_xH_yO_z} + \mathrm{CO} + \mathrm{CO_2} + \mathrm{H_2O(g)} \qquad \text{(Char oxidation)} \qquad (4.3)$$

This heterogeneous char oxidation is incomplete, which may produce a fuel mixture of hydrocarbons and CO [38,39], as also shown in the cone-calorimeter measurement (Fig. 4.5a-b). Moreover, the internal heat release from the char oxidation may further pyrolyze the wood in-depth as

$$\mathrm{Wood} \xrightarrow[\text{Smouldering}]{\text{Internal heating}} \mathrm{Char} + \mathrm{Pyrolyzates} \qquad \text{(Wood pyrolysis)} \quad (4.1b)$$

Especially, the lignin component, which has a higher pyrolysis temperature (400-500 °C) than the cellulose and hemicellulose components [40], may continue to pyrolyze and produce a small amount of flammable gas fuel before being oxidized to ash.

As the surface temperature increases with the external radiation, eventually, it may become hot enough (>700 °C) to either pilot the flame or supports an auto-ignition of the fuel/air mixture. As illustrated in Fig. 4.8(b), it is hypothesized that the near-limit blue flame may be maintained by the mixture produced from both char-oxidation and in-depth wood-pyrolysis reactions of smouldering combustion

$$\text{Smouldering emission} + \mathrm{O_2} \xrightarrow{\text{hot surface}} \mathrm{CO_2} \qquad \text{(Near-limit blue flame)} \quad (4.4)$$

There are two pieces of supporting evidence, (1) the discrete blue flame partially covers the char may allow the oxygen diffusion inside to maintain the char oxidation that releases heat to sustain in-depth pyrolysis (mainly lignin), (2) the CO emission, as the sign of smouldering, in the blue-flame region in Fig. 4.5(b) (60 kW/m^2) is comparable to the pure smouldering region in Fig. 4.5(a) (30 kW/m^2), as part of the CO may be consumed by blue flame (CO/CO$_2$ ratio during smouldering process generally increases as external irradiation increases [25]).

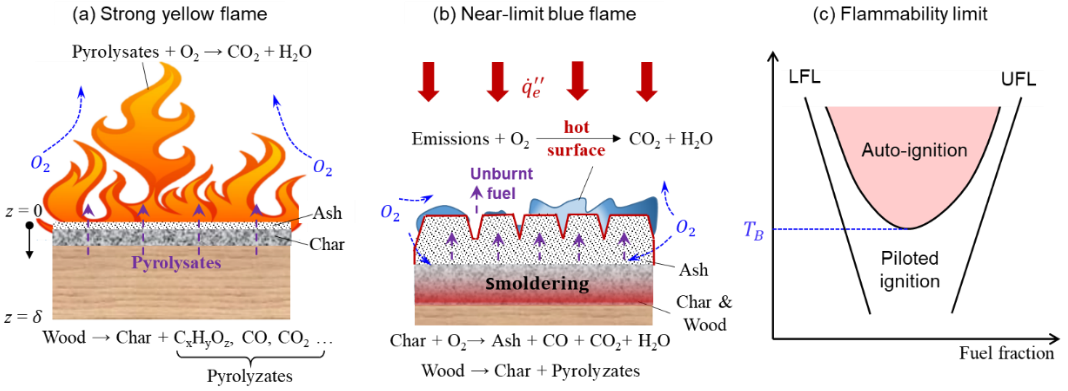

Fig. 4.8. Schematic diagrams of (a) strong yellow flame, (b) weak blue flame, and (c) the flammability limit for piloted and auto-ignition.

The critical surface temperature of $T_B \approx 700$ °C to sustain the blue flame may be the minimum auto-ignition temperature (AIT) of the mixed hydrocarbons and CO produced from smouldering, as illustrated in Fig. 4.8(c). Below this temperature, the flammable mixture cannot be ignited without a pilot source. Above this temperature, the auto-ignition of the fuel-lean mixture not only ensures the existence of flame but also acts as a piloted source to ignite the nearby lean mixture. Because the release of smouldering emission is not uniform across the wood sample, the random ignition and flame propagation on the fuel surface makes the flame flicker around. In other words, this blue flame might be partially premixed. As the flame reaction takes place near the hot surface, and the fuel mass flux is small, the role of buoyancy may be too small to create a clear conical shape. Moreover, the colour of a fuel-lean near-limit flame is pale blue because the low burning rates may result in small flames with small residence time, preventing agglomeration of soot [41,42].

In short, two necessary conditions are hypothesized for this unique blue flame,

(I) The robust in-depth pyrolysis should be sustained by the internal smouldering combustion and external heating; and

(II) A hot surface temperature (>700 °C) over the auto-ignition temperature should be

maintained by the external radiation.

Further decreasing the fuel mass flux to about 1 g/m^2·s, the composition of the fuel-lean mixture near the hot surface may become lower than the lean flammability limit, giving rise to extinction. On the other hand, for non-charring fuels like PMMA, the surface temperature cannot reach 700 °C, because pyrolysis reactions will be completed before exceeding 450 °C, as shown in Figs. A4.1(b) and A4.2(b).

To further explain the combustion mechanism responsible for the near-limit blue flame and verify the aforementioned two hypotheses, the future research could establish two different numerical models to decouple this complex problem. First, a solid-phase model is constructed to demonstrate the necessity of smouldering combustion (or char oxidation) in maintaining the pyrolysis reaction and a long-lasting fuel mass flux of 1~4 g/m^2·s after the extinction of strong yellow flame. Then, a gas-phase DNS model can be constructed to demonstrate the necessity of a hot surface and a critical mass flux to main a near-limit flame that is rarely affected by buoyancy.

4.4 Conclusions

In this study, a unique wood combustion mode showing a near-limit blue flame was identified as an intermediate combustion mode between the buoyancy-controlled yellow flame and the smouldering combustion. The blue flame may appear only if the external radiation exceeds a critical value of about 40 kW/m^2 and the surface temperature higher than 700°C. This near-limit flame tends to attach to the hot charring and smouldering surface and may be only affected by buoyancy effect slightly. Below the critical irradiation, the intense yellow flame directly transitions to smouldering when the mass flux decreases to about 4.0 g/m^2·s for all wood samples. Above the critical irradiation, on the other hand, the near-limit blue flame may still survive until the mass flux of 1.0 g/m^2·s. Thus, it may redefine the flame extinction limit of timber materials under external radiation.

This work hypothesizes two necessary conditions for the occurrence of near-limit blue flame, (I) in-depth pyrolysis sustained by the internal smouldering combustion, and (II) the hot surface maintained by large external radiation to extend the flammability limit or achieve autoignition. The future work will focus on emission gas compositions from different combustion stages, as well as numerical simulations coupling gas-phase and solid-phase processes. This unique blue flame may play an essential role in the transition between flaming and smouldering and help evaluate the fire risk of timber materials under real fire scenarios.

Acknowledgements

This work is supported by the National Natural Science Foundation of China (No. 51876183, 51806230), HK PolyU Startup Fund (1-BE04), and the SKLFS Open Fund (No. HZ2019-KF02). S. Lin would like to thank Dr J. Gao and Dr J. Ji for valuable discussion.

References

[1] Barber D. Tall Timber Buildings: What's Next in Fire Safety ? Fire Technol 2015;51:1279–84.

[2] Richter F, Atreya A, Kotsovinos P, Rein G. The effect of chemical composition on the charring of wood across scales. Proc Combust Inst 2019;37:4053–61.

[3] Richter F, Kotsovinos P, Rackauskaite E, Rein G. Thermal Response of Timber Slabs Exposed to Travelling Fires and Traditional Design Fires. Fire Technol 2020.

[4] Crielaard R, van de Kuilen JW, Terwel K, Ravenshorst G, Steenbakkers P. Self-extinguishment of cross-laminated timber. Fire Saf J 2019;105:244–60.

[5] Song J, Chen C, Zhu S, Zhu M, Dai J, Ray U, et al. Processing bulk natural wood into a high-performance structural material. Nature 2018;554:224–8.

[6] Boarin P, Calzolari M, Davoli P. Two timber construction models: tradition without innovation or innovation without tradition? 2018.

[7] Drysdale D. An Introduction to Fire Dynamics. 3rd ed. Chichester, UK: John Wiley & Sons, Ltd; 2011.

[8] Prior R. The entire wooden interior of Notre Dame Cathedral has been lost. CNN 2019.

[9] Emberley R, Inghelbrecht A, Yu Z, Torero JL. Self-extinction of timber. Proc Combust Inst 2017;36:3055–62.

[10] Bilbao R, Mastral JF, Aldea ME, Ceamanos J, Betrán M, Lana JA. Experimental and theoretical study of the ignition and smouldering of wood including convective effects. Combust Flame 2001;126:1363–72.

[11] Bartlett AI, Hadden RM, Bisby LA. A Review of Factors Affecting the Burning Behaviour of Wood for Application to Tall Timber Construction. Fire Technol 2019;55:1–49.

[12] Boonmee N, Quintiere JG. Glowing and flaming autoignition of wood. Proc Combust Inst 2002;29:289–96.

[13] Boonmee N, Quintiere JG. Glowing ignition of wood: The onset of surface combustion. Proc Combust Inst 2005;30 II:2303–10.

[14] Richter F, Atreya A, Kotsovinos P, Rein G. The effect of chemical composition on the charring of wood across scales. Proc Combust Inst 2017;000:1–9.

[15] Emberley R, Do T, Yim J, Torero JL. Critical heat flux and mass loss rate for extinction of flaming combustion of timber. Fire Saf J 2017;91:252–8.

[16] Moghtaderi B, Novozhilov V, Fletcher DF, Kent JH. A New Correlation for Bench-scale Piloted Ignition Data of Wood. Fire Saf J 2006;29:41–59.

[17] Vermesi I, Richter F, Chaos M, Rein G. Ignition and Burning of Fibreboard Exposed to Transient Irradiation. Fire Technol 2020.

[18] Shi L, Chew MYL. Influence of moisture on autoignition of woods in cone calorimeter. J Fire Sci 2012;30:158–69.

[19] Huang X, Li K, Zhang H. Modelling bench-scale fire on engineered wood : Effects of transient flame and physicochemical properties. Proc Combust Inst 2017;36:3167–75.

[20] Richter F, Rein G. Heterogeneous kinetics of timber charring at the microscale. J Anal Appl Pyrolysis 2019;138:1–9.

[21] Richter F, Rein G. A multiscale model of wood pyrolysis to study the role of chemistry and heat transfer at the mesoscale. Combust Flame 2020;216:316–25.

[22] Rein G. Smouldering Combustion. SFPE Handb Fire Prot Eng 2014;2014:581–603.

[23] Gratkowski MT, Dembsey NA, Beyler CL. Radiant smouldering ignition of plywood. Fire Saf J 2006;41:427–43.

[24] Wang S, Ding P, Lin S, Huang X, Usmani A. Deformation of wood slice in fire: Interactions between heterogeneous chemistry and thermomechanical stress. Proc Combust Inst 2021;38:5081–90.

[25] Lin S, Sun P, Huang X. Can peat soil support a flaming wildfire? Int J Wildl Fire 2019;28:601–13.

[26] Bartlett AI, Hadden RM, Hidalgo JP, Santamaria S, Wiesner F, Bisby LA, et al. Auto-extinction of engineered timber: Application to compartment fires with exposed timber surfaces. Fire Saf J 2017;91:407–13.

[27] Richter F, Jervis FX, Huang X, Rein G. Burning rate of wood pyrolysis, smouldering, and flaming: Effect of oxygen. Combust Flame 2021.

[28] Cuevas J, Torero JL, Maluk C. Flame extinction and burning behaviour of timber under varied oxygen concentrations. Fire Saf J 2020:103087.

[29] Arnórsson SM, Hadden RM, Law A. The Variability of Critical Mass Loss Rate at Auto-Extinction. Fire Technol 2020.

[30] Babrauskas V. Journal of Fire Protection Ignition of Wood : A Review of the State of the Art. J Fire Prot Eng 2002;12:163–89.

[31] Smucker BD, Mulky TC, Cowan DA, Niemeyer KE, Blunck DL. Effects of fuel content and density on the smouldering characteristics of cellulose and hemicellulose. Proc Combust Inst 2019;37:4107–16.

[32] Wang S, Huang X, Chen H, Liu N. Interaction between flaming and smouldering in hot-particle ignition of forest fuels and effects of moisture and wind. Int J Wildl Fire 2017;26:71–81.

[33] Babrauskas V. The Cone Calorimeter. In: Hurley M, editor. SFPE Handb. Fire Prot. Eng. 5th Editio, London: Springer; 2016, p. 952–80.

[34] Lin S, Huang X, Urban J, McAllister S, Fernandez-Pello C. Piloted ignition of cylindrical wildland fuels under irradiation. Front Mech Eng 2019;5:54.

[35] Rich D, Lautenberger C, Torero JL, Quintiere JG, Fernandez-Pello C. Mass flux of combustible solids at piloted ignition. Proc Combust Inst 2007;31:2653–60.

[36] Delichatsios MA, Delichatsios MM. Critical Mass Pyrolysis Rates for Extinction of Fires over Solid Materials. Fire Saf Sci Fifth Int Symp 1997:153–64.

[37] Delichatsios MA. Piloted ignition times, critical heat fluxes and mass loss rates at reduced oxygen atmospheres. Fire Saf J 2005;40:197–212.

[38] Rein G, Cohen S, Simeoni A. Carbon emissions from smouldering peat in shallow and strong fronts. Proc Combust Inst 2009;32 II:2489–96.

[39] Wu D, Schmidt M, Huang X, Verplaetsen F. Self-ignition and smouldering characteristics of coal dust accumulations in O2/N2 and O2/CO2 atmospheres. Proc Combust Inst 2017;36:3195–202.

[40] Stefanidis SD, Kalogiannis KG, Iliopoulou EF, Michailof CM, Pilavachi PA, Lappas AA. A

study of lignocellulosic biomass pyrolysis via the pyrolysis of cellulose, hemicellulose and lignin. J Anal Appl Pyrolysis 2014;105:143–50.

[41] Lin K-C, Faeth GM. State Relationships of Laminar Permanently-Blue Opposed-Jet Hydrocarbon-Fueled Diffusion Flames. Int J Environ Combust Tech Vol I 2000:53–79.

[42] Lin KC, Faeth GM. Hydrodynamic suppression of soot emissions in laminar diffusion flames. J Propuls Power 1996;12:10–7.

PART B: Quenching Limit of Smouldering: Theory, Numerical Verification and Application

The classical concepts of quenching and quenching distance of premixed flame have provided solid foundations for the design of flame arrestors as well as many other the fire protection systems of industrial equipment and processes. However, no study has systematically addressed the quenching dynamics of smouldering and quantified the corresponding quenching distance experimentally and numerically and explored it applications to enrich the fire-fighting strategies, thus, there is a big knowledge gap.

This part includes three chapters (5-7), with the focus on the quenching limits and quenching diameter of smouldering combustion. Chapter 5 explores the quenching limits and applicability of quenching diameter in smouldering through laboratory-scale experiments, where the measured quenching diameter of smouldering was about 10 cm. Chapter 6 develops a 2-D numerical model based on open-source code Gpyro and a previously developed 5-step kinetics of peat to verify the quenching diameter of smouldering combustion and further explore the effects of lateral overall heat transfer coefficient, oxygen concentration and ambient temperature on the extinction limits. Chapter 7 explores the applications of quenching distance of smouldering combustion through constructing firebreak for extinguishing peat fire.

CHAPTER 5: Quenching Limits of Smouldering: Fire under the Wall Cooling

Summary:

Smouldering fire is the slow, low-temperature, and flameless combustion phenomenon in porous fuels. Smouldering is different from flaming regarding the chemical and transport processes, despite sharing many similarities in ignition and fire spread. In this work, we explored the applicability of quenching and quenching diameter in smouldering. The smouldering of dry organic soil was initiated in the 25-cm long tubular reactor with different diameters from 4 cm to 15 cm. The thermal boundary and oxygen supply of the smouldering reactor were varied by using different wall materials and opening configurations, respectively. The quenching of smouldering was found as the diameter of the reactor decreased, the same as the quenching of the premixed flame. The minimum smouldering temperature (~250 ℃) and propagation rate (~0.5 cm/h or 0.1 mm/min) were found before quenching. The measured quenching diameter of smouldering was about 10 cm (much larger than the flame) and comparable to the thickness of reaction front (similar to the flame). The quenching diameter of smouldering increases as the wall cooling increases and the oxygen supply decreases. The influence of oxygen supply is unique to the smouldering quenching phenomenon as it affects the mode of smouldering propagation. This work helps understand the persistence and extinction limit of smouldering and the prevention and suppression strategies for smouldering fire.

This chapter is based on "S. Lin, X. Huang (2021) *Quenching of Smouldering: Effect of Wall Cooling on Extinction*, **Proceedings of the Combustion Institute** 38(3): 5015-5022. doi: 10.1016/j.proci.2020.05.017."

5.1 Introduction

Quenching, in terms of combustion, refers to the flame extinction by cooling [1,2]. The quenching distance (or thickness/diameter) is a critical length below which flame can no longer propagate through [1,3]. Concepts of flame quenching and quenching distance are of practical significance in the design of flame arrestor [3], as well as, the fire protection system of many industrial equipment and processes. Fundamentally, the quenching of the premixed flame is attributed to the cooling from the reactor wall that decreases the flame temperature below the threshold of chain reaction [1]. The quenching behaviours and quenching distance of flame have been extensively studied, and key influence factors include the fuel type and concentration [4], thermal boundary [5,6], and flow conditions (laminar or turbulent) [7]. For a laminar premixed flame, quenching occurs on the scale of millimetre that is comparable to the flame thickness [1,2]. However, to the best of authors' knowledge, no study has systematically addressed the quenching dynamics of smouldering and quantified the corresponding quenching distance, thus, there is a big knowledge gap.

Smouldering is the slow, low-temperature, and flameless burning of porous fuels, and is the most persistent type of combustion [8,9]. Smouldering can be easily initiated by a weak heat source or even self-ignited, such as those in silos and storage units [10]. Once ignited, it is extremely difficult to extinguish [8,11], such as the smouldering firebrands [12] and peat soils [13,14] in wildland fire. In general, there are many similarities between flaming and smouldering fire behaviours [8,14,15]. For solid fuels, pyrolysis is a necessary step for both smouldering and flaming ignition, and transition often occurs between flaming and smouldering [16–18]. For charring materials, fire-spread modes of both flaming and smouldering can be maintained, and both fire-spread rates vary with the fuel type, oxygen supply (or wind), and heat losses [8,14]. Therefore, it is reasonable to expect the quenching and quenching distance (or diameter) of smouldering like those of flame.

On the other hand, smouldering is also very different from the flaming in terms of combustion chemistry, transport processes, and time scales [8]. Fundamentally, the flame is dominated by the homogeneous oxidation of gaseous fuel, while smouldering is sustained by the heterogeneous oxidation on the surface of solid fuel [8,17]. The characteristic temperature (~500 °C), propagation rate (~1 cm/h), and heat of combustion (~10 MJ/kg) of smouldering are lower than those of flame [8,14,15,17–21]. The extinction of smouldering occurs with the increasing fuel moisture content [22], the decreasing pressure [23], and oxygen concentration [24,25] or by using suppression agents [11,26]. Rein [8,9] predicted the critical sample size of 15 cm for sustaining smouldering in the rectangular polyurethane foam, but it has not been verified by the experiment.

The purpose of this experimental study is to explore whether the classical concept of flame quenching and quenching diameter can be extended to smouldering. Considering the heat loss and oxygen supply are two key parameters that control the burning and propagation of smouldering [8], different conditions of wall cooling and oxygen supply were applied to the reactor to determine the quenching limit of smouldering. The quenching diameter was compared with the thickness of the smouldering front, and the minimum values of the smouldering temperature and propagation rate before quenching were quantified.

5.2 Experiment

5.2.1 Setup and controlling parameters

The dry organic peat soil, as a representative fuel that is prone to smoulder, was chosen in the experiment (Fig. 5.1a). This type of moss peat soil has an organic content of above 95%, and was studied previously in [14,17,22]. The element analysis of peat sample shows 44.2, 6.1, 49.1, 0.5, 0.1% mass fractions for C, H, O, N and S, respectively. Before the test, the peat soil was first oven-dried at 90 °C for 48 h [14], and its bulk density and porosity were measured to be 150 ± 10 kg/m^3 and 0.90, respectively [17]. The shape of the peat soil particle was coarse, and its size was about 1 mm, leaving a large pore space between particles [21].

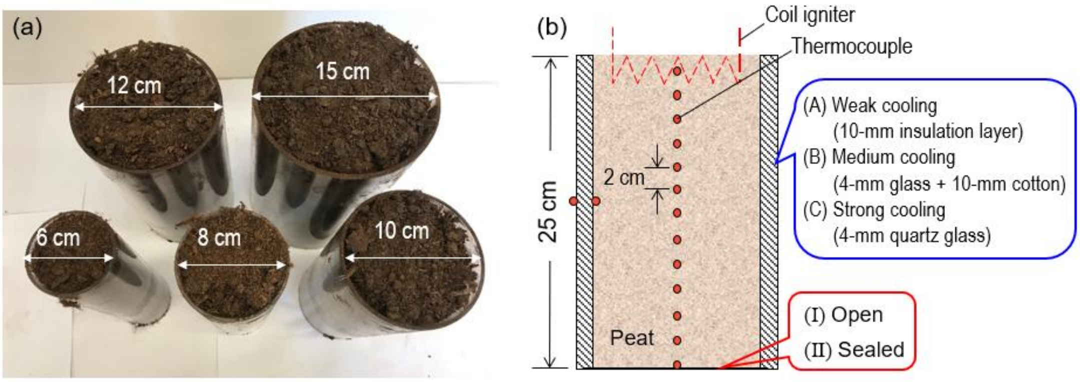

Fig. 5.1. (a) Photos of peat soil and tubular smouldering reactors with different diameters, (b) schematic diagrams for the smouldering reactor, and controlling parameters of wall cooling and oxygen supply.

The peat soil was filled into a group of 25-cm long tubular smouldering reactors with different diameters (D) from 4 cm to 15 cm, as shown in Fig. 5.1. Such tubular reactors were also widely used in other smouldering experiments [27,28]. Three reactor walls with different thermal resistances (R) were selected to vary the cooling condition:

(A) *Weak cooling*: 10-mm ceramic insulation layer (0.1 W/m-K) with R_A (thermal resistance) = 0.1 m^2-K/W;

(B) *Medium cooling*: 4-mm quartz glass (1.0 W/m-K) covering by 10-mm cotton insulation layer (0.15 W/m-K) with R_B = 0.06 m^2-K/W, and

(C) *Strong cooling*: 4-mm quartz glass (1.0 W/m-K) with R_C = 0.004 m^2-K/W.

The smouldering reactor was vertically placed with the top surface open. To vary the oxygen supply to the reactor, the bottom surface was kept open with metal mesh to hold the fuel (i.e., a good oxygen supply) or sealed by the insulation board (0.05 W/m-K) (i.e., a poor oxygen supply), as illustrated in Fig. 5.1(b). The ambient temperature is 23 ± 2 °C, and the relative humidity is about 50 ± 10 %.

5.2.2 Ignition method and test procedures

A coil heater was placed 1 cm below the fuel top free surface. The ignition protocol was fixed at 100 W for 0.5 h, the same as previous work [21,22], which was strong enough to initiate smouldering. Unlike the visible flame propagation, it was difficult to judge the success of smouldering propagation by visual observation [14,17]. Therefore, an array of 13 K-type thermocouples with the 100-μm bead was inserted into the sample along the axis. These thermocouples were placed from 1 cm to 25 cm below the top free surface with the 2-cm interval to monitor the temperature and the location of the smouldering front [21]. Temperatures of inner and outer wall surfaces were also measured by two thermocouples (~13 cm below the free surface), as shown in Fig. 5.1(b).

Quenching test was started with the largest reactor (D =15 cm). If smouldering successfully propagated to the bottom, the reactor diameter was then decreased gradually until the smouldering front could no longer propagate, i.e., the smouldering quenching, so that the quenching diameter (D^*) could be determined. Afterward, conditions of wall cooling and oxygen supply were changed to explore the variation of quenching diameter. For each scenario, tests were repeated at least twice, and good experimental repeatability was found.

5.3 Results and discussion

5.3.1 Smouldering quenching phenomena

Figure 5.2(a) shows the thermocouple measurements of a successful smouldering propagation in the 15-cm wide reactor with the bottom sealed under the weak cooling. Once ignited, the smouldering front gradually propagated downward, and the temperature decreased from 500 °C to 350 °C with increasing depth. After 48 h, most of the peat soils burnt into ash with the mass loss above 90% of the original mass. Figure 5.2(b) shows an example of smouldering quenching (or failed propagation) through a 6-cm wide reactor. During ignition, the sample temperature could reach about 500 °C, but after ignition, it gradually decreased to ambient temperature within 5 h. For all quenched cases, the mass loss of peat soil was below 20% of the original mass.

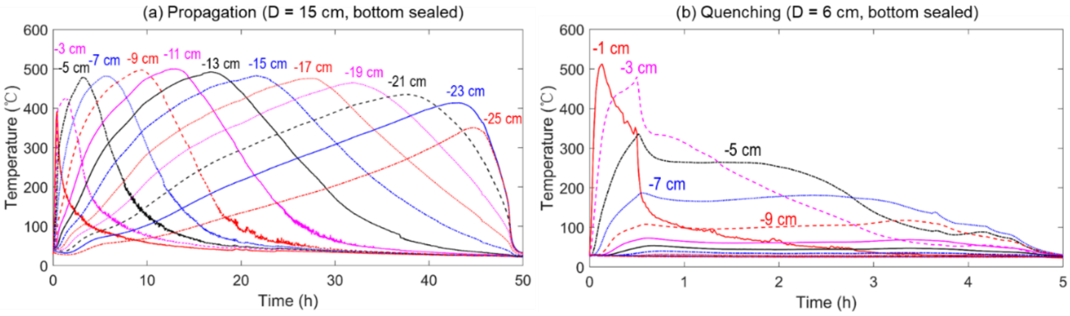

Fig. 5.2. Thermocouples data of (a) successful smouldering propagation in the 15-cm wide reactor, and (b) smouldering quenching in the 6-cm wide reactor with the bottom sealed under a weak wall cooling (1 kW/m^2). The negative sign means that the thermocouple is below the reactor's top free surface.

To better compare different cooling conditions of the reactor wall, the approximate and simplified one-dimensional cooling flux through the wall ($\dot{q}''_w$) in the slow and quasi-steady-state smouldering propagation may be expressed as:

$$\dot{q}''_w = \frac{T_{wi} - T_{wo}}{R_w} = h(T_{wo} - T_\infty) + \varepsilon\sigma(T_{wo}^4 - T_\infty^4) \approx k_F \frac{T_{sm} - T_{wi}}{D/2} \tag{5.1}$$

where T_{sm} is the characteristic temperature of smouldering, T_{wi} and T_{wo} are the inner and outer wall temperatures, T_∞ is the ambient temperature, h is convective coefficient, ε is the emissivity, σ is the Stefan-Boltzmann constant, and k_F is the thermal conductivity of fuel. The thermal resistance of the reactor wall is $R_w = \sum \delta_i / k_i$, where δ_i and k_i are the thickness and thermal conductivity of i^{th} wall layer, respectively. Based on temperature measurements in the experiment, the cooling fluxes for three walls were found to be $\dot{q}''_{wA}$ = 1.0 ± 0.1 kW/m^2 (weak cooling), $\dot{q}''_{wB}$ = 1.6 ± 0.3 kW/m^2 (medium cooling), and $\dot{q}''_{wC}$ = 2.4 ± 0.6 kW/m^2 (strong cooling).

5.3.2 Quenching diameter of smouldering

The experimental outcomes of smouldering propagation (●) and quenching (×) are summarized in

Fig. 5.3. The quenching of smouldering occurs as the diameter of reactor decreases, and the quenching diameter increases as the cooling flux increases. Therefore, both smouldering quenching behaviours are essentially the same as the quenching of the premixed flame [4–6]. Specifically, if the oxygen supply is good by opening the bottom of reactor (Fig. 5.3a), as the wall cooling flux increases from 1 kW/m^2 to 2.4 kW/m^2, the quenching diameter increases from 5 ± 1 cm to 11 ± 1 cm. Note that the smouldering quenching diameter has a length scale of several centimetres, which is 1~2 orders of magnitude larger than the flaming quenching distance (~1 mm) [1–5].

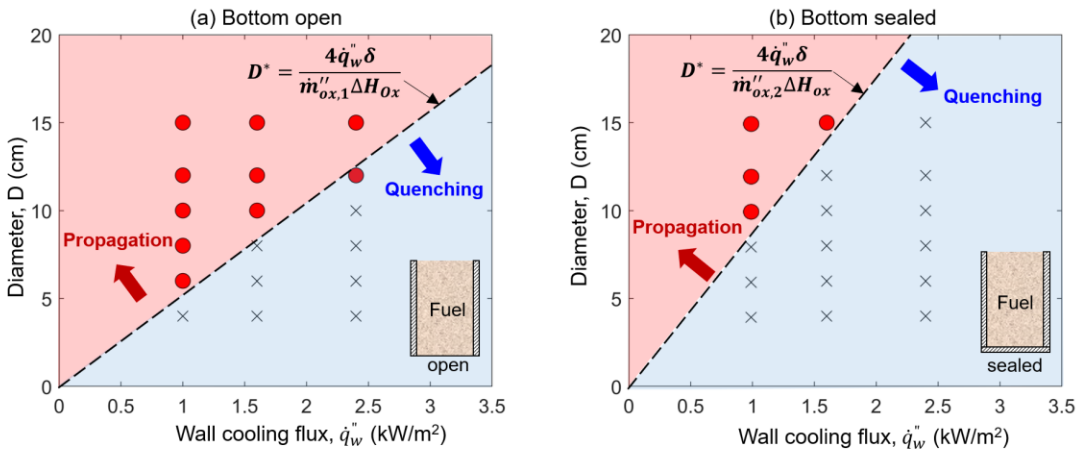

Fig. 5.3. Experimental outcomes of (a) bottom open with a good oxygen supply, and (b) bottom sealed with a poor oxygen supply, where smouldering propagation uses ● and quenching uses ×.

To further explain the influence of wall cooling on the smouldering quenching diameter (D^*), a simplified energy conservation equation is applied to a propagating smouldering front with the thickness of δ, as illustrated in Fig. 5.4(a). At the quenching diameter (D^*), the heat loss from the cold wall ($\dot{Q}_w$) is equal to the heat generation from the smouldering zone ($\dot{Q}_{sm} = \dot{Q}_{ox}$) due to oxidation as

$$\dot{Q}_w = \dot{Q}_{sm} = \dot{Q}_{ox} \tag{5.2}$$

$$\dot{q}_w''(\pi D^*\delta) = \dot{m}_F''\left(\frac{\pi}{4}D^{*2}\right)\Delta H_F = \dot{m}_{ox}''\left(\frac{\pi}{4}D^{*2}\right)\Delta H_{ox} \tag{5.3}$$

$$D^* = \frac{4\dot{q}_w''\delta}{\dot{m}_F''\Delta H_F} = \frac{4\dot{q}_w''\delta}{\dot{m}_{ox}''\Delta H_{ox}} \tag{5.4}$$

where $\dot{m}_F''$ is the smouldering burning flux of fuel, ΔH_F is the heat of smouldering combustion of fuel which is sensitive to the burning conditions, $\dot{m}_{ox}''$ is the mass flux of oxygen (i.e., the rate of oxygen supply), and ΔH_{ox} is the heat of oxidation. A similar expression was previously derived for the rectangular fuel sample in [9]. Eq. (5.4) reveals that the smouldering quenching diameter is proportional to the wall cooling flux, which explains the trend of experimental data in Fig. 5.3.

If the oxygen supply is reduced by sealing the bottom of the reactor (Fig. 5.3b), the quenching diameter also increases with the wall cooling flux, following the same trend of the bottom-open case in Fig. 5.3(a). On the other hand, under the same cooling flux, quenching becomes easier, and the quenching diameter increases, because of the reduced oxygen supply from the bottom. Specifically, at the cooling flux of 1 kW/m^2, the quenching diameter (D^*) increases from 5 ± 1 cm with the bottom open to 9 ± 1 cm with the bottom sealed. Such a trend can also be explained by Eq. (5.4), where the quenching diameter is inversely proportional to the rate of oxygen supply ($\dot{m}''_{ox}$).

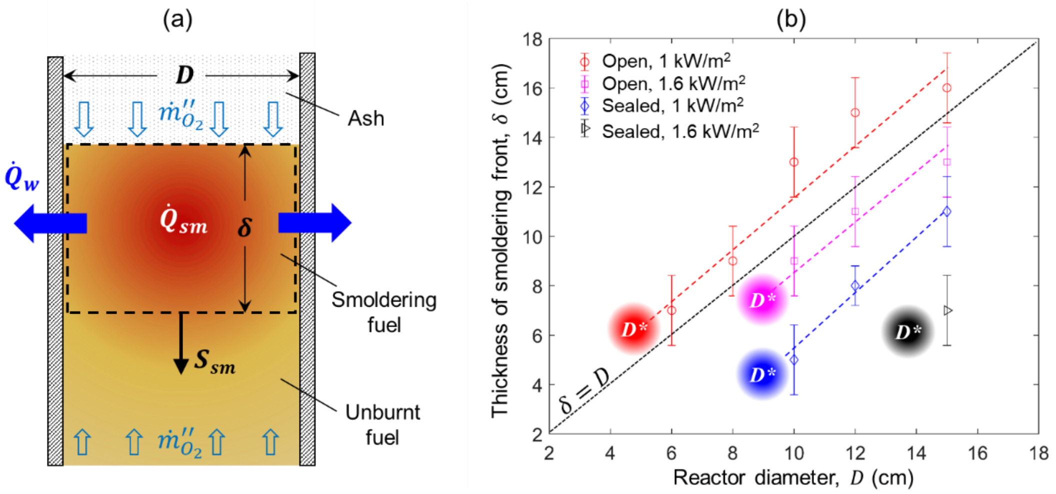

Fig. 5.4. (a) Schematics for smouldering quenching, and (b) thickness of smouldering front (δ) *vs*. reactor diameter (D), where the shadowed point indicates the quenching diameter (D^*) and minimum thickness (δ^*).

5.3.3 Smouldering front thickness

By defining a minimum smouldering temperature of 250 °C, the average thickness of smouldering front (δ) in successfully propagated cases can be estimated based on the thermocouple data (e.g. Fig. 5.2a). Figure 5.4(b) summarizes the thickness of the smouldering front, which increases with the reactor diameter as well as the oxygen supply. For example, with the bottom open and the weak cooling flux of 1 kW/m^2, the thickness of the smouldering front increases from 7 cm to 16 cm, as the reactor diameter increases from 6 cm to 15 cm.

Table 5.1. Measured quenching diameter (D^*) and minimum smouldering front thickness (δ^*).

Wall cooling	**Weak**		**Medium**		**Strong**	
Oxygen supply	**Open**	**Sealed**	**Open**	**Sealed**	**Open**	**Sealed**
$\dot{q}''_w$	1.0 ± 0.1		1.6 ± 0.3		2.4 ± 0.6	
D^* (cm)	5 ± 1	9 ± 1	9 ± 1	13.5 ± 1.5	11 ± 1	>15
δ^* (cm)	6 ± 1	4 ± 1	7 ± 1	6 ± 1	7 ± 1	-
D^*/δ^*	0.8 ± 0.1	2.3 ± 0.6	1.3 ± 0.1	2.3 ± 0.5	1.6 ± 0.3	-

Moreover, the minimum thickness of the smouldering front (δ^*) can be estimated by a linear extrapolation towards the quenching diameter, as indicated by the shadowed points in Fig. 5.4(b). As summarized in Table 5.1, the value of δ^* ranges from 4 to 7 cm, which is insensitive to the wall cooling, but slightly decreases with the decreasing oxygen supply. The comparison further shows that the minimum smouldering front thickness and the quenching distance are comparable (i.e., $D^* \sim \delta^*$). Such behaviour is similar to the premixed flame whose quenching distance (or diameter) is comparable to flame thickness [1–5].

To further explain the relationship between the smouldering thickness and quenching diameter, the analogy could be made between the burning of premixed flame and smouldering propagation [9,14]. Considering a 1-step global smouldering reaction

$$\text{Fuel} + v\text{O}_2 \rightarrow (1+v)\ \text{Products} \tag{5.5}$$

Then, the smouldering burning flux of fuel can be described as

$$\dot{m}''_{ox}/v = \dot{m}''_F \approx \rho_F S_{sm} \tag{5.6}$$

where $v = 1 \sim 2$ is the oxygen stoichiometric coefficient [17,29], ρ_F is the fuel density, S_{sm} is the smouldering burning speed, and the burnout of fuel is assumed after smouldering propagation. By balancing the advection and diffusion terms in the energy equation like the laminar premixed flame [2], the smouldering burning speed (S_{sm}) could be approximated as

$$S_{sm} \approx \frac{2\alpha_F}{\delta} \tag{5.7}$$

where $\alpha_F = k_F/(\rho_F c_p)$ is the thermal diffusivity. The heat of smouldering can be estimated as

$$\Delta H_F \approx (1+v)c_p(T_{sm} - T_o) \tag{5.8}$$

where T_o is the initial temperature and c_p is the specific heat. By substituting Eqs. (5.1,6-8) into Eq. (5.4), the quenching diameter becomes

$$D^* \approx \frac{4k_F \frac{T_{sm} - T_{wi}}{D^*/2} \delta^*}{\rho_F \frac{2\alpha_F}{\delta^*}(1 + v)c_p(T_{sm} - T_o)} = \frac{4}{(1 + v)} \sqrt{\frac{T_{sm} - T_{wi}}{T_{sm} - T_o}} \delta^* \tag{5.9}$$

which explains why the smouldering quenching diameter is comparable to the thickness of the smouldering front in Fig. 5.4(b). As the wall cooling increases, the wall temperature (T_{wi}) decreases so that the ratio of D^*/δ^* increases. By sealing the reactor bottom, the smouldering temperature (T_{sm}) increases due to the change of smouldering-propagation mode (see more discussions in Section 4.3.5), so that the ratio of D^*/δ^* also increases. Both trends of D^*/δ^* are consistent with experimental measurements in Table. 5.1

5.3.4 Smouldering temperature and propagation rate

Figure 5.5 shows the effect of reactor diameter, wall cooling, and oxygen supply on the (peak) smouldering temperature (T_{sm}) and the (downward) propagation rate (S_{sm}). For this dry peat soil, the smouldering temperature is no more than 500 °C, which is similar to the literature data [14,22], and as expected, it is much lower than the minimum temperature of flame (~1300 K) [2]. The propagation of smouldering is in a creeping manner (about 1 ~ 6 cm/h), which is at least two orders of magnitude slower than the flame-spread rate over solid fuel [3] or the burning velocity of premixed flame [2]. As the wall cooling increases, both the smouldering temperature and propagation rate decrease. For increasing the oxygen supply by opening the bottom, the smouldering propagation rate, as expected, increases significantly, but the smouldering temperature decreases, because of the change in mode of smouldering propagation (discussed in Section 4.3.5).

Moreover, as the reactor diameter decreases, both the smouldering temperature and propagation rate continuously decrease. Eventually, at the quenching limit, the *minimum temperature to maintain smouldering* is found to be about 250 °C, which is close to the threshold temperature for char oxidation found in the thermogravimetric analysis of this fuel [17]. Also, the *minimum smouldering propagation rate* before quenching is found to be about 0.5 cm/h or 0.1 mm/min.

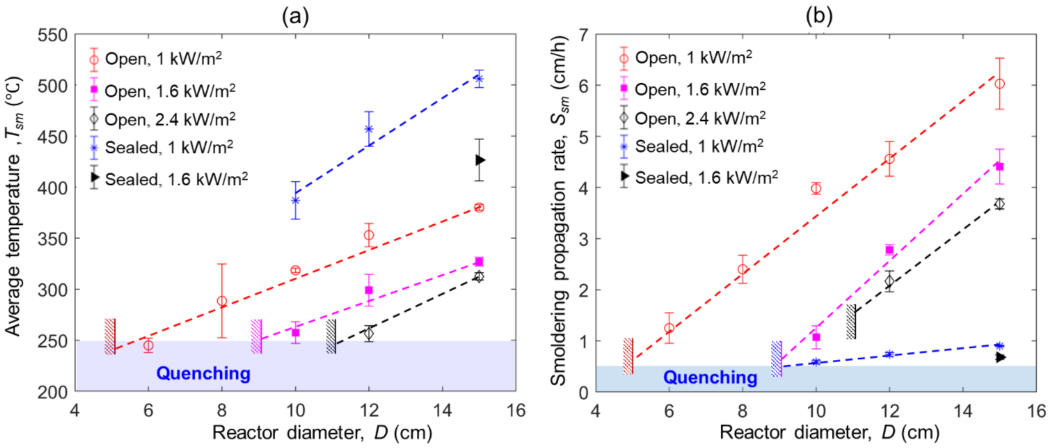

Fig. 5.5. (a) Mean smouldering temperature (T_{sm}), and (b) downward smouldering propagation rate (S_{sm}) as a function of reactor diameter (D), wall cooling flux, and oxygen supply.

5.3.5 Influence of oxygen supply

Figure 5.6 compares the temperature profile of successful smouldering propagation with (a) bottom sealed and (b) bottom open, where the reactor diameter is 12 cm and the weak cooling flux of 1 kW/m^2 is applied. For the bottom-sealed reactor in Figs. 5.2(a) and 5.6(a), after ignition, the smouldering front gradually propagates downward to the bottom and the top free surface regresses [21], as illustrated in Fig. 5.7(a). As the oxygen diffuses from the top free surface, it is forward smouldering propagation where the reaction front moves due to the burnout of fuel [14,21], similar to the motion of candle flame or the burning of premixed flame. After burnout, a sandwich residue structure is observed (Stage III in Fig. 5.7a) where the top and bottom thin layers of char is not burnt due to the heat loss to the environment [21].

With the reactor bottom open, there is an extra oxygen supply from the bottom, which could be dominant, due to the chimney effect, and much larger than the oxygen diffusion from the top [18]. In Fig. 5.6(b), the smouldering propagation has two stages, (1) 1st-stage downward propagation and (b) 2nd-stage bidirectional propagation, as illustrated Fig. 5.7(b). Compared with bottom-sealed case in Fig. 5.6(a), the 1st downward propagation is faster, while the temperature is lower (see more comparisons in Fig. 5.5). Under the upward airflow, such a downward (opposed) propagation is fundamentally a continuous ignition process, that is, the newly ignited smouldering front moving towards the airflow [14]. Thus, it is different from the downward (forward) propagation in Figs. 5.6(a) and 5.7(a). Note that as small amount of oxygen still diffuses from the top surface, a slow burning process remains below the ash layer (see Stage II).

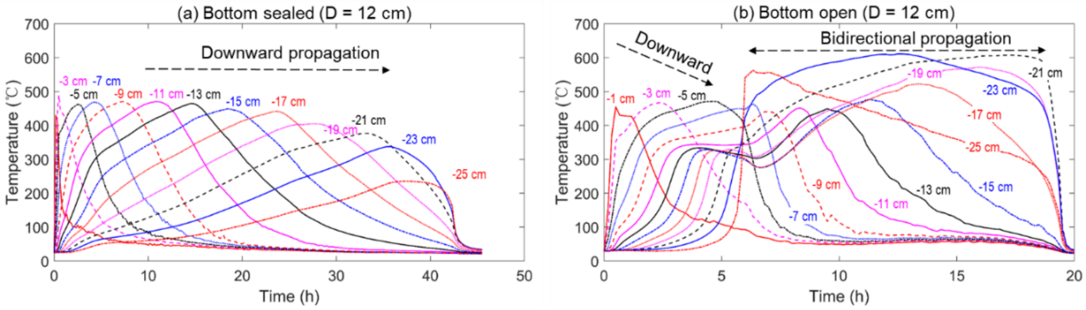

Fig. 5.6. Thermocouple data of smouldering propagation in the 12-cm wide reactor under the cooling flux of 1 kW/m^2, (a) bottom sealed with the downward propagation, and (b) bottom open with the downward-to-bidirectional propagation. The negative sign means thermocouple is below the reactor's top free surface.

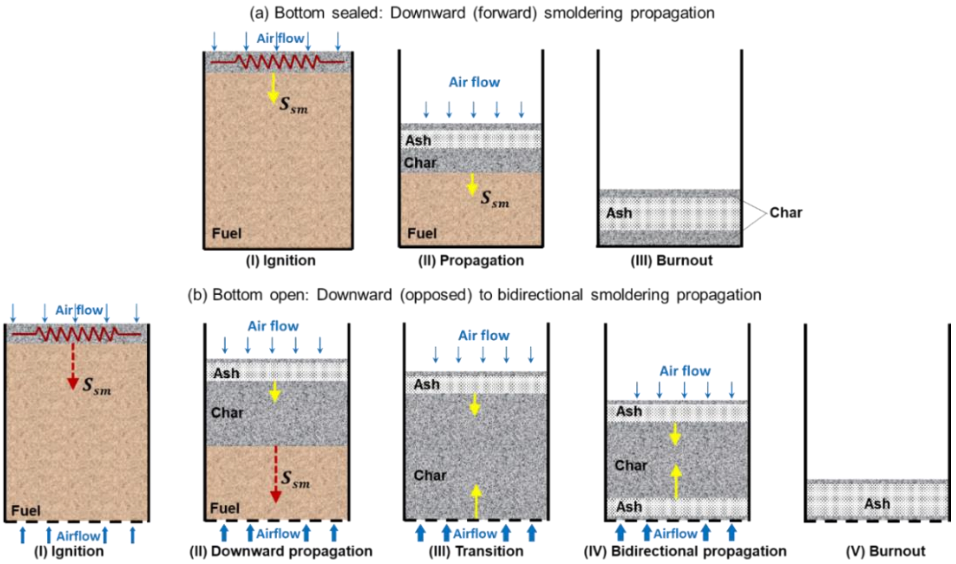

Fig. 5.7. Schematic diagrams of (a) single-stage downward (forward) smouldering propagation, and (b) 2-stage smouldering from downward (opposed) propagation to bidirectional propagation.

After the smouldering front reaches the bottom (about 6 h in Fig. 5.6b), both smouldering fronts on the top and bottom start to propagate towards the centre, that is, a bidirectional forward propagation or burning (see Stage III and IV in Fig. 5.7b). Because of large oxygen supply and good insulation by ash layers, the 2nd-stage bidirectional has a higher temperature of about 600 °C, and the overall burnout time is about 20 h, much shorter than 45 h in the single-stage downward smouldering propagation in Fig. 5.6(a). Note that in experiment, as long as the 1-step propagation was successful, the second bidirectional propagation would not be quenched.

5.4 Conclusions

In this work, quenching of smouldering was observed as the reactor diameter decreased, which is the same as the quenching of flame. The smouldering quenching diameter was quantified for the first time, which is on the order of centimetre and much larger than the flame. Like the flame, the smouldering quenching diameter is also comparable to the thickness of the reaction front, and it increases as the wall cooling increases and the oxygen supply decreases, which are explained analytically. The minimum smouldering temperature (~250°C) and propagation rate (~0.5 cm/h or 0.1 mm/min) was found at the quenching limit.

The oxygen supply plays a unique role in smouldering propagation and quenching. By opening both ends of the reactor, the single-stage downward (forward) propagation transitions to the 2-stage downward-to-bidirectional propagation. Future experiments will be conducted to determine the smouldering quenching distance for different fuels and under controlled oxygen flux, and numerical simulations are needed to reveal the underlying physical process and heterogeneous chemistry behind the minimum smouldering temperature and propagation rate.

Acknowledgements

This study received financial support from the National Natural Science Foundation of China (NSFC grant No. 51876183) and HK PolyU (1-BE04). The authors thank Prof. Cangsu Xu (Zhejiang University) and Dr. Caiyi Xiong (HK PolyU) for the valuable discussion.

References

[1] Williams FA. Combustion Theory. 2nd ed. CRC Press; 1985.

[2] R.Turns S. An Introduction to Combustion: Concepts and Application. 3rd ed. India: McGraw-Hill Education (India) Private Limited; 2012.

[3] Quintiere JG. Fundamentals of Fire Phenomena. New York: John Wiley; 2006.

[4] Bai B, Chen Z, Zhang H, Chen S. Flame propagation in a tube with wall quenching of radicals. Combust Flame 2013;160:2810–9.

[5] Kim N Il, Maruta K. A numerical study on propagation of premixed flames in small tubes. Combust Flame 2006;146:283–301.

[6] Veeraragavan A. On flame propagation in narrow channels with enhanced wall thermal conduction. Energy 2015;93:631–40.

[7] Haq MZ, Sheppard CGW, Woolley R, Greenhalgh DA, Lockett RD. Wrinkling and curvature of laminar and turbulent premixed flames. Combust Flame 2002;131:1–15.

[8] Rein G. Smouldering Combustion. SFPE Handb Fire Prot Eng 2014;2014:581–603.

[9] Rein G. Smouldering Combustion Phenomena in Science and Technology. Rev Lit Arts Am 2009;1:3–18.

[10] Babrauskas V. Ignition Handbook. Issaquah, WA: Fire Science Publishers/Society of Fire Protection Engineers; 2003.

[11] Lin S, Cheung YK, Xiao Y, Huang X. Can rain suppress smouldering peat fire ? Sci Total Environ 2020;727:138468.

[12] Manzello SL, Suzuki S, Gollner MJ, Fernandez-Pello AC. Role of firebrand combustion in large outdoor fire spread. Prog Energy Combust Sci 2020;76:100801.

[13] Rein G. Smouldering Fires and Natural Fuels. In: Claire M. Belcher, editor. Fire Phenom. Earth Syst., New York: John Wiley & Sons, Ltd.; 2013, p. 15–34.

[14] Huang X, Rein G. Upward-and-downward spread of smouldering peat fire. Proc Combust Inst 2019;37:4025–33.

[15] Ohlemiller T, Lucca D. An experimental comparison of forward and reverse smoulder propagation in permeable fuel beds. Combust Flame 1983;54:131–47.

[16] Xie Q, Zhang Z, Lin S, Huang X, Qu Y. Smouldering Fire of High-Density Cotton Bale Under Concurrent Wind. Fire Technol 2020.

[17] Lin S, Sun P, Huang X. Can peat soil support a flaming wildfire? Int J Wildl Fire 2019;28:601–13.

[18] Santoso MA, Christensen EG, Yang J, Rein G. Review of the Transition From Smouldering to Flaming Combustion in Wildfires. Front Mech Eng 2019;5.

[19] Anderson MK, Sleight RT, Torero JL. Downward smoulder of polyurethane foam: Ignition signatures. Fire Saf J 2000;35:131–47.

[20] Torero JL, Fernandez-Pello a. C, Kitano M. Opposed Forced Flow Smouldering of Polyurethane Foam. Combust Sci Technol 1993;91:95–117.

[21] Huang X, Rein G. Downward Spread of Smouldering Peat Fire: the Role of Moisture, Density and Oxygen Supply. Int J Wildl Fire 2017;26:907–18.

[22] Huang X, Restuccia F, Gramola M, Rein G. Experimental study of the formation and collapse of an overhang in the lateral spread of smouldering peat fires. Combust Flame 2016;168.

[23] Yamazaki T, Matsuoka T, Nakamura Y. Near-extinction behaviour of smouldering combustion under highly vacuumed environment. Proc Combust Inst 2019;37:4083–90.

[24] Hadden RM, Rein G, Belcher CM. Study of the competing chemical reactions in the initiation and spread of smouldering combustion in peat. Proc Combust Inst 2013;34:2547–53.

[25] Huang X, Rein G. Interactions of Earth’s atmospheric oxygen and fuel moisture in smouldering wildfires. Sci Total Environ 2016;572:1440–6.

[26] Tuomisaari M, Baroudi D, Latva R. Extinguishing smouldering fires in silos: BRANDFORSK project 745-961. VTT Publ 1998:2–74.

[27] Yermán L, Wall H, Torero JL. Experimental investigation on the destruction rates of organic waste with high moisture content by means of self-sustained smouldering combustion. Proc Combust Inst 2017;36:4419–26.

[28] Pironi P, Switzer C, Gerhard JI, Rein G, Torero JL. Self-sustaining smouldering combustion for NAPL remediation: Laboratory evaluation of process sensitivity to key parameters. Environ Sci Technol 2011;45:2980–6.

[29] Rein G. Smouldering Combustion Phenomena in Science and Technology. Int Rev Chem Eng 2009;1:3–18.

CHAPTER 6: Numerical Verification of Smouldering Quenching and Near-Limit Propagation

Summary:

Smouldering is slow, low-temperature, and flameless burning of porous fuel and one of the most persistent types of combustion phenomena. The influence of heat loss on propagation and quenching behaviours of smouldering combustion is of practical significance but still poorly understood. In this chapter, based on the open-source code Gpyro, a physics-based 2-D computational model that integrates the mechanisms of heat transfer, mass transfer, and chemistry is built to investigate the effect of lateral heat loss on the propagation, quenching and quenching diameter of smouldering combustion in 25-cm high peat samples. According to the simulation results, quenching occurs as the sample diameter decreases, and the quenching diameter increases from 5±1 cm to 21±1 cm as the overall lateral heat transfer coefficient increases from 0.25 W/m^2-K to 2.0 W/m^2-K, agreeing well with the experimental observation. Further analysis demonstrates that the smouldering temperature and propagation rate increase as the diameter of the peat column increases or lateral heat loss coefficient decreases, but when the sample diameter is sufficiently large, their sensitivities to the dimension of the smouldering system and insulation properties diminish significantly. Finally, the influences of the ambient temperature and mass fraction of oxygen on the quenching diameter are explored. This is the first time to use a comprehensive physics-based model to predict the quenching behaviour of smouldering combustion at different ambient conditions, which provides a better understanding of the persistence and extinction limit of smouldering combustion.

This chapter is based on "S. Lin, H. Yuan and X. Huang (2021) *A Computational Study on the Quenching and Near-Limit Propagation of Smouldering Combustion.* **Combustion and Flame** (under review)."

6.1 Introduction

Smouldering is slow, low-temperature and flameless burning of porous fuel and one of the most persistent types of combustion phenomena [1–3]. As a heterogeneous process, smouldering is sustained by the heat evolved when oxygen molecules directly attack the hot surface of condensed-phase reactive porous media [1–4]. In general, smouldering could be initiated by a weaker heat source or even self-heating [5–7], providing a shortcut to flaming combustion through the smouldering-to-flaming transition that follows a sudden increase in spread rate, heat release and hazard [8–11]. Smouldering combustion is the primary cause and driving phenomenon of residential fires (e.g., upholstered furniture and mattresses fires) [12,13], industrial fires (e.g., fires in silos and storage units) [14], and natural fires (e.g., subsurface fire in peatlands or abandoned coal mines) [15–18], posing severe threats to humans and environment. On the other hand, some beneficial applications of smouldering combustion have been developed over the past few decades, such as the manufacture of carbon-negative biochar for energy production [19], smouldering-controlled prescribed burning for wildfire management [20], and waste removal technology for waste management [21,22]. Thus, a better understanding of smouldering combustion is vital to mitigate the smouldering fire hazard and optimize the applications of smouldering system.

Heat loss is one of the critical mechanisms that control smouldering combustion [1,2,23], and therefore has substantial implications toward understanding its propagation limits and quenching behaviours [24,25]. For flaming combustion, the quenching distance (or thickness/diameter) is defined as a critical length, below which flame can no longer propagate through because of the flame-wall interaction that decreases the flame temperature below the threshold of chain reactions (Fig. 6.1a) [26–29]. It is of practical significance in the design of flame arrestor as well as other fire protection systems [30,31]. Analogous to the quenching behaviour of premixed flame, heat loss is also an essential factor during smouldering propagation, which may weaken the chemical reactions [32] and hence lead to the occurrence of quenching (Fig. 6.1b) [24,33]. Quenching behaviour and quenching diameter of smouldering combustion were first theoretically studied by Rein [2,34] and then experimentally verified in our previous study [24]. The experimental measurement demonstrated that the quenching diameter of smouldering was about 10 cm (at least two orders of magnitude larger than that of flame), which was comparable to the smouldering front thickness (similar to the flame) [24]. In addition, this diameter was also found to increase as the lateral wall cooling flux or the overall heat transfer coefficient increases

[24]. Moreover, as the reactor diameter decreases, both the smouldering temperature and the minimum smouldering propagation rate decrease and eventually approach threshold values at the quenching limit [24]. Afterwards, we further explored the application of quenching through constructing firebreak to control smouldering peat fire, that is, ensuring the peat layer is thinner than the quenching thickness (Fig. 6.1c) [33].

The numerical studies on quenching and quenching distance of premixed flame have been conducted for decades, establishing many insightful understandings [27,28,35]. However, to the best of the authors' knowledge, no computational study has been conducted yet to study the quenching behaviour of smouldering combustion. Therefore, a comprehensive computational model is required to better understand the underlying mechanisms behind this phenomenon.

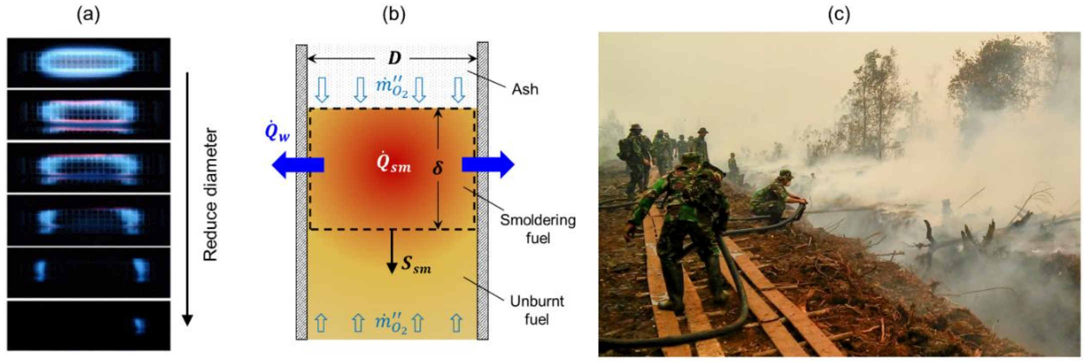

Fig. 6.1. (a) Effect of surface-flame interaction on flame quenching, where the separation between two parallel plates was decreased from 5.49 mm (top) to 5.05 mm (bottom) [29], and (b) schematic diagram of smouldering quenching in tubular reactor owing to the lateral heat loss [24], and (c) applying quenching theory to control smouldering peat fire using a trench-shaped firebreak where the peat layer is thinner than quenching thickness (Credit: David Gaveau) [33].

The computational study on smouldering was initiated by Ohlemiller [1], who established the governing equations to simulate this persistent combustion phenomenon. Afterwards, a number of numerical simulations were performed to investigate the smouldering combustion of different porous media, including peat [15,36–45], cellulose [1,46], coal [47,48], polyurethane foam [49] and char [50] with chemical schemes of different complexities using the 1-D model. Based on these works, Yang et al. [44] developed a 2-D axis-symmetric model for the natural downward spread of peat fire and reported the importance of lateral heat loss. However, previous studies mainly focused on the ignition and propagation of smouldering, whereas the quenching behaviour of smouldering combustion has not received sufficient attention.

To fill this knowledge gap, in this work, we develop a comprehensive 2-D model based on open-source code Gpyro [51,52] and a previously developed 5-step kinetics of peat [15,38,40,42] to investigate the quenching and quenching diameter of smouldering combustion in 25-cm high peat columns that were experimentally studied previously [24]. The lateral heat loss is considered by setting an overall heat transfer coefficient (U) related to the total thermal resistance [53]. The computational results are compared with and verified by the experimental observation [24]. Finally, the influences of ambient temperature and mass fraction of oxygen on the quenching diameter of smouldering combustion are explored.

6.2 Computational model

In-depth smouldering spread in the vertical direction can be well studied using column peat samples as done before in the experiments of Benscoter et al. [40] and Huang et al. [38,42]. Once the top layer is ignited, the peat sample is first dried, then pyrolyzes to char, and eventually oxidizes to ash, forming a smouldering front. After ignition, this smouldering front either becomes self-sustaining and starts to propagate downwards or stops at the ignition zone depending on the fuel characteristics and ambient conditions [24,33,36,40].

In previous, for the first time, we have conducted experimental studies on the quenching diameter of smouldering combustion [24]. As the simulation of these experiments is the starting point of the present paper, a brief introduction on the experimental details is given here. The dry organic peat soil, a representative fuel that is prone to smoulder, was chosen in the experiment. Before the test, the peat soil was first oven-dried at 90 °C for 48 h [38], and its bulk density and air-dried moisture content were 150 ± 10 kg/m^3 and 5%, respectively [5]. The peat soil was filled into tubular smouldering reactors with different diameters (D) from 4 cm to 15 cm. Three reactor walls were selected to vary the lateral cooling condition, and their overall heat transfer coefficients were approximated as 0.58, 0.77 and 1.25 W/m^2-K, respectively, which were calculated by Eq. (6.1), where R_{tot} and A are total thermal resistance per unit area and wall area, δ_i and k_i are the thickness and thermal conductivity of i^{th} wall layer, respectively [24,53]. A coil heater was placed 1 cm below the fuel top free surface. The ignition protocol was fixed at 100 W for 0.5 h, the same as previous work [42,54], which was strong enough to initiate a robust smouldering front. The quenching test was started with the largest reactor (D =15 cm). If smouldering successfully propagated to the bottom, the reactor diameter was then decreased gradually until the smouldering front could no longer propagate, which was regarded as the smouldering quenching. The critical peat diameter where quenching was observed is defined as the quenching diameter (D^*) [24] .

$$U = \frac{1}{R_{tot}A} = \frac{1}{\sum \frac{\delta_i}{k_i} + \frac{1}{h_\infty}} \tag{6.1}$$

As the peat sample is in the shape of the cylinder, the quenching behaviour of smouldering combustion via wall cooling can be considered as a 2-D process (see Fig. 6.2). Therefore, a 2D model is built here using Gpyro. Gpyro is a generalized open-source code for combustible solids and has been used to simulate the pyrolysis and smouldering of various porous media such as peat [15,36,38,42], wood [55–57], PU foam [58] and coal [7,47]. It is therefore used here as well. With a gas-phase convective-diffusive solver that simulates the diffusion of gas species from the ambient into the decomposing porous materials, Gpyro is capable of calculating the transient composition of gaseous species (both reactant and products) at different locations [7,58]. By coupling the solver with separate transient conservation equations of gaseous and condensed phase mass, species and energy, the temperature and species distributions inside the reacting porous media can be well simulated [43,51,52].

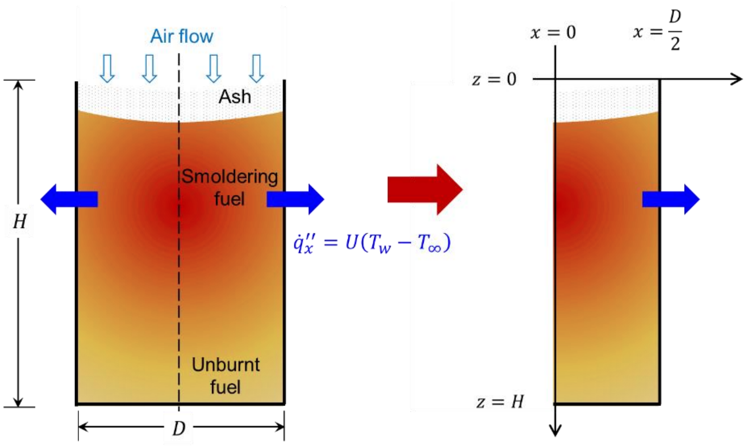

Fig. 6.2. Schematic diagram of the 2-D computational domain for the in-depth propagation of smouldering in a 25-cm deep peat column.

The computational domain is a 25-cm top-open peat column, as shown in Fig. 6.2. Similar to our previous experimental study [24], the simulation of smouldering propagation or quenching starts with a large peat-column diameter. If smouldering successfully propagates to the bottom without an apparent decrease in temperature, propagation rate and heat release rate, then the diameter of the sample is decreased gradually until a quenching case is found. Due to the geometrical symmetry, the computational domain can be half of the real sample [43] to save computational cost and time, as shown in Fig. 6.2.

6.2.1 2-D governing equations

The model solves the 2-D transient conservation equations for condensed and gaseous phases in the absence of gravity, and thermal equilibrium is assumed between gas and condensed-phase species. The governing conservation equations are provided here, including the conservation of mass (Eq. 6.2), species (Eq. 6.3) and energy (Eq. 6.4) in the condensed phase as well as the mass (Eq. 6.5), species (Eq. 6.6) and momentum (Darcy's law) (Eq. 6.7) in the gas phase. The subscripts i, j and k represent the number of condensed-phase species, gas-phase species, and reaction, *d* and *f* refer to the destruction and formation of species, and *z* and *x* refer to vertical and horizontal directions, respectively. The details of the mathematical formation of these equations can be found in [52];

$$\frac{\partial \bar{\rho}}{\partial t} = -\dot{\omega}'''_{fg} \tag{6.2}$$

$$\frac{\partial (\bar{\rho} Y_i)}{\partial t} = \dot{\omega}'''_{fi} - \dot{\omega}'''_{di} \tag{6.3}$$

$$\frac{\partial (\bar{\rho} \bar{h})}{\partial t} = k \frac{\partial}{\partial x}\left(\frac{\partial T}{\partial x}\right) + k \frac{\partial}{\partial z}\left(\frac{\partial T}{\partial z}\right) + \dot{\omega}'''_{di}(-\Delta H_i) \tag{6.4}$$

$$\frac{\partial}{\partial t}\left(\rho_g \overline{\psi}\right) + \frac{\partial \dot{m}''_x}{\partial x} + \frac{\partial \dot{m}''_z}{\partial z} = \dot{\omega}'''_{fg} \tag{6.5}$$

$$\frac{\partial}{\partial t}\left(\rho_g \overline{\psi} Y_j\right) + \frac{\partial}{\partial x}\left(\dot{m}''_x Y_j\right) + \frac{\partial}{\partial z}\left(\dot{m}''_z Y_j\right) = -\frac{\partial}{\partial x}\left(\overline{\psi} \rho_g D_{eff} \frac{\partial Y_j}{\partial x}\right) - \frac{\partial}{\partial z}\left(\overline{\psi} \rho_g D_{eff} \frac{\partial Y_j}{\partial z}\right) + \dot{\omega}'''_{fj} - \dot{\omega}'''_{dj} \tag{6.6}$$

$$\dot{m}''_z = -\frac{\kappa}{\nu}\frac{\partial p}{\partial z} \quad \dot{m}''_x = -\frac{\kappa}{\nu}\frac{\partial p}{\partial x} \qquad \left(\rho_g = \frac{P\overline{M}}{RT}\right) \tag{6.7}$$

For the symmetrical plane $(x = 0)$, adiabatic and impermeable boundary conditions are applied, as shown in Eq. (6.8) and Eq. (6.9). At the wall boundary $(x = D/2)$, no mass transfer is considered (Eq. 6.10). To include the lateral heat loss, an overall heat transfer coefficient (U) is applied to represent the cooling effect from the lateral wall (Eq. 6.11), which can be calculated using Eq. (6.1).

$$k \left.\frac{\partial T}{\partial x}\right|_{x=0} = 0 \tag{6.8}$$

$$\bar{\psi}\rho_g D_{eff}\frac{\partial Y_j}{\partial x}\bigg|_{x=0} = 0 \tag{6.9}$$

$$\bar{\psi}\rho_g D_{eff}\frac{\partial Y_j}{\partial x}\bigg|_{x=\frac{D}{2}} = 0 \tag{6.10}$$

$$k\frac{\partial T}{\partial x}\bigg|_{x=\frac{D}{2}} = -U_{x=\frac{D}{2}}\left(T|_{x=\frac{D}{2}} - T_\infty\right) \tag{6.11}$$

$$-k\frac{\partial T}{\partial x}\bigg|_{z=0} = \dot{q}_e'' - h_{c,z=0}(T|_{z=0} - T_\infty) - \varepsilon\sigma(T^4|_{z=0} - T_\infty^4)\ (0 \le t \le 30\ \text{min})$$

$$-k\frac{\partial T}{\partial x}\bigg|_{z=0} = -h_{c,z=0}(T|_{z=0} - T_\infty) - \varepsilon\sigma(T^4|_{z=0} - T_\infty^4)\ (t > 30\ \text{min}) \tag{6.12}$$

$$-\bar{\psi}\rho_g D_{eff}\frac{\partial Y_j}{\partial x}\bigg|_{z=0} = -h_{m,z=0}\left(Y_j|_{z=0} - Y_j^\infty\right) \tag{6.13}$$

$$\bar{\psi}\rho_g D_{eff}\frac{\partial Y_j}{\partial x}\bigg|_{z=H} = 0 \tag{6.14}$$

$$-k\frac{\partial T}{\partial x}\bigg|_{z=H} = h_{c,z=H}(T|_{z=H} - T_\infty) \tag{6.15}$$

At the top free surface ($z = 0$), both convective ($h_{c,z=0} = 10\ \text{W/m}^2\cdot\text{K}$) and radiative heat loss are considered (Eq. 6.12). Within the first 30 min, irradiation of 30 kW/m^2($\dot{q}_e''$) is applied at $z = 0$ to simulate the ignition by the coil heater [36,42]. The mass transfer of gas species on the top free surface is calculated through Eq. (6.13). Based on the heat-mass transfer analogy, the mass transfer coefficient can be approximated as $h_{m,z=0} = h_{c,z=0}/C_g = 9.09\ \text{g/m}^2\cdot\text{s}$, where C_g is the specific heat capacity of gas species and is assumed to be constant at $1{,}100\ \text{J/kg}\cdot\text{K}$ in the simulation [58]. At the bottom boundary ($z = 25$ cm), the mass flux is set to zero (Eq. 6.14), and heat loss through the insulating board attached to the ground in the experiment is simulated by setting a convective coefficient of $h_{c,z=H} = 0.1\ \text{W/m}^2\cdot\text{K}$ (Eq. 6.15). The ambient pressure and temperature are assumed to be 1 atm and 300 K. The whole computational domain has the same initial gas composition as the ambient air ($Y_{O_2} = 0.232$ and $Y_{N_2} = 0.768$). The solution starts to converge at $\Delta z = \Delta x = 0.1\ \text{mm}$ and $\Delta t = 0.01\ \text{s}$. Further reducing the cell size and time step by a factor of 2 gives no significantly different results, so the calculations are sufficiently resolved.

6.2.2 Chemical kinetics

Heterogeneous reaction *k* of condensed species *A* is represented in mass basis as

$$A_k + \sum_{j=1}^{N} \nu_{j,k}'\ \text{gas}\ j \rightarrow \nu_{B,k}B_k + \sum_{j=1}^{N} \nu_{j,k}''\ \text{gas}\ j \tag{6.16}$$

where $\nu = 1 + (\rho_B/\rho_A - 1)\chi_k$ is the stoichiometric coefficient, and χ_k quantifies the shrinkage or intumescent of the cell size. The destruction rate of condensed species A in reaction k is expressed using Arrhenius law as

$$\dot{\omega}'''_{dA_k} = \frac{(\bar{\rho}Y_{A_k}\Delta z)_\Sigma}{\Delta z} A_k \, exp\left(-\frac{E_k}{RT}\right)\left(\frac{\bar{\rho}Y_{A_k}\Delta z}{(\bar{\rho}Y_{A_k}\Delta z)_\Sigma}\right)^{n_k} Y_{O_2}^{n_{O_2,k}} \qquad (6.17)$$

$$(\bar{\rho}Y_i\Delta z)_\Sigma \equiv (\bar{\rho}Y_i\Delta z)|_{t=0} + \int_0^t \dot{\omega}'''_{fi}(\tau)\Delta z(\tau)d\tau \qquad (6.18)$$

The formation rate of condensed species B and all gases from reaction k are $\nu_{B,k}\dot{\omega}'''_{dA_k}$ and $\dot{\omega}'''_{fg_k} = (1-\nu_{B,k})\dot{\omega}'''_{dA_k}$ [52]. The corresponding heat of reaction is $\dot{Q}'''_k = -\dot{\omega}'''_{dA_k}\Delta H_k$ [52].

The 5-step kinetic scheme developed in [15] is used here as it has been shown to be valid to simulate downward smouldering in previous studies [42]. This 5-step scheme includes one drying step, one pyrolysis step and three oxidation steps of peat, β-char and α-char, as shown in Eq. (6.19-23).

$$\text{Peat}\cdot\nu_{w,dr}\text{H}_2\text{O} \rightarrow \text{Peat} + \nu_{w,dr}\text{H}_2\text{O(g)} \qquad (dr) \qquad (6.19)$$

$$\text{Peat} \rightarrow \nu_{\alpha,pp}\,\alpha\text{-Char} + \nu_{g,pp}\text{Gas} \qquad (pp) \qquad (6.20)$$

$$\text{Peat} + \nu_{O_2,po}\text{O}_2 \rightarrow \nu_{\beta,po}\beta\text{-Char} + \nu_{g,po}\text{Gas} \qquad (po) \qquad (6.21)$$

$$\beta\text{-Char} + \nu_{O_2,\beta o}\text{O}_2 \rightarrow \nu_{a,\beta o}\text{Ash} + \nu_{g,\beta o}\text{Gas} \qquad (\beta o) \qquad (6.22)$$

$$\alpha\text{-Char} + \nu_{O_2,\alpha o}\text{O}_2 \rightarrow \nu_{a,\alpha o}\text{Ash} + \nu_{g,\alpha o}\text{Gas} \qquad (\alpha o) \qquad (6.23)$$

where $\nu_{w,dr} = \text{MC}$ and subscripts w, p, α, β, and a represent water, peat, α-char, β-char and ash respectively. Four gaseous species, including oxygen (O_2), nitrogen (N_2), vapour (H_2O) and combustion products are considered. For simplification, all gaseous species are assumed to have unit Schmidt number, same diffusivity and specific heat [52]. However, for the gas diffusing into porous media, the gas diffusivity has to be treated differently from that in the open air because of the tortuous channels of fluid inside the porous media [48]. Tortuosity (τ) is commonly used to describe diffusion inside porous media [59], and is expressed as the ratio of actual average length (L_{tortuous}) of the channel to the straight-line distance (L_{straight}) of porous materials as $\tau = L_{\text{tortuous}}/L_{\text{straight}}$., The effective mass diffusivity (D_{eff}) of gas species can be calculated using Eq. (6.24) [43,59].

$$D_{\text{eff}} = \left(\frac{1}{\tau}\right)^2 D_{\text{free}} \qquad (6.24)$$

where D_{free} is the mass diffusivity of gas species in the open air. The details of the gas diffusion model can be found in [48].

6.2.3 Parameter selection

Physical properties of all condensed-phase species are obtained from [36] and listed in Table 6.1, where the subscript s and o and represents the solid physical properties (i.e., $\psi = 0$) and bulk physical properties, respectively. For porous media, the effective thermal conductivity includes the radiation heat transfer across pores [52] as shown below

$$k_i = k_{s,i}(1 - \psi_i) + \gamma_i \sigma T^3 \tag{6.25}$$

where $\gamma = {\sim}10^{-4} - 10^{-3}$ m is dependent on the pore size (d_p) as $\gamma \sim d_p = 1/S\rho$ with a soil particle surface area of $S \sim 0.05\ \mathrm{m^2/g}$ [60]. The permeability ($K \sim {d_p}^2$) is on the scale of $10^{-12} - 10^{-9}$ m^2 [36]. The averaged properties of condensed-phase species in each cell are calculated by weighting appropriate mass or volume fractions as [36,58]

$$\bar{\rho} = \sum X_i \rho_i, \bar{k} = \sum X_i k_i, \bar{c} = \sum Y_i c_i, X_i = \bar{\rho} \frac{Y_i}{\rho_i} \tag{6.26}$$

The kinetic and stoichiometric parameters of the 5-step reactions for the peat sample are also obtained from [36] and listed in Table 6.2.

Table 6.1. The physical parameters of condensed-phase species.

Species (i)	$\rho_{s,i}$ (kg/m^3)	$\rho_{o,i}$ (kg/m^3)	ψ_i (-)	$k_{s,i}$ (W/m-K)	$c_{p,i}$ (J/kg-K)
Water	1000	1000	-	0.6	4186
Peat	1500	1100	0.927	1.0	1840
α-Char	1300	135	0.896	0.26	1260
β-Char	1300	135	0.896	0.26	1260
Ash	2500	19.5	0.992	0.8	880

Table 6.2. Reaction parameters and gaseous yields of 5-step reaction for peat sample [36].

Parameter	*dr*	*pp*	*po*	*βo*	*αo*
lgA_k (lg (s^{-1}))	8.12	5.92	6.51	1.65	7.04
E_k (kJ/mol)	67.8	93.3	89.8	54.4	112
n_k (-)	2.37	1.01	1.03	0.54	1.85
$\nu_{B,k}$ (kg/kg)	0	0.75	0.65	0.03	0.02
ΔH_k (MJ/kg)	2.26	0.5	-3.54	-19.5	-19.5
$\nu_{O_2,k}$ (kg/kg)	0	0	0.27	1.48	1.49

6.3 Computational results

6.3.1 Base cases

A successful smouldering propagation and complete combustion of the peat sample is defined as: the smouldering front gradually propagates downwards and reaches the bottom without clear deceleration of propagation rate and temperature decrease [24]. In the present study, two base cases are first presented to demonstrate the propagation and quenching behaviour of smouldering combustion. The peat sample has a uniform dry bulk density of 150 kg/m^3 and an air-dried moisture content of 5%, the same as the peat used in our previous experiments [24]. A lateral heat transfer coefficient of $U = 0.58\ \mathrm{W/m^2K}$ was set to represent the lateral heat loss from the side boundary to the ambient. Fig. 6.3 shows the simulated temperature profiles at the same location of thermocouples, where the experimental data in [24] are presented as well for comparison. In general, a reasonably good agreement can be observed between computational predictions and experimental data. In the case of successful smouldering propagation (Fig. 6.3a-b), right after ignition (30 min), both experimental and simulated smouldering front gradually propagates downwards. The peak smouldering temperature decreases from approximately 500 ºC to 300 ºC as smouldering propagates from top to bottom. By comparison, in the case of quenching (Fig. 6.3c-d), during the ignition, the sample temperature can still reach 500 ºC, but afterwards, it decreases to ambient temperature within 10 h. Overall, the shape of predicted temperature profiles, peak temperatures, and fire spread durations are consistent with experimental observations, which demonstrates our model’s capability to simulate the propagation and quenching of smouldering combustion.

In order to better display the transient characteristics, the 2-D profiles of temperature and heat release rate (HRR) are also presented in Fig. 6.4, where the left and right sides of the symmetric plane represent the profiles of temperature and HRR, respectively. When the diameter is 12 cm (Fig. 6.4a) and the overall lateral heat transfer coefficient is 0.58 W/m^2-K, right after the ignition, a hot region with intense heat emitted emerges at the top of the sample. Afterwards, it gradually spread downwards without clear deceleration of propagation rate. At $t = 40$ h, the smouldering propagates to the bottom and eventually burns out about 90% of the original mass. For comparison, a quenching case, where the diameter of the sample decreases to 6 cm, is shown in Fig. 6.4(b). It could be seen in this case, right after the ignition, the sample temperature also reaches above 500 °C and can even propagate downwards for a certain period (from $t = 0.5\ \mathrm{h}$ to $t = 5\ \mathrm{h}$). However, after that, the temperature of the smouldering front decreases significantly with less heat emitted. At t=10 h, the smouldering is quenched at the middle of the column. All these predictions are in line with our experimental observations reported in [24].

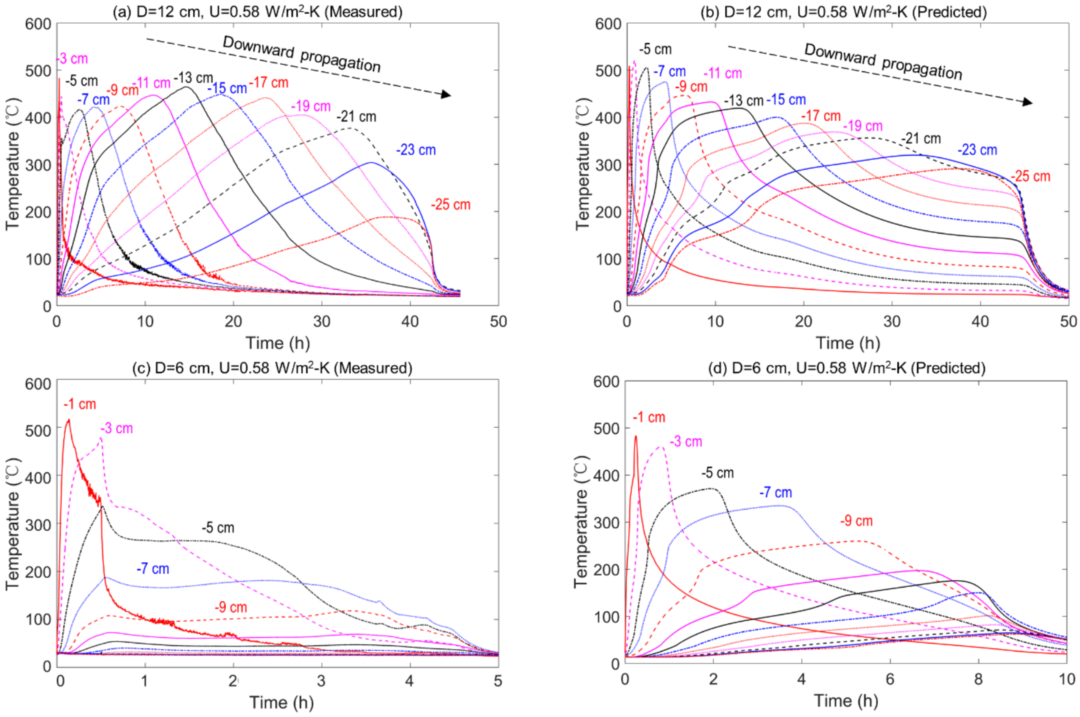

Fig. 6.3. Comparison of measured [24] and predicted temperature histories of (a-b) successful propagation sample with a diameter of 12 cm, and (c-d) failed propagation sample with a diameter of 6 cm, where the overall lateral heat transfer coefficient is 0.56 W/m^2-K.

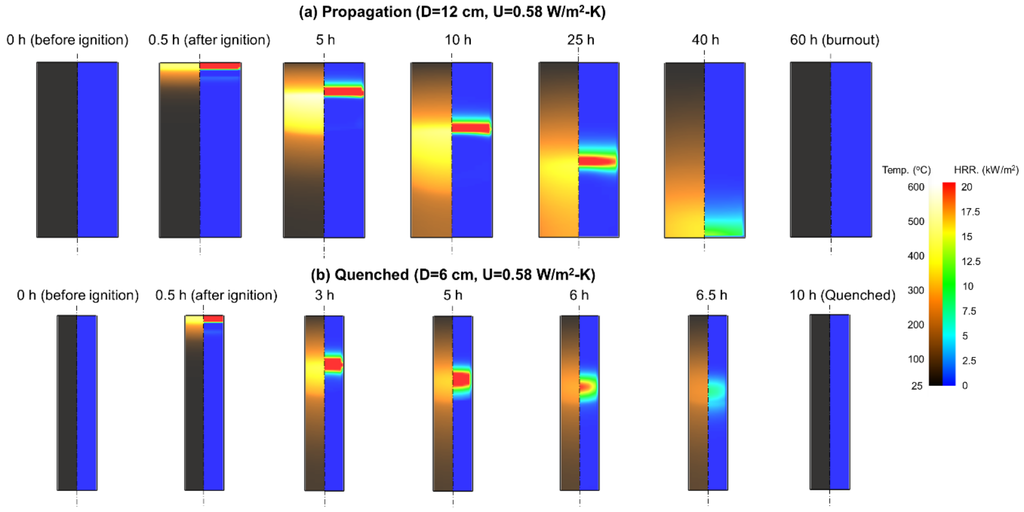

Fig. 6.4. Transient profiles of temperature and heat release rate of (a) smouldering propagation in a 25-cm high peat column with $D = 12$ cm, $U = 0.58\,\mathrm{W/m^2\cdot K}$, and (b) smouldering quenching with $D = 6$ cm, $U = 0.58\,\mathrm{W/m^2\cdot K}$.

6.3.2 Smouldering quenching diameters at different cooling conditions

Following the two base cases above, we further simulate the propagation and quenching for peat samples with different sizes and lateral heat loss coefficients to find quenching diameters at different cooling conditions. Fig. 6.5 summarizes the prediction results (dashed line) and compares with the experimental data (markers) in [24]. In general, simulations show a satisfactory agreement with experimental measurements, with an average error of less than 2 cm. The effect of lateral heat loss is also well predicted by the model; that is, the quenching diameter (*D**) increases as the lateral heat transfer coefficient (*U*) increases. For example, as *U* increases from 0.25 W/m^2-K to 2.0 W/m^2-K, *D** increases from 5±1 cm to 21±1 cm, which is 2-3 orders of magnitude larger than the scale of quenching distance of the premixed flame (~1 mm) [24,61]. These predictions agree well with our experimental measurements [24], and our model is therefore further validated.

To explain the influence of lateral heat loss on the quenching diameter, a simplified heat transfer process could be applied to a propagating smouldering front with a thickness of δ inside a duct, as illustrated in Fig. 6.2. At the extinction limit (when D=D^*), the heat released inside the duct must approximately balance with the rate of heat loss through the lateral direction ($\dot{Q}_{sm} = \dot{Q}_{loss}$) as

$$\dot{m}_F'''\Delta H\left(\frac{\pi D^{*2}}{4}\cdot\delta\right) = U\Delta T(\pi D^*\delta) \tag{6.27}$$

Rearrange Eq. 6.27, we have

$$D^* = \frac{4U\Delta T}{\dot{m}_F'''\Delta H_{sm}} = \frac{4U\Delta T}{\dot{m}_{air}'''Y_{O_2}\Delta H_{ox}} \tag{6.28}$$

where $\dot{m}_{air}'''$, Y_{O_2}, ΔH_{ox} are the volumetric air flow, mass fraction of oxygen and heat of oxidation respectively, ΔT is temperature difference between the temperature of smouldering front near the wall and ambient. From Eq. 6.28, D^* increases as U increases, successfully explaining the predicted trend in Fig. 6.5.

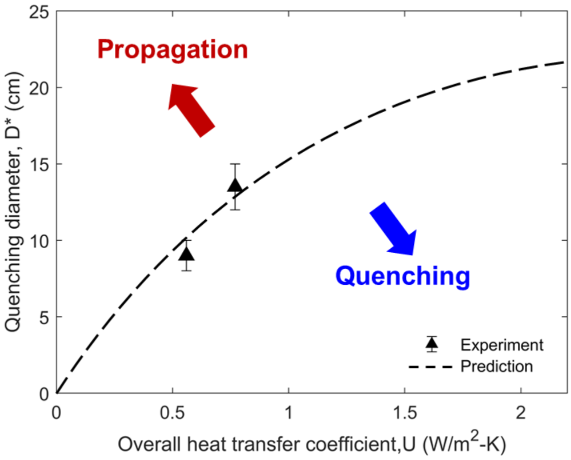

Fig. 6.5. Predicted quenching diameter of smouldering combustion vs overall heat transfer coefficient in the lateral direction, where the experimental result from Lin and Huang (2021) [24] are plotted for comparison.

6.3.3 Smouldering temperature and propagation rate

Smouldering temperature and propagation rate are two key parameters that describe the characteristics of smouldering combustion, their sensitivities to the lateral insulation and system size are thus of vital importance and are worth further investigation.

Fig. 6.6 summarizes the effect of the diameter (D) of peat column and overall lateral heat transfer coefficient (U) on the (peak) smouldering temperature (T_{sm}) and the forward propagation rate (S_{sm}). Both smouldering temperature and propagation rate increase as the diameter of the peat column increases, agreeing well with experimental measurements [24]. For example, at U=0.58 $\mathrm{W/m^2 \cdot K}$, as D increases from 10 cm to 40 cm, the smouldering temperature and propagation rate increase from 380 °C to 820 °C and 0.61 cm/h to 1.6 cm/h, respectively. The effect of lateral heat loss is also correctly predicted by the model. Both smouldering temperature and propagation rate decrease as the lateral heat loss increases. For example, at D = 20 cm, as U increases from 0.58 to 2.0 $\mathrm{W/m^2 \cdot K}$, the smouldering temperature and propagation rate decrease from 645 ºC to 370 ºC and 1.29 cm/h to 0.68 cm/h, respectively. It is worth noting that once D increases to a sufficiently large value, the sensitivity of the smouldering temperature and propagation rate to the dimension of the smouldering system and insulation property diminishes significantly. Such a size threshold may help maximize the combustion efficiency of the smouldering system and provide practical implications toward the cost-saving design of smouldering reactor [25].

On the other hand, as D decreases, both the smouldering temperature and propagation rate continuously decrease and eventually approach the critical values at the extinction limits. As shown in Fig. 6.6(b), the minimum smouldering propagation rate is predicted to be 0.5 cm/h, consistent with the experimental observation [24] and the minimum smouldering temperature is predicted to be 350 ºC, which also agrees well with the experimental measurement.

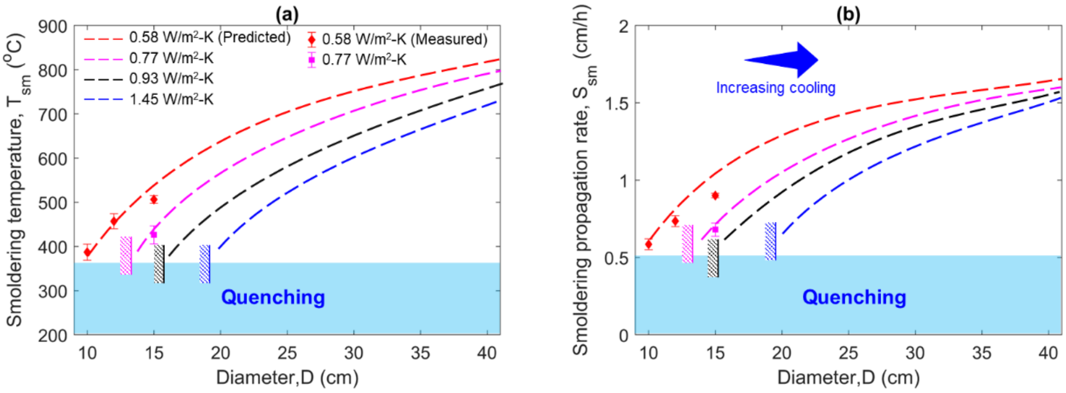

Fig. 6.6. (peak) smouldering temperature (T_{sm}) and average propagation rate (S_{sm}) as a function of the diameter of peat column (D) and overall lateral heat transfer coefficient (U), where the dashed lines represent the predicted results, and the markers represent the experimental data from [24].

6.3.4 Sensitivity to ambient temperature

The ambient temperatures (T_∞) are expected to vary in different scenarios. This might affect the smouldering thresholds and the quenching behaviour of smouldering combustion. Herein, the sensitivity of the quenching diameter to ambient temperature is investigated by varying T_∞ within a wide range (from 0 ºC to 200 ºC).

Computational results show that the quenching diameter of smouldering combustion (D*) decreases as the ambient temperature increases, as shown in Fig. 6.7(a). For example, at U=0.58

$\mathrm{W/m^2 \cdot K}$, the quenching diameter of smouldering combustion decreases from 13 cm to 1 cm as the initial ambient temperature increases from 0 ºC to 200 ºC. As ambient temperature increases (ΔT decreases), the heat loss to the ambient temperature decreases (Eq. 6.27). At the same time, oxidation rate and the corresponding heat-generation rate ($\dot{m}_F'''\Delta H_{sm}$) increase. These changes can lead to a smaller D^*, which can be well explained by Eq. 6.28, which shows that D^* is proportional to the temperature difference and inversely proportional to the heat-generation rate. Note that as the ambient temperature continues to increase, the quenching diameter gradually approaches zero, indicating that there would be no quenching if the heat loss to ambient becomes sufficiently small.

Moreover, Fig. 6.7 (b-c) further summarizes the predicted smouldering temperatures and propagation rates at different ambient temperatures. It is seen that T_∞ has a significant impact on both smouldering temperature and propagation rate. At D = 8 cm and U=0.58 $\mathrm{W/m^2 \cdot K}$, as T_∞ rises from 50 ºC to 200 ºC, T_{sm} increases from 400 ºC to 620 ºC. At the same time, the propagation rate increases by 4 times from 0.5 cm/h to 2.5 cm/h. Since the ambient temperature can be high in some specific scenarios (real fire situation), it is worthy to further explore the effect of ambient temperature on the propagation of smouldering combustion in future work.

6.3.5 Sensitivity to the mass fraction of oxygen

Smouldering combustion defines a lower oxygen threshold (~11%) for fire activity on Earth [45]. As oxygen supply is another critical mechanism that controls smouldering combustion, we also investigate the sensitivity of the quenching diameter of smouldering combustion to oxygen supply. Fig. 6.7(d) shows the computational predictions of the influence of mass fraction of oxygen (Y_{O_2}) on D^*. Given U=0.58 $\mathrm{W/m^2}$-K, as Y_{O_2} increases from 23.2% to 40%, D^* decreases from 13 cm to 5 cm. Therefore, a lower oxygen supply is expected to make the quenching of smouldering easier. Such a trend can also be explained by Eq. 6.28, where the quenching diameter of smouldering combustion is inversely proportional to the mass fraction of oxygen (i.e., $D^* \propto 1/Y_{O_2}$).

Also, the effect of the mass fraction of oxygen on the smouldering temperature and propagation rate is predicted and summarized in Fig. 6.7(e-f). Analogous to the increased ambient temperature, the larger mass fraction of oxygen results in a higher smouldering temperature and a larger propagation rate. Further increasing the mass fraction of oxygen or ambient temperature, the smouldering-to-flaming transition may also occur. However, such behaviour is not well modelled and may be beyond the capability of the current model.

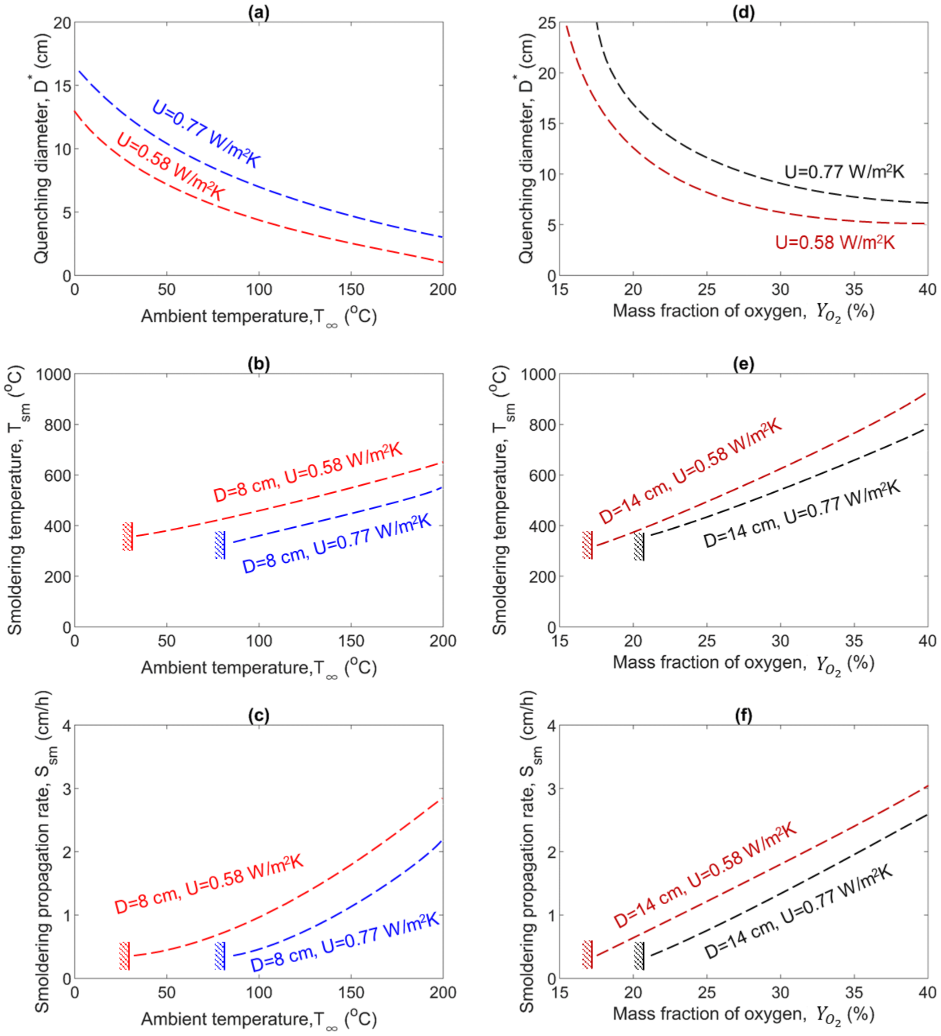

Fig. 6.7. Predicted effect of ambient temperatures (T_∞) (a-c) and mass fractions of oxygen (Y_{O_2}) (d-f) on the quenching diameters of smouldering combustion, smouldering temperature and propagation rate.

6.4 Conclusions

In this chapter, a 2-D model that simulates the smouldering of peat column is built using open-source code Gpyro. Based on this model, we computationally study the quenching diameter of smouldering combustion for the first time. The computational predictions show that the quenching diameter of smouldering combustion (D*) increases from 5±1 cm to 21±1 cm as the overall lateral heat transfer coefficient (U) increases from 0.25 W/m^2-K to 2.0 W/m^2-K, agreeing well with the experimental observation. The influence of peat column diameter (D) and the overall lateral heat transfer coefficient (U) on the smouldering temperature (T_{sm}) and propagation rate (S_{sm}) is also investigated. In general, T_{sm} and S_{sm} would increase with a larger sample diameter or less lateral heat loss, but their sensitivities diminish if D is sufficiently large. Finally, the sensitivity of quenching diameter of smouldering combustion to ambient temperature (T_∞) and mass fraction of oxygen (Y_{O_2}) is explored. It is seen that lowering T_∞ or Y_{O_2} makes the quenching of smouldering combustion significantly easier. The influence of T_∞ and Y_{O_2} on the propagation and quenching of smouldering is of both practical and theoretical importance, it is worthy to further study them in future work. This is the first time to use a comprehensive physics-based model to predict the quenching behaviour of smouldering combustion at different ambient conditions, thus helping understand the persistence and extinction limit of smouldering and support the prevention and suppression strategies for smouldering fire.

Acknowledgements

This research is funded by the National Natural Science Foundation of China (NSFC) No. 51876183, RGC Postdoctoral Fellowship Scheme, and the Society of Fire Protection Engineers (SFPE) Educational & Scientific Foundation. S. Lin would like to thank Dr H. Yuan for sharing the use of Gpyro. Warm helps from Atif Ali Khan, Zhuojun Nan, and Peiyi Sun (Hong Kong PolyU) are also well acknowledged.

References

[1] Ohlemiller TJJ. Modeling of smouldering combustion propagation. Prog Energy Combust Sci 1985;11:277–310.

[2] Rein G. Smouldering Combustion. SFPE Handb Fire Prot Eng 2014;2014:581–603.

[3] Rein G. Smouldering Fires and Natural Fuels. In: Claire M. Belcher, editor. Fire Phenom. Earth Syst., New York: John Wiley & Sons, Ltd.; 2013, p. 15–34.

[4] Torero JL, Gerhard JI, Martins MF, Zanoni MAB, Rashwan TL, Brown JK. Processes defining smouldering combustion: Integrated review and synthesis. Prog Energy Combust Sci 2020;81.

[5] Lin S, Sun P, Huang X. Can peat soil support a flaming wildfire? Int J Wildl Fire 2019;28:601–13.

[6] Restuccia F, Huang X, Rein G. Self-ignition of natural fuels: Can wildfires of carbon-rich soil start by self-heating? Fire Saf J 2017;91:828–34.

[7] Yuan H, Restuccia F, Richter F, Rein G. A computational model to simulate self-heating ignition across scales, configurations, and coal origins. Fuel 2019;236:1100–9.

[8] Bar-Ilan A, Putzeys OM, Rein G, Fernandez-Pello AC, Urban DL. Transition from forward smouldering to flaming in small polyurethane foam samples. Proc Combust Inst 2005;30:2295–302.

[9] Putzeys O, Bar-Ilan A, Rein G, Fernandez-Pello AC, Urban DL. The role of secondary char oxidation in the transition from smouldering to flaming. Proc Combust Inst 2007;31 II:2669–76.

[10] Chao CYH, Wang JH. Transition from smouldering to flaming combustion of horizontally oriented flexible polyurethane foam with natural convection. Combust Flame 2001;127:2252–64.

[11] Santoso MA, Christensen EG, Yang J, Rein G. Review of the Transition From Smouldering to Flaming Combustion in Wildfires. Front Mech Eng 2019;5.

[12] Quintiere J. Principles of Fire Behaviour. New York: Alar Elken; 1997.

[13] Xie Q, Zhang Z, Lin S, Huang X, Qu Y. Smouldering Fire of High-Density Cotton Bale Under Concurrent Wind. Fire Technol 2020.

[14] Villacorta E, Haraldseid I, Mikalsen RF, Hagen BC, Erland S, Kleppe G, et al. Onset of smouldering fires in storage silos: Susceptibility to design, scenario, and material parameters. Fuel 2021;284.

[15] Huang X, Rein G. Smouldering combustion of peat in wildfires: Inverse modelling of the drying and the thermal and oxidative decomposition kinetics. Combust Flame 2014;161:1633–44.

[16] Turetsky MR, Benscoter B, Page S, Rein G, Van Der Werf GR, Watts A. Global vulnerability of peatlands to fire and carbon loss. Nat Geosci 2015;8:11–4.

[17] Zhao X, Xiao H, Wang Q, Ping P, Sun J. Study on spontaneous combustion risk of cotton using a micro-calorimeter technique. Ind Crops Prod 2013;50:383–90.

[18] Lin S, Cheung YK, Xiao Y, Huang X. Can rain suppress smouldering peat fire？Sci Total Environ 2020;727:138468.

[19] Hernandez-Soriano MC, Kerré B, Kopittke PM, Horemans B, Smoulders E. Biochar affects carbon composition and stability in soil: A combined spectroscopy-microscopy study. Sci Rep 2016;6:1–13.

[20] SA F, CC，Hardy. Modeling Smouldering Emissions From Prescribed Broadcast Burns in the Pacific-Northwest. Int J Wildl Fire 1994;4:135–42.

[21] Yermán L, Wall H, Torero JL. Experimental investigation on the destruction rates of organic waste with high moisture content by means of self-sustained smouldering combustion. Proc Combust Inst 2017;36:4419–26.

[22] Solinger R, Grant GP, Scholes GC, Murray C, Gerhard JI. STARx Hottpad for smouldering treatment of waste oil sludge: Proof of concept and sensitivity to key design parameters. Waste Manag Res 2020;38:554–66.

[23] Huang X, Gao J. A review of near-limit opposed fire spread. Fire Saf J 2020:103141.

[24] Lin S, Huang X. Quenching of smouldering: Effect of wall cooling on extinction. Proc Combust Inst 2021;38:5015–22.

[25] Rashwan TL, Torero JL, Gerhard JI. Heat losses in applied smouldering systems: Sensitivity analysis via analytical modelling. Int J Heat Mass Transf 2021;172:121150.

[26] Turns S. An Introduction to Combustion: Concepts and Applications. McGraw-Hill Education; 2011.

[27] Ganter S, Heinrich A, Meier T, Kuenne G, Jainski C, C. Rißmann M, et al. Numerical analysis of laminar methane–air side-wall-quenching. Combust Flame 2017;186:299–310.

[28] Demesoukas S, Caillol C, Higelin P, Boiarciuc A, Floch A. Near wall combustion modeling in spark ignition engines. Part A: Flame-wall interaction. Energy Convers Manag 2015;106:1426–38.

[29] Kim KT, Lee DH, Kwon S. Effects of thermal and chemical surface-flame interaction on flame quenching. Combust Flame 2006;146:19–28.

[30] Williams FA. Combustion Theory. 2nd ed. CRC Press; 1985.

[31] Quintiere JG. Fundamental of Fire Phenomena. New York: John Wiley; 2006.

[32] Rashwan TL, Torero JL, Gerhard JI. Heat losses in a smouldering system: The key role of non-uniform air flux. Combust Flame 2021;227:309–21.

[33] Lin S, Liu Y, Huang X. How to Build a Firebreak to Stop Smouldering Peat Fire : Insights from a Laboratory-Scale Study. Int J Wildl Fire 2021.

[34] Rein G. Smouldering Combustion Phenomena in Science and Technology. Rev Lit Arts Am 2009;1:3–18.

[35] Han J, Yamashita H, Hayashi N. Numerical study on the spark ignition characteristics of a methane-air mixture using detailed chemical kinetics. Effect of equivalence ratio, electrode gap distance, and electrode radius on MIE, quenching distance, and ignition delay. Combust Flame 2010;157:1414–21.

[36] Huang X, Rein G, Chen H. Computational smouldering combustion: Predicting the roles of moisture and inert contents in peat wildfires. Proc Combust Inst 2015;35:2673–81.

[37] Yang J, Chen H. Natural Downward Smouldering of Peat : Effects of Inorganic Content and Piled Bed. Fire Technol 2018.

[38] Huang X, Rein G. Upward-and-downward spread of smouldering peat fire. Proc Combust Inst 2019;37:4025–33.

[39] Huang X, Rein G. Thermochemical conversion of biomass in smouldering combustion across scales: The roles of heterogeneous kinetics, oxygen and transport phenomena. Bioresour Technol 2016;207:409–21.

[40] Huang X, Rein G. Computational study of critical moisture and depth of burn in peat fires. Int J Wildl Fire 2015;24:798–808.

[41] Huang X, Rein G. Interactions of Earth's atmospheric oxygen and fuel moisture in smouldering wildfires. Sci Total Environ 2016;572:1440–6.

[42] Huang X, Rein G. Downward Spread of Smouldering Peat Fire: the Role of Moisture, Density and Oxygen Supply. Int J Wildl Fire 2017;26:907–18.

[43] Yuan H, Restuccia F, Rein G. Spontaneous ignition of soils : a multi-step reaction scheme to simulate self-heating ignition of smouldering peat fires. Int J Wildl Fire 2021.

[44] Yang J, Chen H, Liu N. Modeling of Two-Dimensional Natural Downward Smouldering of Peat. Energy and Fuels 2016;30:8765–75.

[45] Yang J, Liu N, Chen H, Gao W, Tu R. Effects of atmospheric oxygen on horizontal peat smouldering fires: Experimental and numerical study. Proc Combust Inst 2018;000:1–9.

[46] Di Blasi C. Mechanisms of Two-Dimensional Smouldering Propagation through Packed Fuel Beds. Combust Sci Technol 1995;106:103–24.

[47] Han Y, Richter F, Rein G. A multi-step reaction scheme to simulate self-heating ignition of coal: Effects of oxygen adsorption and smouldering combustion. Proc Combust Inst 2020;38:4717–25.

[48] Yuan H, Restuccia F, Rein G. Computational study on self-heating ignition and smouldering spread of coal layers in flat and wedge hot plate configurations. Combust Flame 2020;214:346–57.

[49] Rein G, Carlos Fernandez-Pello a., Urban DL. Computational model of forward and opposed smouldering combustion in microgravity. Proc Combust Inst 2007;31:2677–84.

[50] He F, Zobel N, Zha W, Behrendt F. Effects of physical properties on one-dimensional downward

smouldering of char: Numerical analysis. Biomass and Bioenergy 2009;33:1019–29.

[51] Lautenberger C. Gpyro-A Generalized Pyrolysis Model for Combustible Solids: Users'Guide. Berkeley: 2016.

[52] Lautenberger C. Gpyro-A Generalized Pyrolysis Model for Combustible Solids:Technical Reference. Berkeley: 2014.

[53] Incropera FP. Principles of heat and mass transfer. John Wiley; 2007.

[54] Huang X, Restuccia F, Gramola M, Rein G. Experimental study of the formation and collapse of an overhang in the lateral spread of smouldering peat fires. Combust Flame 2016;168:393–402.

[55] Richter F, Atreya A, Kotsovinos P, Rein G. The effect of chemical composition on the charring of wood across scales. Proc Combust Inst 2019;37:4053–61.

[56] Richter F, Rein G. A multiscale model of wood pyrolysis in fire to study the roles of chemistry and heat transfer at the mesoscale. Combust Flame 2020;216:316–25.

[57] Huang X, Li K, Zhang H. Modelling bench-scale fire on engineered wood : Effects of transient flame and physicochemical properties. Proc Combust Inst 2017;36:3167–75.

[58] Lautenberger C, Fernandez-Pello C. Generalized pyrolysis model for combustible solids. Fire Saf J 2009;44:819–39.

[59] Epstein N. On tortuosity and the tortuosity factor in flow and diffusion through porous media. Chem Eng Sci 1989;44:777–9.

[60] De Jonge H, Mittelmeljer-Hazeleger MC. Adsorption of CO2 and N2 on soil organic matter: Nature of porosity, surface area, and diffusion mechanism. Environ Sci Technol 1996;30:408–13.

[61] Williams FA. Combustion Theory. 2nd ed. California: The Benjamin/Cummings Publishing Company, Inc.; 1985.

CHAPTER 7: Firebreak for Smouldering Wildfires: from Combustion Theory to Firefighting Application

Summary

Smouldering wildfire is an important disturbance to peatlands worldwide, and it contributes significantly to global carbon emissions and provides positive feedback to climate change. Herein, we explore the feasibility of firebreaks to control smouldering peat fires through laboratory-scale experiments. The dry-mass moisture content (MC) of peat soil varied from 10% (air-dried) to 125%. We found that smouldering peat fire may be successfully extinguished above the mineral soil layer, even if the peat layer is not entirely removed. There are two criteria for an effective peat firebreak: (I) adding water to make the peat layer sufficiently wet (> 115% MC in the present work), and (II) ensuring that the peat layer is thinner than the quenching thickness (< 5 cm). Criterion I may fail if the water table declines or the peat layer is dried by surface fires and hot weather, thus satisfying Criterion II is more attainable. A sloped, trench-shaped firebreak is recommended to guide water flow and help maintain high peat moisture content. This work provides a scientific foundation for fighting and mitigating smouldering wildfires and guides protective measures for field-scale peat fire experiments.

This chapter is based on "S. Lin, Y. Liu and X. Huang (2021) *How to Build a Firebreak to Stop Smouldering Peat Fire: Insight from a Laboratory-Scale Study.* **International Journal of Wildland Fire** 30(6): 454-461. doi: 10.1071/WF20155."

7.1 Introduction

Smouldering fire is slow-moving, low-temperature, and flameless, and is the driving burning phenomenon in global peatlands and an important disturbance to the global ecosystem [1–4]. Although peatland only covers 2-3% of Earth's land surface, it is a significant carbon sink, holding approximately 25% of the planet's terrestrial soil carbon, close to the carbon amount in the atmosphere [5]. Therefore, peat fire is a global source of carbon emissions and the leading cause of regional haze events, especially in Southeast Asia and boreal regions [4,6,7]. In 2019, slash-and-burn activities in Indonesia accidentally resulted in peatland wildfires that burned for several months, producing a thick and hazardous smoke layer over Indonesia and nearby countries that posed severe health issues to a large population [8].

In recent decades, global warming has increased fire frequency and severity in peatlands; therefore, fire regimes have changed [9–11]. Once ignited, despite extensive rain or other firefighting attempts, smouldering peat fire may burn for months and even for years [1,12,13]. Many research efforts have been targeted to understand the characteristics of smouldering peat fire, such as combustion chemistry [14], ignition [15–17], fire spread [18–24] and emissions [6,25–31]. However, compared with these profound studies on ignition and fire behaviour, very few studies are available to control and extinguish these persistent smouldering wildfires [13].

With respect to the fire triangle, three methods can be applied to extinguish a fire, namely starving (by removing the fuel), smothering (by removing the oxygen), and cooling (or quenching by removing the heat) [32]. To suppress large-scale peat fires, except for cooling, neither starving nor smothering is practical [13,33]. In real fire scenarios, if the peat is sufficiently wet with dry-mass moisture content (MC_p) higher than 100~200%, it can be protected by its own moisture, which could be defined as the *peat fire threshold* [15,16,22,34,35]. Today, water is still the most widely-used cooling agent in fighting peat fires [36–38]. However, water is not always accessible near the fire scene, and firefighting operations are risky due to the extreme heat and smoke [39]. In practice, building a firebreak or barrier could be more effective in controlling and mitigating the hidden peat fires [40], as illustrated in Fig. 7.1. For example, to suppress a peat fire in Scotland in 2008, the Fire Service and Regional Army dug a trench as the firebreak which was 5 m wide and 0.5–2 m deep (down to the mineral soil layer) around the perimeter of the fire by excavating peat soils [1].

The firebreak, also known as the fireguard, is built to prevent the fire from escaping existing burning regions, which is widely used in the fire protection of wildland-urban interface (WUI) and prescribed fires [41,42]. A conventional firebreak is a strip of land denuded of all flammable materials. It may be constructed with a grader, plough, excavator, or just a shovel before or during the wildfire [43]. Such a firebreak is designed based on the knowledge of flaming ignition to prevent flame spread and the proliferation of firebrands, so it may not be effective in controlling smouldering wildfires [44].

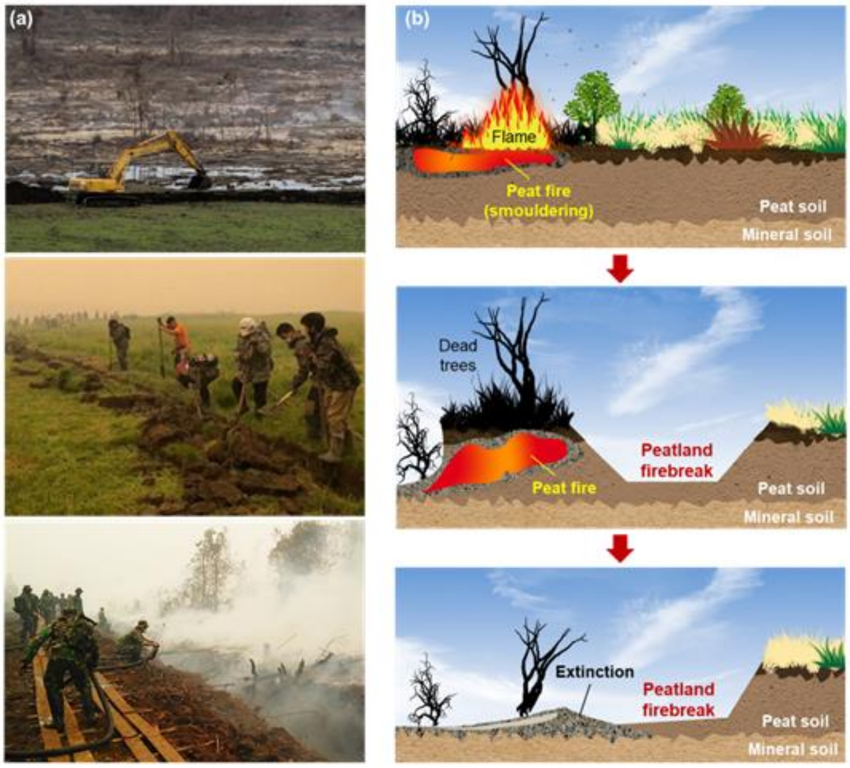

Fig. 7.1 (a) Practices of making a firebreak to control peat fires (Credit: Rob Gunstone, Ignacio Villaverde), and (b) schematics of smouldering fire in peatland and the concept of making a trench-shaped firebreak.

Considering the massive scale of peatlands and underground fires, digging a trench into the peat soil layer to make a firebreak is a quite costly process in practice (see Fig. 7.1). If the trench is too shallow and a thick peat layer remains, the smouldering fire can still cross the firebreak. One the other hand, if the trench is made too deep, valuable time and human resources are wasted, especially during an urgent peat fire event. As the thickness of the peat layer varies in the field, it is challenging to design and build a firebreak for peatlands in the scale of km that balances the effectiveness and cost. To the best of the authors' knowledge, no study has explored the feasibility and reliability of firebreaks in controlling smouldering peat fires; thus there is a significant knowledge gap.

This work aims to explore the applicability and minimum requirements of a firebreak for smouldering peat fires through laboratory-scale experiments. A trench-shaped firebreak was built above a mineral sand layer to mimic a real firebreak in peatlands. The maximum thickness of the remaining peat layer was explored under the principles of cooling or quenching, (I) by peat moisture and (II) by underlying mineral layer. The research outcomes provide a scientific foundation for underground wildfire fighting and the design criteria for the protective measures of large-scale peat fire experiments in the field.

7.2 Experimental methods

Ideally, for a firebreak, if all organic peat soils are entirely removed, and only the mineral soil layer remains, the smouldering fire can be well confined. However, the real thickness of the peat layer is not uniform, and the soil moisture profile and inorganic content vary greatly with locations. Moreover, it is practically impossible to quickly identify the peat layer's thickness or remove it completely. Nevertheless, even if the peat layer is not entirely removed, as long as the remaining peat layer is wet and thin enough, the smouldering fire can be quenched by its moisture or the bottom mineral soil layer [33,45]. Thus, the laboratory experiments aim to determine the remaining peat layer's maximum thickness to break the smouldering peat fire successfully.

The tested organic-rich (~97%) peat soil was moss peat from Estonia (see Fig. 7.2a), which had been used in a series of previous studies [13,17,33,38]. Such a high-organic peat soil has the highest smouldering fire risk, which defines the worst peat fire scenario. Therefore, the criteria for breaking smouldering fire in this peat can guarantee effectiveness in other peat soils with lower organic contents. The peat soil was first oven-dried at 90 °C for 48 h, and the dry bulk density was measured to be 145 $kg \cdot m^{-3}$. The element analysis shows a mass fraction of 44.2 (C), 6.1 (H), 49.1 (O), 0.5 (N), 0.1(S) % [17]. Once the dried peat was exposed to ambient, it immediately absorbed the air moisture to reach a new equilibrium with $MC_p \approx 10\%$, defined as the air-dried peat. To obtain the desired MC_p, the oven-dried peat was mixed with the corresponding amount of water [17,46]. Afterwards, the sample was shaken and left in a sealed box to equilibrate and homogenate. For wet peat samples, the MC_p ranged from 25% to 125%, with an interval of 25%, where the uncertainty was within 5%.

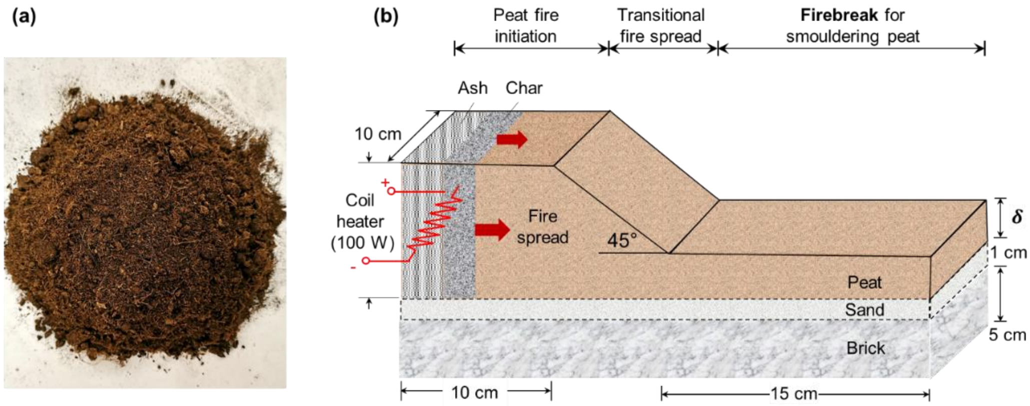

Fig. 7.2 (a) Photos of moss peat soil tested in this experiment, and (b) schematics of the experimental design.

A top-open smouldering reactor was designed to mimic a trench-shaped firebreak, as shown in Fig. 7.2b. All sides of the reactor were made of metal mesh to provide support and sufficient oxygen to the soil layer. Below the peat layer, there was a 1-cm layer of fine mineral sand plus a brick to simulate the mineral soil layers. The dry bulk density of sand was approximately 1,500 $kg \cdot m^{-3}$. The sands with three different moisture contents (MC_s) were selected to vary the bottom cooling condition: (i) weak cooling $MC_s \approx 0\%$ (dry sand), (ii) medium cooling $MC_s = 15\%$ (wet sand), and (iii) strong cooling, $MC_s = 30\%$ (saturated sand). Note that sand is ten times denser than peat soil, so the absolute mass of water in mineral sands with $MC_s = 15\%$ is still higher than that in peat soils with $MC_p = 125\%$.

A 10-cm coil heater was buried 5 cm below the top free surface and attached to the left-hand side to initiate a consistent and robust smouldering fire. The ignition protocol was set at 100 W for 30 min, which was strong enough to initiate a robust smouldering fire [18]. Initially, the peat sample thickness was 10 cm, and the peat soil was left to burn and spread laterally for 10 cm to self-stabilize (see Fig. 7.2b). Considering the structural safety and stability of firebreaks in the field [47], instead of a right-angle transition to the lower-level firebreak section, a sloped wedge transition section (45°) was designed to prevent landslide.

The effective length of the simulated firebreak was 15 cm, and the thickness of the peat layer (δ_p) was varied from 1 cm to 9 cm, referring to our previous work [33]. If smouldering fire successfully spread for 15 cm without clear deceleration but ultimately burned through the peat layer, the tested thickness was then gradually decreased at an interval of 2 cm until successfully breaking/quenching the fire. Then, the maximum thickness of the peat layer allowed for the firebreak (δ_p^*) could be obtained.

Afterwards, the influence of the soil moisture profile (i.e., both MC_p and MC_s) was also explored. Throughout these experiments, the ambient temperature was 23±2 °C, and the relative humidity was about 50 ±10%. For each scenario, tests were repeated at least twice, and for tests near the limits, three or four repeating tests were conducted to ensure repeatability. Our results showed excellent repeatability roughly because of the use of commercial peat soil with uniform density, particle size, and organic content [38]. In total, about 250 experiments were conducted to explore the minimum requirements of an effective firebreak.

7.3 Results and discussion

7.3.1 Phenomena of peat fire spread and extinction

As the peat moisture content was increased to 125%, the spread of smouldering peat fire was no longer sustained, regardless of the thickness of the peat layers. In the literature, fire extinction due to high peat moisture content (Quenching Type I) has been widely observed, and the maximum value of MC_p varies with the type of peat soil burned and the wildfire conditions [15,16,22,35]. For this specific peat soil, the maximum peat moisture or the *fire threshold* is about $MC_p \approx 115\%$. Note that for downward fire spread, the maximum MC_p could be higher because of the heat insulation provided by the top ash layer [48,49].

Figure 7.3 compares the effect of remaining peat-layer thicknesses (δ_p) on breaking the smouldering peat fire. After the 0.5-h ignition process, a robust smouldering fire gradually spread forward for 10 cm before passing through the transitional wedge section. Then, in the transitional area, the fire front would slow down and self-adjust. Afterwards, the smouldering fire entered the firebreak section and attempted to spread. For the failed firebreak with a thickness of 7 cm, 50% MC_p, and 30% MC_s (Fig. 7.3), the smouldering fire successfully spread forward without a clear deceleration process. Eventually, the organic peat layer was consumed and turned into ash. Further extending the firebreak length over 15 cm, the smouldering fire could still spread across the firebreak. In other words, this firebreak could not stop/break the peat fire, because the remaining layer of organic soil in the firebreak was not thin enough to be quenched by the mineral layer.

As the remaining thickness of peat layers was decreased to 1 cm (Fig. 7.3b), the smouldering fire could no longer spread after passing through the transition section. Instead, the smouldering fire front was entirely stopped and extinguished within 5 cm into the firebreak. Therefore, as long as the remaining peat layer is thin enough, the smouldering fire could be quenched by the underlying cold mineral soil layer (Quenching Type II). The scientific principle of the smouldering quenching process was demonstrated previously [33].

7.3.2 Limiting conditions of peatland firebreak

The experimental outcomes of firebreaks are summarized in Fig. 7.4a-c with different peat-layer thicknesses (δ_p) and soil layer moisture profiles ($\mathrm{MC_p}$ and $\mathrm{MC_s}$), where '○' and '×' represent the spread and extinction of smouldering fire, respectively. First of all, no fire was sustained if the peat moisture was above 115% (Quench Type I).

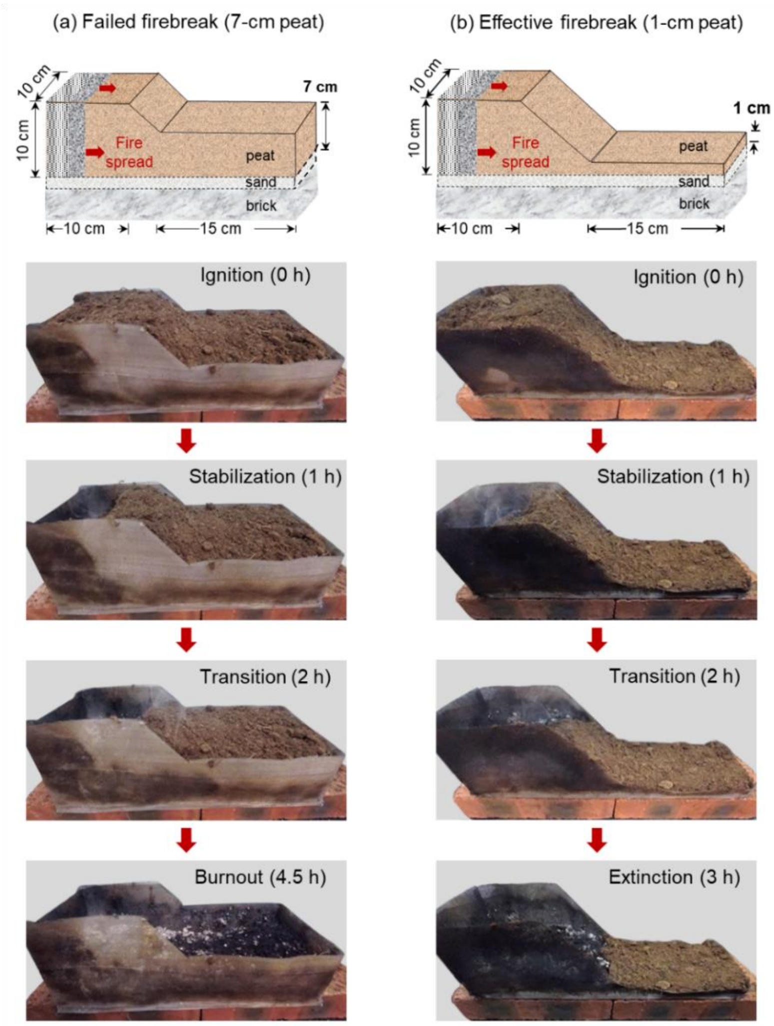

Fig. 7.3 Snapshots of the smouldering peat fire spread in the laboratory-scale firebreak, (a) failed firebreak with 7-cm thick peat layer, 50% $\mathrm{MC_p}$, and 30% $\mathrm{MC_s}$, and (b) successful firebreak where fire extinction due to cooling with 1-cm thick peat layer, 50% $\mathrm{MC_p}$, and 30% $\mathrm{MC_s}$

Secondly, the quenching (or breaking) of smouldering peat fire also occurred if the thickness of the peat layer (δ_p) in the firebreak decreased, due to the cooling from the underlying mineral soil layer (Quenching Type II). As the mineral layer got wetter or the value of MC_s increased, a thicker peat layer was needed to maintain the fire spread, because of the increased cooling from the bottom mineral layer, as shown in Fig. 7.4a-c and further compared in Fig. 7.4d. Specifically, for air-dried peat ($MC_p = 10\%$), the dry mineral soil layer was difficult to quench the peat fire (Fig. 7.4a), unless the peat layer was entirely removed. On the other hand, for a saturated mineral soil layer, the smouldering fire can be well isolated, even if the peat layer above was 2 cm (Fig. 7.4c).

Moreover, both quenching effects emerged for smouldering spread over a wetter peat layer. Then, the maximum peat thickness allowed to remain in the firebreak (δ_p^*) increased with the moisture content of peat (MC_p) and substrate mineral sand (MC_s). In other words, a wetter soil profile made the quenching of smouldering fire easier. For example, when the mineral sand layer was saturated, as MC_p increased from 10% to 100%, the value of δ_p^* increased from 1 cm to 7 cm. Therefore, in the practice of digging the break against the peat fire, as long as the remaining peat layer in the firebreak is wet and less than 5-10 cm (depending on soil types), the firebreak will be relatively effective.

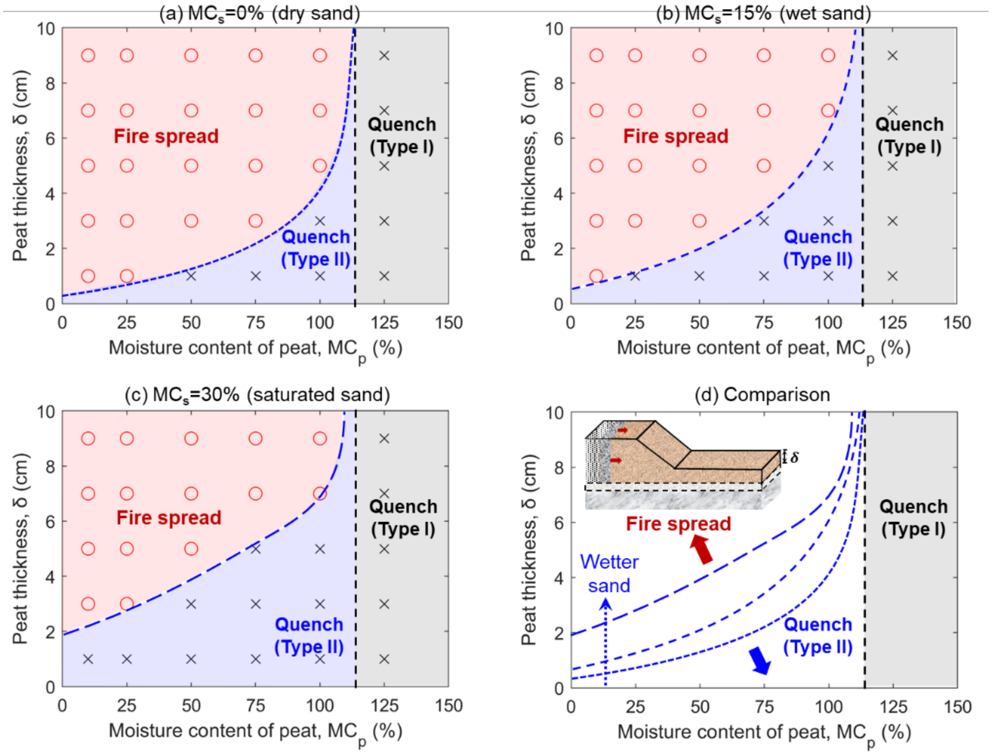

Fig. 7.4. Experimental outcomes of the peat fire spread in the firebreaks with different MCs of peat soils and inorganic sands (fire spread '○' and quenching '×').

7.3.3 Limiting conditions of peatland firebreak

To scientifically understand the influence of the soil moisture profile on the required thickness of smouldering firebreaks in peatlands, an approximate and simplified heat transfer analysis based on the energy conservation equation can be adopted. The smouldering region in the firebreak is chosen as the control volume, similar to Lin and Huang (2020a). Figure 7.5 illustrates the energy balance for a horizontally propagating smouldering front within the firebreak where the peat layer has a thickness of δ_p. At the extinction limit (δ_p^*), the net heat released from the smouldering fire region ($\dot{Q}_{sm}$) should just overcome the heat loss to the ambient atmosphere ($\dot{q}''_{\infty}$) and conduction to the bottom mineral soil layer ($\dot{q}''_{cond}$), as well as enabling the evaporation of the peat moisture ($\dot{Q}_{ev}$). That is,

$$(\dot{q}''_{\infty} + \dot{q}''_{cond})\Delta x = \dot{Q}_{sm} + \dot{Q}_{ev} = \dot{m}''_F \delta_p^* \left(\Delta H_{sm}^* - MC_p \Delta H_{ev}\right) \tag{7.1}$$

where Δx is the length of the smouldering front that is comparable to δ_p^* [33]; $\dot{m}''_F$ is the mass-loss flux of burning peat; and ΔH_{sm}^* is the heat of smouldering combustion of peat, where the combustion process is weak and incomplete at the near-extinction temperature of 250~300 °C.

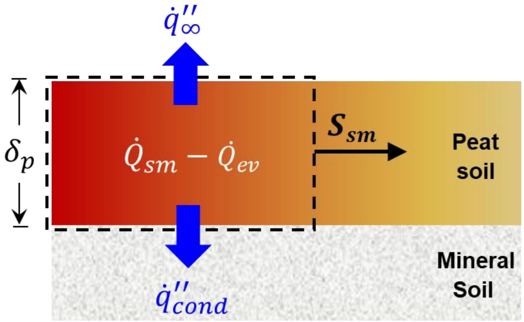

Fig. 7.5. Schematics for the energy balance for a horizontally propagating smouldering front.

If the entire peat and mineral layers are dry, the fire risk within the firebreak is the highest, although such a scenario may be rare in nature. Thus, smouldering fire can spread across the firebreak even with a very thin peat layer. This thinnest limit of the peat layer ($\delta_{p,min}^*$) is

$$(\dot{q}''_{\infty} + \dot{q}''_{cond})\Delta x = \dot{m}''_F \delta_{p,min}^* \Delta H_{sm}^* \tag{7.2}$$

By dividing Eq. (7.2) by Eq. (7.3), we have

$$\delta_p^* = \delta_{p,min}^* + \frac{\delta_{p,min}^* \Delta H_{ev}}{\Delta H_{sm}^* - \mathrm{MC_p} \Delta H_{ev}} \mathrm{MC_p} \tag{7.3}$$

where the maximum peat moisture for smouldering (or the limit of Quenching Type I) is

$$\mathrm{MC}_{\mathrm{p,\,max}} = \frac{\Delta H_{sm}^{*}}{\Delta H_{ev}} \tag{7.4}$$

Eq. 7.3 predicts that as the peat becomes wetter (i.e., a larger $\mathrm{MC_p}$), the limiting thickness of the firebreak first increases almost linearly. When the peat moisture approaches the limit of Quenching Type I ($\mathrm{MC_{p,max}}$), the thickness of the peat layer becomes irrelevant, which agrees with the test data in Fig. 7.4.

The influence of sand moisture is reflected by the bottom heat conduction ($\dot{q}''_{cond}$), which is used to evaporate the water of the sand layer within a thermal-penetration thickness of δ_s as

$$\dot{q}''_{cond}\Delta x = \dot{m}''_{w}\delta_s\Delta H_{ev} = \rho_s S_{sm}^{*} MC_s \delta_s \Delta H_{ev} \propto MC_s \tag{7.5}$$

where $S_{sm}^{*} \approx 0.1$ mm/min is the minimum spread rate of the peat fire [33]. By substituting Eq. 7.5 into Eq. 7.2 and Eq. 7.3, we have

$$\delta_p^{*} \propto \delta_{p,min}^{*} \propto MC_s \tag{7.6}$$

Therefore, as the bottom sand moisture content (MC_s) increases, the smouldering fire is more vulnerable to extinction, even if the thicker peat layer remains. In short, the proposed heat-transfer analysis successfully explains the experimental results in Fig. 7.4d.

7.3.4 Implication of peatland firebreak in practice

Ideally, as long as $\mathrm{MC_p}$ is beyond the *fire threshold* (or it is sufficiently wet), the smouldering fire can be effectively isolated and even self-extinguished, which is regarded as a successful peatland firebreak based on Criterion I. However, in the real peat fire scenario, wetting the peatland by rain or firefighting water spray may become invalid, considering a peat fire can last for weeks or even months. On the other hand, a wet soil layer can be quickly dried by surficial flaming front or slowly dried by sunshine and hot weather. If the peatland firebreak is dried before the peat fire is entirely suppressed, it can no longer isolate the burning area or break the smouldering peat fire.

Therefore, the most effective and reliable peatland firebreak needs to satisfy Criterion II, that is, removing the majority of peat layers and ensuring the thickness of the remaining peat layer in the firebreak is less than 5 cm. Then, without removing the entire peat soil layer, the firebreak can prevent the hidden peat fire from creeping cross the firebreak and escaping from the burning zone, regardless of the weather change. Moreover, the sloped, trench-shaped firebreak is recommended, as the sloped wedge creates a transition to weaken smouldering intensity, slow down fire spread, and avoid landslide or collapse [47] in situ. The trench-shaped firebreak can also guide the water to flow into the firebreak like the drainage systems [50], which helps maintain a high water table and keep the peat soil layers wetter than the *fire threshold*.

The proposed design criteria of peat firebreaks can be applied to control real smouldering wildfires and offer a protective measure for field-scale peatland fire experiments. For peatland managers and firefighters, different layers of fire protection measures may be considered. Note that as the peat is heterogeneous in nature, the borderline of the quench/spread curves has some uncertainty. Therefore, it is recommended to sample peat soils and conduct small-scale experiments to identify their *fire threshold* in terms of moisture contents ($\mathrm{MC}_{\mathrm{p,\,max}}$). Then, the thickness of the peat layer and moisture profile of the entire soil layer at different locations should be determined, so that different fire zones with similar fire hazards may be divided. Afterwards, referring to the criteria in Fig. 7.4, precautionary firebreaks can be created along with the areas with a thin and wet peat layer to minimize the cost and workforce. Finally, the trench-shaped firebreak can be quickly constructed by excavating the minimum amount of peat layer and adding a minimum amount of water, which saves the firefighting resource and maximizes efficiency. However, this firebreak method would not be simply upscaled for flaming wildfires, as firebrands may easily break through most firebreaks. Large-scale peat fire experiments in the field and more firefighting practices are required to develop scientific guidelines for peat firebreaks.

7.4 Conclusions

In this work, we conducted bench-scale peat fire experiments to explore the scientific foundation and design criteria for constructing peatland firebreaks. We found that the smouldering peat fire can be successfully isolated above the mineral soil layer, even if the peat layer is not completely removed. There are two criteria for an effective peat firebreak: (I) adding water to make the peat layer sufficiently wet (> 115% MC in the present work), and (II) ensuring the peat layer is thinner than the quenching thickness (< 5 cm). Criterion I may fail if the water table declines or the peat layer is dried by the hot weather and surface fires; thus, satisfying Criterion II is more reliable.

Moreover, the sloped, trench-shaped firebreak is recommended to avoid a landslide and guide the water flow to keep the peat layer wet. This work provides a scientific foundation for fighting and mitigating underground wildfires and guides protective measures for field-scale peat fire tests. Future research should quantify the influence of inorganic content and ambient temperature on the design of peatland firebreaks and verify the effectiveness of firebreaks in real peatland wildfires.

Acknowledgements

This work is funded by the National Natural Science Foundation of China (No. 51876183) and the Society of Fire Protection Engineers (SFPE) Educational & Scientific Foundation. S. Lin would like to thank the warm help of Y. Liu for the help in the lab.

References

[1] Rein G. Smouldering Fires and Natural Fuels. In: Claire M. Belcher, editor. Fire Phenom. Earth Syst., New York: John Wiley & Sons, Ltd.; 2013, p. 15–34.

[2] Turetsky MR, Benscoter B, Page S, Rein G, Van Der Werf GR, Watts A. Global vulnerability of peatlands to fire and carbon loss. Nat Geosci 2015;8:11–4.

[3] Turetsky M, Wieder K, Halsey L, Vitt D. Current disturbance and the diminishing peatland carbon sink. Geophys Res Lett 2002;29:7–10.

[4] Page SE, Siegert F, Rieley JO, Boehm H V., Jayak A, Limink S, et al. The amount of carbon released from peat and forest fires in Indonesia during 1997. Nature 2002;420:61–6.

[5] Gorham E. The future of research in canadian peatlands: A brief survey with particular reference to global change. Wetlands 1994;14:206–15.

[6] Poulter B, Christensen NL, Halpin PN. Carbon emissions from a temperate peat fire and its relevance to interannual variability of trace atmospheric greenhouse gases. J Geophys Res Atmos 2006;111:1–11.

[7] Moreno L, Jiménez ME, Aguilera H, Jiménez P, de la Losa A. The 2009 Smouldering Peat Fire in Las Tablas de Daimiel National Park (Spain). Fire Technol 2011;47:519–38.

[8] Normile D. Indonesia’s fires are bad, but new measures prevented them from becoming worse. Science (80-) 2019.

[9] Kohlenberg AJ, Turetsky MR, Thompson DK, Branfireun BA, Mitchell CPJ. Controls on boreal peat combustion and resulting emissions of carbon and mercury. Environ Res Lett 2018;13.

[10] Mack MC, Bret-Harte MS, Hollingsworth TN, Jandt RR, Schuur EAG, Shaver GR, et al. Carbon loss from an unprecedented Arctic tundra wildfire. Nature 2011;475:489–92.

[11] Liu Y, Stanturf J, Goodrick S. Trends in global wildfire potential in a changing climate. For Ecol Manage 2010;259:685–97.

[12] Ballhorn U, Siegert F, Mason M, Limin S. Derivation of burn scar depths and estimation of carbon emissions with LIDAR in Indonesian peatlands. Proc Natl Acad Sci 2009;106:21213–8.

[13] Lin S, Cheung YK, Xiao Y, Huang X. Can rain suppress smouldering peat fire ? Sci Total Environ 2020;727:138468.

[14] Huang X, Rein G. Smouldering combustion of peat in wildfires: Inverse modelling of the drying and the thermal and oxidative decomposition kinetics. Combust Flame 2014;161:1633–44.

[15] Frandsen WH. The influence of moisture and mineral soil on the combustion limits of smouldering forest duff. Can J For Res 1987;16:1540–4.

[16] Frandsen WH. Ignition probability of organic soils. Can J For Res 1997;27:1471–7.

[17] Lin S, Sun P, Huang X. Can peat soil support a flaming wildfire? Int J Wildl Fire 2019;28:601–13.

[18] Huang X, Restuccia F, Gramola M, Rein G. Experimental study of the formation and collapse of an overhang in the lateral spread of smouldering peat fires. Combust Flame 2016;168:393–402.

[19] Huang X, Rein G. Downward Spread of Smouldering Peat Fire: the Role of Moisture, Density and Oxygen Supply. Int J Wildl Fire 2017;26:907–18.

[20] Huang X, Rein G. Upward-and-downward spread of smouldering peat fire. Proc Combust Inst 2019;37:4025–33.

[21] Christensen EG, Fernandez-Anez N, Rein G. Influence of soil conditions on the multidimensional spread of smouldering combustion in shallow layers. Combust Flame 2020;214:361–70.

[22] Prat-Guitart N, Rein G, Hadden RM, Belcher CM, Yearsley JM. Propagation probability and spread rates of self-sustained smouldering fires under controlled moisture content and bulk density conditions. Int J Wildl Fire 2016;25:456–65.

[23] Palamba P, Allo R, Kosasih E, Nugroho Y. Effect of surface dry layer thickness on the smouldering combustion of a stratified moisture content peat layer. Int J Adv Sci Technol 2020;29:2117–39.

[24] Yang J, Chen H. Natural Downward Smouldering of Peat : Effects of Inorganic Content and Piled Bed. Fire Technol 2018.

[25] Hu Y, Christensen E, Restuccia F, Rein G. Transient gas and particle emissions from smouldering combustion of peat. Proc Combust Inst 2019;37:4035–42.

[26] Hu Y, Fernandez-Anez N, Smith TEL, Rein G. Review of emissions from smouldering peat fires and their contribution to regional haze episodes. Int J Wildl Fire 2018;27(5):293.

[27] Black RR, Aurell J, Holder A, George IJ, Gullett BK, Hays MD, et al. Characterization of gas and particle emissions from laboratory burns of peat. Atmos Environ 2016;132:49–57.

[28] Rein G, Cohen S, Simeoni A. Carbon emissions from smouldering peat in shallow and strong fronts. Proc Combust Inst 2009;32 II:2489–96.

[29] Wakhid N, Hirano T, Okimoto Y, Nurzakiah S, Nursyamsi D. Soil carbon dioxide emissions from a rubber plantation on tropical peat. Sci Total Environ 2017;581–582:857–65.

[30] Heil A, Langmann B. Release and dispersion of vegetation and peat fire emissions in the atmosphere over Indonesia 1997/1998. Atmos Chem Phys 2004;4:2145–60.

[31] Aurell J, Hays MD, George IJ, Geron CD, Black RR, Preston WT, et al. Volatile and semivolatile organic compounds in laboratory peat fire emissions. Atmos Environ 2016;132:163–70.

[32] Quintiere JG. Fundamental of Fire Phenomena. New York: John Wiley; 2006.

[33] Lin S, Huang X. Quenching of smouldering: Effect of wall cooling on extinction. Proc Combust Inst 2021;38:5015–22.

[34] Huang X, Rein G. Computational study of critical moisture and depth of burn in peat fires. Int J Wildl Fire 2015;24:798–808.

[35] Huang X, Rein G. Interactions of Earth's atmospheric oxygen and fuel moisture in smouldering wildfires. Sci Total Environ 2016;572:1440–6.

[36] Ramadhan ML, Palamba P, Imran FA, Kosasih EA, Nugroho YS. Experimental study of the effect of water spray on the spread of smouldering in Indonesian peat fires. Fire Saf J 2017;91:671–9.

[37] Blake D, Lu K, Horwitz P, Boyce MC. Fire suppression and burnt sediments: Effects on the water chemistry of fire-affected wetlands. Int J Wildl Fire 2012;21:557–61.

[38] Lin S, Huang X. An experimental method to investigate the water-based suppression of smouldering peat fire. MethodsX 2020;7.

[39] Saharjo BH. What it takes to put out forest fires. The Concersation 2019.

[40] Migalenko K, Nuianzin V, Aleksandr Z, Andrii D, Pozdieiev S. Development of the technique for restricting the propagation of fire in natural peat ecosystems. Eastern-European J Enterp Technol 2018;1.

[41] Weir JR, Bidwell TG, Stevens R, Mustain J. Firebreaks for Prescribed Burning 2015.

[42] DFES. A Guide to Constructing and Maintaining Fire-breaks. Gov West Autralia Dep Fire Emergeny Serv 2016.

[43] Wilson A. Width of firebread that is necessary to stop grass fires: some field experiments. Can J For Res 1988;18:682–7.

[44] Purnomo DMJ, Bonner M, Moafi S, Rein G. Using cellular automata to simulate field-scale flaming and smouldering wildfires in tropical peatlands. Proc Combust Inst 2020;000:1–9.

[45] Miyanishi K, Johnson EA. Process and patterns of duff consumption in the mixedwood boreal forest. Can J For Res 2002;32:1285–95.

[46] Christensen E, Hu Y, Restuccia F, Santoso MA. Experimental methods and scales in smouldering wildfires. In: Pereira P, editor. Fire Eff. soils State Art Methods, CSIRO; 2018, p. 267–80.

[47] Duncan JM, Wright S, Brandon T. Soil Strength and Slope Stability. New Jersey: John Wiley & Sons, Inc.; 2014.

[48] Benscoter BW, Thompson, D. K., Waddington JM, Flannigan MD, Wotton BM, de Groot WJ, Turetsky MR. Interactive effects of vegetation, soil moisture and bulk density on depth of burning of thick organic soils. Int J Wildl Fire 2011;20:418–29.

[49] Zaccone C, Rein G, D'Orazio V, Hadden RM, Belcher CM, Miano TM. Smouldering fire signatures in peat and their implications for palaeoenvironmental reconstructions. Geochim Cosmochim Acta 2014;137:134–46.

[50] Kanwar RS, Colvin TS, Melvin SW. Comparison of Trenchless Drain Plow and Trench Methods of Drainage Installation 1986:456–61.

PART C: Environmental Impacts on Smouldering Limits: Wind, Weather and Climate

Smouldering limits are sensitive to the environmental conditions. In particular, the airflow or wind is crucial to smouldering propagation, because it could increase both the oxygen supply and the heat loss. However, so far, no study has addressed the smouldering propagation at large wind speeds over 10 m/s and the blow-off limits of persistent smouldering fire. Also, for large-scale peatland fires, as the human-based firefighting may not achieve desired effect, most of the smouldering peat fires were extinguished by natural extensive rain. However, the extinction limit of smouldering peat fire under rainfall is still unclear. Moreover, owing to the climate change, the arctic and boreal regions have suffered from it worst wildfire season and longest burning duration in the form of burning organic soils. Therefore, the vulnerability of organic peat soil to the wildfires and the positive feedback of smouldering peatland fires to the global warming are worth exploring.

This part includes three chapters (8-10), with the focus of the environmental impacts on the smouldering limits. Chapter 8 quantifies the smouldering propagation rate on consolidated biomass and the blow-off limit under concurrent and opposed external airflows up to 50 m/s, where the effects of fuel diameter and density are thoroughly discussed. Chapter 9 assesses the underlying mechanism of rain in suppressing the smouldering peat fire in the shallow soil layer up to 15 cm deep through laboratory experiments, where the minimum rainfall intensity and depth to suppress smouldering peat fire is found. Chapter 10 quantifies the minimum environmental temperature that allows the moist peat to smoulder, and then apply a typical vertical soil temperature profile to estimate the future depth of burn and carbon emissions in boreal peatland fires under the impact of global warming.

CHAPTER 8: Blow-off Limits of Smouldering Fire under External Airflow

Summary:

The propagation of smouldering combustion and the blow-off limit are of practical importance in evaluating the fire dynamics of solid fuels, but the scientific understanding is still limited. In this work, we quantify the smouldering propagation rate on consolidated biomass and the blow-off limit under concurrent and opposed external airflows up to 50 m/s. The incense cylinders with different diameters (1.5-5 mm) and densities (720-1,100 kg/m^3) are tested. As the airflow velocity increases, smouldering propagation rate first increases to its maximum value (Oxygen-limited Regime), and subsequently remains stable (Thermal Regime), regardless of the airflow direction. Afterwards, it slightly decreases (Chemical Regime) until blow-off, and the blow-off of opposed smouldering is easier, similar to the pattern of flame spread. The blow-off airflow velocity (13~46 m/s) of smouldering combustion is around ten times larger than that of flaming combustion, and it decreases as the fuel diameter or density increases. This work advances the fundamental understanding of the smouldering propagation, blow-off and its persistence nature; thus, helping guide the fire suppression strategies of smouldering.

This Chapter is based on "S. Lin, T. H. Chow, and X. Huang (2021) *Smouldering Propagation and Blow-off on Consolidated Fuel under External Airflow.* **Combustion and Flame** (Accepted)".

8.1 Introduction

Smouldering is a slow, low-temperature, and flameless burning of porous fuels and one of the most persistent types of combustion phenomena [1–3]. Smouldering combustion is a heterogeneous process sustained when oxygen directly attacks the hot fuel surface, different from the flame regarding the combustion chemistry and transport processes [2,3]. Smouldering can be ignited easily by a weak heat source [2–4] or even self-ignited, which usually occur in silos and large fuel piles [5], creating a shortcut to more intensive flaming fires (through smouldering-to-flaming transition). Moreover, it is also challenging to detect and suppress the hidden smouldering fire. For example, the colossal piles of World Trade Centre debris continued to smoulder for more than half a year, despite substantial firefighting operations [6]. Natural smouldering, such as the underground fires in peatlands or coal mines, is one of the most extensive and longest-lasting fire phenomena on Earth [7,8]. Therefore, it is vital to deepen our understanding of smouldering fire dynamics.

The fire spread (propagation) process is of practical significance in evaluating the impact of fire events [9–12]. The fire spread is a continuous ignition and burning process [13], depending on both environment (e.g., wind [10,11,14–16], oxygen [17–19], pressure [20,21], and gravity [22]) and fuel factors (e.g., type/array [23], moisture [16,24], density [25], orientation [26], and size [27,28]). Based on the relative direction to the airflow (or wind), fire spread can be classified into the concurrent and opposed modes [9–11]. In the literature, most studies have focused on the characteristics of flame spread on solid fuels [9–11,29], rather than the smouldering spread.

Smouldering combustion is controlled by the competition between the oxygen supply and the heat transfer to and from the reaction zone [3,30,31]. Therefore, the airflow or wind is crucial to smouldering propagation, because it could increase both the oxygen supply and the heat loss [15,28,32]. By applying an external airflow (or environmental wind), smouldering propagation may become faster because of the increased oxygen supply (O_2-limit regime) [1,11,17]. Afterwards, the excessive airflow may also help trigger gas-phase homogenous oxidation under some specific conditions and result in smouldering-to-flaming (StF) transition [33]. However, for flaming fires, flame spread increases with wind speed due to increased convective heating on the unburnt fuel, rather than increased oxygen supply [33]. On the other hand, the porosity and permeability of fuel also affect the oxidation-controlled smouldering processes. For high-permeability fuels, such as cotton [15,34], pine needle [35], and PU foam [36], oxygen can diffuse into the porous fuel to maintain an internal smouldering propagation. For low-permeability consolidated fuels like wood [37], fibreboard [1], and coal chunk [8], smouldering can only propagate from outside to inside like a regression process, because oxygen could only diffuse through the porous char that is produced from the first-stage pyrolysis process [11]. Further increasing the airflow velocity, the cooling effect becomes dominant, so eventually smouldering extinction or blow-off will occur, just like the blow-off of flame [38].

In the literature, the blow-off of flame on solid fuels has been extensively studied over the last 50 years [4,11]. For example, Loh and Fernandez-Pello [39] showed that the concurrent rate flame spread over the thin paper first increased with the airflow velocity (< 1 m/s) but became almost constant until blow-off at about 3 m/s. A similar trend and blow-off wind speed were also observed for the concurrent flame spread on thin electrical wires [40]. In general, the blow-off of opposed flame spread is easier, usually at an airflow velocity lower than 1 m/s [41,42]. Comparatively, the research on the blow-off of smouldering is limited; and generally, it is more difficult to blow off persistent smouldering fire. Palmer [1] found that the blow-off limit of opposed smouldering propagation over fibreboard was about 7 m/s, but the concurrent smouldering propagation could still be sustained at 10 m/s [1,11]. Like the flame, most smouldering extinction processes result from a local energy imbalance, where the cooling rate is larger than the heat-release rate from exothermic oxidations [4,38,43]. Thus, decreasing oxygen concentration and pressure promotes the blow-off of smouldering under a smaller airflow [19,20]. So far, no study has addressed the smouldering propagation at large wind speeds over 10 m/s and the blow-off limits of persistent smouldering fire; thus, there is a big knowledge gap.

This work investigated both concurrent and opposed smouldering propagations over cylindrical consolidated biomasses (incenses) with different fuel diameters (1.5-5 mm) and densities (720-1,100 kg/m^3). The external airflow velocity up to 50 m/s in a small wind tunnel was applied to explore the blow-off limits. The theoretical analysis was proposed to explain the influence of environmental and fuel properties on smouldering propagation and critical conditions of blow-off.

8.2 Experimental methods

8.2.1 Materials

The cylindrical consolidated rod (i.e., incense), a representative biomass fuel that is prone to smouldering combustion, was tested in this work (Fig. 8.1a). The incense is an aromatic biotic material that is widely used in cultural and religious events in Asia. It mainly consists of mixed wood dust from the aromatic plants (e.g., from sage and cedar) and has homogenous porosity and composition [44]. The thermal analysis (TGA-DSC) of this incense was conducted. The details of the front and cross-section of the incense are also shown in Fig. 8.1a. Unlike the cotton bales and plastic foams, the dust particles inside the incense are densely packed, so oxygen cannot directly flow or diffuse into its internal structure.

Before the test, the incenses were first oven-dried at 75 ºC for at least 48 h. Afterwards, all samples were placed into an electronic dry cabinet to avoid the re-absorbing of moisture from the air. To explore the effect of fuel diameter (d) and density (ρ) on the smouldering propagation, two groups of experiments were designed:

(I) three sample diameters of 1.5, 2.5 and 5.0 mm with a constant fuel density of 720 kg/m^3, and

(II) three sample densities of 720, 920 and 1,100 kg/m^3 with a constant diameter of 1.5 mm.

To help estimate the rate of smouldering propagation, the long incense rod was cut into 10-15 cm samples and marked like a ruler with an interval of 1 cm (see Fig. 8.1a).

8.2.2 Environmental control

The experiments of smouldering propagation and blow-off under external airflow were conducted inside a small wind tunnel. The customized tubular wind tunnel was made of quartz glass and had an inner diameter (D) of 2 cm and a length of 20 cm, as illustrated in Fig. 8.1(b). The airflow (20.9% oxygen) from the compressed tank was fed through the bottom of the quartz glass tube, and then homogenized through a layer of small steel beads. A similar setup was used previously to study the flame spread [22] and smouldering propagation [19] under opposed flow with different oxygen mass fractions. Before the test, the airflow velocity (U_a up to 50 m/s) was controlled and measured by a precision anemometer.

For an internal flow in a circular tube of diameter D, the Reynolds number (Re_D) can be calculated as $Re_D = U_a D/\upsilon$, where $\upsilon \approx 16 \times 10^{-6}$ m^2/s is kinematic viscosity of the air at ambient temperature [45]. In other words, when the airflow velocity is larger than 2 m/s, the mainstream flow inside the tube is turbulent (Re_D> 2,300) where its velocity profile is relatively flat. On the other hand, the Reynolds number for the external airflow over the fuel surface ($Re_F = U_a d/\upsilon$) is much smaller than the turbulent limit of 5×10^5, so the boundary-layer flow on the fuel surface is laminar.

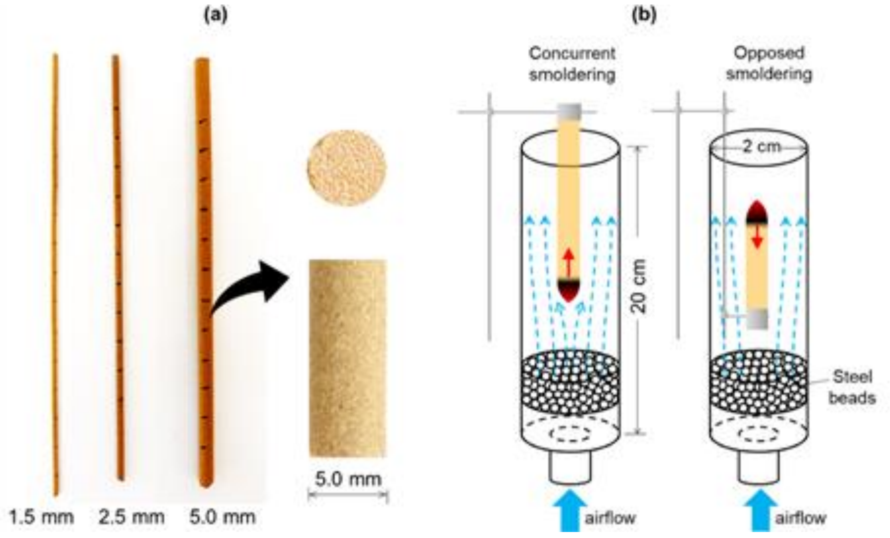

Fig. 8.1. (a) Photos of cylindrical incenses with different diameters with enlarged details of surface and cross-section, and (b) schematic of experimental setups for concurrent and opposed smouldering propagation under external airflow.

8.2.3 Test procedure

The biomass sample was ignited by a torch at one end, and then inserted into the middle part of the wind tunnel and fixed vertically at the tube axis by a sample holder, as shown in Fig. 8.1(b). The ignited end was placed on the bottom for the concurrent smouldering propagation, while for the opposed propagation, the ignited end was on the top. Afterwards, wind with prescribed speed was applied, and shortly after, the smouldering propagation reached the quasi-steady state. The external wind was applied in a step-increase manner from no wind (i.e., $U_a \approx 0$ as the base case) until the critical airflow velocity for blow-off (U_{ex}) was found. To start a new test under a different wind velocity, a fresh fuel sample was used.

A side-view digital video camera was used to capture the time history of the smouldering front. Through image analysis frame by frame, the instantaneous smouldering propagation rate (V_{sm}) can be calculated as $V_{sm} = \Delta x/\Delta t$, where Δt is the required duration for a smouldering front to propagate for a certain distance of Δx. Then, we could judge whether a steady-state propagation was reached. For each scenario, tests were repeated at least three times to quantify the standard deviations, and more repeating tests were conducted near the blow-off limit. In general, good experimental repeatability was found. During the tests, the ambient temperature (T_a) was 23 ± 2 ºC, and the relative humidity was 50

± 10%.

8.3 Results and discussion

8.3.1 Smouldering phenomena

Fig. 8.2(a) and (b) shows some typical photos of concurrent and opposed smouldering propagation under different airflow velocities of 0, 5, and 10 m/s with fuel diameters of 1.5, 2.5, and 5.0 mm. As the wind velocity increased, the smouldering of incense was stronger due to a better oxygen supply, where the reaction surface was hot enough to emit visible light (glowing incandescence) [11]. However, no smouldering-to-flaming transition was observed in the present work, different from those low-airflow cases in [19–21]. This was probably because the external wind (usually < 5 m/s [39–42]) was already large enough to blow off the flame. On the other hand, except for oxygen supply, the permeability of a fuel and its ability to remain consolidated may also affect this transition [33]. Nevertheless, increasing the oxygen concentration could promote the transition to flame in a smaller airflow [33].

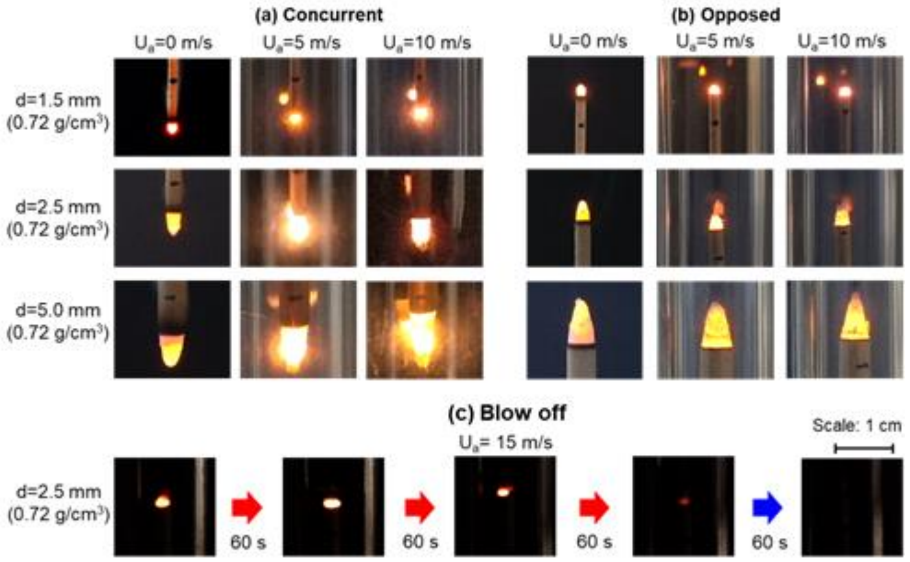

Fig. 8.2 Smouldering propagation on incense rods of 1.5, 2.5, and 5.0-mm diameters under (a) concurrent, and (b) opposed airflow velocities of 0, 5, and 10 m/s; and (c) blow-off for smouldering on a 2.5-mm incense under the opposed airflow velocity of 15 m/s.

Moreover, compared to the opposed propagation, the glowing zone is brighter for the concurrent propagation under the same airflow velocity. The length of the glowing zone (δ_{sm} or smouldering front thickness) increased as the fuel diameter increased, but it was insensitive to the airflow velocity unless near the blow-off limit. Fig. 8.2(c) also shows a typical blow-off process for the smouldering over a 2.5-mm thick incense, where the opposed airflow velocity was increased to 15 m/s. Gradually, the smouldering (glowing) zone became weaker, flatter, and smaller. After maintaining for about 3 min, the smouldering was eventually blown off.

8.3.2 Smouldering propagation rate vs. airflow direction

Fig. 8.3 compares the rate of smouldering propagation at different airflow directions. As expected, the concurrent smouldering propagation is much faster than the opposed propagation, and the trend of which is essentially the same as flame spread [11]. For example, for a 2.5-mm thick incense, the smouldering propagation rate is around 1.9 cm/min under a concurrent airflow of 5 m/s, tripling that under an opposed airflow. In general, the fire spread can be viewed as a continuous ignition process [9,11]. Thus, its rate is driven by the heat transfer from the oxidation zone ($\dot{q}''$) and resisted by the fuel thermal inertia ($\rho_F \Delta h_F$) [11] as

$$V_{sm} = \frac{\dot{q}'' L_p}{\rho_F \delta_T c_F (T_{sm} - T_a)} \approx \frac{\dot{q}''}{\rho_F \Delta h_F} = \frac{\text{Fire driving force}}{\text{Material resistance}} \tag{8.1}$$

where ρ_F, c_F, T_{sm}, and $\Delta h_F = c_F(T_{sm} - T_o)$ are the fuel density, specific heat capacity, smouldering temperature, and enthalpy change, respectively. For smouldering fire propagation, the preheated length (L_p) from glowing char-oxidation zone to the unburnt zone is close to the thermal penetration depth (δ_T), both of which are the characteristic length of heat conduction in solid fuel [11].

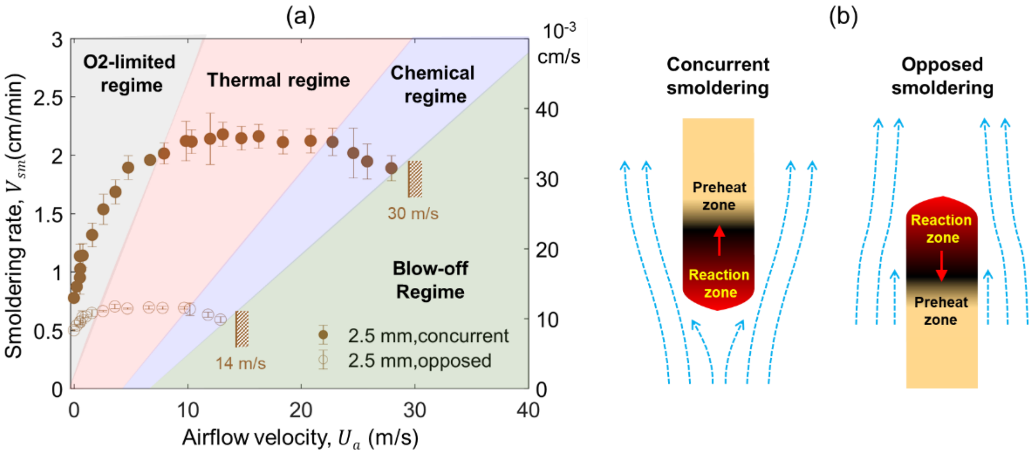

Fig. 8.3. (a) Comparison of smouldering propagation rate under external concurrent and opposed airflow, where the markers show the average values and error bars show the standard deviations, and (b) schematic diagrams of smouldering propagation under concurrent and opposed airflow.

As illustrated in Fig. 8.3(b), for concurrent smouldering propagation, the airflow can directly attack the conical reaction front, so partial airflow may permeate into the porous glowing zone in the form of a Darcy flow. The excessive oxygen supply intensifies the char oxidation and increases smouldering temperature (see strong incandescence in Fig. 8.2(a)), so a larger preheating flux ($\dot{q}''$) will be conducted from the reaction front to the preheat zone. In addition, the conical glowing zone may preheat the airflow boundary layer, which can preheat the downstream unburnt fuel via convection. Both effects of the concurrent airflow can speed up the smouldering propagation.

In contrast, for the smouldering propagation under opposed airflow, the cool airflow can directly cool the unburnt zone, reducing the preheating from the hot glowing zone ($\dot{q}''$) to the preheat zone. Furthermore, the oxygen can only reach the char surface via diffusion of the boundary layer, rather than the pressure-driven Darcy flow under concurrent airflow. Thus, the oxygen supply is less sufficient, slowing down the smouldering propagation. The relatively limited oxygen supply of opposed smouldering is also reflected by a weaker glowing zone in Fig. 8.2(b).

8.3.3 Effect of airflow velocity

Fig. 8.3 also illustrates the effect of airflow velocity on the smouldering propagation rate, where a similar trend is found for both concurrent and opposed propagations (see more comparisons in Figs. 8.4a-b and 8.5a-b). That is, as the external airflow velocity increases, the smouldering propagation rate first increases rapidly to the maximum value (O_2-limited Regime) and then remains constant over a wide range of airflow velocities (Thermal Regime). Subsequently, the propagation rate slightly decreases (Chemical Regime) until blow-off, following a similar pattern of concurrent flame spread [40,41].

In a small-airflow regime, the smouldering temperature increases with airflow velocity, indicated by a brighter glowing zone. Therefore, oxygen supply controls the smouldering propagation in this regime, while the cooling effect of airflow is negligible. For example, as the concurrent airflow velocity increases from 0 m/s to 3 m/s, the rate of smouldering propagation on the 2.5-mm thick fuel monotonically increases from 0.8 cm/min to 1.6 cm/min. Such an increasing trend is defined as the O_2-limited Regime, referring to the terminology widely used for the opposed flame spread [11,14,17].

For a consolidated fuel, the smouldering propagation could be regarded as a burning or fuel-regression process, similar to the burning of a candle or the premixed flame [11,15,28]. Therefore, the smouldering propagation rate (V_{sm}) is the same as the regression rate ($\dot{R}$) as

$$V_{sm} = \dot{R} = \frac{\dot{m}_F''}{\rho_F} = \frac{\dot{m}_a''}{\nu\rho_F} = \frac{\rho_a Y_{ox}}{\nu\rho_F} u_a \qquad \text{(O}_2\text{-limited Regime)} \tag{8.2}$$

where u_a is the velocity of internal airflow inside the conical porous char. Its magnitude could be estimated by the Darcy's law for the concurrent smouldering or by the diffusion within the boundary layer for opposed smouldering as

$$u_a = \begin{cases} \dfrac{k}{\phi\mu d}\Delta p = \dfrac{k}{\phi\mu d}\left(\dfrac{1}{2}\rho_a U_a^2\right) \propto \dfrac{U_a^2}{d} & \text{(concurrent)} \\ \\ \dfrac{h_m}{\rho_a} = \dfrac{h}{\rho_a c_p} = Nu\dfrac{\alpha}{d} \propto \dfrac{Re^{\frac{1}{2}}}{d} \propto \left(\dfrac{U_a}{d}\right)^{\frac{1}{2}} & \text{(opposed)} \end{cases} \tag{8.3}$$

where the Nusselt number changes with flow velocity and diameter as $Nu \approx C \cdot Re^{1/2} Pr^{1/3}$. For opposed smouldering propagation, the internal airflow velocity still changes with the external airflow (U_a) but is several orders of magnitude smaller than that of concurrent smouldering propagation. Therefore, the smouldering propagation rate at the O$_2$-limited Regime increases with the airflow velocity, regardless of the flow direction (see Fig. 8.3a).

Continuously increasing the airflow velocity, the smouldering propagation rate becomes stable. For example, the concurrent propagation rate on the 2.5-mm thick fuel remains at 2.1 ± 0.3 cm/min from 7 m/s to 23 m/s in Fig. 8.3(a), regardless of the airflow velocity. In this large-airflow regime, the unlimited oxygen supply no longer affects the smouldering propagation rate. Instead, the thermal conduction within the fuel ($\dot{q}'' \approx \lambda_F (T_{sm} - T_o)/\delta_T$) starts to dominate the smouldering propagation [11]. This behaviour is similar to the Thermal Regime of the flame spread, where the preheating of flame controls the rate of flame spread [41,46]. Based on Eq. (8.1), the smouldering propagation rate at the Thermal Regime is free of oxygen effect and reach the maximum value as

$$V_{sm} = V_{max} = \frac{\dot{q}''}{\rho_F c_F (T_{sm} - T_o)} = \frac{\lambda_F (T_{sm} - T_o)/\delta_T}{\rho_F c_F (T_{sm} - T_o)} \approx \frac{\alpha_F}{\delta_T} \qquad \text{(Thermal Regime)} \tag{8.4}$$

where λ_F and α_F are the fuel thermal conductivity and diffusivity, and δ_T is the thermal length within the fuel. Therefore, the Thermal-Regime smouldering propagation rate is insensitive to the external airflow velocity.

Further increasing the external airflow velocity, the smouldering propagation rate eventually starts to decrease. It is because the cooling effect of external airflow (see Fig. 8.3b) on char-oxidation reaction at the smouldering front can no longer be neglected. Then, the smouldering propagation rate is controlled by the competition between smouldering heat release and environmental cooling as

$$V_{sm} = \frac{\dot{q}''_{sm} - \dot{q}''_{loss}}{\rho_F c_F (T_{sm} - T_a)} = \frac{\rho_F \delta_T \dot{\omega}'''_{sm} \Delta H_{sm} - \dot{q}''_{loss}}{\rho_F c_F (T_{sm} - T_a)} \quad \text{(Chemical Regime)} \quad (8.5)$$

where $\dot{\omega}_{sm}$ and ΔH_{sm} are the rate and heat of smouldering reaction, respectively. Analogous to the flame spread [11,17], such a smouldering propagation is called the Chemical Regime or the Quenching Regime [28]. Thus, as the airflow increases, the convective cooling ($\dot{q}''_{loss}$) increases to slow down the smouldering propagation. Eventually, the cooling rate of airflow exceeds the heat release rate of smouldering ($\dot{q}''_{loss} > \dot{q}''_{sm}$), so the blow-off or the quenching by airflow occurs (discussed more in Section 7.3.4). Similar smouldering extinction behaviours were also observed in the quenching by the cold wall [28] and fuel moisture [24].

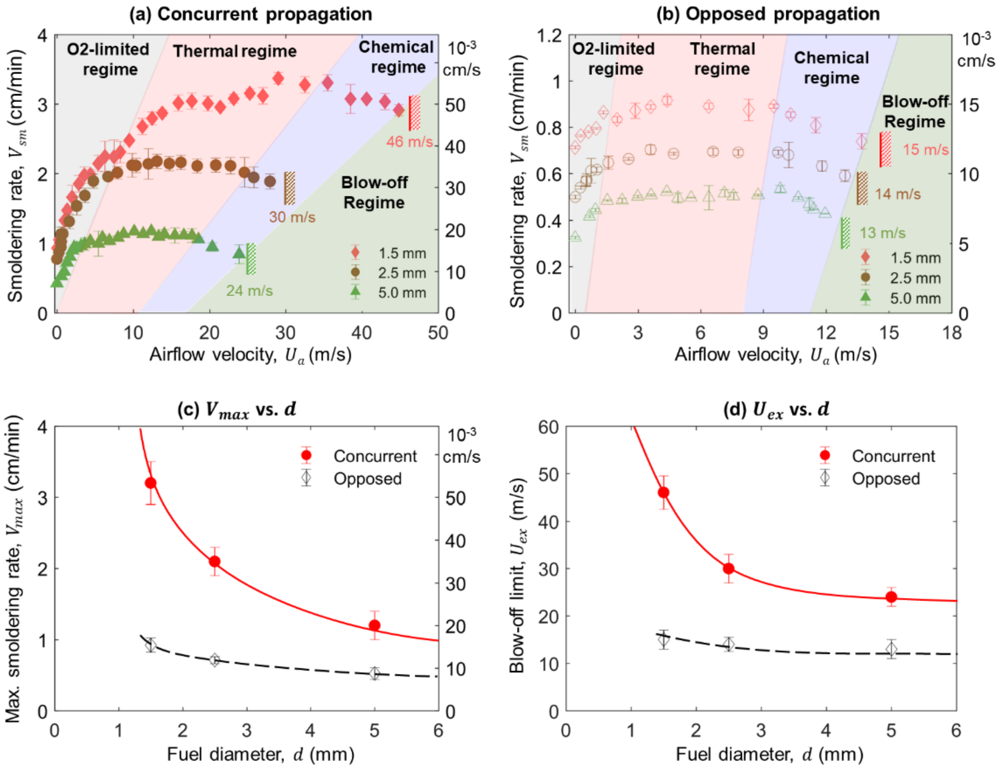

Fig. 8.4 Effect of fuel diameter on the rate of smouldering propagation under (a) concurrent and (b) opposed airflow, (c) maximum smouldering propagation rate and (d) blow-off limits.

8.3.4 Smouldering blow-off limits

Table 8.1 and Fig. 8. 4(d) and 5(d) summarize the blow-off limits of both concurrent and opposed smouldering propagation over incenses with different fuel diameters and densities. Clearly, the blow-off of concurrent smouldering propagation is much more difficult than opposed smouldering propagation. For example, for 2.5-mm thick incense, the blow-off limits of concurrent and opposed smouldering propagation are 30 m/s and 14 m/s, respectively. As discussed in Section 7.3.2 and Fig. 8.3(b), compared to the smouldering propagation under concurrent airflow, the opposed airflow can directly attack the preheat zone, thus increasing cooling efficiency on the unburnt fuel. Therefore, smouldering propagation is easier to achieve blow-off under opposed airflow. Such a trend is also similar to the flame spread, where the blow-off of opposed flame spread can be achieved in a smaller wind speed [22].

On the other hand, as shown in Fig. 8.4(d), when the fuel density is 720 kg/m^3, as the fuel diameter increases from 1.5 mm to 5.0 mm, the blow-off airflow velocity (U_{ex}) of smouldering propagation decreases from 46 m/s to 24 m/s under the concurrent airflow and from 15 m/s and 13 m/s under the opposed airflow, respectively. Similarly, as shown in Fig. 8.5(d), the blow-off limits of both concurrent and opposed smouldering decrease as the fuel density increases from 720 kg/m^3 to 1,100 kg/m^3 with a same fuel diameter of 1.5 mm (see more analysis in Section 8.3.5 and 8.3.6).

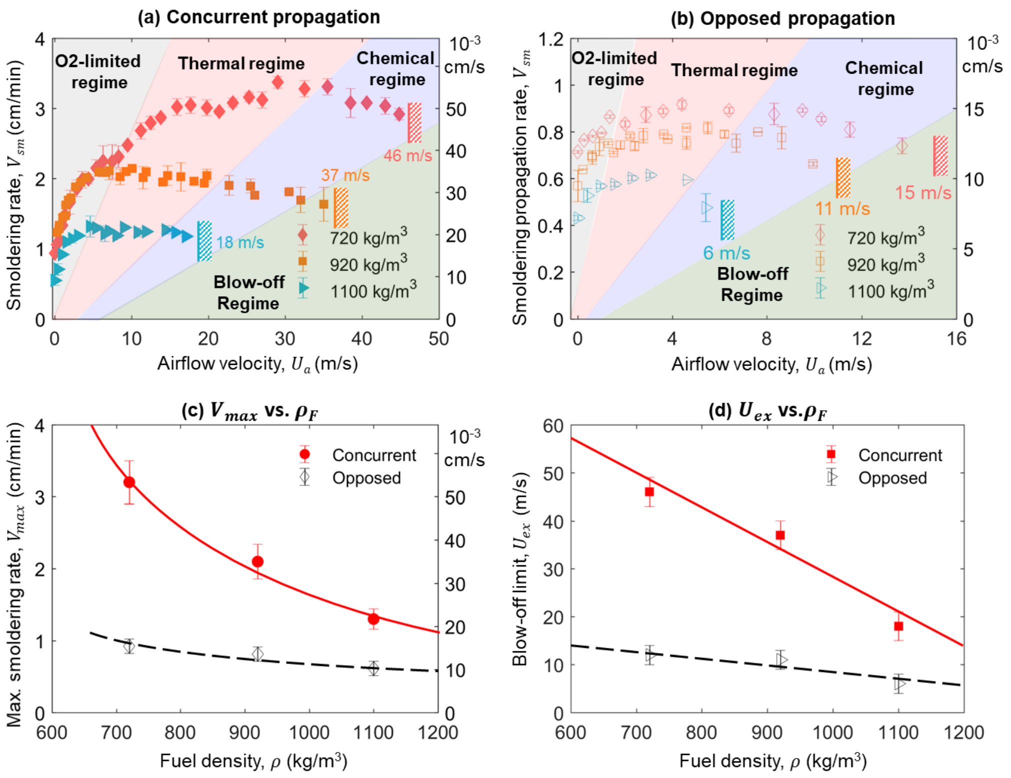

Fig. 8.5 Effect of fuel density on the rate of smouldering propagation under (a) concurrent and (b) opposed airflow, (c) maximum smouldering propagation rate, V_{max}, and (d) blow-off airflow velocity, U_{ex}.

More importantly, all the blow-off airflow velocities of smouldering (13-46 m/s) in the present work are higher than those of flame spread, for example, the concurrent flame spread over thin wire (2 m/s) [40] and thin cellulose (~5.5 m/s) [47], or the opposed flame spread over PMMA rod (~3m/s) [22], thin paper/PMMA sheet (~1 m/s) [41] and thin cellulose (0.4-1 m/s) [42]. The observed blow-off airflow velocity of incense is also higher than 7 m/s of the opposed smouldering propagation over fibreboard [1]. Approximately, the blow-off airflow velocity of smouldering propagation is about one order of magnitude larger than that of flame spread, so that smouldering is much more persistent than flaming.

Table 8.1. The maximum smouldering propagation rate (V_{max}) and blow-off airflow velocity (U_{ex}) over incenses with different fuel diameters and densities.

Diameter, d (mm)	Density, ρ (kg/m^3)	Maximum smouldering rate, V_{max} (cm/min)		Blow-off limit, U_{ex} (m/s)	
		Concurrent	opposed	Concurrent	opposed
1.5	720	3.2	0.9	46	15
2.5	720	2.1	0.7	30	14
5.0	720	1.2	0.5	24	13
1.5	920	2.1	0.8	37	11
1.5	1,100	1.3	0.6	18	8

8.3.5 Effect of fuel diameter

Fig. 8.4(a-b) further compare the effect of fuel diameter (d) on smouldering propagation under external airflow. For both concurrent and opposed smouldering propagation, the propagation rate increases as the fuel diameter decreases, in consistent with the flame spread in the literature where the fuel characteristic length is smaller than 10 mm [27,48]. For example, under the airflow velocity of 5 m/s, as the fuel diameter increases from 1.5 mm to 5 mm, the concurrent smouldering propagation rate decreases from 2.1 cm/min to 1.1 cm/min, and the opposed smouldering propagation rate declines from 0.9 cm/min to 0.5 cm/min. Clearly, the maximum smouldering propagation rate also decreases with the fuel diameter, as further compared in Fig. 8.4(c). From Eqs. (8.2,8.3), the internal airflow velocity (u_a) inside the conical porous char is inversely correlated with fuel diameter (d), thus the rate of oxygen supply decreases as the fuel diameter increases. As a result, the rate of smouldering propagation decreases with the fuel diameter, agreeing with the experimental results in Fig. 8.4.

The concept of B number (i.e., Spalding mass transfer number) has been widely used to estimate the flaming burning rate of liquid droplet fuels and solids [49–52]. The same concept can be adopted in describing smouldering burning (or propagation). For a cylindrical rod, the smouldering propagation is two dimensional in axial and radial directions (see the top view of control volume in Fig. 8.6). Considering the smouldering propagation in the radial direction and the analogy with flaming burning of droplet [13,50,51] or cylindrical rod [52], the burning flux ($\dot{m}_F''$) of incense can also be approximated as

$$\dot{m}_F'' = C\frac{\lambda_F}{c_F d}\ln(1+B) \tag{8.6}$$

where C is a fitting correlation, and B is a constant for a given fuel. Thus, the smouldering rate in the axial direction is comparable to the observed smouldering rate in the radial direction as

$$V_{sm} \approx V_{sm,r} \approx \frac{\dot{m}_F''}{\rho} \approx \frac{\alpha_F}{d} \tag{8.7a}$$

which decreases with the fuel diameter [50], agreeing with the experimental results in Fig. 8.4(a-c). Because of the curvature effect, the conductive heat flux concentrates towards smaller radius. A similar expression can also be derived from Eq. (8.4), with the diameter as the thermal length ($\delta_T \approx d$) as

$$V_{sm} \approx \frac{\alpha_F}{\delta_T} \approx \frac{\alpha_F}{d} \tag{8.7b}$$

As seen from Fig. 8.2, the smouldering front thickness (δ_T) increases as the fuel diameter increases (d).

On the other hand, as discussed in Section 7.3.4, the blow-off limit of smouldering was found to decrease as the fuel diameter increases (Fig. 8.4d). This trend is opposite to the flame spread, where the blow-off of a thinner fuel occurs at a smaller airflow velocity and the same critical strain rate ($a^* = U_{ex}/d$) [22,40]. Therefore, the definition of critical strain rate for blow-off may not be applicable to smouldering combustion. To explain the influence of fuel diameter on the smouldering blow-off limit (U_{ex}), a simplified energy conservation equation is applied to the near-limit reaction zone (see the front view of control volume in Fig. 8.6. At the blow-off extinction limit, the smouldering rate is zero; the reaction-zone thickness is minimal ($\delta_{sm} \ll d$); and the bottom size is already quenched by the large wind. Then, the heat generation in the oxidation reaction zone is equal to the convective heat loss due to the airflow ($\dot{q}_\infty''$) and the conduction to the preheat zone ($\dot{q}_{cond}''$) as

$$(\pi d\delta_{sm})\dot{m}''_{O_2,max}\Delta H_{ox} = (\pi d^2)(T_{sm}-T_a)\left(h+\frac{\lambda_F}{\delta_{sm}}\right) \tag{8.8}$$

where the convective heat loss from the side for the thin oxidation zone is neglected, and the oxidation rate from the side has reached a maximum and can no longer increases with airflow.

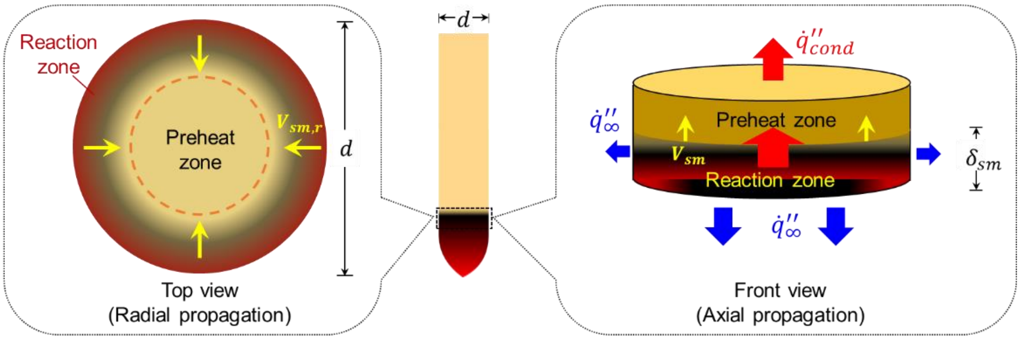

Fig. 8.6. Schematic diagram of the 2-D (radial and axial) smouldering propagation on a cylindrical fuel and the main heat transfer processes.

Then, the required convective cooling coefficient (h) can be derived, which also increases with the increased airflow velocity and the decreased fuel diameter, as

$$h = \frac{C_{sm}}{d} - \frac{\lambda_F}{\delta_{sm}} = Nu\frac{\lambda_a}{d} \propto \left(\frac{U_{ex}}{d}\right)^{\frac{1}{2}} \tag{8.9}$$

where $C_{sm} = \delta_{sm}\dot{m}''_{O_2,max}\Delta H_{ox}/(T_{sm}-T_a)$ is a smouldering constant. Thus, the dependence of blow-off airflow velocity with fuel diameter can be expressed as

$$U_{ex} \propto d\left(\frac{C_{sm}}{d} - \frac{\lambda_F}{\delta_{sm}}\right)^2 \propto \frac{1}{d} \tag{8.10}$$

Therefore, as the fuel diameter (d) increases, the required external airflow velocity to blow off smouldering fire decreases, agreeing with experimental results in Fig. 8.4(d). Note that if the fuel diameter further decreases below 1 mm, the strong wind may easily break and remove the smouldering zone. Then, the extinction is no longer a blow-off but a fuel-removal, which needs further experimental verification.

8.3.6 Effect of fuel density

Fig. 8.5(a-b) also shows the effect of fuel density on the concurrent and opposed smouldering propagation rate, where the maximum rate of smouldering propagation was further compared in Fig.

8.5c. As expected, as the fuel density decreases, the smouldering propagation rate increases, agreeing with the theoretical analysis of Eqs. (8.1) and (8.2) where the maximum propagation rate is inversely proportional to the fuel density ($V_{sm} \propto 1/\rho_F$). For example, as the fuel density increases from 720 to 1,100 kg/m^3 under the wind velocity of 10 m/s, the smouldering propagation rate decreases from 2.1 cm/min to 1.3 cm/min for the concurrent spread and from 0.9 cm/min to 0.5 cm/min for the opposed spread, respectively.

As the fuel density of porous medial increases, the thermal conductivity increases ($\lambda_F \propto \rho_F$), so that the heat conduction from reaction zone to the preheat zone also increases. For the blow-off limit in Eq. (8.9), we have

$$U_{ex} \propto d\left(\frac{C_{sm}}{d} - \frac{\lambda_F}{\delta_{sm}}\right)^2 \sim (-\lambda_F) \sim (-\rho_F) \qquad (8.11)$$

which decreases with the thermal conductivity and density of fuel. Thus, the required blow-off airflow velocity decreases as the fuel density increase, agreeing with the experimental results in Fig. 8.5(d).

8.4 Conclusions

In this chapter, we use experimental approaches to investigate the smouldering propagation and blow-off over cylindrical incenses under concurrent and opposed external wind up to 50 m/s. There are no experimental data on the smouldering propagation at large wind speeds over 10 m/s and the blow-off limits of persistent smouldering fire before this study. For concurrent smouldering propagation, partial airflow may permeate into the porous glowing zone in the form of a Darcy flow, while the oxygen can only reach the char surface via diffusion for opposed smouldering propagation. Also, the conical glowing zone may preheat the concurrent airflow boundary layer to preheat the downstream unburnt fuel, which further promotes the concurrent smouldering propagation faster than the opposed propagation.

We also found that the smouldering propagation rate is very sensitive to the airflow rate. As external airflow velocity increases, the smouldering propagation rate first increases (O_2-limited Regime), and then remains stable at its maximum value for a wide range of airflow velocity (Thermal Regime). Afterwards, it slightly decreases (Chemical Regime) until blow-off. Comparatively, the flame-spread rate increases with the wind speed due to increased convective heating rather than increased oxygen supply. This is a significant difference between smouldering and flaming spread, because smouldering combustion is controlled by both oxygen supply and heat loss.

We report for the first time that the blow-off airflow velocity of smouldering propagation (13~46 m/s) is around one order of magnitude larger than that of flame spread, and it decreases as the fuel diameter or density increases. Blowing-off concurrent smouldering propagation is also more difficult than opposed propagation, similar to the blow-off of flame spread. Future numerical simulations are needed to reveal the underlying physical and chemical process of smouldering propagation and blow-off under different airflow velocities.

Acknowledgements

This research is funded by the National Natural Science Foundation of China (NSFC) No. 51876183 and the Society of Fire Protection Engineers (SFPE) Educational & Scientific Foundation. The authors thank Dr Supan Wang (Nanjing Tech Univ.) for helping conduct thermal analysis of the incense sample and T. H. Chow for the help in the lab. The comments from Dr Han Yuan (Hong Kong PolyU) are also acknowledged.

References

[1] Palmer KN. Smouldering combustion in dusts and fibrous materials. Combust Flame 1957;1:129–54.

[2] Rein G. Smouldering Combustion. SFPE Handb Fire Prot Eng 2014;2014:581–603.

[3] Ohlemiller TJJ. Modeling of smouldering combustion propagation. Prog Energy Combust Sci 1985;11:277–310.

[4] Torero JL, Gerhard JI, Martins MF, Zanoni MAB, Rashwan TL, Brown JK. Processes defining smouldering combustion: Integrated review and synthesis. Prog Energy Combust Sci 2020;81.

[5] Restuccia F, Ptak N, Rein G. Self-heating behaviour and ignition of shale rock. Combust Flame 2017;176:213–9.

[6] Koya L, Gard C. Investigating the Attacks on the World Trade Center. First edit. New York: The Rosen Publishing Group, Inc.; 2018.

[7] Rein G. Smouldering Fires and Natural Fuels. In: Claire M. Belcher, editor. Fire Phenom. Earth Syst., New York: John Wiley & Sons, Ltd.; 2013, p. 15–34.

[8] Song Z, Huang X, Kuenzer C, Zhu H, Jiang J, Pan X, et al. Chimney effect induced by smouldering fire in a U-shaped porous channel: A governing mechanism of the persistent underground coal fires. Process Saf Environ Prot 2020;136:136–47.

[9] Williams FA. Mechanisms of fire spread. Symp Combust 1977;16:1281–94.

[10] Gollner MJ, Miller CH, Tang W, Singh A V. The effect of flow and geometry on concurrent flame spread. Fire Saf J 2017;91:68–78.

[11] Huang X, Gao J. A review of near-limit opposed fire spread. Fire Saf J 2020:103141.

[12] Fernandez-Pello AC, Hirano T. Controlling mechanisms of flame spread. Combust Sci Technol 1983;32:1–31.

[13] Quintiere JG. Fundamentals of Fire Phenomena. New York: John Wiley; 2006.

[14] Fernandez-Pello a. C, Ray SR, Glassman I. Downward Flame Spread In an Opposed Forced

Flow. Combust Sci Technol 1978;19:19–30.

[15] Xie Q, Zhang Z, Lin S, Huang X, Qu Y. Smouldering Fire of High-Density Cotton Bale Under Concurrent Wind. Fire Technol 2020.

[16] Huang X, Restuccia F, Gramola M, Rein G. Experimental study of the formation and collapse of an overhang in the lateral spread of smouldering peat fires. Combust Flame 2016;168:393–402.

[17] Kumar A, Shih HY, T'ien JS. A comparison of extinction limits and spreading rates in opposed and concurrent spreading flames over thin solids. Combust Flame 2003;132:667–77.

[18] Konno Y, Hashimoto N, Fujita O. Downward flame spreading over electric wire under various oxygen concentrations. Proc Combust Inst 2019;37:3817–24.

[19] Kadowaki O, Suzuki M, Kuwana K, Nakamura Y, Kushida G. Limit conditions of smouldering spread in counterflow configuration: Extinction and smouldering-to-flaming transition. Proc Combust Inst 2020;000:1–9.

[20] Yamazaki T, Matsuoka T, Nakamura Y. Near-extinction behaviour of smouldering combustion under highly vacuumed environment. Proc Combust Inst 2019;37:4083–90.

[21] Sato J, Sato K, Hirano T. Fire spread mechanisms along steel cylinders in high pressure oxygen. Combust Flame 1983;51:279–87.

[22] Huang X, Link S, Rodriguez A, Thomsen M, Olson S, Ferkul P, et al. Transition from opposed flame spread to fuel regression and blow off: Effect of flow, atmosphere, and microgravity. Proc Combust Inst 2019;37:4117–26.

[23] Gollner MJ, Williams FA, Rangwala AS. Upward flame spread over corrugated cardboard. Combust Flame 2011;158:1404–12.

[24] Lin S, Liu Y, Huang X. How to Build a Firebreak to Stop Smouldering Peat Fire : Insights from a Laboratory-Scale Study. Int J Wildl Fire 2021.

[25] Huang X, Rein G. Downward Spread of Smouldering Peat Fire: the Role of Moisture, Density and Oxygen Supply. Int J Wildl Fire 2017;26:907–18.

[26] Zhou Y, Gong J, Jiang L, Chen C. Orientation effect on upward flame propagation over rigid polyurethane foam. Int J Therm Sci 2018;132:86–95.

[27] Jiang L, He JJ, Sun JH. Sample width and thickness effects on upward flame spread over PMMA surface. J Hazard Mater 2018;342:114–20.

[28] Lin S, Huang X. Quenching of smouldering: Effect of wall cooling on extinction. Proc Combust Inst 2021;38:5015–22.

[29] Fernandez-Pello AC. Flame Spread Modeling. Combust Sci Technol 1984;39:119–34.

[30] Torero JL, Fernandez-Pello AC, KitanO M. Opposed forced flow smouldering of polyurethane foam. Combust Sci Technol 1993;91:95–117.

[31] Kuwana K, Suzuki K, Tada Y, Kushida G. Effective Lewis number of smouldering spread over a thin solid in a narrow channel. Proc Combust Inst 2017;36:3203–10.

[32] Valdivieso JP, Rivera J de D. Effect of Wind on Smouldering Combustion Limits of Moist Pine Needle Beds. Fire Technol 2014;50:1589–605.

[33] Santoso MA, Christensen EG, Yang J, Rein G. Review of the Transition From Smouldering to Flaming Combustion in Wildfires. Front Mech Eng 2019;5.

[34] He M, Ding L, Yu L, Ji J. Effect of density on the smouldering characteristics of cotton bales ignited internally. Proc Combust Inst 2020;000:1–9.

[35] Wang S, Huang X, Chen H, Liu N. Interaction between flaming and smouldering in hot-particle

ignition of forest fuels and effects of moisture and wind. Int J Wildl Fire 2017;26:71–81.

[36] Bar-Ilan A, Putzeys OM, Rein G, Fernandez-Pello AC, Urban DL. Transition from forward smouldering to flaming in small polyurethane foam samples. Proc Combust Inst 2005;30:2295–302.

[37] Emberley R, Inghelbrecht A, Yu Z, Torero JL. Self-extinction of timber. Proc Combust Inst 2017;36:3055–62.

[38] Dosanjh SS, Pagni PJ, Fernandez-Pello AC. Forced cocurrent smouldering combustion. Combust Flame 1987;68:131–42.

[39] Loh HT, Fernandez-Pello AC. Flow Assisted Flame Spread Over Thermally Thin Fuels. West States Sect Combust Inst 1984:65–74.

[40] Lu Y, Huang X, Hu L, Fernandez-Pello C. Concurrent Flame Spread and Blow-Off Over Horizontal Thin Electrical Wires. Fire Technol 2019;55:193–209.

[41] Fernandez-Pello AC, Ray SR, Glassman I. Flame spread in an opposed forced flow: the effect of ambient oxygen concentration. Symp Combust 1981;18:579–89.

[42] Carmignani L, Celniker G, Bhattacharjee S. The Effect of Boundary Layer on Blow-Off Extinction in Opposed-Flow Flame Spread over Thin Cellulose: Experiments and a Simplified Analysis. Fire Technol 2017;53:967–82.

[43] Leach S V, Ellzey JL, Ezekoye OA. Convection , Pyrolysis , and Damko Extinction of Reverse Smouldering Combustion. Twenty-Seventh Symp Combust 1998:2873–80.

[44] Yamazaki T, Matsuoka T, Li Y, Nakamura Y. Applicability of a Low-Pressure Environment to Investigate Smouldering Behaviour Under Microgravity. Fire Technol 2020;56:209–28.

[45] Incropera FP. Principles of heat and mass transfer. John Wiley; 2007.

[46] De Ris JN. Spread of a laminar diffusion flame. Symp Combust 1969;12:241–52.

[47] Wang S, Wang S, Zhu K, Xiao Y, Lu Z. Near Quenching Limit Instabilities of Concurrent Flame Spread over Thin Solid Fuel. Combust Sci Technol 2016;188:451–71.

[48] Ayani MB, Esfahani JA, Mehrabian R. Downward flame spread over PMMA sheets in quiescent air: Experimental and theoretical studies. Fire Saf J 2006;41:164–9.

[49] Rich D, Lautenberger C, Torero JL, Quintiere JG, Fernandez-Pello C. Mass flux of combustible solids at piloted ignition. Proc Combust Inst 2007;31 II:2653–60.

[50] Kanury AM. Rate of charring combustion in a fire. Symp Combust 1973;14:1131–42.

[51] Sun P, Wu C, Zhu F, Wang S, Huang X. Microgravity combustion of polyethylene droplet in drop tower. Combust Flame 2020;222:18–26.

[52] Lee CK. Burning rate of fuel cylinders. Combust Flame 1978;32:271–6.

CHAPTER 9: Extinction Limit of Smouldering Peat Fire under Rainfall

Summary:

Smouldering wildfire in peatlands contributes significantly to global carbon emissions and regional haze events, which is one of the largest and most persistent fire phenomena on Earth. Here we assess the underlying mechanism of rain in suppressing the smouldering peat fire in the shallow soil layer up to 15 cm deep through laboratory experiments. We show that the minimum rainfall intensity to extinguish the peat fire is roughly 4 mm/h, so that the persistent light rain cannot suppress such smouldering wildfire. The required rain duration, Δt (min), for extinguishing smouldering peat fire decreases with the rainfall intensities, I (mm/h), as $\log_{10}\Delta t = -1.15\log_{10} I + 3.3$, and is much longer than that for extinguishing flaming wildfire. We also identify that the required rainfall depth for extinguishing peat fire gradually decreases with the rainfall intensity and approaches a minimum value of 13 mm under violent rain. As rainfall intensity increases, the carbon emission flux from peat fire decreases. Therefore, we conclude that the short-term violent rain is most effective for suppressing the persistent smouldering peat fire. This research helps evaluate the impact of weather on the development of peat fire and improve the prediction of carbon emissions from peat fire with the use of regional weather models.

This Chapter is based on "S. Lin, Y. K. Cheung, Y. Xiao and X. Huang (2020) *Can Rain Suppress Smouldering Peat Fire?* **Science of the Total Environment** 727: 138468. doi: 10.1016/j.scitotenv.2020.138468" and "S. Lin and X. Huang (2020) *An Experimental Method to Investigate the Water-Based Suppression of Smouldering Peat Fire*. **MethodsX** 7: 100934. doi: 10.1016/j.mex.2020.100934".

"

9.1 Introduction

Peatlands are important ecosystems in the boreal and tropical regions, which not only support the biological diversity for a wide range of wildlife habitats but also store 25% of the planet's terrestrial organic carbon, i.e., approximately the same mass of carbon that is in the atmosphere [1,2]. Peat fire is the driving phenomenon of wildfire in peatlands, such as those that cause widespread destruction of ecosystems and episodes of haze in South Asia, North America, and north-east Europe [3–6]. Peat fire is one of the largest and longest-lasting fire phenomena on Earth, and it can sustain for months and even for years despite extensive rain, weather changes, or fire-fighting attempts [7]. Recently in September of 2019, large deposits of peat in Kalimantan and Sumatra were ignited and burned for several months, covering Indonesia and nearby countries with haze and causing the cancellation of enormous flights due to poor visibility [8]. Moreover, the annual release of ancient carbon from peat fires is approximately equivalent to 15% of human-made carbon emissions [3,5,9–12].

Peat fire is dominated by smouldering, a slow, low-temperature, and flameless form of combustion [13,14]. Smouldering peat fire is different from regular flaming wildfire in its chemistry, transport processes, and time scales [15]. Peat can hold a high water content to prevent the ignition, but natural or anthropogenic-induced droughts can increase the risk of peat fire [5,16]. The ignition source for peat fire can be natural, such as lightning, flaming wildfire [17], self-heating [18], and volcanic eruption, or anthropogenic, such as deforestation, poor land management, accidental ignition, and arson [7]. Most recent peat fires were initiated on the surface by the flaming wildfires. The probability of ignition depends on the moisture content, mineral content, and other physicochemical properties [13,17–20]. Once ignited, smouldering fire can easily burn out an organic soil layer of more than 50 cm deep over an extensive area [7,11,21,22].

Fundamentally, three approaches can be used to extinguish the fire, that is, burnout, smothering, and cooling [23]. For peat fire, burnout of peat soils is unacceptable since it will severely destroy the essential peatland resources and ecosystem, as well as release a significant amount of toxic and greenhouse gases into the atmosphere [5,24,25]. Smothering is to extinguish the fire by removing or reducing oxygen. However, peat fire can be sustained in an extremely low oxygen concentration [26,27], and there is neither a natural mechanism nor a manmade technique to prevent the diffusion of oxygen into the soil layer in the field scale. Therefore, quenching the peat fire by different cooling methods is the only practical approach, and water is the most widely used cooling agent in firefighting efforts. In reality, peat fire can also be quenched under several conditions, (i) the presence of an inorganic soil layer; (ii) the presence of a thick wet soil layer; (iii) the suppression of heavy continuous rains, and (iv) active firefighting [7,28]. However, compared with extensive studies on the ignition and development of peat fire, very few studies are available on how to extinguish these smouldering wildfires.

Because of the persistence of peat fire, a short-term man-made water spray is not able to stop the fire spread [29]. Compared to flaming wildfire, smouldering wildland fire require at least 50% more water to extinguish the same amount of burning fuel [7]. Some chemical foaming agents can easily penetrate into peat soil and shield the burning peat particles from the oxygen supply [30], but the required quantity to suppress any real peat fire is enormous. In fact, limited trials in the literature have demonstrated the ineffectiveness of all man-made suppression methods in controlling or extinguishing any massive peat fire [29,31,32]. On the other hand, the authors have identified a research gap surrounding the natural suppression of peat fire by rain.

Rain is a crucial part of the Earth's water cycle [33,34], and it may decelerate the wildfire spread by wetting the fuels and even directly extinguish the flame [35]. For the recent wildfire in Amazonas, Brazil, the burning area decreased significantly when the regional rainfall increased [36]. Although the suppression effect of rain on smouldering wildfire is still mostly unknown, it is hypothesized that the rain droplets can penetrate into the burning peat layer, and if the rainwater can overcome the combustion heat, eventually peat fire can be quenched. Nevertheless, if the peat fire was not entirely extinguished by rain, re-ignition could happen after an extended time, especially when the drought season arrives [29,37]. Thus, it is necessary to thoroughly explore the effectiveness of rain in suppressing peat fire and identify the critical rainfall intensity and depth.

Herein, well-controlled experiments were conducted to explore the possibility of the suppression of smouldering peat fire by rain. Rainfall intensities (I) of 'light (< 2 mm/h),' 'moderate (2-10 mm/h),' 'heavy (10-50 mm/h),' and 'violent (>50 mm/h)' were tested up to 400 mm/h. The required rainfall duration (Δt), rainfall depth (d), as well as, the mass loss per unit area of peat sample ($\Delta m_p''$) and carbon emissions of peat fire ($\Delta m_C''$) under different rainfall intensities were analyzed in detail. The minimum rainfall intensity (I_{min}) and rainfall depth (d_{min}) to extinguish the peat fire was also quantified.

9.2 Materials and Methods

9.2.1 Peat soil sample

The organic-rich moss peat soil (Fig. 9.1) tested in the experiment came from the Netherlands, and it had an organic matter of about 96%. The bulk density of oven-dried peat was measured to be 145 kg/m^3 (±5%). The peat sample had an open-pore structure and an overall porosity of about 0.90. The element analysis for the peat organic matter showed 44.2/6.1/49.1/0.5/0.1% mass fraction for C/H/O/N/S, respectively [17]. Because peat soils could become hydrophobic under a high-temperature drying process [38–40], all peat samples were dried in an oven at a constant temperature of 40 °C, which is close to the ambient temperature of tropical regions in the dry season. During the drying, the weight and moisture content of peat were measured every 1 h until its moisture content was close to 50 ± 5%, and its (wet) bulk density reached 218 ± 10 kg/m^3. The peat sample was similar to the natural drought condition found in previous work [17,20,41]. Afterward, samples were stored in the sealed boxes for homogenization. Before the experiment, the subsample of peat was collected and dried to ensure the value of sample moisture content.

9.2.2 Initiation of peat fire

The peat sample was placed in a mesh basket of a cylindrical shape with a diameter of 100 mm and a height of 150 mm (Fig. 9.1). During the filling-in process, the peat samples were shaken to ensure the bulk density of moist peat was close to 218 kg/m^3, and the sample mass was 256 ± 5 g.

For ignition, an 8-cm long coil igniter ($Cr_{20}Ni_{80}$) was placed 5 cm below the top free sample surface to start the smouldering peat fire. The ignition power was fixed to 60 W for 60 min to initiate a robust peat fire [29]. The temperature profiles of peat at 0 cm (surface) and 5 cm, 10 cm and 15 cm below the top surface were carefully monitored using armored K-type thermocouples with 1-mm probe diameter. After ignition, the basket of peat sample was placed into a larger cylindrical mesh basket with a diameter of 200 mm and a height of 150 mm. In order to simulate the natural state and mimic a real boundary condition, the space between two baskets was filled with unheated peat soils. Afterward, the entire setup was left to burn and self-stabilize for another 30 min before the start of rain suppression.

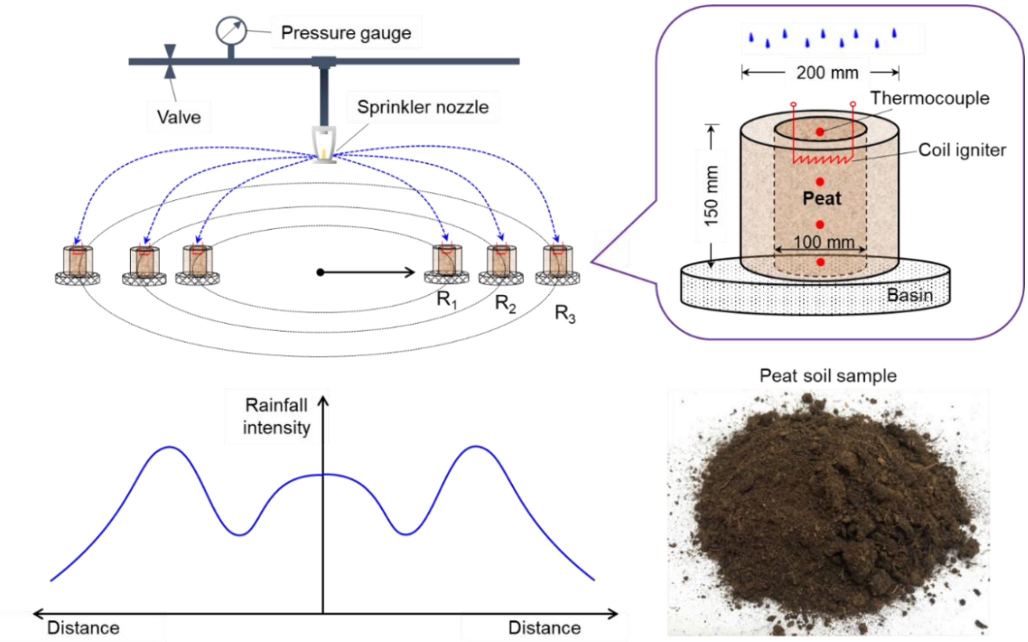

Fig. 9.1. Experimental materials and setup. Photo of peat soil sample for smouldering fire suppression test and the illustration of rain suppression simulated by a sprinkler system and rainfall intensity distribution.

9.2.3 Simulated rain

The simulated rain-suppression experiments were conducted in a wet chamber with an area of 6 m × 10 m and a height of 3.5 m. The artificial rain was produced by a water sprinkler system that included a sprinkler nozzle, a pressure gauge, and a valve, as illustrated in Fig. 9.1. The vertical distance between the nozzle and the sample surface was fixed to 2.5 m. The median water droplet diameter depends on the water pressure, sprinkler orifice diameter, and the surface tension of the air-water interface (0.073 N/m). The value of the median water droplet diameter was calculated to be about 1.5 mm, which is within the range of typical raindrop sizes [42]. Therefore, the simulated raindrop size in this experiment is close to the natural rain. With the sprinkler spray, the intensity of simulated rainfall changed with the location. Thus, the distribution of rainfall intensity (Fig. 9.1) was measured by multiple cylindrical containers (with a diameter of 10 cm and a height of 15 cm) at the interval of 20 cm. Given a fixed rainfall duration ($\Delta t = 10$ min), the local rainfall intensity can be calculated by measuring rainfall depth (d) as $I = d/\Delta t$. Then, the desired rainfall intensity can be achieved by placing the burning sample at a specific location.

9.2.4 Experiment procedure

The rain-suppression experiments were conducted to determine the required rainfall duration (Δt), rainfall depth (d), as well as, the mass loss per unit area of peat sample ($\Delta m''_p$) and carbon emissions of peat fire ($\Delta m''_C$) under different rainfall intensities. After igniting the peat fire for 60 min and stabilizing the burning for another 30 min, the sprinkler system was activated for a prescribed duration.

Unlike the suppression of a flame, it was not possible to instantaneously determine by visual inspection whether the smouldering peat fire was extinguished or not [29]. Thus, after the artificial rainfall, the sample was left for another 24 h to determine if the peat fire survived or not. If the temperatures inside the sample re-rose above 250°C, i.e., the minimum smouldering temperature of peat [17], and the peat sample eventually burned out, the fire-suppression was considered as a failure. Then, experiments were continued with fresh peat samples under a longer rainfall duration until the critical rainfall duration and depth were found.

For the extinguished peat fire, the sample residue was oven-dried at 100 °C for 48 h to obtain the end dry mass (m_e). The mass loss quantified the carbon emissions of peat fire under different suppression activities. To measure the mass loss during fire suppression, the initial sample mass (m_i) after the 90-min ignition and burning stage was first measured. After the initial burning stage, the sample was immersed into 8-L water for quick extinction, and then dried in the oven to obtain m_i. Thus, the burning mass flux of peat ($\Delta m''_p$ in kg/m^2) under different rainfall intensities is

$$\Delta m''_p = \frac{m_i - m_e}{A} \tag{9.1a}$$

where $A = 8\times10^{-3}$ m^2 is the cross-section area of the cylindrical peat sample. For this peat soil, the mass fraction of carbon is around 44% [17,43], so that the carbon emissions ($\Delta m''_C$ in kg/m^2) can then be estimated as

$$\Delta m''_C = 44\%\Delta m''_p \tag{9.1b}$$

Note that CO_2, CO, CH_4, and NH_3 are the four major gas species emitted from peat fire [25]. Comparatively, CO_2 and CH_4 are the dominant greenhouse gases, but CO and NH_3 are toxic gases and can impact the atmosphere through the photochemical process [25,44].

9.2.5 Control experiments

The baseline experiment of peat fire was conducted without any rain suppression, so that the burning characteristics were compared with those with different levels of rain suppression. To compare the required rainfall duration for extinguishing smouldering and flaming wildfires, the rain-suppression experiment for flaming wood cribs fire was also conducted. The wood crib was made of cylindrical wood rods with a length of 8 cm and a diameter of 1 cm [45], which aimed to mimic the common flaming fire on twigs and was similar to past studies [46]. The flaming wood crib had a burning area similar to the smouldering peat fire, thus, ensuring fair comparison. The wood cribs were ignited by a lighter for 1 min, followed by 1 min of self-burning before the artificial rain suppression. The extinguishing limit of the flaming wood crib was determined in the same way as those of the smouldering peat fire.

9.3 Results and Discussion

9.3.1 Effective of fire suppression by rain

The effectiveness of rain of different intensities on suppressing peat fire is quantified against the rainfall duration (Δt), rainfall depth (d), mass loss of burning peat ($\Delta m_p''$), and carbon emissions per unit area of peat fire ($\Delta m_C''$) in Fig. 9.2. We found that the minimum rainfall intensity (I_{min}) to be roughly 4 mm/h (Fig. 9.2a), below which the peat soil could completely burnout like those without any rain suppression. Therefore, the smouldering peat fire may not be suppressed by a light rain regardless of the rainfall duration. Moreover, as expected, the required suppression duration decreases with increasing rainfall intensity [47].

For example, when the rainfall intensity increases from 30 mm/h to 100 mm/h, the required suppression duration decreases from 40 ± 3 min to 10 ± 1 min. An empirical correlation between the suppression duration and the rainfall intensity can be formulated as

$$\log_{10} \Delta t = -1.15 \log_{10} I + 3.3 \tag{9.2}$$

where common units of min for Δt and mm/h for I are used. The logarithm with base 10 is used in fitting with the R^2 coefficient of 0.99, and excellent linearity is shown in Fig. 9.2b.

Figure 9.2a further compares the required suppression duration between the smouldering peat fire and flaming wood-crib fire. Under the same rainfall intensity, the suppression duration of smouldering peat fire is much higher than that of flaming wood crib fire. For example, when the rainfall intensity is around 125 mm/h, the required suppression duration for smouldering peat fire is about 7 min, while for flaming wood crib fire, only 20 s is required for extinguishing the flame. For peat fire, the water in fuel beds tends to find the path of least flow resistance [32,48], and the peat soil becomes hydrophobic after high-temperature heating from the smouldering combustion [38,49,50]. Therefore, it is more difficult for rainwater to arrive and remain in the underground burning zone. In contrast, for the flaming wood crib, raindrops can reach and cool the burning wood more directly and effectively. An empirical correlation for rain suppression of the flaming wood-crib fire, $\log_{10} \Delta t = -\log_{10} I + 1.9$, can also be obtained, where the R^2 coefficient was found to be 0.92. The minimum rainfall intensity to suppress the flaming wood-crib fire was identified as about 12 mm/h (i.e., a heavy rain), which was much larger than 4 mm/h found for the smouldering peat fire. Because the power or heat release rate of flaming fire is much greater than that of smouldering fire, greater threshold for rainfall intensity is expected to suppress a flame.

As shown in Fig. 9.2c, once the rainfall intensity exceeds I_{min} (4 mm/h), the required rainfall depth also shows a negative correlation with the rainfall intensity, following a similar trend of required rainfall duration in Fig. 9.2a. In particular, when the rainfall intensity increases from 30 ± 1 mm/h to 40 ± 2 mm/h, the rainfall depth decreases from 19 ± 1 mm to 17 ± 1 mm. More importantly, when the rainfall intensity further increases, the rainfall depth gradually approaches a critical value (~13 mm) for the violent rain, which can be defined as minimum rainfall depth (d_{min}).

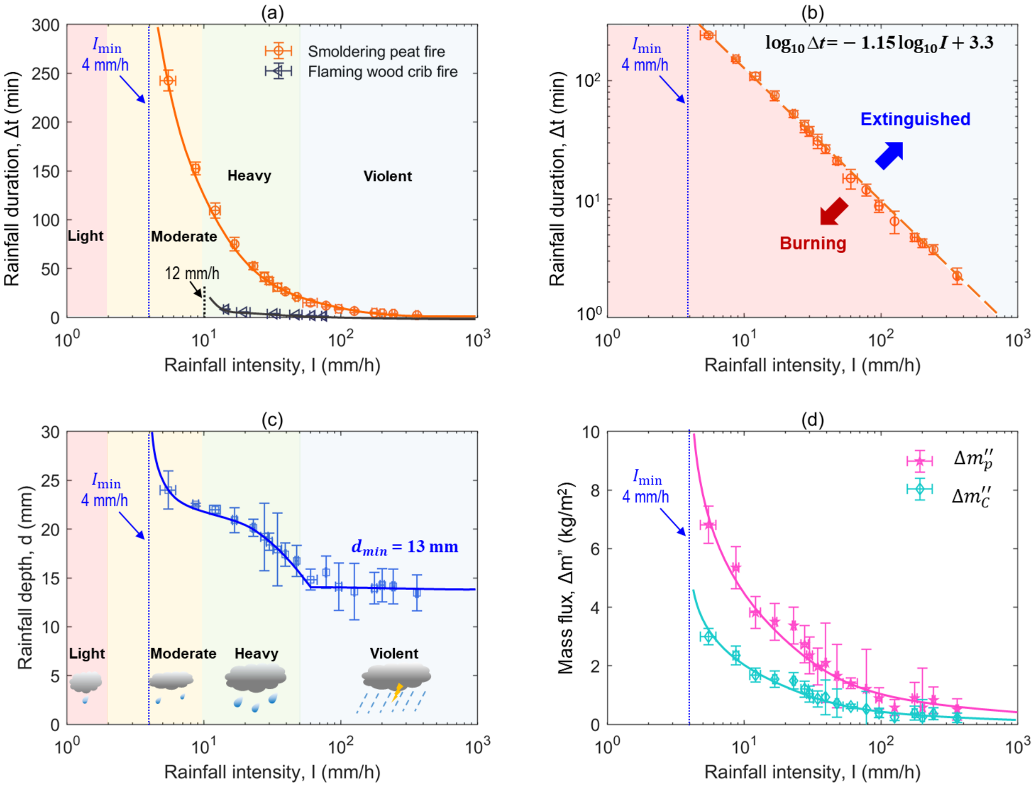

Fig. 9.2. Limiting conditions for extinguishing smouldering peat fire by rain. (a) The rainfall intensity vs. duration, (b) base-10 logarithm of suppression duration, (c) rainfall depth, (d) minimum mass loss of dry peat and carbon emissions, where the error bars show the standard deviation.

Figure 9.2d compares the mass loss of peat per unit area after successful suppression. As expected, the burning mass loss of peat decreases with the increase in rainfall intensity, indicating that more peat soils were consumed under lighter rain. For example, when the rainfall intensity increases from 30 mm/h to 100 mm/h, the mass loss decreases from 2.4 ± 0.6 kg/m^2 to 0.9 ± 0.3 kg/m^2. When the rainfall intensity is very small, rainwater will be quickly evaporated by the hot smouldering fire, and the rainwater cannot penetrate the burning zone, resulting in a maximum mass loss [29]. With a heavier rain, the burning zone is slowly penetrated and cooled by rainwater, meanwhile the smouldering fire continues to spread downward and burn out more fresh soil. With a violent rain, raindrops can flush over the soil layer to immediately extinguish the fire and minimize the burning of peat (see more details in Fig. 9.3). Figure 9.2d also estimates the corresponding carbon emissions per unit area from peat fire under different rainfall intensities, considering that the carbon content of this peat is about 44%. With the correction of rainfall influence, the prediction of carbon emissions from the peat fire can be improved and combined with the regional wildfire weather model [51].

9.3.2 Peat fire behaviours under rain suppression

Baseline experiments were conducted to determine the burning characteristics of the smouldering peat fire without the influence of rain. Once the peat was ignited and started to spread downward, a thin black char layer was formed on the free surface, which did not convert into white ash. The black char layer has also been observed in the field, because of large heat loss to the environment [22]. Below this thin char layer, there was a white ash layer as the char was further oxidized [37].

Figure 9.3a shows a group of thermocouple measurements of the baseline experiment, where the typical smouldering spread over a 15 cm-deep sample lasted for about 6 h. During the forced ignition by the coil heater, the temperature near the ignition zone (i.e., $T_{-5\text{ cm}}$ at 5 cm below the free surface) first increased and then remained stable at around 100 °C, indicating the robust on-going process of water evaporation. After a short period of drying, $T_{-5\text{ cm}}$ rapidly increased to a peak of around 500 °C. Once the coil igniter was off, $T_{-10\text{ cm}}$ (10 cm below the surface) first dropped but soon increased again, indicating that the smouldering fire becomes self-sustained [22]. Meanwhile, both T_0 and $T_{-5\text{ cm}}$ decreased due to burnout, and the thermocouple started to record the gas temperature, showing a high-frequency fluctuation. Figure 9.3b show the temperature evolution of peat fire under a rainfall intensity of 3 mm/h for more than 500 min. Despite of some fluctuation, the temperature evolutions are similar to the baseline measurement, and the entire 15-cm deep peat was burnout before the rain stops. In other words, a rainfall of 3 mm/h cannot suppress the smouldering peat fire.

Figure 9.3c-d compares the temperature evolutions of peat fire under a rainfall intensity of 35 mm/h (i.e., heavy rain) for 20 min (failed suppression) and 50 min (successful suppression). To better analyse the burning and suppression processes, we divided the temperature profile into three stages: (I) ignition and burning, (II) rain suppression, and (III) outcome. After the forced ignition for 60 min and following self-sustained burning for another 30 min, the surface of the peat sample shrank, exposing the thermocouples (T_0 and $T_{-5\ \mathrm{cm}}$). Once the simulated rain was activated (Stage II), those exposed thermocouples were directly cooled by raindrops to the ambient temperature. In the early stage of rain suppression, due to the intense water evaporation in the burning zone and the absorption of peat soils in the upper layer, it was difficult for raindrops to penetrate to deeper regions, so the decrease of $T_{-10\ \mathrm{cm}}$ was small. For the same reason, the temperature at the bottom ($T_{-15\ \mathrm{cm}}$) even increased initially.

For the failed fire suppression (Fig. 9.3c) after raining for 20 min, the visible white smoke was likely water vapor, because the measured temperature was still higher than 200 ℃. It was not possible to immediately determined by visual inspection whether the peat fire was suppressed or not, so that the in-situ detection of real underground peat fire remains a great challenge [37]. With thermocouple readings, we found in Stage III the $T_{-10\ \mathrm{cm}}$ first fluctuated shortly, and then showed a sudden increase to above 500 ℃, indicating a failed fire suppression. Despite the top peat layer that was wetted and extinguished by rain, they would be soon re-ignited. Eventually, the entire peat sample was burnout like the base case in Fig. 9.3a, except that the burning duration increased to about 500 min. Note that a short rain duration can still wet the peat and slow down the fire spread, although it may not extinguish the peat fire. Therefore, after rainfall, human firefighting effort will become more effective to extinguish the persistent peat fire completely.

For the successful fire suppression (Fig. 9.3d), white smoke was also observed from peat after raining for 50 min. Afterward, despite some fluctuations, $T_{-10\ \mathrm{cm}}$ gradually decreased to ambient temperature, and re-ignition did not occur, because the minimum temperature for igniting smouldering peat fire of about 250 ℃ [17] was not reached. Considering the self-ignition risk of peat [18], peat fire cannot be fully extinguished unless the sample temperature profile is lower than the self-ignition point. It is recommended that the suppression effort should be extended until the measured sample temperature was below 80 ℃ [29]. Setting a more sophisticated criterion for the successful suppression of peat fire needs more lab and field experiments.

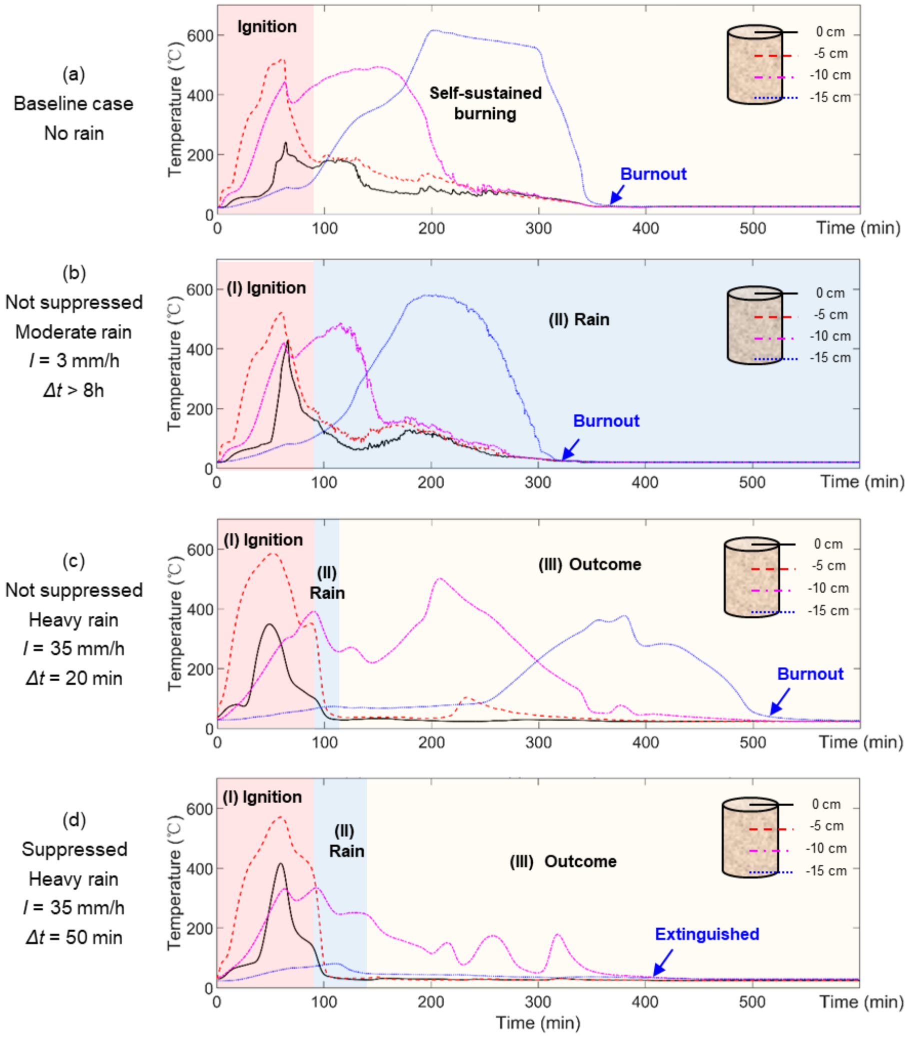

Fig. 9.3. Temperature measurements of the baseline and rain-suppression fire experiment, (a) baseline experiment, (b) failed fire suppression with rainfall intensity of 3 mm/h for more than 500 min, (c) failed fire suppression with rainfall intensity of 35 mm/h for 20 min, and (d) successful fire suppression with rainfall intensity of 35 mm/h for 50 min.

9.3.3 Minimum rainfall intensity for extinguishing

For rainfall intensity lighter than 4 mm/h, the smouldering peat fire behaviour is similar to that without rainfall, as compared in Fig. 9.3a-b. In other words, the rainwater will be directly evaporated by the hot burning zone on the surface layer (Fig. 9.4a), so that raindrops are not able to penetrate through the burning zone regardless of rainfall duration. As the rainfall intensity reaches the level of moderate and heavy rain (4-50 mm/h), the rainwater starts to penetrate and cool the burning zone (Fig. 9.4b). Thus, as the rainfall intensity increases, the required suppression duration and rainfall depth, as well as the carbon emissions are reduced. For a violent rain (>50 mm/h), a large amount of rainwater quickly flushes over and cools down the burning soil layer, and eventually quenching the smouldering peat fire (Fig. 9.4c). With the extinction limits obtained in Fig. 9.2, it is possible to identify the effectiveness of rainfall in suppressing peat fire in situ, evaluate the probability of re-ignition after rain, and provide more information to guide the follow-up human firefighting activities.

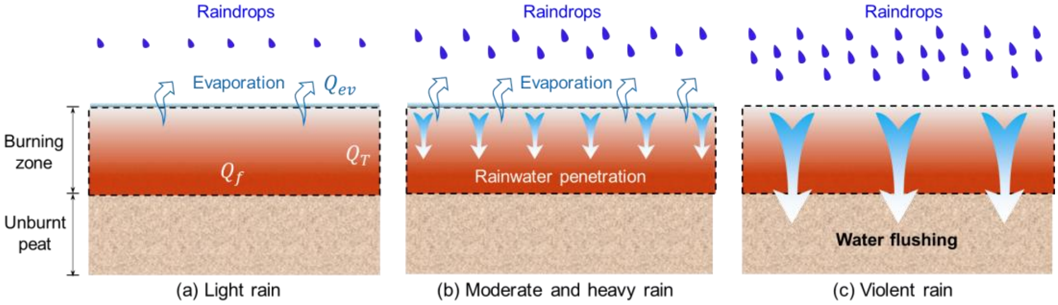

Fig. 9.4. Different modes of rain suppression. (a) Light rain where all raindrops are evaporated by the smouldering peat fire, and (b) moderate and heavy rain where raindrops penetrate to the burning zone, and (c) violent rain where the rainwater flushes through the burning zone.

To scientifically understand the suppression limit of the peat fire, the minimum temperature to sustain the smouldering peat fire ($T_{min} \approx 250$ °C) is defined [17]. Below this threshold or ignition temperature, the exothermic char-oxidation reaction becomes too weak to overcome the environmental cooling and maintain the peat fire. Then, an energy-conservation equation is proposed to explain the process of rain suppression. At the extinction limit, the heat released from the smouldering fire zone (Q_f) during rainfall and the extra thermal energy stored in peat (Q_T) should be able to evaporate all raindrops (Q_{ev}) as

$$Q_f + Q_T = Q_{ev} \tag{9.3a}$$

which can be further expressed as

$$\dot{m}_p'' \Delta H_{sm} \Delta t + \delta_{sm} \rho_p c_p (T_{sm} - T_{min}) = d \rho_w \Delta H_w \tag{9.3b}$$

where $\dot{m}_p''$ is the burning flux of peat fire, ρ_p is the dry peat density, ΔH_{sm} is the heat of smouldering combustion, δ_{sm} is the thickness of the smouldering reaction zone, c_p is the specific heat of peat, T_{sm} is the instant smouldering temperature, T_{min} is the minimum temperature for smouldering fire, d is the rainfall depth, ρ_w is the water density, and ΔH_w is the overall heat of vaporization of water.

The minimum rainfall intensity (I_{min}) occurs when the rainwater only balances the heat release without weakening the burning zone ($Q_c = Q_{ev}$), as shown in Fig. 9.4a. Otherwise, the burning zone will become smaller and eventually extinguish. Thus

$$\dot{m}_p'' \Delta H_{sm} \Delta t = d\rho_w \Delta H_{ev} = I_{min} \Delta t \rho_w \Delta H_w \qquad (9.4a)$$

By reorganizing, the minimum rainfall intensity ($I_{min,cal}$) can be calculated as

$$I_{min,cal} = \frac{\dot{m}_p'' \Delta H_{sm}}{\rho_w \Delta H_w} \qquad (9.4b)$$

where $\dot{m}_p''$ = 0.2 g/(m^2·s^1), ρ_w= 1000 kg/m^3, and $\Delta H_w = c_w(T_b - T_a) + \Delta H_{ev}$ = 2.4 MJ/kg are found from the literature [17,22]. The calculated minimum rainfall intensity is 3.3 mm/h, close to the experimental measurement of 4 mm/h.

9.3.4 Minimum rainfall depth

Once the rainfall intensity exceeds the minimum value, the extra rainwater will start to penetrate and wet the burning fire zone (Fig. 9.4b). With I_{min}, Eq. 9.3b can be expressed as

$$\delta_{sm} \rho_p c_p (T_{sm} - T_{min}) = (I - I_{min}) \Delta t \rho_w \Delta H_w \qquad (9.5a)$$

Then, we can estimate the required rainfall depth (d) given a rainfall intensity (I)

$$d = \varphi \frac{I}{I - I_{min}} \qquad (9.5b)$$

where $\varphi = \delta_{sm} \rho_p c_p (T_{sm} - T_{min}) / (\rho_w \Delta H_w)$ is a constant for the given peat soil. Therefore, the required rainfall depth decreases with the increasing rainfall intensity, agreeing with Fig. 9.2c.

When the rain becomes violent (I > 50 mm/h), the required suppression duration is very short ($\Delta t \rightarrow 0$), and the temperature of rainwater will not increase to 100 °C to trigger massive evaporation (see Fig. 9.4c). Thus, both the chemical energy and water evaporation can be neglected. Then, a minimum amount of rainwater (d_{min}) is required to directly quench the burning zone ($Q_T = Q_{ev}$) as

$$\delta_{sm} \rho_p c_p (T_{sm} - T_{min}) = d_{min} \rho_w c_w (T_w - T_a) \qquad (9.6a)$$

where T_w is the temperature of rainwater after flushing through the burning zone. Therefore, the minimum rainfall depth can be expressed as

$$d_{min} = \frac{\delta_{sm} \rho_p c_p (T_{sm} - T_{min})}{\rho_w c_w (T_w - T_a)} \qquad (9.6b)$$

Given that $\delta_{sm} \approx 0.1$ m, $\rho_p = 145$ kg/m^3, and $T_{sm} \approx 400$ °C measured from experiments [20,22], as well as, literature values of $c_w \approx 4.2$ kJ/(kg·K), $c_p \approx 2$ kJ/(kg·K) and $T_{min} = 250$ °C [17], and $T_{w,max} = 100$ °C, we can then calculate the upper limit of minimum rainfall depth to be 15 mm, which also successfully explains the experimental measurement of 13 mm.

Note that current fire-suppression experiments are conducted for the peat fire in the shallow soil layer up to 15 cm deep, which is the first step to understand the effectiveness of rain and other water-based strategies in suppressing peat fire. The peat fire in the field can also survive in the deep soil layer [7,37]. These deep underground peat fires can be more difficult to suppress, requiring a longer rainfall duration and a larger rainfall depth. Therefore, more experiments will be conducted in the future to investigate rain suppression of deep underground peat fire with larger-scale field experiments, where the fire-suppression effectiveness by the varied rainfall scenarios will be explored.

8.4 Conclusions

In this research, we assess the underlying mechanism of rain in suppressing the peat fire in the shallow soil layer up to 15 cm deep through laboratory experiments. The minimum rainfall intensity to extinguish the peat fire is found to be roughly 4 mm/h, so that the persistent light rain cannot extinguish such smouldering wildfire. The required rainfall duration, Δt (min), for extinguishing peat fire decreases with the rainfall intensities, I (mm/h), as $\log_{10} \Delta t = -1.15 \log_{10} I + 3.3$. For example, for a heavy rain of 30 mm/h, it takes at least 40 min to extinguish the smouldering peat fire near the ground surface. Such a required rainfall duration is much longer than that for a small flaming wildfire ($\log_{10} \Delta t = -\log_{10} I + 1.9$).

We also identify that the required rainfall depth to extinguish the peat fire gradually decreases with the rainfall intensity and approaches a minimum value of 13 mm under violent rain. As rainfall intensity increases, the carbon emission flux from peat fire decreases. Therefore, the short-term violent rain is most effective for extinguishing the persistent peat fire. This research helps evaluate the impact of weather on the development of peat fire and improve the prediction of global carbon emissions from peat fire with the use of regional weather model.

Acknowledgements

This research is funded by National Science Foundation of China (NSFC) No. 51876183. The authors thank for the inspiration from Prof. Guillermo Rein (Imperial College London). S. Lin would like to thank Y. K. Cheung and Y. Xiao for the help in the lab.

References

[1] Montzka SA, Dlugokencky EJ, Butler JH. Non-CO 2 greenhouse gases and climate change. Nature 2011;476:43–50.

[2] Park SW, Kim JS, Kug JS. The intensification of Arctic warming as a result of CO2 physiological forcing. Nat Commun 2020;11:1–7.

[3] Batir JF, Hornbach MJ, Blackwell DD. Ten years of measurements and modeling of soil

temperature changes and their effects on permafrost in Northwestern Alaska. Glob Planet Change 2017;148:55–71.

[4] Helmore E. “Unprecedented”: more than 100 Arctic wildfires burn in worst ever season. Guard 2019.

[5] Héon J, Arseneault D, Parisien MA. Resistance of the boreal forest to high burn rates. Proc Natl Acad Sci U S A 2014;111:13888–93.

[6] Vinas M-J. NASA studies how arctic wildfires change the world. NASA 2019.

[7] Page SE, Siegert F, Rieley JO, Boehm H V., Jayak A, Limink S, et al. The amount of carbon released from peat and forest fires in Indonesia during 1997. Nature 2002;420:61–6.

[8] Nelson K, Thompson D, Hopkinson C, Petrone R, Chasmer L. Peatland-fire interactions: A review of wildland fire feedbacks and interactions in Canadian boreal peatlands. Sci Total Environ 2021;769:145212.

[9] Mack MC, Bret-Harte MS, Hollingsworth TN, Jandt RR, Schuur EAG, Shaver GR, et al. Carbon loss from an unprecedented Arctic tundra wildfire. Nature 2011;475:489–92.

[10] Kohlenberg AJ, Turetsky MR, Thompson DK, Branfireun BA, Mitchell CPJ. Controls on boreal peat combustion and resulting emissions of carbon and mercury. Environ Res Lett 2018;13.

[11] Xu J, Morris PJ, Liu J, Holden J. PEATMAP: Refining estimates of global peatland distribution based on a meta-analysis. Catena 2018;160:134–40.

[12] Lin S, Sun P, Huang X. Can peat soil support a flaming wildfire? Int J Wildl Fire 2019;28:601–13.

[13] Turetsky MR, Benscoter B, Page S, Rein G, Van Der Werf GR, Watts A. Global vulnerability of peatlands to fire and carbon loss. Nat Geosci 2015;8:11–4.

[14] Grau-Andrés R, Davies GM, Gray A, Scott EM, Waldron S. Fire severity is more sensitive to low fuel moisture content on Calluna heathlands than on peat bogs. Sci Total Environ 2018;616–617:1261–9.

[15] Jones BM, Grosse G, Arp CD, Miller E, Liu L, Hayes DJ, et al. Recent Arctic tundra fire initiates widespread thermokarst development. Sci Rep 2015;5:1–13.

[16] Koven CD, Ringeval B, Friedlingstein P, Ciais P, Cadule P, Khvorostyanov D, et al. Permafrost carbon-climate feedbacks accelerate global warming. Proc Natl Acad Sci U S A 2011;108:14769–74.

[17] Gibson CM, Chasmer LE, Thompson DK, Quinton WL, Flannigan MD, Olefeldt D. Wildfire as a major driver of recent permafrost thaw in boreal peatlands. Nat Commun 2018;9:3041.

[18] Wilkinson SL, Tekatch AM, Markle CE, Moore PA, Waddington JM. Shallow peat is most vulnerable to high peat burn severity during wildfire. Environ Res Lett 2020;15:104032.

[19] Dobinski W. Permafrost. Earth-Science Rev 2011;108:158–69.

[20] Belcher CM, Yearsley JM, Hadden RM, Mcelwain JC, Rein G. Baseline intrinsic flammability of Earth ’ s ecosystems estimated from paleoatmospheric oxygen over the past 350 million years. Proc Natl Acad Sci 2010;107:22448–22453.

[21] Huang X, Rein G. Interactions of Earth’s atmospheric oxygen and fuel moisture in smouldering wildfires. Sci Total Environ 2016;572:1440–6.

[22] Frandsen WH. The influence of moisture and mineral soil on the combustion limits of smouldering forest duff. Can J For Res 1987;16:1540–4.

[23] Lin S, Huang X. Quenching of smouldering: Effect of wall cooling on extinction. Proc Combust Inst 2021;38:5015–22.

[24] Lin S, Liu Y, Huang X. How to Build a Firebreak to Stop Smouldering Peat Fire : Insights from a Laboratory-Scale Study. Int J Wildl Fire 2021.

[25] Girardin MP, Mudelsee M. Past and Future Changes in Canadian Boreal Wildfire. Ecol Appl 2008;18:391–406.

[26] Hanes CC, Wang X, Jain P, Parisien MA, Little JM, Flannigan MD. Fire-regime changes in canada over the last half century. Can J For Res 2019;49:256–69.

[27] Flannigan M, Stocks B, Turetsky M, Wotton M. Impacts of climate change on fire activity and fire management in the circumboreal forest. Glob Chang Biol 2009;15:549–60.

[28] Schuur EAG, McGuire AD, Schädel C, Grosse G, Harden JW, Hayes DJ, et al. Climate change and the permafrost carbon feedback. Nature 2015;520:171–9.

[29] Léger E, Dafflon B, Robert Y, Ulrich C, Peterson JE, Biraud SC, et al. A distributed temperature profiling method for assessing spatial variability in ground temperatures in a discontinuous permafrost region of Alaska. Cryosphere 2019;13:2853–67.

[30] Lin S, Cheung YK, Xiao Y, Huang X. Can rain suppress smouldering peat fire ? Sci Total Environ 2020;727:138468.

[31] Huang X, Rein G. Downward Spread of Smouldering Peat Fire: the Role of Moisture, Density and Oxygen Supply. Int J Wildl Fire 2017;26:907–18.

[32] Rein G. Smouldering Fires and Natural Fuels. In: Claire M. Belcher, editor. Fire Phenom. Earth Syst., New York: John Wiley & Sons, Ltd.; 2013, p. 15–34.

[33] Smith LC, Beilman DW, Kremenetski K V., Sheng Y, MacDonald GM, Lammers RB, et al. Influence of permafrost on water storage in West Siberian peatlands revealed from a new database of soil properties. Permafr Periglac Process 2012;23:69–79.

[34] Wang X, Jiang D, Lang X. Future extreme climate changes linked to global warming intensity. Sci Bull 2017;62:1673–80.

[35] Sirin AA, Makarov DA, Gummert I, Maslov AA, Gul'be YI. Depth of Peat Burning and Carbon Loss during an Underground Forest Fire. Contemp Probl Ecol 2020;13:769–79.

[36] Benscoter BW, Thompson, D. K., Waddington JM, Flannigan MD, Wotton BM, de Groot WJ, Turetsky MR. Interactive effects of vegetation, soil moisture and bulk density on depth of burning of thick organic soils. Int J Wildl Fire 2011;20:418–29.

[37] Davies GM, Gray A, Rein G, Legg CJ. Peat consumption and carbon loss due to smouldering wildfire in a temperate peatland. For Ecol Manage 2013;308:169–77.

[38] Ballhorn U, Siegert F, Mason M, Limin S. Derivation of burn scar depths and estimation of carbon emissions with LIDAR in Indonesian peatlands. Proc Natl Acad Sci 2009;106:21213–8.

[39] Treat CC, Jones MC, Camill P, Gallego-Sala A, Garneau M, Harden JW, et al. Effects of permafrost aggradation on peat properties as determined from a pan-Arctic synthesis of plant macrofossils. J Geophys Res Biogeosciences 2016;121:78–94.

[40] Huang X, Rein G. Upward-and-downward spread of smouldering peat fire. Proc Combust Inst 2019;37:4025–33.

[41] Oechel WC, Vourlitis GL, Verfaillie J, Crawford T, Brooks S, Dumas E, et al. A scaling approach for quantifying the net CO2 flux of the Kuparuk River Basin, Alaska. Glob Chang Biol 2000;6:160–73.

[42] Zoltai SC, Morrissey LA, Livingston GP, De Groot WJ. Effects of fires on carbon cycling in North American boreal peatlands. Environ Rev 1998;6:13–24.

[43] Shaver GR, Chapin FS. Production: Biomass relationships and element cycling in contrasting

arctic vegetation types. Ecol Monogr 1991;61:1–23.

[44] Mcguire AD, Anderson LG, Christensen TR, Scott D, Laodong G, Hayes DJ, et al. Sensitivity of the carbon cycle in the Arctic to climate change. Ecol Monogr 2009;79:523–55.

[45] Boden TA, Marland G, Ndres RJ. Global, Regional, and National Fossil-Fuel CO2 Emissions (1751 - 2014). Environ Syst Sci Data Infrastruct a Virtual Ecosyst (United States); Carbon Dioxide Inf Anal Cent (CDIAC), Oak Ridge Natl Lab (ORNL), Oak Ridge, TN (United States) 2017.

[46] Reyes A V., Cooke CA. Northern peatland initiation lagged abrupt increases in deglacial atmospheric CH4. Proc Natl Acad Sci U S A 2011;108:4748–53.

[47] Turetsky MR, Abbott BW, Jones MC, Walter Anthony K, Olefeldt D, Schuur EAG, et al. Permafrost collapse is accelerating carbon release. Nature 2019;569:32–4.

[48] IPCC. Climate change 2007: Synthesis Report. Geneva,Switzerland: 2007.

[49] Szép R, Bodor Z, Miklóssy I, Niță IA, Oprea OA, Keresztesi Á. Influence of peat fires on the rainwater chemistry in intra-mountain basins with specific atmospheric circulations (Eastern Carpathians, Romania). Sci Total Environ 2019;647:275–89.

[50] Hobara S, McCalley C, Koba K, Giblin AE, Weiss MS, Gettel GM, et al. Nitrogen fixation in surface soils and vegetation in an arctic tundra watershed: A key source of atmospheric nitrogen. Arctic, Antarct Alp Res 2006;38:363–72.

[51] Yoshikawa K, Bolton WR, Romanovsky VE, Fukuda M, Hinzman LD. Impacts of wildfire on the permafrost in the boreal forests of interior Alaska. J Geophys Res D Atmos 2003;108:8148.

[52] Ding Y, Zhang S, Zhao L, Li Z, Kang S. Global warming weakening the inherent stability of glaciers and permafrost. Sci Bull 2019;64:245–53.

[53] Hugelius G, Loisel J, Chadburn S, Jackson RB, Jones M, MacDonald G, et al. Large stocks of peatland carbon and nitrogen are vulnerable to permafrost thaw. Proc Natl Acad Sci U S A 2020;117:20438–46.

[54] Camill P. Permafrost thaw accelerates in boreal peatlands during late-20th century climate warming. Clim Change 2005;68:135–52.

[55] Biskaborn BK, Smith SL, Noetzli J, Matthes H, Vieira G, Streletskiy DA, et al. Permafrost is warming at a global scale. Nat Commun 2019;10:1–11.

[56] Spencer CN, Gabel KO, Hauer FR. Wildfire effects on stream food webs and nutrient dynamics in Glacier National Park, USA. For Ecol Manage 2003;178:141–53.

[57] Kump LR, Mackenzie FT. Regulation of atmospheric O2: Feedback in the microbial feedbag. Science (80-) 1996;271:459–60.

[58] Smith HG, Sheridan GJ, Lane PNJ, Nyman P, Haydon S. Wildfire effects on water quality in forest catchments: A review with implications for water supply. J Hydrol 2011;396:170–92.

[59] Santos RMB, Sanches Fernandes LF, Pereira MG, Cortes RMV, Pacheco FAL. Water resources planning for a river basin with recurrent wildfires. Sci Total Environ 2015;526:1–13.

CHAPTER 10: Climate-Induced Arctic Peatland Smouldering Fire and Carbon Loss

Summary:

Boreal peatlands are increasingly vulnerable to wildfires as climate change continues accelerating. Fires consume substantial quantities of organic soils and rapidly transfer large stocks of terrestrial carbon to the atmosphere. Herein, we quantify the minimum environmental temperature that allows the moist peat to smoulder, as the fire threshold of peatlands. We then apply a typical vertical soil temperature profile to estimate the future depth of burn and carbon emissions in boreal peatland fires under the impact of global warming. If the boreal region continues warming at a rate of 0.44 °C/decade, we estimate that the carbon loss from the boreal peat fires on a warmer soil layer may increase from 143 Mt in 2015 to 544 Mt in 2100 and reach a total of 28 Gt in the 21st century. If the global human efforts successfully reduce the boreal warming rate to 0.3 °C/decade, the peat fire carbon loss would drop by 21% to 22 Gt in the 21st century. This work helps understand the vulnerability of boreal peatland to more frequent and severer wildfires driven by global warming and estimate climate-induced carbon emissions from boreal peatland fires in the 21st century.

This Chapter is based on "S. Lin, Y. Liu and X. Huang (2021) *Climate-induced boreal peatland fire and carbon loss in the 21st century.* **Science of the Total Environment** 796: 148924. doi: 10.1016/j.scitotenv.2021.148924"

10.1 Introduction

Climate change is accelerating, and its effects are deteriorating as man-made greenhouse gas emissions continue rising [1,2]. In the Arctic and boreal (subarctic) region, the ambient temperature has increased a warming rate of ~0.44 °C/decade [3]. As the environmental conditions become more favourable for wildfires, the boreal region has suffered from its worst wildfire season and the longest-lasting burning duration [4,5]. Unlike the burning of trees and shrubs in lower-latitude regions, a significant portion of boreal wildfires is in the form of flameless burning or smouldering of organic soils and permafrost in peatlands [6]. Wildfire is a climate-sensitive process that may rapidly transfer large stocks of terrestrial carbon to the atmosphere [7,8], representing positive feedback that accelerates climate warming as projected by Earth System Models [9].

Peatlands are integral parts of boreal landscapes in the northern hemisphere, occupying roughly 4×10^6 km^2 of Earth land [42], with around 480 Gt of carbon stored in terrestrial soils [10]. Peat consists primarily of partially decayed vegetation accumulated on the Earth surface under acidic, anaerobic, and close to water-saturated conditions [11]. Pristine peatlands or permafrost in the boreal region may hold a large amount of soil water, and their low temperature also restricts the direct burning of soil [12–14]. However, global warming has already led to changes in the fire regime [10]. In the permafrost peatland regions, climate change deepens the active layer [15] and makes previously frozen organic matter available to microbial decomposition [16], promoting more frequent peatland fires [17].

The upper peat layer is most vulnerable to ambient condition and often has a high burn severity during wildfires [18]. During the fire season, the upper soil layer becomes warmer under a higher ambient temperature, so the upper soil layer temperature decreases with depth [19]. Once ignited from the top surface, the smouldering fire starts to propagate downwards until the deeper soil layer is colder and wetter than the fire threshold. The smouldering fire threshold of peat has been an emerging research topic, and the critical influencing factors include oxygen concentration [20,21], moisture content [21], inorganic content [22], and fuel configurations [23,24]. Although it has been argued that the frequency and severity of wildfires in the boreal region have been increasing as a result of global warming [17], there is still not enough quantitative data on such a trend [25–27]. Several Earth-system models have been applied to predict the carbon loss from the arctic and boreal regions under global warming [28], but the impact of peatland fires is rarely included. Therefore, it is urgent to understand the fire severity in the arctic and boreal peatlands and the associated fire carbon emissions under different global warming scenarios.

In this work, we interpret the peat fire threshold as a function of the minimum environmental temperature vs soil gravimetric moisture content (MC). Afterwards, based on the field measurement of the vertical soil temperature profile in the boreal peatland of Alaska [29], this fire threshold will be used to estimate the depth of burn (DOB) in boreal peatlands. We then further project the carbon emissions from the boreal peatland fires under different global warming scenarios in the 21st century. This research aims to explore how global warming has deteriorated the fire hazards in arctic and boreal peatlands and how this process will give feedback to climate change and impact the Earth ecosystem.

10.2 Experimental methods

10.2.1 Peat soil collection

The properties of boreal peat soils may vary with the time, space and depth with huge variabilities and uncertainties. Therefore, a moss peat sample from Estonian boreal forest with high organic content (>97%), uniform density and homogenous particle size was selected as the typical boreal peat soil (Fig. 10.1) [12,30]. Such high-organic content peat soil has the highest smouldering fire risk, thus defining the worst peat fire scenario [24]. The estimation based on this kind of high-organic peat may provide an upper limit of global carbon loss from boreal peat fires.

The peat soil was first oven-dried at 90 °C for 48h, and the oven-dried bulk density was 145 kg/m^3. Afterwards, the oven-dried peat soil was thoroughly mixed with the corresponding water to obtain the desired gravimetric moisture contents [12,30]. For example, 1 kg of dry peat, by mixing with 1 kg of water, produced 2 kg of wet peat of 100% MC. The mixed peat samples were stored inside a sealed box for homogenization naturally for at least another 48 h before the fire test [31]. As the thoroughly dried peat (i.e., MC $\leq$ 10%) was rare in nature, the targeted MCs for fire tests varied from 25% to 150%, with an interval of 25%.

For each test, the 1.5 L peat sample was placed inside a smouldering reactor that had an inner cross-section area of 10 cm × 10 cm and a height of 15 cm (Fig. 10.1). The reactor was made of 1-cm thick ceramic insulation boards, and its outer surface was covered by several thin layers of aluminium foil to prevent gas leakage and limit the radiative heat loss [31]. In the process of filling the peat soils into the reactor, the moist sample was consolidated to ensure the dry bulk density fixed to 145 kg m^{-3}, regardless of the MC.

10.2.2 Environment control

Experiments were conducted in a temperature-controlled freezer from -45 °C to 20 °C or an oven from 25 °C to 45 °C. The internal volumes of the freezer (40×40×110 cm^3) and oven (44×59×68 cm^3) were two orders of magnitude greater than the 1.5-L smouldering reactor. Two vents with a 2.5-cm diameter were designed on the back of the chamber to ensure that both the oxygen supply and smoke ventilation were sufficient. A small fan was installed inside the chamber to help homogenize the airflow. The oxygen concentration was stabilized at 20.9% during the burning process, as measured by an oxygen sensor. Several boxes of water/ice were placed inside the chamber, which increased the system thermal inertia and reduced the influence of fire heat release on the controlled environment temperature.

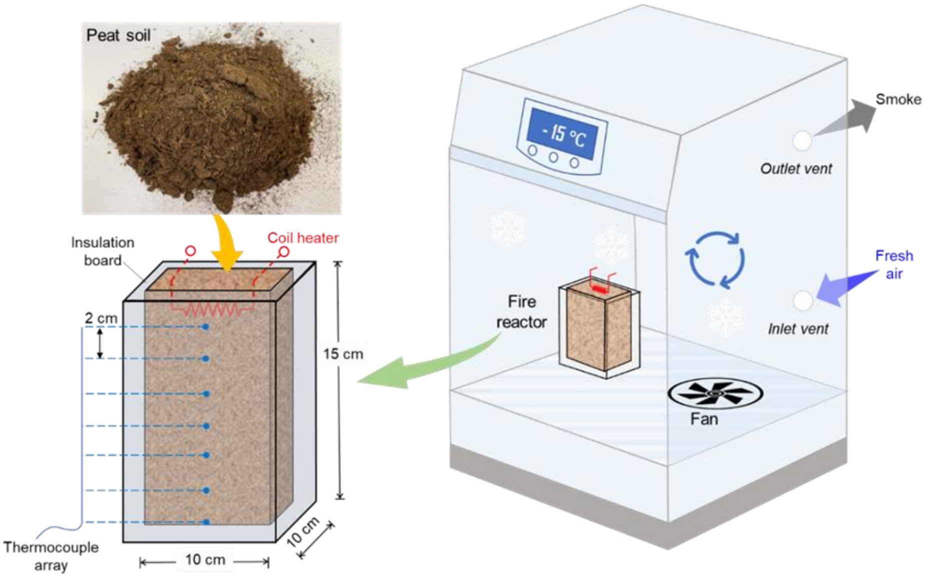

Fig. 10.1. Photo of peat soil and schematic diagram of the fire reactor and temperature-controlled chamber.

Initially, the temperature inside the chamber was set to a prescribed value and monitored by several thermocouples. To monitor the temperature profile of the peat sample, seven armoured K-type thermocouples with a bead diameter of 1 mm were placed from 3 cm to 15 cm below the top free surface with an interval of 2 cm (Fig. 10.1). When the default temperature sensor of freeze/oven and all thermocouples inside reached the prescribed temperature and stabilized for hours, the desired test environment was ready.

10.2.3 Initiation of the peat fire

For ignition, a 10-cm long coil heater made of 0.3-mm thick $Cr_{20}Ni_{80}$ wire was buried into the peat sample 1.5 cm below the top free surface. The ignition protocol was fixed at 100 W for 30 min, so it was strong enough to initiate a robust and uniform smouldering front in a peat sample with MC up to 150% at the ambient temperature of 20-30 °C [30,31]. For the smouldering peat fire, it is difficult to judge the success of ignition and fire spread visually, especially when the fire front is below the free surface [32]. Nevertheless, the thermocouple array inside the peat sample could monitor the entire ignition and fire-propagation processes. For a fixed peat gravimetric moisture content, if the sample was successfully ignited and self-propagating, the environmental temperature was lowered to test a fresh sample until the fire could no longer propagate. Then, the minimum environmental temperature for this moist peat was found. For each test scenario, at least three repeating fire tests were conducted to quantify the experimental uncertainty.

10.2.4 Estimation of carbon emissions from peat fires

The typical arctic and boreal peat layer temperature profile during the fire season in Alaska was applied to estimate the depth of burn, where the soil temperature decreases with depth [29]. From a database of 12,705 measurements, the average MC of in northern hemisphere peat within the upper peat layers down to 58 cm is about 82% [33]. It was assumed that the ignited smouldering fire would propagate downward until reaching the soil layer where the temperature was too cold to maintain the fire. This minimum environmental temperature is defined as the peatland fire threshold. Then, we can estimate the possible depth of burn if the fire occurs.

Afterwards, the carbon emission flux of the burnt peatland ($\dot{m}_C''$) [kg C/m^2] may be estimated as $\dot{m}_C'' = \rho \cdot C \cdot DOB$, where ρ is the dry bulk density of soil on the surface layer of boreal peatland, and C is the carbon mass fraction of peat [7,9]. It was also assumed that the peatland soil temperature profile near the ground surface would increase simultaneously [3]. The annual carbon emissions from all peatland fires [Mt/year] may be estimated as $\dot{m}_C = \eta \cdot A \cdot \dot{m}_C''$, where η and A are the annual burn probability [%/year] and the total land area [km^2] of peatlands, respectively.

10.3 Results and Discussion

10.3.1 Peat fire behaviours

Our experiments reveal the fire threshold of peatlands on Earth, that is, the minimum environmental temperature that just allows a self-sustained smouldering fire on the peat soil. Fig. 10.2 shows the temperature measurements of two experimental cases at the controlled environmental temperature of -5 °C, where one sample has the MC of 25% (Fig. 10.2a), and the other has the MC of 75% (Fig. 10.2b). Before ignition, the peat sample was cooled down to the prescribed environment temperature and stabilized for several hours. During the ignition process, the temperature near the electrical heater quickly increased above 400 °C, indicating a robust heating process. After 30 min, the heating power was turned off, then a sudden drop in temperature was observed. A successful ignition was defined if the smouldering fire propagated downwards with the soil temperature above 250 °C for a significant period after the external heating (see Fig. 10.2a) [20,23]. In contrast, a failed ignition was defined if all measured soil temperatures decreased gradually to the environmental temperature after the heating source was turned off (see Fig. 10.2b).

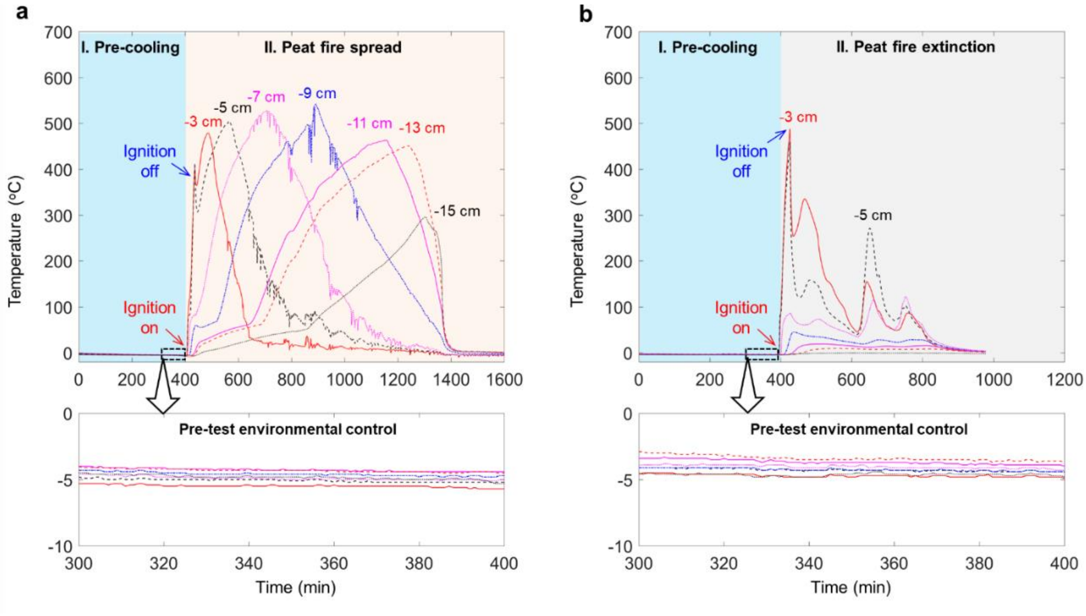

Fig. 10.2. Thermocouple data of (a) successful smouldering propagation in the peat of MC=25%, and (b) failed smouldering spread (extinction) in the peat of MC=75% at the environmental temperature of -5 °C.

10.3.2 The vulnerability of boreal peatland

Fig. 10.3 summarizes the fire threshold of peat on Earth in terms of the minimum environmental temperature that just allows a self-sustained smouldering fire (T_{crt}). As expected, the minimum temperature that allows the smouldering of peat soil increases with the soil moisture. For example, as the MC increases from 50% to 75%, the minimum temperature increases from -20 °C to 5 °C. For the frozen soils (< 0 °C), if the gravimetric moisture content is higher than 75%, it is resistant to a smouldering fire. However, global warming drives the soil temperature to continue increasing at the rate of about 0.44 °C/decade in boreal peatlands [3]; thus, the vulnerability of peatland to smouldering wildfires may increase over time. The deteriorating peatland fire severity, indicated by massive burnt soils, may release a tremendous amount of terrestrial carbon to accelerate global warming, creating positive feedback.

Two linear correlations are found for the smouldering fire threshold of peatland as a function of the minimum environmental temperature and the peat gravimetric moisture content, that is, $\mathrm{T}_{crt}^{-} = 82\mathrm{MC} - 57$ for the frozen peat soil (or permafrost) and $\mathrm{T}_{crt}^{+} = 42\mathrm{MC} - 28$ for nonfrozen peat soil. As extra heat is required to thaw the permafrost, the fire threshold of frozen peatlands (permafrost) is more sensitive to the soil moisture profile. The average MC of 82% for the boreal peatland, based on massive field measurements [33], was used in the subsequent analysis. With this gravimetric moisture content, the corresponding minimum environmental temperature allowing a stable smouldering peat fire is about 6.5 °C. Although global warming may dry the soil and reduce the soil moisture, such an effect may be compensated by the increase in precipitation [34]. Thus, compared to the soil temperature, the average MC in boreal peatlands may be less sensitive to global warming.

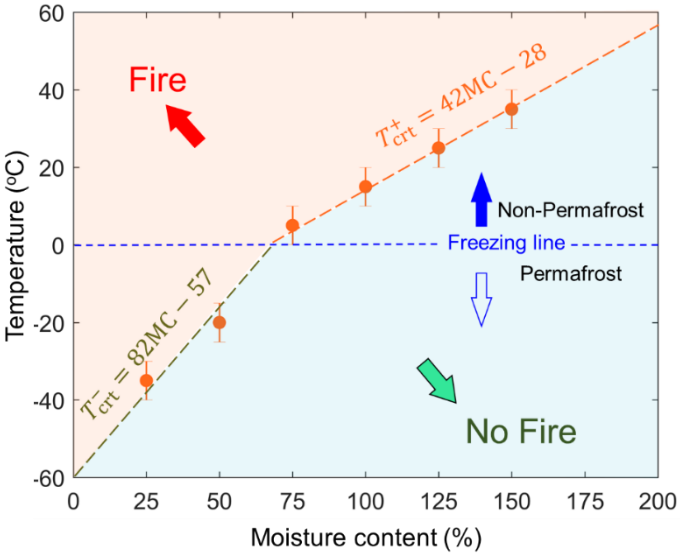

Fig. 10.3. The vulnerability of peat soil with different gravimetric moisture contents, represented by the minimum environmental temperature that allows a self-sustained smouldering front to propagate.

10.3.3 Depth of burn and carbon loss

If a smouldering fire is ignited on the peatland by lightning or human activities, it may spread both laterally and in-depth until the soil layer is too cold or too wet to maintain the fire. After extinction, the depth of burn (DOB) may be used to estimate the fire emissions [7]. Fig. 10.4 shows the vertical summer soil temperature over the top 1.5 m based on the measurement of a long-term monitoring station in the boreal peatland of Alaska [29]. During the hot and dry fire season, the soil temperature shows a decreasing trend with the depth over the top layer [19]. Under the current global warming rate, the temperature of boreal peatland may increase at the rate of 0.44 °C/decade [3], and Fig. 10.4 shows the expected soil temperature profile in 2050 and 2100. We then illustrate the fire threshold of peat (i.e., 6.5 °C) from Fig. 10.3 in terms of average soil moisture of 82% (plotted as black dash line in Fig. 10.4), and the potential DOB could be quantified if a fire occurs (Fig. A10.2b).

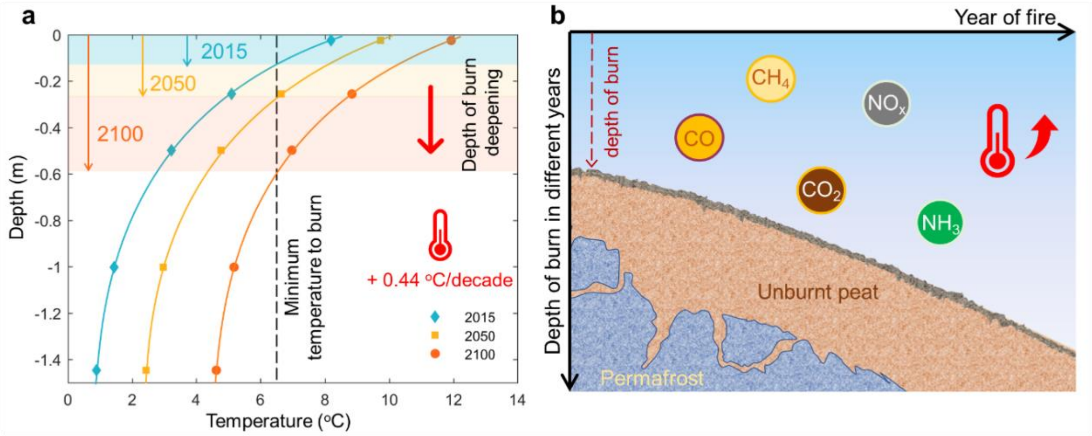

Fig. 10.4. (a) The measured vertical soil temperature profile in Alaska in the summer of 2015 [29] and the projected temperature profile in 2050 and 2100 at the warming of 0.44 °C/decade [3], where the shadow part represents the potential deepening depth of burn per smouldering peatland fire due to the warming, and (b) simplified illustration of the future depth of burn (DOB).

Fig. 10.4 shows that based on the acquired fire-threshold boundary, the top 0.16 m thick boreal peat layer would be burnt during wildfires in 2015. This predicted DOB is close to multiple field measurements at several boreal and subarctic peatlands in Russia [35], Alberta, Canada [36], Scottish Highlands [37], and Northern Alaska [9], whereas it is lower than that in tropical peatland fires [7,38]. Thus, the reliability of this model is verified by the historical data. Under the warming rate of

0.44 °C/decade, the potential depth of burn is projected to increase to about 0.28 m in 2050 and 0.60 m in 2100, showing 79% and 280% increments compared to the year 2015 (Fig. A10.2b). Based on our model, an empirical correlation can be established to estimate future DOB [m] in boreal peatlands as a function of the soil moisture, global warning rate, and year as

$$DOB = 2.36[42\mathrm{MC} - 28 - \alpha(Y - 2015)]^{-0.38} - 1 \qquad (10.1)$$

where Y is the year, and α (°C/year) is the warming rate in boreal peatlands. The R^2 coefficient of this correlation is 0.92. If the soil is severely dried to MC < 70%, the fire has the potential to reach the frozen soil layer (permafrost) with a greater depth of burning, following $DOB = 2.36[82MC - 57 - \alpha(Y - 2015)]^{-0.38} - 1$. Although such peatland fire scenarios are still rare under the current arctic and boreal temperature, such a probability may increase in future driven by the accelerating climate change.

Referring to literature measurement [9,12,20,39,40], the mean carbon content of boreal peat is relatively stable at around 45±5%, while the dry bulk density has a wide range from 50 to 300 kg/m^3 and increases with the depth. By using a typical dry bulk density of 100 kg/m^3, the current carbon emission flux from smouldering peat fire is estimated to be 7.1 kg C/m^2 (Fig. A10.2c), which is within the field measurement of 0.4-9.5 kg C/m^2 during the 2007 Anaktuvuk River fire in Alaska [9,41].

About 0.5% of the entire boreal peatland is expected to burn annually [42]. Thus, the average carbon loss flux from the entire boreal peatland is 0.036 kg C/m^2/year in 2015, which is higher than the annual net ecosystem carbon gain without fire (0.03 kg C/m^2) [9,41,43]. Peatlands are the most abundant in the boreal region, where they cover roughly 4×10^6 km^2 of Earth land, that is, 80% of peatland in the world [13]. Under the burn probability of 0.5% [42], the annual total burned area is estimated to be 2×10^4 km^2/year in the boreal peatland. We can then estimate that the annual carbon loss in 2015 is around 143 Mt C/year (Fig. 10.5), which is ~50 times the annual net C sink for the entire arctic and subarctic tundra biome (3-4 Mt C/year) [44].

10.3.4 Carbon loss at different global warming scenarios

As the DOB is expected to increase with global warming, we can scale up Eq. 10.1 and predict the future carbon emission flux per peat fire [kg C/m^2] after the year 2015 as $\dot{m}_C'' = 106[42 \cdot \mathrm{MC} - 28 - \alpha(Y - 2015)]^{-0.38} - 45$. Under the current boreal warming rate of 0.44 °C/decade [3], the carbon emission flux may increase from 7.1 kg C/m^2 in 2015 to 12.8 kg C/m^2 in 2050 and 27.2 kg C/m^2 in 2100 (Fig. A10.2c). Then, by assuming that the annual burn probability is fixed to 0.5%/year in the 21st century, we can predict the future annual carbon emissions from all boreal peatland fires [Mt C/year] as

$$\dot{m}_C = 2100[42MC - 28 - \alpha(Y - 2015)]^{-0.38} - 900 \tag{10.2}$$

Thus, the warmer peatland may approximately release 256 Mt C/year in 2050 and 544 Mt C/year in 2100, that is, almost 100-200 times of annual net C sink for the current entire arctic tundra biome [44]. We further estimate the cumulative carbon loss as 28 Gt net over the entire 21st century (see subplot in Fig. 10.5 and Fig. A10.2d). Such a carbon loss is almost three times that from burning fossil fuels in 2014 (~10 Gt) [45] and 1.6% of 1,700 Gt carbon stock in permafrost [28,46,47].

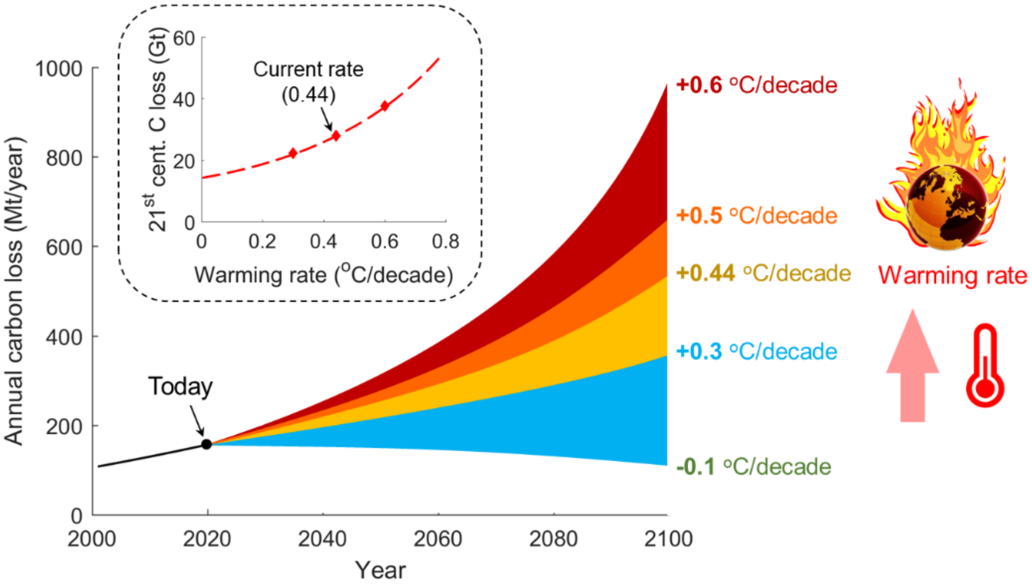

Fig. 10.5. Estimates of carbon loss in the 21st century from boreal peatland fires under different warming scenarios.

The anthropological greenhouse gas emissions are expected to increase in the next few decades continuously [44]. The Intergovernmental Panel on Climate Change (IPCC) estimates that the Earth may warm by 6 °C in the 21st century, if the whole world has not implemented any climate reduction policies [48]. Therefore, herein we further estimate the potential carbon loss during the fire at different warming scenarios by the year 2100 (Fig. 10.5). If future human-made greenhouse emissions further exacerbate the boreal warming rate to 0.6 °C/decade, the potential carbon loss from all boreal peatland fires may increase to 969 Mt in 2100, which is almost seven times the current level and doubles the emissions in 2100 under the current warming rate of 0.44 °C/decade. And the total carbon loss may reach 38 Gt during the 21st century. On the other hand, if current climate and energy policies are successfully implemented to reduce the warming rate to 0.3 °C/decade, we estimate a reduced carbon loss to 360 Mt in 2100, that is, about 21% decrease compared to the current warming rate, and the total carbon loss may decrease to 22 Gt during the 21st century. Therefore, slowing down the global warming rate may effectively reduce greenhouse gas emissions from peatland fires.

10.3.5 Fire impact on the Earth ecosystem

Nitrogen is one of the critical elements that control plant productivity in the ecosystem. Therefore, the soil nitrogen loss in fire may affect the postfire carbon absorption for an extended period [9,49]. Herein, we simultaneously estimate the nitrogen (N) loss from boreal peatland fires (Fig. A10.3). Assuming the mean peat nitrogen content of 1.5% [39] and the same burn probability of 0.5% [42], the estimated average nitrogen loss flux from the entire boreal peatland is 1.19 g N/m^2/year in 2015, and it may sharply increase to 4.54 g N/m^2/year in 2100 under the current trend of warming. In contrast, the annual nitrogen accumulation rate due to both deposition and biological fixation in Alaska is estimated to be at most 0.16 g N/m^2/year [9,50], which is one order magnitude smaller than the nitrogen loss rate. Therefore, the nitrogen loss from smouldering fire in peatlands is an irreversible process and even worse than carbon losses.

Except for the direct carbon emissions through extensive burning, in the permafrost regions, the wildfires in peatlands also have a long-term impact on the deeper permafrost layer. For example, it was estimated that the postfire ground thermal conductivity might increase ten times, whereas the surface albedo may decrease by 50% [51]. Furthermore, wildfires in peatlands within permafrost regions cause the unburned permafrost to thaw through the deepening of the active layer and the expansion of talik on the peat plateaus (Fig. 10.4b) [17]. The impacts of permafrost thawing include the increasing surface runoff, dissolving organic matter and methylmercury in surface water, loss of wildlife habitat, reducing land use, and increasing greenhouse gas emissions due to the microbial decomposition [17,28,52]. It was projected that no peatland permafrost would remain after global warming for 6 °C [53], and more frequent wildfires would accelerate this process [17].

Projections also suggest that the slow thawing may release about 200 Gt of carbon over the next 300 years under the current warming scenario [47]. Nevertheless, it might be vastly underestimated without considering the carbon emissions from peatland fire. As we projected, the carbon emissions from boreal peatland fires would accelerate under climate warming, and the extent of permafrost thaw would also expand due to the extensive heating from the underground peat fires. With the postfire expansion of thawing permafrost, substantial quantities of organic soil may become vulnerable to biodegradation by microorganisms [17]. Consequently, enormous greenhouse gases, including carbon dioxide, methane, and nitrous oxide, may be released into the atmosphere, intensifying the positive feedback to climate change and deteriorating the ecosystem [47,54,55].

The extensive wildfires could transport substantial quantities of particulates and volatile compounds via the atmosphere and produce large fluxes of nutrients into the ocean ecosystem [56]. In particular, the cycle of nitrogen (N) and phosphorous (P) are two main contributors to the ocean's primary productivity [57]. Fire improves the supply of N and P to the ocean either via aerial deposition from aerosol and smoke or by increasing the influx of ash (rich in P) into the ocean [20]. The increase of P and N contributes to the growth and reproduction of aquatic plants, algae, and cyanobacteria [56,58]. The resulting oxygen reduction in the water may cause massive deaths of fish and other species and release enormous toxic gases [59]. As we predict a climate-induced increase of fire severity and precipitation in boreal peatlands, these extra N and P fluxes from fires would potentially exacerbate global water eutrophication and ecological damage. Therefore, it is imperative for water quality management strategies to consider the impact of increasing peatland fires on marine ecosystems.

10.4 Conclusions

In this chapter, we reveal the smouldering fire threshold of boreal peatlands as a function of environmental temperature (-45 - 40 °C) and gravimetric moisture contents (25% to 150%). Based on the data of vertical soil temperature profile, we then successfully predict the depth of burn in boreal peatlands to be 0.16 m in 2015 that is close to multiple field measurements. We predict the future depth of burn as $DOB = 2.36[42\mathrm{MC} - 28 - \alpha(Y - 2015)]^{-0.38} - 1$, given a boreal warming rate, α (°C/year). Under the current boreal warming rate of 0.44 °C/decade, we estimate that the carbon emissions per unit burnt boreal peatlands may increase from 7.1 kg C/m^2 in 2015 to 12.8 kg C/m^2 in 2050 and 27.2 kg C/m^2 in 2100. With a burning area of 0.5%, the total soil carbon emissions in the entire 2×10^4 km^2 boreal peatlands may increase from 143 Mt in 2015 to 256 Mt in 2050 and 544 Mt in 2100. The cumulative carbon loss of the 21st century is estimated to be 28 Gt, which is three times of emissions from burning fossil fuels in 2014.

If the current energy policies successfully reduce the warming rate to 0.3 ℃/decade, we predict a reduction of one third carbon emissions from boreal peatland fires. With increasing fire frequency and severity under a warming climate, emissions from boreal peatland fires are expected to influence the ecosystem through multiple biogeochemical processes. This research helps evaluate the fire risks of boreal peatlands and estimate climate-induced carbon emissions from boreal peatland fires in the 21st century. Future research efforts will be taken to improve the accuracy further and quantify the uncertainties of our model.

Acknowledgements

This research is funded by the National Natural Science Foundation of China (NSFC) No. 51876183 and the SFPE Educational & Scientific Foundation (Student Research Grant). S. Lin would like to thank Y. Liu for the help in the lab.

References

[1] Montzka SA, Dlugokencky EJ, Butler JH. Non-CO 2 greenhouse gases and climate change. Nature 2011;476:43–50.

[2] Park SW, Kim JS, Kug JS. The intensification of Arctic warming as a result of CO2 physiological forcing. Nat Commun 2020;11:1–7.

[3] Batir JF, Hornbach MJ, Blackwell DD. Ten years of measurements and modeling of soil temperature changes and their effects on permafrost in Northwestern Alaska. Glob Planet Change 2017;148:55–71.

[4] Helmore E. “Unprecedented”: more than 100 Arctic wildfires burn in worst ever season. Guard 2019.

[5] Héon J, Arseneault D, Parisien MA. Resistance of the boreal forest to high burn rates. Proc Natl Acad Sci U S A 2014;111:13888–93.

[6] Vinas M-J. NASA studies how arctic wildfires change the world. NASA 2019.

[7] Page SE, Siegert F, Rieley JO, Boehm H V., Jayak A, Limink S, et al. The amount of carbon released from peat and forest fires in Indonesia during 1997. Nature 2002;420:61–6.

[8] Nelson K, Thompson D, Hopkinson C, Petrone R, Chasmer L. Peatland-fire interactions: A review of wildland fire feedbacks and interactions in Canadian boreal peatlands. Sci Total Environ 2021;769:145212.

[9] Mack MC, Bret-Harte MS, Hollingsworth TN, Jandt RR, Schuur EAG, Shaver GR, et al. Carbon loss from an unprecedented Arctic tundra wildfire. Nature 2011;475:489–92.

[10] Kohlenberg AJ, Turetsky MR, Thompson DK, Branfireun BA, Mitchell CPJ. Controls on boreal peat combustion and resulting emissions of carbon and mercury. Environ Res Lett 2018;13.

[11] Xu J, Morris PJ, Liu J, Holden J. PEATMAP: Refining estimates of global peatland distribution based on a meta-analysis. Catena 2018;160:134–40.

[12] Lin S, Sun P, Huang X. Can peat soil support a flaming wildfire? Int J Wildl Fire 2019;28:601–13.

[13] Turetsky MR, Benscoter B, Page S, Rein G, Van Der Werf GR, Watts A. Global vulnerability

of peatlands to fire and carbon loss. Nat Geosci 2015;8:11–4.

[14] Grau-Andrés R, Davies GM, Gray A, Scott EM, Waldron S. Fire severity is more sensitive to low fuel moisture content on Calluna heathlands than on peat bogs. Sci Total Environ 2018;616–617:1261–9.

[15] Jones BM, Grosse G, Arp CD, Miller E, Liu L, Hayes DJ, et al. Recent Arctic tundra fire initiates widespread thermokarst development. Sci Rep 2015;5:1–13.

[16] Koven CD, Ringeval B, Friedlingstein P, Ciais P, Cadule P, Khvorostyanov D, et al. Permafrost carbon-climate feedbacks accelerate global warming. Proc Natl Acad Sci U S A 2011;108:14769–74.

[17] Gibson CM, Chasmer LE, Thompson DK, Quinton WL, Flannigan MD, Olefeldt D. Wildfire as a major driver of recent permafrost thaw in boreal peatlands. Nat Commun 2018;9:3041.

[18] Wilkinson SL, Tekatch AM, Markle CE, Moore PA, Waddington JM. Shallow peat is most vulnerable to high peat burn severity during wildfire. Environ Res Lett 2020;15:104032.

[19] Dobinski W. Permafrost. Earth-Science Rev 2011;108:158–69.

[20] Belcher CM, Yearsley JM, Hadden RM, Mcelwain JC, Rein G. Baseline intrinsic flammability of Earth ' s ecosystems estimated from paleoatmospheric oxygen over the past 350 million years. Proc Natl Acad Sci 2010;107:22448–22453.

[21] Huang X, Rein G. Interactions of Earth's atmospheric oxygen and fuel moisture in smouldering wildfires. Sci Total Environ 2016;572:1440–6.

[22] Frandsen WH. The influence of moisture and mineral soil on the combustion limits of smouldering forest duff. Can J For Res 1987;16:1540–4.

[23] Lin S, Huang X. Quenching of smouldering: Effect of wall cooling on extinction. Proc Combust Inst 2021;38:5015–22.

[24] Lin S, Liu Y, Huang X. How to Build a Firebreak to Stop Smouldering Peat Fire : Insights from a Laboratory-Scale Study. Int J Wildl Fire 2021.

[25] Schuur EAG, McGuire AD, Schädel C, Grosse G, Harden JW, Hayes DJ, et al. Climate change and the permafrost carbon feedback. Nature 2015;520:171–9.

[26] Léger E, Dafflon B, Robert Y, Ulrich C, Peterson JE, Biraud SC, et al. A distributed temperature profiling method for assessing spatial variability in ground temperatures in a discontinuous permafrost region of Alaska. Cryosphere 2019;13:2853–67.

[27] Lin S, Cheung YK, Xiao Y, Huang X. Can rain suppress smouldering peat fire ? Sci Total Environ 2020;727:138468.

[28] Huang X, Rein G. Downward Spread of Smouldering Peat Fire: the Role of Moisture, Density and Oxygen Supply. Int J Wildl Fire 2017;26:907–18.

[29] Rein G. Smouldering Fires and Natural Fuels. In: Claire M. Belcher, editor. Fire Phenom. Earth Syst., New York: John Wiley & Sons, Ltd.; 2013, p. 15–34.

[30] Smith LC, Beilman DW, Kremenetski K V., Sheng Y, MacDonald GM, Lammers RB, et al. Influence of permafrost on water storage in West Siberian peatlands revealed from a new database of soil properties. Permafr Periglac Process 2012;23:69–79.

[31] Wang X, Jiang D, Lang X. Future extreme climate changes linked to global warming intensity. Sci Bull 2017;62:1673–80.

[32] Sirin AA, Makarov DA, Gummert I, Maslov AA, Gul'be YI. Depth of Peat Burning and Carbon Loss during an Underground Forest Fire. Contemp Probl Ecol 2020;13:769–79.

[33] Benscoter BW, Thompson, D. K., Waddington JM, Flannigan MD, Wotton BM, de Groot WJ,

Turetsky MR. Interactive effects of vegetation, soil moisture and bulk density on depth of burning of thick organic soils. Int J Wildl Fire 2011;20:418–29.

[34] Davies GM, Gray A, Rein G, Legg CJ. Peat consumption and carbon loss due to smouldering wildfire in a temperate peatland. For Ecol Manage 2013;308:169–77.

[35] Ballhorn U, Siegert F, Mason M, Limin S. Derivation of burn scar depths and estimation of carbon emissions with LIDAR in Indonesian peatlands. Proc Natl Acad Sci 2009;106:21213–8.

[36] Treat CC, Jones MC, Camill P, Gallego-Sala A, Garneau M, Harden JW, et al. Effects of permafrost aggradation on peat properties as determined from a pan-Arctic synthesis of plant macrofossils. J Geophys Res Biogeosciences 2016;121:78–94.

[37] Huang X, Rein G. Upward-and-downward spread of smouldering peat fire. Proc Combust Inst 2019;37:4025–33.

[38] Oechel WC, Vourlitis GL, Verfaillie J, Crawford T, Brooks S, Dumas E, et al. A scaling approach for quantifying the net CO2 flux of the Kuparuk River Basin, Alaska. Glob Chang Biol 2000;6:160–73.

[39] Zoltai SC, Morrissey LA, Livingston GP, De Groot WJ. Effects of fires on carbon cycling in North American boreal peatlands. Environ Rev 1998;6:13–24.

[40] Shaver GR, Chapin FS. Production: Biomass relationships and element cycling in contrasting arctic vegetation types. Ecol Monogr 1991;61:1–23.

[41] Mcguire AD, Anderson LG, Christensen TR, Scott D, Laodong G, Hayes DJ, et al. Sensitivity of the carbon cycle in the Arctic to climate change. Ecol Monogr 2009;79:523–55.

[42] Boden TA, Marland G, Ndres RJ. Global, Regional, and National Fossil-Fuel CO2 Emissions (1751 - 2014). Environ Syst Sci Data Infrastruct a Virtual Ecosyst (United States); Carbon Dioxide Inf Anal Cent (CDIAC), Oak Ridge Natl Lab (ORNL), Oak Ridge, TN (United States) 2017.

[43] Reyes A V., Cooke CA. Northern peatland initiation lagged abrupt increases in deglacial atmospheric CH4. Proc Natl Acad Sci U S A 2011;108:4748–53.

[44] Turetsky MR, Abbott BW, Jones MC, Walter Anthony K, Olefeldt D, Schuur EAG, et al. Permafrost collapse is accelerating carbon release. Nature 2019;569:32–4.

[45] IPCC. Climate change 2007: Synthesis Report. Geneva,Switzerland: 2007.

[46] Szép R, Bodor Z, Miklóssy I, Niță IA, Oprea OA, Keresztesi Á. Influence of peat fires on the rainwater chemistry in intra-mountain basins with specific atmospheric circulations (Eastern Carpathians, Romania). Sci Total Environ 2019;647:275–89.

[47] Hobara S, McCalley C, Koba K, Giblin AE, Weiss MS, Gettel GM, et al. Nitrogen fixation in surface soils and vegetation in an arctic tundra watershed: A key source of atmospheric nitrogen. Arctic, Antarct Alp Res 2006;38:363–72.

[48] Yoshikawa K, Bolton WR, Romanovsky VE, Fukuda M, Hinzman LD. Impacts of wildfire on the permafrost in the boreal forests of interior Alaska. J Geophys Res D Atmos 2003;108:8148.

[49] Ding Y, Zhang S, Zhao L, Li Z, Kang S. Global warming weakening the inherent stability of glaciers and permafrost. Sci Bull 2019;64:245–53.

[50] Hugelius G, Loisel J, Chadburn S, Jackson RB, Jones M, MacDonald G, et al. Large stocks of peatland carbon and nitrogen are vulnerable to permafrost thaw. Proc Natl Acad Sci U S A 2020;117:20438–46.

[51] Camill P. Permafrost thaw accelerates in boreal peatlands during late-20th century climate warming. Clim Change 2005;68:135–52.

[52] Biskaborn BK, Smith SL, Noetzli J, Matthes H, Vieira G, Streletskiy DA, et al. Permafrost is warming at a global scale. Nat Commun 2019;10:1–11.

[53] Spencer CN, Gabel KO, Hauer FR. Wildfire effects on stream food webs and nutrient dynamics in Glacier National Park, USA. For Ecol Manage 2003;178:141–53.

[54] Kump LR, Mackenzie FT. Regulation of atmospheric O2: Feedback in the microbial feedbag. Science (80-) 1996;271:459–60.

[55] Smith HG, Sheridan GJ, Lane PNJ, Nyman P, Haydon S. Wildfire effects on water quality in forest catchments: A review with implications for water supply. J Hydrol 2011;396:170–92.

[56] Santos RMB, Sanches Fernandes LF, Pereira MG, Cortes RMV, Pacheco FAL. Water resources planning for a river basin with recurrent wildfires. Sci Total Environ 2015;526:1–13.

CHAPTER 11: Concluding Remarks and Future Works

11.1 Impacts of the present research

In this thesis, near-limit smouldering fire dynamics including ignition limit, transition limit, propagation limit and extinction limit have been studied.

The ignition of combustible materials is fundamental to fire safety analyses, defining initiation and leading to the eventual growth of sometimes devastating fire events. Therefore, the ignition limits of smouldering combustion have been thoroughly discussed in Part A (Chapter 2-4). In Chapter 2, the ignition limits of organic-rich peat soil are quantified which are insensitive to the moisture contents. Piloting a flame on peat is found to be more difficult than starting a smouldering peat fire, requiring a higher minimum heat flux and three times more ignition energy. Moreover, defining a constant ignition temperature or mass flux is inappropriate for wet wildland fuels which may have a large mositure content. In Chapter 3, we investigated the smouldering ignition limit of multi-layered thin tissue paper by small irradiation spots. The measured minimum spot irradiation for smouldering ignition is not constant but remains much higher than the 11 kW/m^2 measured from cone-calorimeter tests. As the diameter of irradiation spots decreases from 20.0 mm to 1.5 mm, the minimum irradiation necessary for smouldering ignition increases from 17.5 kW/m^2 to 205 kW/m^2, and the ignition energy increases from 0.084 MJ/m^2 to 2.0 MJ/m^2, revealing that the importance of lateral conductive cooling within the fuel becomes dominant for a smaller spot ignition area. Eventually, a physical-based 2-D computational model is built to demonstrate and reproduce the experimental phenomena. After ignition, a flame is sometimes found not to be able to sustain above the charring materials. Nevertheless, extinction of the flame is not the end of a fire, as it may be followed by the smouldering. Such a transition limit of flaming to smouldering is thorougly studied in Chapter. 4, where a unique wood combustion mode showing a near-limit blue flame was identified as an intermediate combustion mode between the buoyancy-controlled yellow flame and the smouldering combustion. Below the critical irradiation (40 kW/m^2), the intense yellow flame directly transitions to smouldering when the mass flux decreases to about 4.0 g/m^2·s for all wood samples. Above the critical irradiation, on the other hand, the near-limit blue flame may still survive until transitioning to smouldering at the mass flux of 1.0 g/m^2·s. Thus, it may redefine the transition limit of flaming to smouldering transition of timber materials under external radiation.

Part B (Chapter 5-7) focuses on the quenching limit and quenching diameter of smouldering combustion. In Chapter 5, the smouldering quenching diameter was quantified for the first time, which is on the order of centimetre and much larger than the flame. Like the flame, the smouldering quenching diameter is also comparable to the thickness of the reaction front, and it increases as the wall cooling increases and the oxygen supply decreases, which are explained analytically. The minimum smouldering temperature (~250℃) and propagation rate (~0.5 cm/h or 0.1 mm/min) was found at the quenching limit. In Chapter 6, a 2-D model was built using open-source code Gpyro to computationally study the quenching diameter of smouldering combustion for the first time. This is the first time to use a comprehensive physics-based model to predict the quenching behaviour of smouldering combustion at different ambient conditions, verifying and enriching our experimental observation. In Chapter 7, the application of combustion theory of quenching and quenching distance in firefighting activities was explored through constructing peat firebreak. There are two criteria for an effective peat firebreak: (I) adding water to make the peat layer sufficiently wet (> 115% MC in the present work), and (II) ensuring the peat layer is thinner than the quenching thickness (< 5 cm). Moreover, the sloped, trench-shaped firebreak is recommended to avoid a landslide and guide the water flow to keep the peat layer wet.

Part C (Chapter 8-10) further explores the environmental impacts on the smouldering limits. In Chapter 8, the smouldering propagation rate on consolidated biomass and the blow-off limit under concurrent and opposed external airflows up to 50 m/s were quantified. As the airflow velocity increases, smouldering propagation rate first increases to its maximum value (Oxygen-limited Regime), and subsequently remains stable (Thermal Regime), regardless of the airflow direction. Afterwards, it slightly decreases (Chemical Regime) until blow-off, and the blow-off of opposed smouldering is easier, similar to the pattern of flame spread. The blow-off airflow velocity (13~46 m/s) of smouldering combustion is around ten times larger than that of flaming combustion, and it decreases as the fuel diameter or density increases. Chapter 9 assessed the underlying mechanism of rain in suppressing the smouldering peat fire in the shallow soil layer up to 15 cm deep through laboratory experiments. The minimum rainfall intensity to extinguish the peat fire is roughly 4 mm/h, so that the persistent light rain cannot suppress such smouldering wildfire. The required rain duration for extinguishing smouldering peat fire decreases with the rainfall intensities, and is much longer than that for extinguishing flaming wildfire. The required rainfall depth for extinguishing peat fire gradually decreases with the rainfall intensity and approaches a minimum value of 13 mm under violent rain. Therefore, the short-term violent rain is most effective for suppressing the persistent smouldering peat fire. In Chapter 10, the smouldering fire threshold of boreal peatlands was revealed as a function of environmental temperature (-45 - 40 °C) and gravimetric moisture contents (25% to 150%). Under the current boreal warming rate of 0.44 ℃/decade, it is estimated that the carbon emissions per unit burnt boreal peatlands may increase from 7.1 kg C/m^2 in 2015 to 12.8 kg C/m^2 in 2050 and 27.2 kg C/m^2 in 2100. With a burning area of 0.5%, the total soil carbon emissions in the entire 2×10^4 km^2 boreal peatlands may increase from 143 Mt in 2015 to 256 Mt in 2050 and 544 Mt in 2100. The cumulative carbon loss of the 21st century is estimated to be 28 Gt, which is three times of emissions from burning fossil fuels in 2014. If the current energy policies successfully reduce the warming rate to 0.3 ℃/decade, a reduction of one third carbon emissions from boreal peatland fires is estimated. With increasing fire frequency and severity under a warming climate, emissions from boreal peatland fires are expected to influence the ecosystem through multiple biogeochemical processes.

11.2 Future work

Smouldering combustion is still an emerging and fascinating multi-discipline topic in combustion, fire ecology and geoscience. Although its critical hazards, significantly few studies have been conducted in each of the related discipline. Many aspects are still not well understood and deserve more in-depth research efforts. Some interesting research are suggested for future research:

1. Peat, as a charring material, can sustain both flaming and smouldering. Therefore, flame can spread over the surface of peat soil, and the size of peat fire can expand much faster than the expected creeping smouldering spread inside the peat layer. However, currently, little research has investigated the flaming peat fires. More insights can be learned by starting with some well-controlled bench-scale experiments to study the rate of flame spread over peat soil under external radiation.
2. Many ignition events leading to both structure and wildland fires occur remotely by a point heating source such as concentrated sunlight. However, to the best of the authors' knowledge, the remote ignition phenomenon by small irradiation spots has not received a detailed and quantitative study, presenting a key knowledge gap. Future experiments and numerical simulations are needed to further reveal the underlying physical and chemical process of smouldering spot ignition for different fuels.

3. The close collaboration with firefighters, forest service and fire ecology communities can improve current wildfire management and inspire more new fundamental research topic. Much more efforts should be taken to transfer the newly found knowledge to othe scientific communities. For example, although two criteria for an effective peat firebreak were established in Chapter 6, how to apply them in real fire scenario is still a issue needs to solve.
4. Currently, there are still little study on developing comprehensive 2-D or 3-D models which could provide more insight on high-dimensional and geometric effects. As smouldering fire is a creeping process, it is time-consuming to model this long-lasting fire phenomenon. Future work should focus on exploring how to balance the accuracy and complexity of model.
5. Smouldering fire can be sustained in an extremely low oxygen concentration (~11%) and propagate below the ground surface. Therefore, it is extremely difficult to detect the existence of smouldering fire in wildlands. Therefore, future work should be focus on the development of new methods to detect the underground smouldering wildfires. As an incomplete combustion process, the CO emissions may play an important role in detecting smouldering fire, which requires further explorations.
6. Boreal peatlands are increasingly vulnerable to wildfires as climate change continues accelerating. Therefore, more accurate models should be established to predict the future carbon loss due to the smouldering wildfires. A new model to predict the climate-induced carbon loss from boreal-arctic peatland fires was built in Chapter 9. Future research will focus on quantifying the influence of different parameters on our model and further improving the predictions of peat fire carbon loss.